NONLINEAR JOINT REPRESENTATION IN PUSHOVER ANALYSIS OF OFFSHORE STRUCTURES

ZHANG YANG

NATIONAL UNIVERSITY OF SINGAPORE

2013

NONLINEAR JOINT REPRESENTATION IN PUSHOVER ANALYSIS OF OFFSHORE STRUCTURES

ZHANG YANG

(B. Eng. Tsinghua University)

A THESIS SUBMITTED

FOR THE DEGREE OF DOCTOR OF PHILOSOPHY

DEPARTMENT OF CIVIL AND ENVIRONMENTAL ENGINEERING

NATIONAL UNIVERSITY OF SINGAPORE

2013

DECLARATION

I hereby declare that this thesis is my original work and it has been written by me in its entirety. I have duly acknowledged all the sources of information which have been used in the thesis.

This thesis has also not been submitted for any degree in any university previously.

Zhang Yang 26. July 2013

ZHANG YANG

26 July 2013

Acknowledgement

I would like to express my deepest gratitude to my supervisors Professor Choo Yoo Sang and Dr. Qian Xudong for their invaluable assistance, patient advice and support throughout my research at National University of Singapore. Without their guidance and persistent help this thesis would not have been possible.

I would like to specially thank Professor Peter Marshall and Dr. Tore Holmås for their helpful discussions and valuable contributions during the project.

Sincere thanks also extend to my colleagues and friends at Center for Offshore Research and Engineering (NUS), Dr. Shen Wei, Dr. Chen Zhuo, Dr. Yang Wuchao, Dr. Li Ya, and Dr. Ou Zhiyong for sharing with me their ideas during the last four years. All experiments have been conducted in the Structural Engineering Laboratory of National University of Singapore with the help of the staff there. I want to thank Mr. Koh and Mr. Ang for their much helpful advice during tests. I heartily acknowledge the support of Lloyd's Register Foundation towards funding my research and development program in the Centre for Offshore Research and Engineering in National University of Singapore.

I would also like to thank my friends Dr. Jin Jiangang, Mr. Lin Kunpeng and Mr. Huang Sixuan for sharing with me happiness in the passed four years.

Finally, my heartfelt thanks go to my parents and my wife for their support during the last few years. Without them, everything I do will be pallid and meaningless.

Table of Contents

Summary

The extended service of steel offshore jackets beyond their initial 20 years design life has become a common practice due to economical considerations. The structural integrity reassessment of such platforms requires advanced nonlinear frame analyses with an accurate representation of local joint responses under overloading conditions. All the existing joint formulations for Circular Hollow Section (CHS) joints remain empirical in nature and lack strong theoretical foundations, which limit their transferability to a wide range of joint geometry, material and loading conditions foreseeable in real offshore platforms.

This study aims to develop a theoretical-based joint representation to capture the load-deformation relationship for CHS X- and K-joints under nonlinear deformations and possible unstable fracture failures. The pushover analysis of offshore jackets will implement the proposed joint formulations to investigate the offshore structural behavior under the predominantly static loading condition. The result will allow rational decisions to be made concerning the structural integrity of existing jacket systems.

The current study investigates the behaviour of CHS X- and K-joints, which remain widely used in offshore jackets and jack-up platforms, based on numerical investigations with judicious calibrations against test results. The numerical simulation benefits from a finite element procedure, which transfers the model generated by a mesh generation program into the general purpose finite element package ABAQUS for the computation and post-processing. The proposed nonlinear formulation describes the load-deformation relationship of the CHS X- and K-joint through a simple function with coefficients dependent on the ultimate strength and the geometric parameters. The current study also proposes an η approach to evaluate the elastic-plastic energy release rate at the deepest crack front location using the plastic work under the load versus the load-line displacement curve for

large-scale tubular X- and K-joints. Coupled with the nonlinear joint formulation and the η approach, the subsequent study presents a new fracture formulation to describe the joint load-deformation characteristics caused by the ductile tearing and consequently unstable fracture failure in tubular joints under monotonically increasing brace tension.

The proposed formulation, implemented as joint-spring elements, provides a convenient approach to estimate the nonlinear joint behavior as well as the load-deformation relationship under the ductile tearing for CHS joints. The study also discusses the applicability of the proposed joint formulation to a realistic jacket structure.

Nomenclature

A area

A_{RF} area reduction factor

A_{crack} area of the crack surface

A_i geometric-dependent constant in the load-deformation formulation (i=1, 2 or 3)

A_{lig} area of the remaining ligament

A_w area of the brace-to-chord intersection

B thickness of the specimen

B_e effective chord length in Ring Model

B_{eff} effective width in the η approach

B_N net thickness for the side-grooved specimen

D_x translation along X-axis

D_y translation along Y-axis

D_z translation along Z-axis

E elastic modulus

I Moment of inertia of a member cross section

J elastic-plastic energy release rate

J_{IC} material critical fracture toughness

J_{ave} average elastic-plastic energy release rate along the crack front

J_{el} elastic component of the elastic-plastic energy release rate

J_i elastic-plastic energy release rate at a crack front location

J_{max} validity limit of the measurable J-resistance

J_{pl} plastic component of the elastic-plastic energy release rate

$\overline{J}$ average elastic-plastic energy release rate in the domain integral approach

K_a effective length factor

K_I stress-intensity factor

K_{MAX} maximum stress-intensity factor

L length of the specimen

L_{weld} weld length along the brace-to-chord intersection

L_r ratio of the available joint strength over the ultimate strength of the intact joint

M applied moment

M_E elastic bending moment

M_p moment capacity at the plastic hinge

M_u ultimate bending moment

M_y elastic yielding moment capacity

P applied load

P_E load at the elastic limit

P_{crack} capacity for the cracked joint

P_{ij} component of 1st Piola-Kirchhoff stress tensor

P_{intact} capacity for the intact joint

P_s joint capacity corresponding to serviceability limit state

P_u peak load

$\overline{P}$ non-dimensional applied load

$\overline{P_u}$ non-dimensional peak load

Q_β geometric parameter for the cracked joint capacity

R_x rotation along X-axis

R_y rotation along Y-axis

R_z rotation along Z-axis

S engineering stress

T kinetic energy density

T_i surface traction

U energy stored in a crack body

U_{pl} joint plastic work under the load versus load-line displacement curve

V_0	undeformed volume
W	width of the specimen
W_e	elastic work done
W_p	plastic work done
a	depth of the crack
a_0	depth of the initial crack
a_{notch}	depth of the machined notch
b	length of the remaining ligament
b_0	length of the remaining ligament for the initial crack
c	width of the surface crack
d_0	outer diameter of the chord
d_1	outer diameter of the brace
e	engineering strain
g	gap between two braces
g'	non-dimensional gap ratio (g/t_0)
k_0	initial stiffness of the joint
l_0	length of the chord
l_1	length of the brace
m	dimensionless constant in the η approach

m_p moment capacity per length at the plastic hinge

n material strain hardening exponent

n_i unit normal vector

q virtual displacement field in the domain integral approach

s position along the crack front

t_0 thickness of the chord

t_1 thickness of the brace

u_i displacement vector

w beam lateral displacement

Γ a counter-clockwise path around a crack tip

Δ_{LLD} load-line displacement

ΔB_i local segment length along the crack front

ΔL increment of the displacement

Δa crack extension

Δa_{max} maximum crack extension

Δ_{pl} plastic deformation

Ψ local dihedral angle

Ω potential energy of the applied load

α chord length to half chord diameter ratio ($\alpha = 2l_0/d_0$)

β brace diameter to chord diameter ratio ($\beta = d_1/d_0$)

δ deformation parameter

δ_B deformation due to the member

δ_E deformation at elastic limit

δ_F deformation due to the joint flexibility

δ_{Yura} Yura's deformation limit

δ_{cr} deformation parameter corresponding to the crack propagation

δ_i limit deformation parameter in the proposed joint formulation

δ_s deformation corresponding to serviceability limit state

δ_u deformation at the peak load

$\overline{\delta}$ non-dimensional deformation

$\overline{\delta_E}$ non-dimensional deformation at elastic limit

$\overline{\delta_u}$ non-dimensional deformation at the peak load

ε strain

ε_y yield strain

ε_p plastic strain

ϕ angle parameter for the surface crack

ϕ_E elastic limit rotation

ϕ_u rotation corresponding to the ultimate moment

φ	angle parameter
γ	chord radius to chord wall thickness ratio ($\gamma = d_0/2t_0$)
λ	plastic limit load parameter ($\lambda = W_p/W_e$)
η	dimensionless constant
θ	angle between the brace and chord centerline
θ_{pl}	plastic rotation
π	total potential energy
σ	true stress
σ_u	material ultimate strength
σ_v	nominal stress corresponding to the maximum shear stress
σ_y	material yield stress
τ	brace wall thickness over chord wall thickness ratio ($\tau = t_1/t_0$)
τ_{max}	maximum shear stress
ω	angle defining the position along the brace-to-chord intersection
ψ	angle parameter in the proposed joint formulation

List of Tables

List of Figures

Chapter 1

Introduction

1.1 Background

Circular Hollow Sections (CHS) remain widely used as structural elements due to their excellent properties in resisting compression, tension, bending and torsion loadings in all directions (Wardenier, 2002). The circular sections provide the optimal shape when exposed to wind and wave loadings because of their low drag coefficients. The significantly smaller surface area of a CHS member requires less protection and maintenance against corrosion as compared with an open section. All these advantages have led to broad applications of CHSs in the offshore industry.

Jacket platforms utilize mainly circular hollow section members to form a space frame supported by pile foundations. Figure 1.1 shows a typical jacket platform accompanied by a drilling unit, jack-up. Since the first modern jacket platform was built in the Gulf of Mexico in 1947, the jacket structure has become the dominant form for permanent offshore platforms in the shallow water region. Past decades have observed more than thousands of jacket platforms erected around the world in water depths from around 30 m to over 400 m.

Fig. 1.1: Typical offshore platforms: jacket and jack-up.

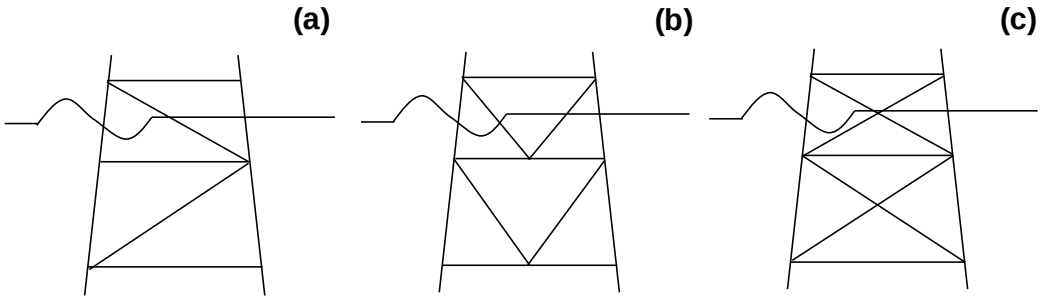

Fig. 1.2: Basic frame patterns in offshore jacket platforms: (a) diagonal brace; (b) K-brace; and (c) X-brace.

Different loading conditions *e.g.,* the significant vertical force or possible seismic loading, require different frame patterns employed in jacket platforms. Figure 1.2 displays several basic frame patterns commonly adopted in practice, including diagonal brace, K-brace and X-brace. Each frame pattern shows the specific load path through the member-connection interaction.

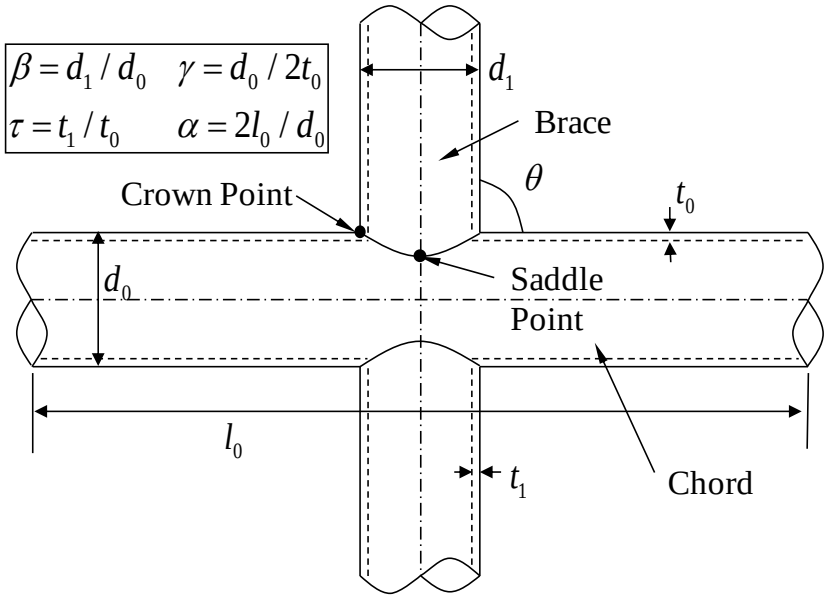

Fig. 1.3: Configuration of a typical CHS X-joint with non-dimensional joint parameters.

In a jacket structure, tubular joints become the dominant type for connections between different CHS members. A tubular joint generally consists of one or more separated bracing members, or braces, welded directly to a main continuous member, or chord. Figure 1.3 displays the configuration of a typical CHS X-joint, together with the practical non-dimensional geometric parameters. Classified based on various geometries and loading conditions, the common type of CHS joints includes: X-, T-, K- and DK- joints.

Practical engineering applications often evaluate the joint capacity and stiffness based on the non-dimensional parameters listed in Fig. 1.3. The brace to the chord diameter ratio, β, determines the brace-to-chord intersection area and dominant load paths under

different brace loading conditions. The chord radius to wall thickness ratio, γ, influences the chord wall resistance to bending, membrane action and shearing stresses under the brace remote loading. The brace to chord wall thickness ratio, τ, affects the stress distribution along the brace-to-chord intersection area. A very small τ may induce an early brace local buckling before the full joint capacity develops. Therefore, most of tubular joints employ a comparable thickness for braces and the chord, $\tau \approx 1.0$. α refers to the chord length to radius ratio, which may introduce the chord end constraint effect regardless of the joint configuration if α remains a small value. It also induces the chord bending effect for T-joints under the axial brace loading and K-joints under the unbalanced brace loading.

1.2 Motivation and Research Gap

Most of the operating offshore platforms possesses a twenty-year design life. However, improvements in the possible oil recovery from several fields have increased the interest for using these structures well beyond their initial design life. Many initiators *e.g.,* the increased topside loading, the additional environmental loading, or the damage found during inspections, *etc.*, activates the reappraisal of structural integrity for these existing jacket structures.

The structural integrity management of offshore jacket structures requires generally the consideration of the environmental loading change, the foundation response and the structural behavior. The seabed subsidence and upwardly revised design wave crests both lead to the increased risk of part or full inundation of the platform deck. The foundation of offshore structures should carry static, cyclic and transient loads without excessive deformations or vibrations in the platform (API, 2010). Eventually, the environmental loading, as well as uncertainties in the foundation response serve to evaluate the jacket

response.

The current design practice for analyzing offshore structures remains based on a linear-elastic frame analysis. The subsequent design procedure ensures that each element of the jacket meets the governing criteria on the component basis. However, the conventional design does not capture the reserve strength of the jacket beyond the required design resistance due to the redundancy and the alternative load path embedded in the frame pattern. Therefore, the reassessment of these old platform structures requires advanced nonlinear frame analyses, where accurate predictions of the static collapse and push-over analyses of structures exhibit an increasing importance.

An accurate evaluation of the nonlinear frame response requires correct representations of the local member and joint behaviors. The research of past decades has formed a strong basis to capture accurately the nonlinear member behavior (Hellan, 1995; Skallerud and Amdahl, 2002). The current design procedure commonly employs strong joint cans to fully develop the member strength so that the member buckling or yielding occurs prior to the joint failure. However, many platforms built before the 1980s adopt joints weaker than connecting members without thickened joint cans (Zettlemoyer, 2010). Due to the underestimation of the deformation and over-estimation of the ultimate capacity for the critical joint, the rigid joint hypothesis may cause severe deviation in the prediction of the frame failure mechanism. Therefore, the rigid joint assumption in the conventional frame analysis becomes no longer applicable in the evaluation of the nonlinear frame response. Improved understandings on the effect of nonlinear joint behavior on the frame response become necessary to develop a joint representation to capture the nonlinear joint characteristics in pushover analyses.

Previous researchers (USFOS, 2009; Dier and Hellan, 2002; Choo *et al.*, 2005) have proposed different joint formulations to characterize the nonlinear joint behavior under different loading conditions based on either numerical data or experimental data. How-

ever, the form of the joint representations and the insufficient database largely retard the accurate prediction of these joint models. All these joint models remain empirical in nature and lack strong theoretical foundations, which limit their transferability to a wide range of joint geometry, material and loading conditions foreseeable in real offshore platforms. The stiffness and capacity of the frame with low redundancy rely significantly on the critical joint components, which will redistribute the load path in the frame system after the member or joint failure. The generalization of a robust joint formulation applicable to different joint configurations becomes important for accurate predictions of the static collapse and push-over analyses of structures.

1.3 Scope of Research and Objective

CHS X- and K-joint remain dominant in the design of offshore jackets and jack-up platforms. The main objective of the current research focuses on developing a theoretical-based joint representation to capture the nonlinear characteristic and the load-deformation relationship for CHS X- and K-joints under different loading conditions. The study aims to integrate the proposed joint formulation into the pushover analysis to investigate the global structural behavior under the predominantly static loading condition. Cyclic and fatigue loading remain out of scope in the current study. The objectives of the research work are:

- To investigate the nonlinear joint behavior for two major types of CHS joint configurations: X- and K-joints.
- To develop the joint load-deformation formulation for CHS X- and K-joints with representation for the ductile tearing and the subsequent unstable fracture failure.
- To evaluate the nonlinear frame behavior by implementing the proposed joint formulations into pushover analyses.

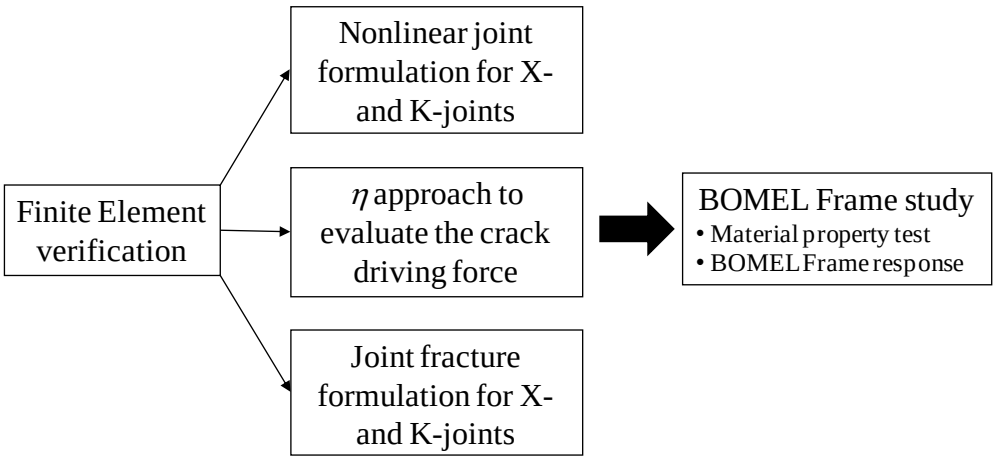

Fig. 1.4: Scope of the research work.

Figure 1.4 displays the frame of the current research work. The verification study firstly ensures the accuracy of finite element modelling procedure employed in the current research. The new joint formulation, verified against individual joint behaviors, characterizes the nonlinear joint load-deformation response before the joint resistance is limited by the material ductility, or extensive plastic deformations in the chord. The η approach, which relates the joint plastic work with the energy release rate, estimates the crack driving force level for a surface crack located at the hot-spot region for CHS joints. Based on the crack driving force level, the joint fracture formulation simulates the load-deformation behavior for CHS joints under ductile tearing and unstable fracture failure. Finally, the global frame analysis incorporates the proposed joint formulation to assess the structural integrity and evaluate the weak joint effect on the frame performance.

1.4 Original Contributions

The current research compares two existing mesh techniques, continuous mesh (Bowness and Lee, 1995) and mesh-tie (Qian *et al.*, 2005) to compute the energy release rate for surface cracks in tubular joints. The study evaluates advantages and disadvantages of

these two approaches in the modeling process and result accuracy.

The study proposes a new nonlinear load-deformation formulation for circular hollow section (CHS) X- and K-joints to be implemented in the pushover analysis of offshore frames, based on calibrated finite element results. The proposed formulation describes the load-deformation relationship of the CHS X- and K-joint through a simple function with coefficients dependent on the ultimate strength and the geometric parameters of the joint. The parametric formulation of coefficients, proposed in the joint representation, provides a convenient approach to characterize the load-deformation curve and eliminates the need for the elastic-plastic, large-deformation finite element analyses on CHS X- and K-joints. The experimental results from the large-scale 2-D and 3-D frame tests validate the accuracy of the proposed formulation, which is implemented in a nonlinear pushover analysis as joint-spring elements.

The current study extends the conventional plastic η approach for simple 2-D fracture specimens with through thickness cracks to large-scale 3-D tubular joints with surface cracks. Following the dimensionless analysis, the study demonstrates the η_{pl} value equals 1. Using the area under the load versus load-line displacement curve, the energy-based η approach estimates the elastic-plastic energy release rate for shallow surface cracks located at the weld toe at the chord near the tension brace in the CHS X- and K-joint. The η approach eliminates the complex pre-processing work and substantial computational resources required in the existing J-integral evaluation methods. The strong correlation between the elastic-plastic crack driving force and the joint plastic work provides a theoretical base for the plastic limit approach (Choo *et al.*, 2003) and proves the plastic work as a possible criterion for establishing a ductility limit for tubular joints (MSL, 2000).

The current work presents a new fracture formulation to describe the ductile tearing and unstable fracture failure for CHS joints under monotonically increasing brace tension. The joint fracture formulation, which allows an extending crack, follows the

load-deformation characteristics prescribed by the elastic-plastic energy release rate and an area reduction factor. This theoretical-based approach estimates closely the deterioration in the joint strength as the crack extends, as demonstrated by the comparison against the experimental results on tubular joints. The comparison against the reported frame test validates the joint formulation and proves its transferability to a wide range of joint geometry.

1.5 Contents of the Current Thesis

Chapter 1 introduces the research background and lays out the scope of proposed research. **Chapter** 2 conducts a comprehensive review on the previous experimental and numerical research on the offshore structural frame and tubular joints. **Chapter** 3 establishes a systematic and verified procedure to model CHS intact or cracked joints subjected to different types of brace loadings conditions. **Chapter** 4 proposes a new load-deformation formulation to describe the load-deformation relationship of the CHS X- and K-joints. **Chapter** 5 establishes a linear relationship between the external plastic work under load versus load-line displacement curve and the crack driving force along a weld-toe surface crack for tubular X- and K-joints. **Chapter** 6 extends the nonlinear joint representation to characterize the joint behavior during ductile tearing and unstable fracture failure. **Chapter** 7 integrates the joint model proposed in the previous chapters into the pushover analysis and performs the verification study on BOMEL frames. The incorporation of the proposed joint formulation into a realistic jacket structure demonstrates the importance of the weak joint simulation. **Chapter** 8 concludes the current research findings and introduces proposals of future work.

Chapter 2

Literature Review

2.1 Introduction

The industry demand for design and construction of offshore platforms initiates the research on tubular joints and frames from the 1950s. In the last 60 years, extensive research focuses on the evaluation of the local joint behavior and proposes different approaches to incorporate the joint effect into the global frame analyses.

This chapter summarizes firstly the previous experimental and numerical research on the local joint flexibility in the elastic range. The discussion then focuses on different analytical models and failure criteria employed in the joint ultimate capacity equation. These failure criteria represent the inherent load transfer mechanism for tubular joints under various loading conditions. The next section reviews the extensive experimental and numerical research on the tubular frame behavior, followed by the description of existing joint models. The summary and discussion provide a sound basis for the subsequent research.

2.2 As-Welded CHS Joint Flexibility

Previous researchers conduct extensive work on the elastic local joint flexibility (LJF) of as-welded joints over last three decades both experimentally and numerically. The early research mainly focuses on the simple planar tubular Y- and X-joint. With the development of the computational technology, the research work in recent years gradually extends to K- and DK- joints, and the numerical simulation becomes more and more dominant.

2.2.1 Experimental Research

Fellser and Spooner (1981) report an experimental study on the local flexibility of tubular Y- joints. The study tests a series of precision-cast epoxy resin models. Based on these 27 small-scale model tests, Fellser *et al.* (1986b) derive empirically elastic flexibility formulas for the Y-joint under the brace axial tension, in-plane bending and out-of-plane bending respectively. These formulas follow the polynomial functions of joint β and γ ratio based on the curve fitting. The result shows a good agreement with that from DNV (1977). Their research proposes a displacement ratio criterion to evaluate the effect of the joint flexibility in the structure analysis. The displacement ratio follows,

$$DR = \frac{\delta_F}{\delta_B} \tag{2.1}$$

where δ_F refers to the displacement at the brace end caused by the non-zero joint flexibility and δ_B denotes the brace member displacement produced by the same loading.

Fellser *et al.* (1986a) derive subsequently the flexibility matrices for multi-brace non-overlapping joints based on the previous test results by assuming that unloaded braces imposes no effect on the flexibility of other loaded brace members. By ignoring terms with the displacement ratio, as defined in Eq. 2.1, smaller than 0.1, their research derives

the polynomial functions for multi-brace gapped joints through the least-square regression analysis. The assumption of the fictitious unloaded braces provides only the upper bound for the joint flexibility, as reflected by the comparison with test results. The difference between the derived stiffness and the experimental test can be within 20% for the K-joint with a zero gap, and up to 60% for overlapped joints.

Tebbett (1982) presents the joint flexibility of three as-welded CHS T-joints and one X-joint under the brace axial tension, compression, in-plane bending and out-of-plane bending based on experimental tests. Underwater Engineering Group (1985) collects all existing results of local joint flexibility into one database. The database contains results of 24 specimens including Fessler's (1986b) epoxy resin models and Tebbett's (1982) steel models.

Kohoutek (1992) investigates the T-joint elastic stiffness under the brace in-plane bending by introducing a rigidity index into the global stiffness matrix. The rigidity index equals 0 for the hinge connection and 1 for the perfect rigid connection. The research calibrates the rigidity index by measuring the natural frequency of the test model. His research establishes a relationship between the rigidity index and the stress concentration factor (SCF) and provides a convenient and non-destructive dynamic approach to estimate the SCF for complicated joints.

Chen *et al.* (2001) report experimental results for 2 DK- and 2 X-joints, which employ various geometrical parameters and experience different loading combinations. The research demonstrates that the joint in-plane-bending elastic stiffness decreases with the increase of the brace inclination angle, θ.

2.2.2 Numerical Research

Bouwkamp (1980) investigates the effect of joint flexibilities on the elastic dynamic response of offshore jacket structures based on finite element analyses. The research models

joint-cans by proposed nine-node doubly curved iso-parametric degenerate shell elements, and employs beam elements to model members between joint-cans.

Efthymiou (1985) develops elastic flexibility parametric formulas for T- and TY-joints using thin-shell elements with welds modeled by solid elements. All finite element models employ a large α ratio to eliminate the chord end constrained effect. The joint experiences the brace out-of-plane bending or in-plane bending with two pin-supported chord ends. The joint flexibility refers to the net local deformation of the brace-to-chord intersection in the brace local coordinate caused by a unit load applied at the brace end. The local deformation derives from subtracting the global beam deformation of both the brace and chord members from the overall brace-end deformation. Axial terms follow the normalization against elastic modulus and the chord diameter, Ed_0, while the in-plane and out-of-plane bending flexibilities follow the normalization against Ed_0^3.

Buitrago *et al.* (1993) extend the previous research to a larger range for CHS T-, X-, gapped K- and overlapped K-joints based on the same FE approach as Efthymiou (1985). The finite element models remain fixed at the chord end against the deformation in all six degree of freedoms. The derived parametric formulas show good agreement with those developed by Efthymiou (1985) for CHS Y- and K-joints.

Ueda *et al.* (1986) present formulas to evaluate the local flexibility of T-, Y- and K-joints under the brace axial loading and in-plane bending conditions. The formulas derive from the results of prototype T-joints modeled by fine shell elements.

Chen and Wang (1985) develop special elements to evaluate the joint flexibility by dividing the brace-to-chord intersection curve into finite segments and treating the brace and chord as two substructures. By considering the equilibrium and compatibility between these two substructures, their research derives parametric formulas for the elastic stiffness of T-, Y- and K-joints (Chen *et al.*, 1990). Following Fellser *et al.*'s work (1986a), the research neglects the unloaded brace in deriving the flexibility of other loaded braces

for K-joints. Xu *et al.* (1996) propose parametric formulas for the elastic stiffness of YT- joint based on the same technique. Chen and Zhang (1993) extend this approach to evaluate the flexibility of one multi-brace tubular DKT- joint. The comparison of the DKT- joint flexibility terms against those from T-, Y-, and K- joints proves that the negligence of unloaded brace leads to the upper bound solution for the actual local joint flexibility in multi-brace joints (Fessler *et al.*, 1986a).

Holmas (1985; 1987) develops shell elements particularly for as-welded CHS joints based on the small-deformation theory. A series of concentrated loads along the brace-to-chord intersection curve represents the remote brace loading. The brace footprint, treated as a rigid body, maintains its shape during the overall loading process. The derived elastic joint flexibilities (Hellan, 1995) show close agreements with the previous result obtained by Fessler *et al.* (1986a), Buitrago (1993), Efthymiou (1985) and Chen (1990).

Romeijn *et al.* (1991) investigate the flexibility for uni-planar and multi-planar joints based on the finite element analysis. The research models T-, Y-, K- and DK- joints using shell elements by fixing the brace and chord ends against the translation and rotation.

Choo *et al.* (2005) investigate the nonlinear joint behavior for CHS X-, T-, K-, and DK- joints based on the finite element method using solid elements. The research models the connection with the complete joint penetration welds following AWS standard (2012). The proposed joint initial stiffness follows a non-dimensional format based on the non-dimensional strength and deformation parameters,

$$k_0 = \frac{P}{\delta}\frac{d_0 \sin\theta}{\sigma_y t_0^2} \tag{2.2}$$

Mirtaheri *et al.* (2009) study the effect of the brace axial force on the CHS Y-joint in-plane-bending stiffness based on FE analyses. The research models 25 joints, with different brace angles and initial axial loadings, using multi-axial shell elements and a

bilinear kinematic hardening material. The results prove the enhancement of the joint capacity in the brace tensile loading due to the reduction of the local buckling of the compression side.

2.2.3 Discussion

Table 2.1 and 2.2 summarize the research method and the geometric range in previous researches on the joint elastic flexibility, where "+" means the data is available at the corresponding loading condition and "-" means the opposite. Most research efforts utilize numerical analyses to examine the joint elastic flexibility, with hardly any experimental evidence for single-brace joints with $\beta = 1$ and for multi-planar joints. For finite element analyses, three dominate approaches exist to analyze the joint elastic flexibility:

1. The first method focuses on the chord deformation by neglecting the stiffening effect of the brace member. The chord wall deforms due to the distributed force along the brace-to-chord intersection caused by the brace loading. This assumption simplifies the analysis but becomes less valid for joints with a small angle of inclination, θ, or a large β ratio, as the contribution from the brace member stiffness increases (Holmas, 1985; Chen and Zhang, 1993).

2. The second approach considers the influence from the loaded brace alone, by ignoring the contribution from the unloaded brace, as assumed in Fessler *et al.*'s (1986a) experiments. This assumption simplifies the multi-brace joint into a single-brace joint, but only provides an upper bound solution for the joint flexibility (Wang *et al.*, 2007).

3. The third technique considers the interaction among all braces. Two treatments exist in considering the boundary condition of unloaded brace ends. The first treatment releases all unloaded brace ends. The local chord deformation corresponding

to the target brace loading also occurs at other brace-to-chord intersection areas (Efthymiou, 1985; Fessler and Spooner, 1981). This treatment reflects the local flexibility of unloaded braces by the cross-flexibility terms between braces. The second treatment fixes all the unloaded brace and chord ends against the translation and rotation. No local chord deformation occurs at the brace-to-chord intersection area for the unloaded brace (Romeijn *et al.*, 1991). This treatment provides a lower bound solution for the joint flexibility in multi-brace joints (Chen and Zhang, 1993).

Table 2.1: Geometry ranges and research methods for experimental tests on the local joint elastic flexibility.

Source	Basis	Y-joint			X-joint			Gapped K-joint			Overlapped K-joint			DK- joint		
		AX	IPB	OPB	AX	IPB	OPB	AX	IPB	OPB	AX	IPB	OPB	AX	IPB	OPB
DNV (1977)	Not avilable	-	+	+												
		$10 < \gamma < 30$														
		$0.33 < \beta < 0.8$														
		$\theta = 90°$														
Tebbett (1982)	4 steel models	+	+	+	+	+	+									
		$20 < \gamma < 32$			$\gamma = 48$											
		$0.3 < \beta < 0.9$			$\beta = 0.53$											
		$\theta = 90°$			$\theta = 90°$											
Fellser *et al.* (1986a)	Araldite models	+	+	+	+	+	+	+	+	+						
		$10 < \gamma < 20$			Based on			Based on								
		$0.35 < \beta < 0.75$			single brace data			single brace data								
		$45° < \theta < 90°$														
Kohoutek (1992)	Free vibration steel models	-	+	-												
		$13 < \gamma < 22$														
		$0.3 < \beta < 1.0$														
		$\theta = 90°$														
Chen *et al.* (2001)	Steel models				+	+	-							+	+	-
					$\gamma = 28$									$\gamma = 28$		
					$\beta < 0.76$									$\beta < 0.76$		
					$\theta = 90°$									$\theta = 51°$		

Table 2.2: Geometry ranges and research methods for numerical analyses on the local joint elastic flexibility.

Source	Basis	Y-joint			X-joint			Gapped K-joint			Overlapped K-joint			DK- joint		
		AX	IPB	OPB	AX	IPB	OPB	AX	IPB	OPB	AX	IPB	OPB	AX	IPB	OPB
Ueda *et al.* (1986)	FEM Shell element	+ $8<\gamma<30$ $0.35<\beta<0.75$ $\theta=90°$	+	-												
Burtrago *et al.* (1993)	FEM shell element	+ $10<\gamma<30$ $0.3<\beta<0.75$ $30°<\theta<90°$	+	+	+ $10<\gamma<30$ $0.3<\beta<0.75$ $30°<\theta<90°$	+	+	+ $10<\gamma<30$ $0.3<\beta<0.75$ $30°<\theta<90°$ $0.02\leq\varsigma\leq0.5$	+	+	+ $10<\gamma<30$ $0.3<\beta<0.75$ $30°<\theta<90°$ $0.02\leq\varsigma\leq0.5$	+	+			
Hellan (1995)	shell formulation	Same as Buitrago			Same as Buitrago			Same as Buitrago			Same as Buitrago					
Romeijin *et al.* (1991)	FEM shell element	+ $8<\gamma<32$ $0.2<\beta<0.65$ $45°<\theta<90°$	+	+				+ $8<\gamma<32$ $0.2<\beta<0.65$ $45°<\theta<90°$	+	+				+ $8<\gamma<32$ $0.2<\beta<0.65$ $45°<\theta<90°$	+	+
Choo *et al.* (2005)	FEM solid element	+ $3.5<\gamma<20$ $0.4<\beta<1$ $\theta=90°$	+	+	+ $3.5<\gamma<20$ $0.4<\beta<1$ $30°<\theta<90°$	+	+	+ $3.5<\gamma<20$ $0.4<\beta<1$ $30°<\theta<60°$	-	-	+ $3.5<\gamma<20$ $0.4<\beta<1$ $30°<\theta<60°$	-	-	+ $3.5<\gamma<20$ $0.4<\beta<1$ $30°<\theta<60°$	-	-

2.3 Analytical Model and Failure Criteria for CHS Joints

2.3.1 Analytical Model

Both experimental and numerical researches provide a huge database for the local joint flexibility formulas. However, all these formulas derive from the curve fitting without an analytical-based mechanics model. The accurate estimation of the joint ultimate strength becomes necessary in generating reliable joint load deformation curves. The analytical models reviewed in this section aim to predict the ultimate strength for tubular joints.

The complex stress fields and associated failure modes in tubular joints often complicate the prediction of the ultimate strength for tubular joints. Based on observations from the experimental and numerical research as well as the plasticity theory, previous researchers propose three major analytical models for CHS joints.

2.3.1.1 Punching Shear Model

The punching shear model (Wardenier, 2002) computes the joint capacity by assuming that the stress around the brace-to-chord intersection area achieves the maximum shear stress at the joint failure, which follows the Von Mises yield criterion,

$$\sigma_y = \sqrt{\frac{1}{2}(\sigma_1^2 + \sigma_2^2 + (\sigma_1 - \sigma_2)^2)} \tag{2.3}$$

where, σ_1 and σ_2 refer to the principal stresses along the brace-to-chord intersection. σ_y denotes the yield strength of the chord material. According to Mohr's circle, the principal stresses become,

$$\sigma_1 = \sigma_\nu - \tau_{max} \tag{2.4}$$

$$\sigma_2 = \sigma_\nu + \tau_{max} \tag{2.5}$$

where τ_{max} and σ_ν refer to the maximum shear stress and corresponding normal stress. The combination of Eqs. 2.3, 2.4 and 2.5 gives,

$$\sigma_y = \sqrt{\sigma_\nu^2 + 3\tau_{max}^2} \tag{2.6}$$

The pure punching shear assumption provides,

$$\sigma_\nu = 0 \tag{2.7}$$

Therefore,

$$\tau_{max} = \frac{\sigma_y}{\sqrt{3}} \tag{2.8}$$

The brace loading component perpendicular to the chord axial direction mainly causes the joint failure. Therefore, The joint resistance derives from the effective punching shear area multiplied by the punching shear stress. For axial loadings with the brace inclination angle, $\theta = 90°$, the punching shear stress distributes as in Fig. 2.1.

$$P = \tau_{max}(\pi d_1 t_0) = \frac{\sigma_y}{\sqrt{3}}(\pi d_1 t_0) \Longrightarrow \frac{P}{\sigma_y t_0^2} = \frac{2\pi}{\sqrt{3}} K_a \beta\gamma \tag{2.9}$$

where K_a refers to the effective brace-to-chord intersection length factor. The plastic bending capacity based on punching shear model, as shown in Fig. 2.2, follows,

$$M_p = 2\int_0^\pi \tau_{max}(\frac{d_1}{2}\sin\varphi)dA = d_1^2 t_0 \frac{\sigma_y}{\sqrt{3}} \tag{2.10}$$

For joints with the brace inclination angle $\theta < 90°$, transformation factors (Wardenier, 2002) follow,

$$K_a = \frac{1 + \sin\theta}{2\sin^2\theta} \tag{2.11}$$

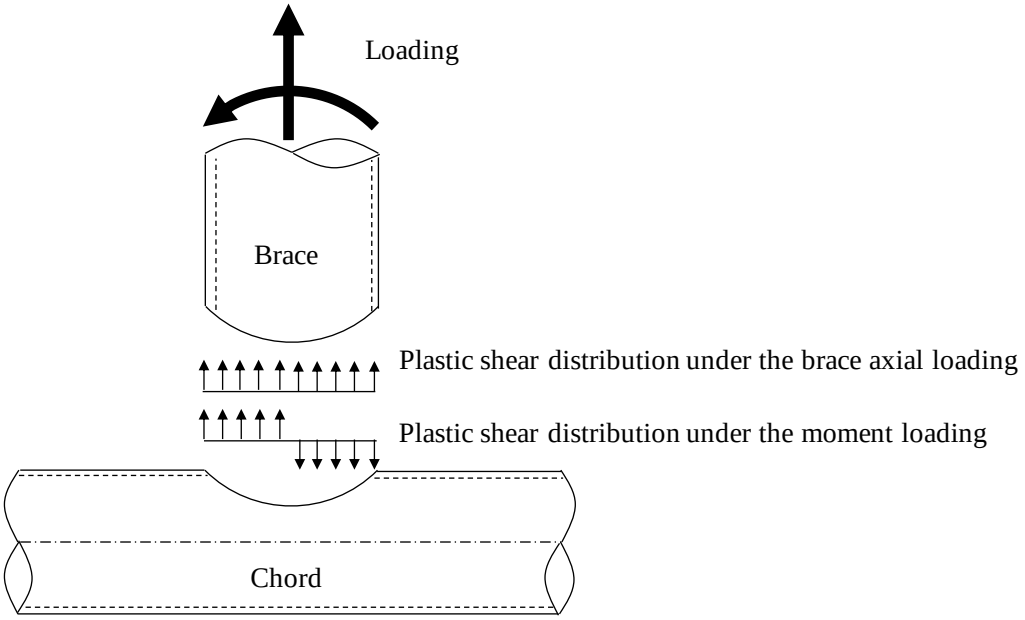

Fig. 2.1: Plastic shear distribution for the punching shear model.

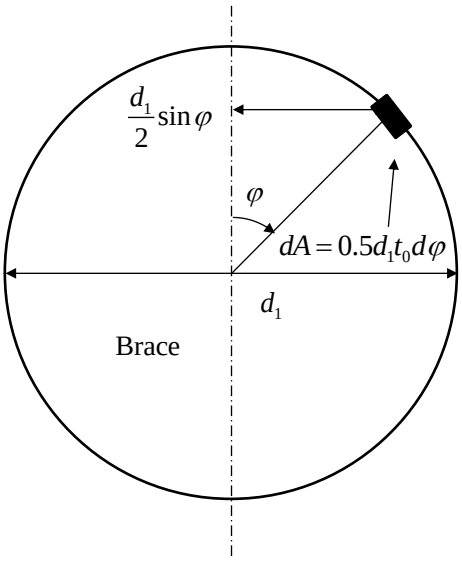

Fig. 2.2: Plastic stress distribution in the punching shear model for the axial bending load.

$$K_a = \frac{1 + 3\sin\theta}{4\sin^2\theta} \tag{2.12}$$

$$K_a = \frac{3 + \sin\theta}{4\sin^2\theta} \tag{2.13}$$

where Eq. 2.11 refers to the length factor for joints under the axial loading, Eq. 2.12 and Eq. 2.13 define the length factor for joints under the in-plane bending moment or the out-of-plane bending moment respectively.

2.3.1.2 Ring Model

Togo (1967) proposes the ring model for simple tubular connections. Paul *et al.* (1993) and van der Vegte (1995) improve this model further. This model approximates the circular chord around the brace-to-chord intersection by a ring with an effective length of B_e as shown in Fig. 2.3. The effective length B_e derives from the calibration with experimental or numerical results.

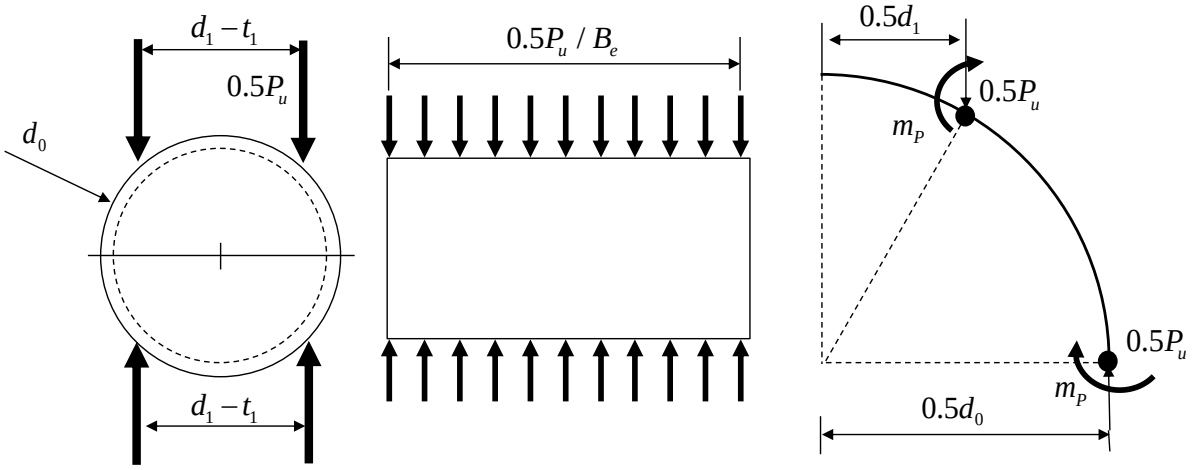

Fig. 2.3: Simplification of the brace load in the ring model for a CHS X-joint under the axial compression.

The ring model assumes two plastic hinges at the ultimate state as shown in Fig. 2.3, represented as m_p.

$$m_p = \frac{1}{4}\sigma_y t_0^2 \tag{2.14}$$

Equilibrium gives,

$$2m_pB_e = \frac{P_u}{2}(\frac{d_0}{2} - \frac{d_1}{2}) \Rightarrow \frac{P_u}{\sigma_y t_0^2} = \frac{2}{1-\beta}(\frac{B_e}{d_0}) \tag{2.15}$$

2.3.1.3 Yield Line Model

The yielding line model often provides a upper bound limit for structures. The complex stress field around the brace-to-chord intersection area in CHS joints introduces difficulties in using the yield line model. Therefore, the yield line model mainly develops for the rectangular hollow section (RHS) joint (Cao *et al.*, 1998a). Some researchers (Makino *et al.*, 1989; Soh *et al.*, 2000) have applied the yield line model to CHS X-joints. So far the research has not extended the yield line model to other types of CHS joints.

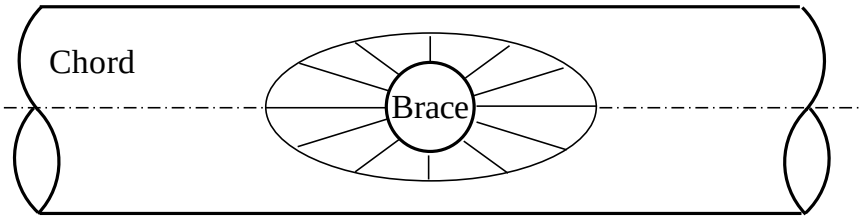

Fig. 2.4: Yield line pattern for an X-joint under the axial brace load.

The yield line model assumes the brace as a rigid body and the chord as a rigid plastic body. The joint ultimate strength derives from equating the external virtual work done by the brace loading to the internal virtual work done by the chord bending and membrane stresses. Figure 2.4 shows the assumed yield line model for an X-joint with a small β ratio. However, the ultimate strength derived from the yield line remains in a complicated mathematical form, which limits its application in the engineering practice.

2.3.2 Failure Criteria

The static ultimate strength of tubular joints often follows the joint resistance at certain chord or brace deformation, which mainly corresponds to three categories:

- Maximum load resistance
- Deformation limit
- Crack initiation

For those CHS joints under the brace compression condition, which commonly show a pronounced peak in their load-deformation curves, the joint static strength follows the first peak resistance. However, for CHS joints under the brace axial tensile loading, in-plane bending moment, or out-of-plane bending conditions, the load-deformation behavior shows an increasing resistance with a growing chord deformation. Thus, the deformation limit and the crack initiation become important criteria in characterizing the joint strength. Previous researchers (Yura *et al.*, 1980; Lu *et al.*, 1994; Van der Vegte *et al.*, 2002; Choo *et al.*, 2003) have proposed different approaches to define the tubular joint capacity based on the deformation limit, the strain limit or the energy limit. These criteria become widely used in the engineering practice.

2.3.2.1 Yura's Deformation Limit

Yura (1980) has proposed a deformation limit to define the ultimate CHS joint strength under various loading conditions based on the corresponding member deformation. For a tubular joint applied with the axial brace loading, the joint achieves its practical deformation limit when the strain reaches $4\varepsilon_y$,

$$\varepsilon_y = \frac{\sigma_y}{E} \tag{2.16}$$

where σ_y denotes the yield strength of brace material, and E refers to Young's modulus. Yura's deformation limit employs a brace length of $30d_1$ (a typical upper limit in offshore structures) to evaluate the deformation limit. Because of the comparable practical limit, the joint deformation δ at each brace end maintains half of the overall brace deformation. Therefore,

$$\delta_{Yura} = \frac{1}{2}(4\varepsilon_y L) = 60\frac{\sigma_y d_1}{E} \tag{2.17}$$

For a tubular joint under the axial bending moment, Yura's deformation limit follows the joint brace rotation. The criterion corresponds to the angle at the end of a simply supported beam sustaining a uniformly distributed loading. The loading induces four times the first yielding strain, ε_y, at the middle section of the beam. This assumption employs the typical beam length of $30d_1$, same as that for the brace axial loading.

Equation 2.19 shows the moment, corresponding to which the first yielding occurs at the mid-span of the beam.

$$\sigma_y = \frac{1}{2}\frac{M_y d_1}{I} \tag{2.18}$$

$$M_y = \frac{1}{8}q_y l^2 \tag{2.19}$$

The rotation of the end point of the simply support beam under the uniformly load follows,

$$\phi = \frac{q_y l^3}{24EI} \tag{2.20}$$

The combination of Eqs. 2.18, 2.19 and 2.20 provides,

$$\phi_{Yura} = 4\phi = \frac{80\sigma_y}{E} \tag{2.21}$$

For axial loaded joints, Yura's deformation limit remains proportional to joint β ratio with the fixed chord diameter, as shown in Eq. 2.17. However, Yura's deformation limit corresponds to neither the serviceability limit state nor the ultimate limit state of the

joint. The limit follows the assumption that the joint capacity can develop fully excessive plastic deformations in members.

2.3.2.2 Lu's Deformation Limit

Lu *et al.* (1994) have proposed a deformation limit for all types of as-welded tubular joints. For a CHS joint subjected to the brace axial loading, an indentation of 1% of the chord diameter, $\Delta_s = 0.01d_0$, at the chord surface refers to the serviceability limit, with the corresponding joint resistance denoted as P_s. An indentation equal to 3% of the chord diameter, $\Delta_u = 0.03d_0$, at the chord surface serves as the ultimate state limit, with the corresponding joint resistance denoted as P_u.

According to Lu *et al.* (1994), for $P_u/P_s > 1.5$, the ultimate state governs, while for $P_u/P_s \leq 1.5$, the serviceability limit state controls. For CHS joints, $P_u/P_s > 1.5$. Therefore, the deformation limit referring to $0.03d_0$ defines the joint ultimate strength. This deformation limit shows the consistency with the deformation corresponding to the peak load for different joint configurations (Lu *et al.*, 1994). For tubular joints subjected to brace bending moments, the research proposes a fixed brace rotation limit of 0.1 rad to provide a conservative prediction on the joint resistance.

2.3.2.3 Plastic Limit Load Approach

Choo *et al.* (2003) propose a plastic limit load approach for the thick-wall joint strength. Figure 2.5 presents the plastic limit load approach, where W_p refers to the plastic work done by the external brace loading and W_e denotes the elastic work under the load versus load-line displacement curve. The joint achieves the ultimate strength at the critical value of $\lambda = W_p/W_e$. The research proposes $\lambda = 3.0$ for various joints configurations and loading conditions. The results show good agreement with the joint capacity obtained by Lu's limit (1994).

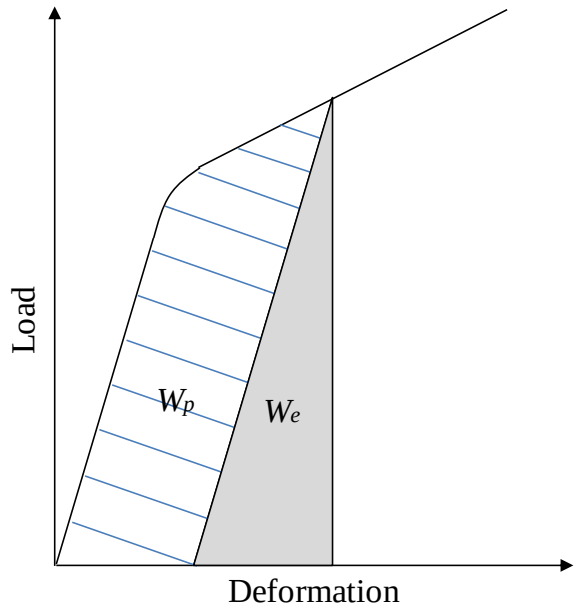

Fig. 2.5: Definition of W_p and W_e in the plastic limit load approach (Choo *et al.*, 2003).

2.3.2.4 Plastic Strain Limit

For CHS joints under the brace tension or bending moment, crack initiation and extension around the brace-to-chord intersection often emerge as the predominant failure mechanism. Some researchers (Dexter and Lee, 1999; Van der Vegte *et al.*, 2002) propose an empirical tensile plastic strain of 0.2, inferred from a typical elongation value in the standard uniaxial tension test for steels, as the failure criterion to represent the onset of ductile tearing in materials near the weld toe of the tension brace. Beyond this strain limit, the load-deformation behavior obtained from the finite element (FE) analysis, where no crack or damage model is involved, becomes potentially un-conservative. However, the significant mesh dependence and the low elongation strain for high strength steels often complicate the extraction of the 20% tensile plastic strain from the finite element model and limit the application of this failure criterion. Besides the tensile plastic strain, the accumulated plastic strain and the stress triaxiality can impose strong effects on the macrocrack initiation.

2.3.2.5 Material Fracture Toughness Limit

The energy release rate in elastic-plastic fracture mechanics, denoted as the J-integral, serves as a parameter to characterize the crack tip stresses and strains for nonlinear materials, under monotonically increasing loading (Rice and Rosengren, 1968). The J-integral refers to the total potential energy change per crack extension area. For a 2-D cracked body of area A, with tractions T_i applied over the bounding curve Γ as shown in Fig. 2.6, the potential energy of the body follows,

$$\pi = U - \Omega = \int_A W dA - \int_\Gamma T_i u_i d\Gamma \tag{2.22}$$

where U denotes the energy stored in the cracked body and Ω is the potential energy of the applied load. W refers to the strain energy density, and u_i denotes the displacement vector. Therefore,

$$J = -\frac{d\pi}{da} = \int_\Gamma W dy - \int_\Gamma T_i \left(\frac{\partial u_i}{\partial x} \right) d\Gamma \tag{2.23}$$

Crack extension occurs when J equals to the critical fracture resistance, J_{IC}, which

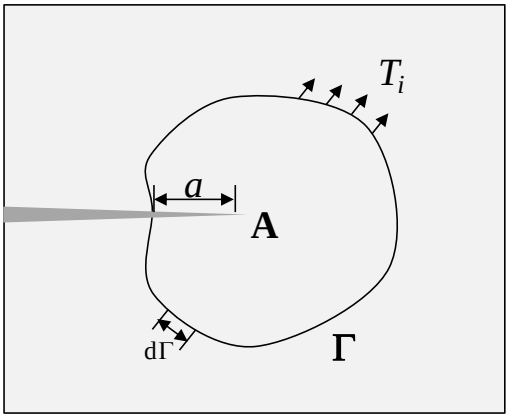

Fig. 2.6: Definition of J-integral in a 2-D cracked body.

remains a inherent mechanical property for the specific material.

Wang *et al.* (2011) employ the elastic-plastic fracture toughness, J_{IC}, obtained from

the standard compact tension, C(T) specimen as a criterion to evaluate the joint strength for cracked thick-walled CHS X-joints under the brace axial tension. The research assumes that the joint fracture failure occurs when the crack driving force exceeds J_{IC}. The result demonstrates the un-conservative estimation from Lu's deformation limit for X-joints under the brace axial tension.

2.4 Research on Frame Behavior

Past few decades observe extensive research on the reserve and residual strength of tubular frames. The experimental results of these tubular frames, which represent typical offshore jacket structures, have provided valuable physical data on research in the frame-joint interaction behavior.

2.4.1 Experimental Benchmark

Gates *et al.* (1977) report a large-scale frame test for an X-braced frame. The frame employs one bay in 4 meters high with a joint can, loaded monotonically to failure. The test program generally focuses on the nonlinear response of the frame subjected to the earthquake loading. The frame experiences a tension brace yielding before the compression member buckling due to the lock-in pre-tension stress. The load-displacement response of the frame indicates a gradual reduction in the overall stiffness with a ductile behavior in the load carrying capacity.

University of California Berkeley carries out two X-braced frame tests in the late 1970s (Zayas *et al.*, 1980). The test employs two one-sixth scale 2D X-braced double-bay frames, which stand more than 8 meters high, under the cyclic loading. The research aims to investigate the frame cyclic inelastic behavior, which determines the survivability of offshore structures in the event of severe seismic ground excitations. The displacement

history applied on the frame represents severe seismic loadings. The tests demonstrate not only the effect of bracing configurations on the nonlinear response of structures but also the significance of relative section sizes. This frame, denoted as Zayas frame, follows the name of its investigator. The Zayas frame test proves the value of large-scale frame tests and provides substantial contribution to the offshore engineering research.

Inoue *et al.* (1984) investigate the effect of the horizontal brace based on a series of tests for two plane frames and two space truss specimens. Instead of conventional tubular joints, the experiment employs gusset plates to attach brace members to the chord, therefore provides fixed end conditions in the gusset plane and pin-ended conditions out of the gusset plane. For one planar frame, the horizontal brace takes an increasingly significant role in resisting the applied load as redistribution from the buckled compression brace occurred, as compared with the planar frame without the horizontal brace.

Ogawa *et al.* (1987) report a series of tests on 15 complete trusses with CHS members and investigate the effect of failure sequence of members and joints. The research evaluates the accuracy of the available joint strength formula. If the joint failure precedes the member buckling, the available strength formulation predicts the joint strength with a sufficient accuracy. If the member buckling precedes the joint failure, the joint experiences the combined bending moment and axial load. Therefore, the joint show a lower capacity than that predicted by the axial load strength formulation. The research also demonstrates the marginal effect due to the difference of boundary conditions in the isolated and actual joints under the static loading.

SINTEF (Søreide *et al.*, 1986) tests two X-brace one-bay three dimensional frames to the ultimate load. The frames, denoted as S1 and S2, have different d_0/t_0 ratios and brace slenderness. Both frames employ thicken joint cans to ensure the dominant member failure. Frame S1 demonstrated a brittle response caused by the tension member fracture. In Frame S2, the global response maintained a positive slope as the alternative bracing

load path compensates for the falling load.

Southwest Research Institute (Grenda *et al.*, 1988) carries out static pushover tests on six planar K-braced single-bay tubular frames. The frames, representing the typical configuration of Bass Strait platforms, employ the overlapped as-welded tubular K-joint in the first four frames and grouted K-joints in the fifth and sixth specimen. The results indicate the insensitivity of the global response to the thickness of the K-joint can, provided that the compression member buckling governs the frame ultimate strength.

The JIP, organized by Billington Osborne-Mass Engineering Limited (BOMEL) and other academic and industrial organizations, investigate two series of 2D large-scale frames under the static loading (Bolt *et al.*, 1994; Bolt, 1995). The subsequent phase of the JIP (Bolt and Billington, 2000) tests one large-scale 3D frame under a series of static loading conditions. The experiment maintains the largest frames tested worldwide by far. The 2D frames consist of six X-braced two-bay frames and four K-braced single-bay frames. The experimental work investigates the effect of joint behavior and framing redundancy on the X-braced frames, and the effect of local joint behavior (including the fracture failure) on the K-braced frames.

Their 3D frame tests further explore the effect of reserve strength, via loading different frame panels consisting of different joint types. In contrast to 2D frames, the interaction between different panels offers additional load-paths in the 3D structure. Both 2D and 3D frames demonstrate the capacity of steel frames in redistributing loads beyond the first component (joint or member) failure. The reserve strength involved in these frames contributes significantly to their ability to sustain the extreme environmental loading.

Paik and Shin (1990) investigate the influence of damage within K-braced plane and space frames, with the support of numerical development of elements to model the damage. The "rigid body" rectangular box sections stiffen the K-joint to protect against the local joint failure. The results indicate the small influence from the the critical member

damage to the peak load sustained by the frame.

2.4.2 Ultimate Strength Prediction

Moses and Liu (1992) present a description of the system reliability formulation, in which they conclude three most important factors affecting the accuracy of the structural models: the material behavior describing brittle, ductile and strain-hardening situations, a reliable system geometry, and correlations between component failure events. The material property refers to the post-yield material behavior. The system geometry, imperfection and boundary conditions, for example, affect the failure mode of the structure. The sequence of the component (joints or members) failure can lead to different load redistributions and consequently different ultimate strength levels.

In the BOMEL JIP (1992), the research performs the pushover analyses using BOMEL's software SAFJAC (Strength Analysis of Frames and JACkets), which has been applied to the re-analysis of existing jacket structures. The program employs plastic hinges and an automatic mesh refinement technique. The nonlinear joint behavior utilizes the load deflection and moment-rotation characteristics through piece-wise linear spring elements. The analysis starts with one quadratic element per member. Mesh refinement applies to members where the plasticity has been developed. The calibration study against the 2D X-braced frame shows good correlations with test results. The difference in the peak loads between the numerical computation and test results remains within 10%.

Hellan (1995) reports an extensive numerical study on the pushover and cyclic frame analyses. The research verifies the nonlinear numerical tool, USFOS (an acronym for Ultimate Strength for Framed Offshore Structures), to produce the accurate column and beam-column behavior. The calibrated nonlinear formulation incorporates residual stresses and geometric imperfections. The basic principle behind USFOS follows the representation of each individual member in the structure by one beam-column element

(USFOS, 2009). Equation 2.24 (USFOS, 2009) shows the 4th-order differential equation for a beam under end forces. The shape function in USFOS adopts the exact solution to Eq. 2.24, enabling one element per member. The program simulates the nonlinear member behavior by incorporating plastic hinges at the ends and at the member mid-point.

$$\frac{d^4w}{dx^4} + \frac{P}{EI}\frac{d^2w}{dx^2} = 0 \tag{2.24}$$

Health and Safety Executives (HSE) conducts its own benchmark study based on large-scale BOMEL 2D frame tests (Nichols *et al.*, 1997). 11 participants performed nonlinear analyses based on four tests on 2D double-bay frames. Uncertainties in the results arise mainly from the use of different softwares. The choices and decisions of the analysts affect the accuracy of the modeling. Material properties impose a significant effect on the accuracy of the analysis. The study concludes that the nonlinear analysis proceeds from the preserve of research to a practical engineering tool.

Skallerud and Amdahl (2002) show that X-braced and redundant structures provide more system strength in addition to the design capacity. The redundant members maintain a higher load level at a much larger deformation as compared with that in K- and diagonal-braced structures. On the other hand, the portal action provides critical alternative load paths under large deformations provided leg members employ large sizes. The initial imperfection, both geometric imperfections and residual stresses, has a significant effect on the buckling strength for members under compression. The research demonstrates the significance of the joint flexibility when the loading effects are close to the joint capacity. In such cases, the modeling of the joint nonlinear behavior becomes essential.

2.5 Joint Frame Interaction

2.5.1 Effect of Joint Flexibility on the Platform Behavior

Previous research has demonstrated the importance of the sufficient joint strength in mobilizing the connected member capacity. However, the joint flexibility also imposes tremendous effect on the structural behavior.

The local joint flexibility tends to relax member end forces and moments through the local chord deflection at the brace-to-chord intersection (Chakrabarti *et al.*, 2005). This relaxation could mobilize more structural components by redistributing the member load. According to Bouwkamp's (1980) research, the inclusion of the local joint flexibility leads to 30% larger calculated displacements at the lower framing level, considerable reductions in brace axial forces and larger moments in the jacket leg.

For the pushover analysis of jacket type structures, Hellan (1995) concludes the insensitivity of the variation in the joint elastic flexibility on the structure collapse behavior. Variation of the joint flexibility by a factor of two results in less than 3% change in the collapse load, which shows the negligible effect on jackets with strong joints. However, results of pushover analyses indicate that the effect of joint flexibility becomes more apparent when a structure exhibits the nonlinear behavior (Mirtaheri *et al.*, 2009). The strength of the joint, if less than the member strength, governs the load carrying capacity of the member. The joint failure modifies the mechanical behavior of the global structure and influences the following global failure modes (Morin *et al.*, 1998).

The redistribution of member loads due to the local joint flexibility in the structural model shows a significant effect on the fatigue life evaluation. The accurate fatigue strength calculation requires the hot spot stress based on the correct force and moment distribution in the frame (Romeijn *et al.*, 1991). The inclusion of the local joint flexility could induce a 2.8 times increase of the fatigue life on average (Chakrabarti *et al.*, 2005).

The inclusion of joint flexibility can increase natural periods of higher modes and induces changes in the mode shape (Bouwkamp *et al.*, 1980). Platforms with flexible connections show a 12.4% increase in higher-mode periods due to the deformability (Mirtaheri *et al.*, 2009). This magnification introduces a detrimental effect for the deeper water platform and the compliant tower.

2.5.2 Joint Model

A natural extension of the work on the joint stiffness focuses on examining the influence of the local joint flexibility on the frame response by implementing the local joint behavior into structural analyses. Two major techniques exist,

- Use of a substructure for the tubular joint.
- Addition of a simple spring in line with the brace member.

2.5.2.1 Substructure

Previous researchers employ different techniques to model the local joint area. The first group, acknowledged as the most accurate technique, models the whole structure by coupling the large-deformation, elastic-plastic three-dimensional finite element substructures for local critical tubular connections with the global continuous beam-element model via the multiple joint constraint (Qian, 2005). The technique simulates the joint-frame interaction behavior with more realistic local joint boundary conditions. However, this approach becomes infeasible when applied to a realistic steel offshore platform analyses with multiple critical joints, which require substantial computational resources in iterating the detailed stress-strain fields in the 3-D local joint model. The consideration of the environmental loading requires the correction of the wave loading and the extrapolation of the member end force, due to the non-consistency of the chord diameter at the sub-

structure boundary. According to Pan's (2002) analysis, the substructure with a chord length of $4.5d_0$ generally provides the satisfactory result.

The second group employs simplified finite element analyses. Boukamp's (1980) analyses model joint cans by modified nine-node doubly curved iso-parametric degenerate shell elements. A formulation in USFOS (2009), denoted as Shell formulation, also models the local brace-to-chord area by shell elements and evaluates the joint elastic stiffness during the frame analysis procedure. Figure 2.7 presents the concept of the shell formulation available in USFOS. This formulation, applicable for most joint geometries, considers the multiple-brace interaction effect. However, this shell formulation underestimates the joint stiffness by ignoring the brace stiffness for CHS joints with large β ratios, as mentioned in section 2.2.3.

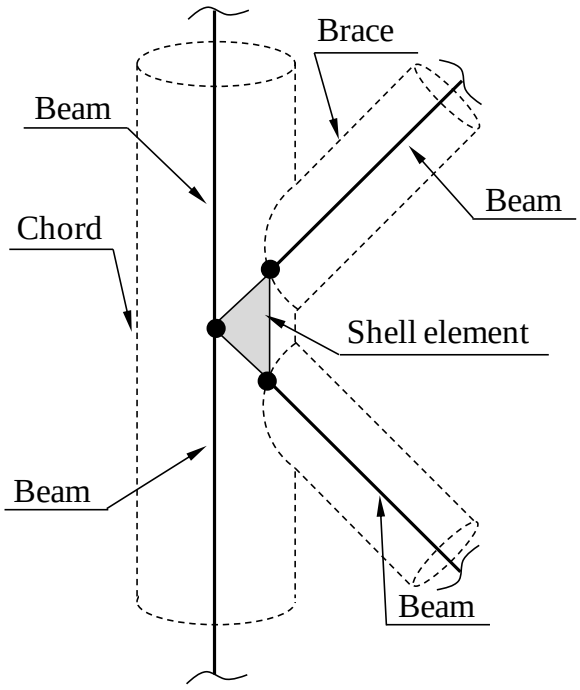

Fig. 2.7: Shell element model for a typical CHS K-joint (Hellan, 1995).

The third group adopts the iteration method. By investigating the nonlinear behavior of YT-joint based on the FE analyses, Hyde (1997) demonstrates that the Y- and T-

brace-end axial displacements, combined as a vector, are normal to the level curves of complementary work in the load space. The research proposes a displacement procedure to predict the non-linear, elastic-plastic relationships of YT- joints. Pan (2002) incorporates this procedure into global frame analyses using the iteration method. This method inputs initial guesses for the substructure interface displacements and forces using the results from a simplified beam element model, then employs the sub-structure analysis to check until the results converge. This method can reduce the number of degree of freedoms and computational time but will encounter problems when the large plasticity occurs.

2.5.2.2 Joint Spring

The second method, the phenomenological representation of the joint behavior through nonlinear joint springs as shown in Fig. 2.8, provides the most straightforward method for practicing engineers, although extra nodes may be required at some cost penalty. The frame analysis incorporates the joint behavior by introducing additional two-node elements between the original chord centre node and new nodes at the chord surface. The properties of these "joint" elements follows certain P-δ and M-θ formulations with suitable adjustments to account for brace load interaction effects.

Ueda (1990) develops the elastic-perfectly-plastic springs for CHS T-, Y- and K-joints by assuming that the resultant nodal force moves along the joint yield surface and the plastic nodal displacements increment vector remains normal to the yield surface. Alanjari *et al.* (2011) employ the same method and proposed joint formulation for two dimensional Y-joint using Fessler's flexibility equations (Fessler *et al.*, 1986b) and Billington's capacity equation (1982). However, this technique fails to predict the nonlinear joint behavior, particularly with respect to the failure load.

Another group of researchers propose three joint spring formulations to simulate the

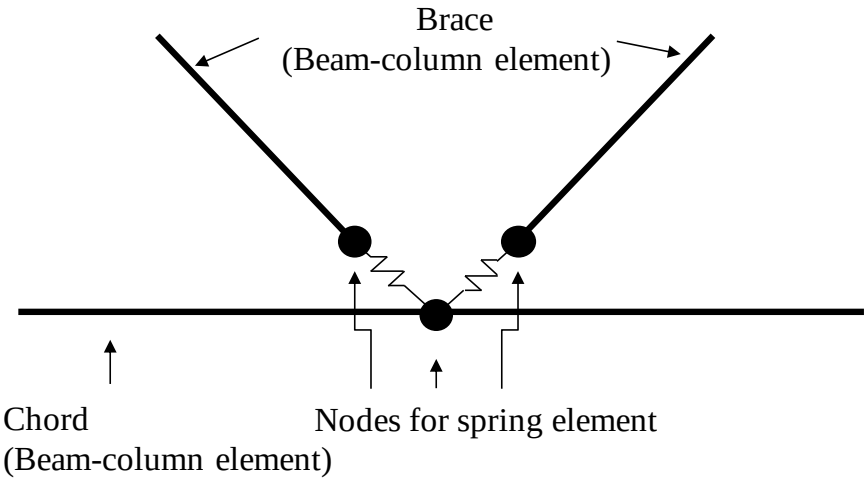

Fig. 2.8: Phenomenological spring elements for a typical CHS K-joint (Qian, 2005).

joint behavior from the elastic stage to the final plastic collapse or the fracture failure.

1. API joint formulation (USFOS, 2009)

   The API formulation employs the joint capacities based on API joint strength equations (API, 2010) and defines the local joint behavior corresponding to different brace deformations. Figure 2.9 displays a typical P-δ curve for CHS joint under brace axial loads using the API joint formulation. In this model, the brace axial deformation corresponding to:

   - 0.1% of the chord diameter defines joint "yielding".
   - 1.0% of the chord diameter defines the joint ultimate capacity.
   - 5.0% of the chord diameter defines the end of maximum capacity.
   - 10% of the chord diameter defines the joint fracture failure with the total loss of the joint capacity.

   The displacement criterion in this joint formulation remains arbitrary and the joint model does not consider joint behavior under the combined brace loading. At large

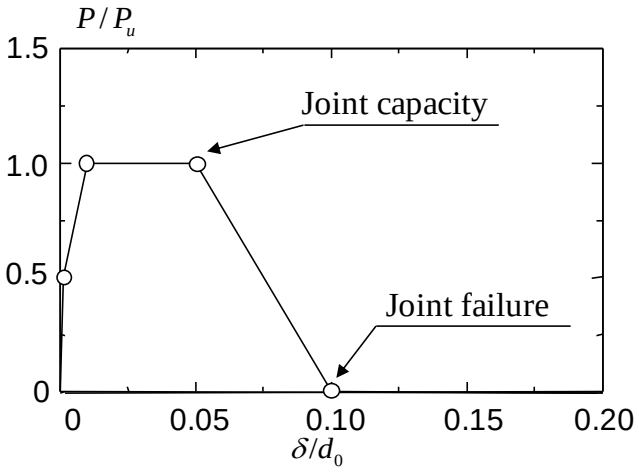

Fig. 2.9: API joint spring formulation.

deformations the joint strength decreases linearly till zero and the corresponding brace member will lose its contribution in the global strength and stiffness.

2. Choo *et al.*'s joint formulation (Choo *et al.*, 2005)

   This joint representation simulates the joint behavior by piece-wise linear springs. For all loading conditions, the joint behavior follows a bilinear model before the joint achieves the ultimate joint strength. For the X-joint under the brace axial compression, a re-development of joint strength occurs at a large deformation level due to the direct contact of two compression braces. Figure 2.10 shows two typical load-deformation curves for CHS joints under the brace axial compression and bending moment.

   For CHS joints under the brace axial tension loading, the joint resistance begins to decrease at $\delta_i = 0.1d_0$ due to the crack initiation following the assumption in the API joint spring and achieves the residual capacity $0.3P_u$ at $\delta_{cr} = 0.11d_0$. The main parameters in determining the joint springs, P_E, P_u, δ_E, and δ_u follow expressions derived from hundreds of finite element results. The result from the global frame analysis incorporated with the joint model agrees with tests results. However, this

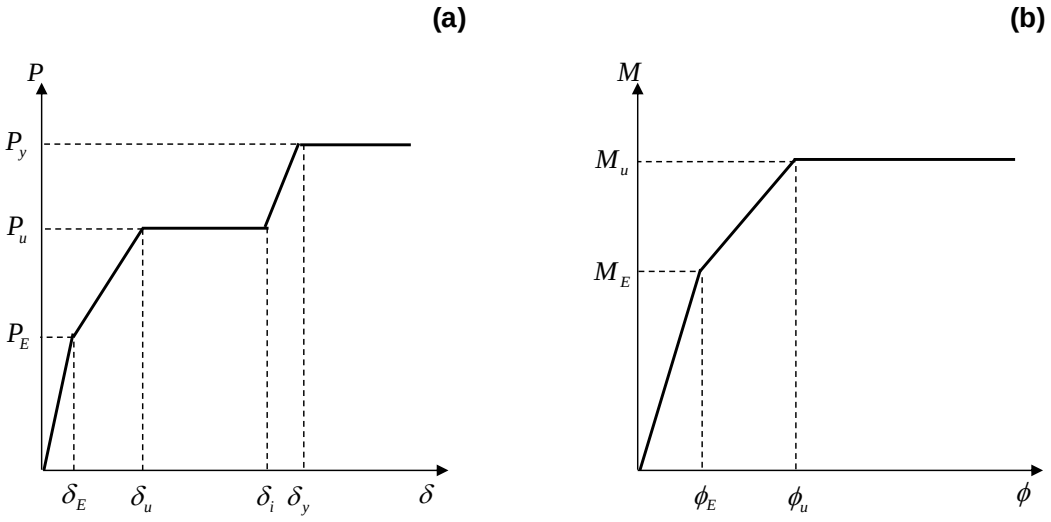

Fig. 2.10: Choo *et al.*'s joint spring (2005) for CHS joints under: (a) axial compression and (b) moment loads.

joint model does not describe the joint behavior under combined brace axial and bending actions. The deformation limit $\delta_i = 0.1d_0$ and the 30% residual strength estimation remain arbitrary to simulate the joint behavior at the fracture failure.

3. MSL formulation

   The joint industry project led by a UK company develops the MSL formulation, which employs a smooth curve based on a semi-empirical method developed from a database of tubular joint tests and FE analyses (Dier and Lalani, 1995; Dier and Hellan, 2002; Lalani, 1993). The MSL formulation, as shown in Fig. 2.11, utilizes the P-δ and M-θ curve which depend on the joint classification as well as the loading conditions. By defining the yield surface and bounding surface, the joint model includes the interaction effect under combined brace loading conditions. The formulation adopts mixed classifications among X-, Y- and K-joint types with evaluation at each load increment step. Joints under the brace axial tensile loading sustain the potentially fracture failure at certain chord deformation. The formula

of MSL joint model follows,

$$P = P_u\{1 - A_1[1 - (1 + 1/\sqrt{A_1})EXP(-A_2\delta/d_0\sigma_y)]^2\} \tag{2.25}$$

where P_u refers to the maximum joint capacity, and the constant A_1 and A_2 denote two empirical parameters based on the joint geometries and loading conditions. Following Eq. 2.25, the displacement of the peak load follows:

$$\delta_u = \frac{\ln(1 + 1/\sqrt{A_1})}{A_2}\sigma_y d_0 \tag{2.26}$$

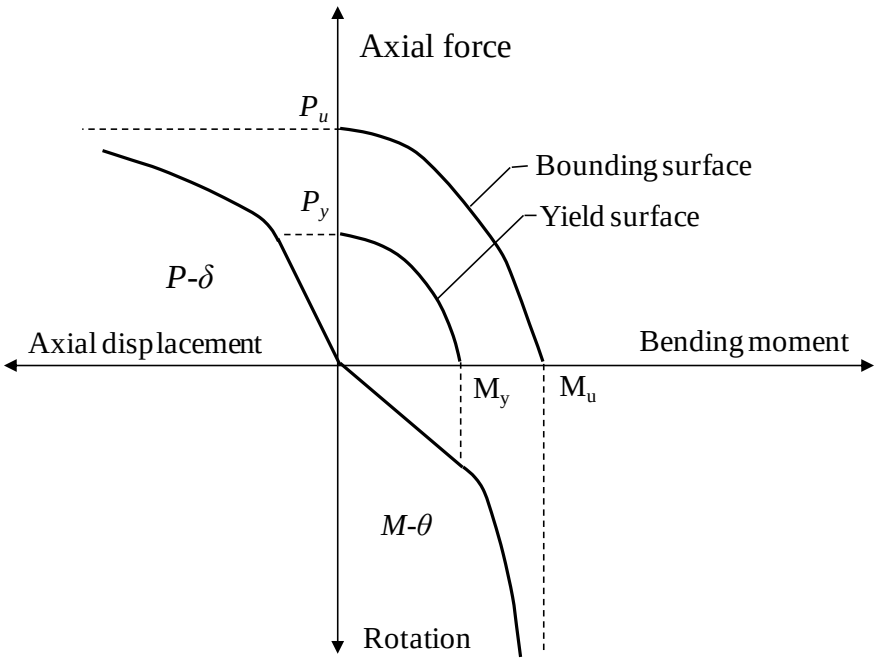

Fig. 2.11: MSL joint formulation (Dier and Hellan, 2002).

However, the MSL formulation, which considers the chord stress effect as well as the brace loads combination, can only describe the characteristics of 2D as-welded joints. The joint formulation employs the ductility limit based on the visible crack observation from very few X-joint test results. For the ductility limit of K-joints,

only two test data exists (MSL, 2000). Many types of early platform joints do not exist in the MSL studies (Zettlemoyer, 2010). The property of the function, as shown in Eq. 2.25, limits its application to simulate the behavior of joints under the in-plane bending, out-of-plane bending or other types of loadings, where the load-deformation behavior shows an increasing resistance with the deformation.

2.6 Summary

This chapter conducts a comprehensive literature review on the research with respect to the local joint flexibility and the existing joint models for tubular joints. Two major analytical models exist and become widely accepted to predict the joint ultimate capacity. Several failure criteria define the joint deformation, corresponding to which the joint ultimate resistance occurs. The study summarized above supports the following conclusions:

1. Extensive research work focuses on the elastic joint flexibility, where the joint flexibility formula is derived from either numerical or experimental data. The experimental results of the large-scale 2D and 3D tubular frames, conducted in the past few decades, provide valuable physical data on research in the frame-joint interaction behavior. The past research indicates the insensitive effect of the joint elastic flexibility on the frame static response if the joint capacity remains sufficient to develop fully the member strength. The behavior of the weak joint exhibits more pronounced effect by governing the member load carrying capacity and modifying the subsequent structural behavior.

2. Plenty of studies address the necessity to implement the joint behavior into the global frame analysis. Joint spring method, with the phenomenological representation of the joint behavior through nonlinear joint elements, provides a convenient

and straightforward approach. The available joint models show the limitation in predicting the reliable nonlinear behavior tubular joints under ductile tearing and unstable fracture failure. The practical engineering requires a more accurate and consistent joint formulation to simulate the tubular joint behavior under the brace tensile loads.

Chapter 3

Verification of Finite Element Models

3.1 Introduction

The equipment capacities and the financial conditions often limit the geometrical ranges and quantities of experimental investigations. The finite element (FE) method proves to be an economical and reliable research approach. However, no FE analysis is complete without a careful calibration. To guarantee the validity of FE results, the current chapter performs a detail verification study.

This chapter begins with a description of the current numerical modeling procedure for tubular joints. The following section investigates various finite element modeling aspects including material property, mesh density, boundary condition, *etc.* The subsequent section verifies the finite element modeling with published test results. The fourth section investigates two typical finite element techniques to model a tubular joint with a surface crack at the critical location. The comparison and discussion provide a solid base for the numerical investigation in the subsequent research.

3.2 Numerical Procedure

The finite element analysis of tubular joints contains three general steps: the pre-processing, the numerical computation and the post-processing. The current finite element modeling process employs two software packages, MSC Patran (2012) and ABAQUS (2012). MSC Patran serves as an open-architecture, general purpose, 3D mechanical computer aided-engineering software package and the acknowledged finite element modeler. With the embedded Patran Command Language (PCL), MSC Patran's analysis preference feature enables the user to customize the analysis codes. The current analysis generates firstly the model by Patran with associated input files for ABAQUS, which exhibits excellent features in material and geometric nonlinear analyses. ABAQUS carries out the subsequent numerical computation and the post-processing.

3.2.1 Material Property

The classical metal plasticity model in ABAQUS permits the simulation of the plastic flow and isotropic hardening for the steel. The nonlinear FE analysis often follows the large deformation theory. The large deformation analysis requires the input of the true stress-plastic strain property of the material. In all analyses except otherwise specified in the current research, the true stress-true strain curve derives from the engineering stress-engineering strain relationship obtained from standard uni-aixal tension tests (ASTM E8/E8M, 2011), as shown in Eq. 3.1 and Eq. 3.2.

$$\varepsilon = ln(1 + e) \tag{3.1}$$

$$\sigma = S(1 + e) \tag{3.2}$$

where S refers to the engineering stress and e denotes the engineering strain, while σ and ε define the true stress and the true strain respectively. Figure 3.1 compares the engineering stress-strain and true stress-strain curve for a typical S355 steel. The engineering stress and the true stress shows a negligible difference at the small strain, as reflected in Eq. 3.2. However, due to the significant reduction of the cross section area, two curves deviate from each other and the engineering stress can no longer characterize the stress state within the reduced cross section area.

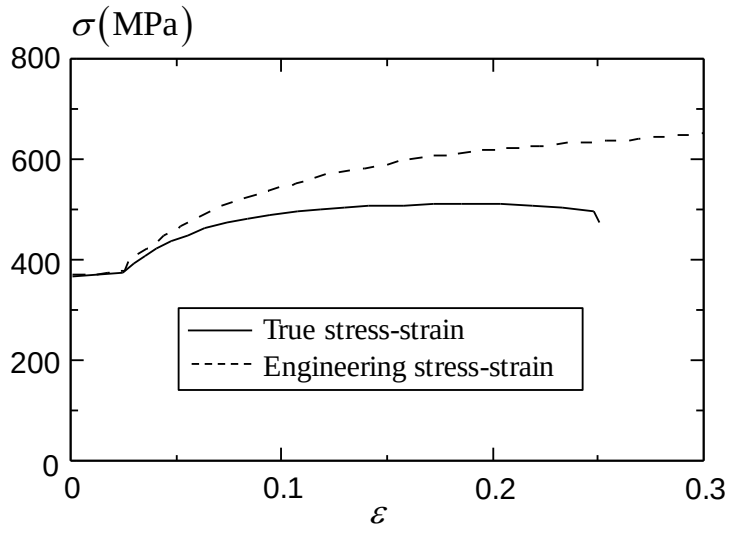

Fig. 3.1: Uni-axial engineering stress-strain and true stress-strain.

When the material achieves the large strain, the engineering stress-engineering strain data become unavailable. The true stress-true strain relationship follows Ranmberg-Osgood's power law,

$$\frac{\varepsilon}{\varepsilon_y} = a(\frac{\sigma}{\sigma_y})^n \tag{3.3}$$

where a and n refer to two constants determined by the curve fitting from the stress-strain plot. The ABAQUS material input requires the true stress-plastic strain relationship,

which follows the description in Eq. 3.4.

$$\varepsilon_p = \varepsilon - \frac{\sigma}{E} \tag{3.4}$$

In order to investigate the stain hardening effect on the load deformation behavior of tubular joints, the current study analyzes a typical X-joint shown in Table 3.1 with two different material post-yielding properties. Figure 3.2 plots the true stress-true strain curve of these two materials, where material 2 refers to the elastic-perfectly-plastic material without strain hardening.

Table 3.1: Joint property for material strain-hardening effect study.

Joint type	d_0(mm)	β	τ	γ	α	σ_y(MPa)
X-	300	0.6	1.0	15	16	355

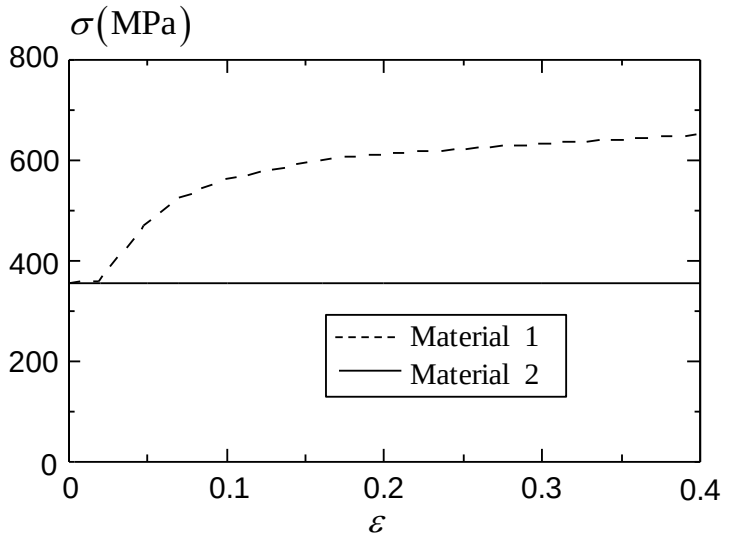

Fig. 3.2: True stress-true strain curve for materials with the same yield strength, σ_y = 355MPa.

Figure 3.3 presents the load-deformation curves for the analyzed X-joint using two different material types. The failure of the X-joint mainly depends on the plastic de-

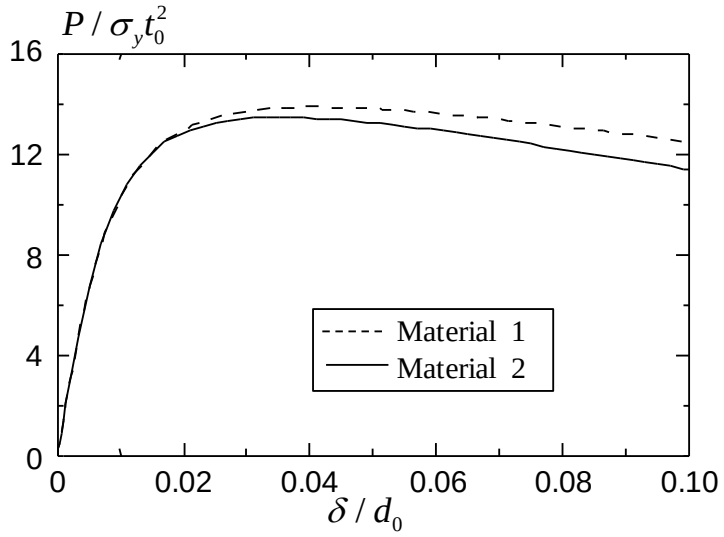

Fig. 3.3: Material strain hardening effect on the load-deformation behavior for an X-joint subjected to the brace axial compression.

formation at the chord material around the brace-to-chord intersection area. At the lower deformation level ($\delta/d_0 < 2\%$), as the loading only mobilizes the plasticity at a small regime near the chord saddle point, the material post-yield property shows a minor effect. However, as the load increases, the increasing plasticity mobilized around the brace-to-chord intersection area enlarges the difference. Nevertheless, the difference in the overall joint resistance still remains within 10% as the developed material plastic strain maintains at a lower level.

3.2.2 Mesh Density and Convergence Analyses

This section conducts a mesh refinement study to verify the finite element mesh generated by the proposed procedure. The X-joint modelled follows six different mesh density schemes, as shown in Fig. 3.4 and Table 3.2.

All six models employ twenty-node solid elements with reduced integration (named C3D20R in ABAQUS) with the brace in-plane bending moment. The X-joint experiences

Table 3.2: The X-Joint property for the mesh density study

Joint	d_0(mm)	β	τ	γ	α	σ_y(MPa)
X-	508	0.8	1.4	17	16	355

the applied loading on the chord top with two brace ends seated on two support rollers, as shown in Fig. 3.8a. Table 3.3 summarizes the mesh convergence scheme and results of the analyses. The material near the joint brace-to-chord intersection area experiences significant membrane, shear and bending stresses during the loading process, therefore requires a refined mesh. The finer mesh in Table 3.3 adopts more element seeds along the brace-to-chord intersection as well as through the chord wall thickness direction.

Table 3.3: Convergence analyses for an X-joint subjected to the brace in-plane bending moment.

Mesh density type	No. of elements	No. of nodes	CPU time (sec)	Seeds around weld profile	Seeds through wall thickness	Ultimate load ($M/\sigma_y d_1 t_0^2$)
1	212	1647	42	4	1	19.11
2	364	2746	80	8	1	18.77
3	808	5894	202	12	1	18.32
4	1736	10033	545	12	2	18.08
5	3464	19737	1378	16	2	18.07
6	8634	44463	5735	20	3	18.01

Figure 3.5 plots the ultimate joint capacity corresponding to Lu's deformation limit (Lu *et al.*, 1994) and the computational time against the number of elements for different mesh density schemes. Mesh density scheme 1 to 3 predict a larger joint in-plane-bending capacity due to a higher chord bending stiffness induced by only one layer of elements (over the thickness). The mesh schemes with two layers of element can capture the stress gradient through the wall thickness. From mesh density type 4 to mesh density type 6, the computational time increases about 10 times while the gain in accuracy maintains

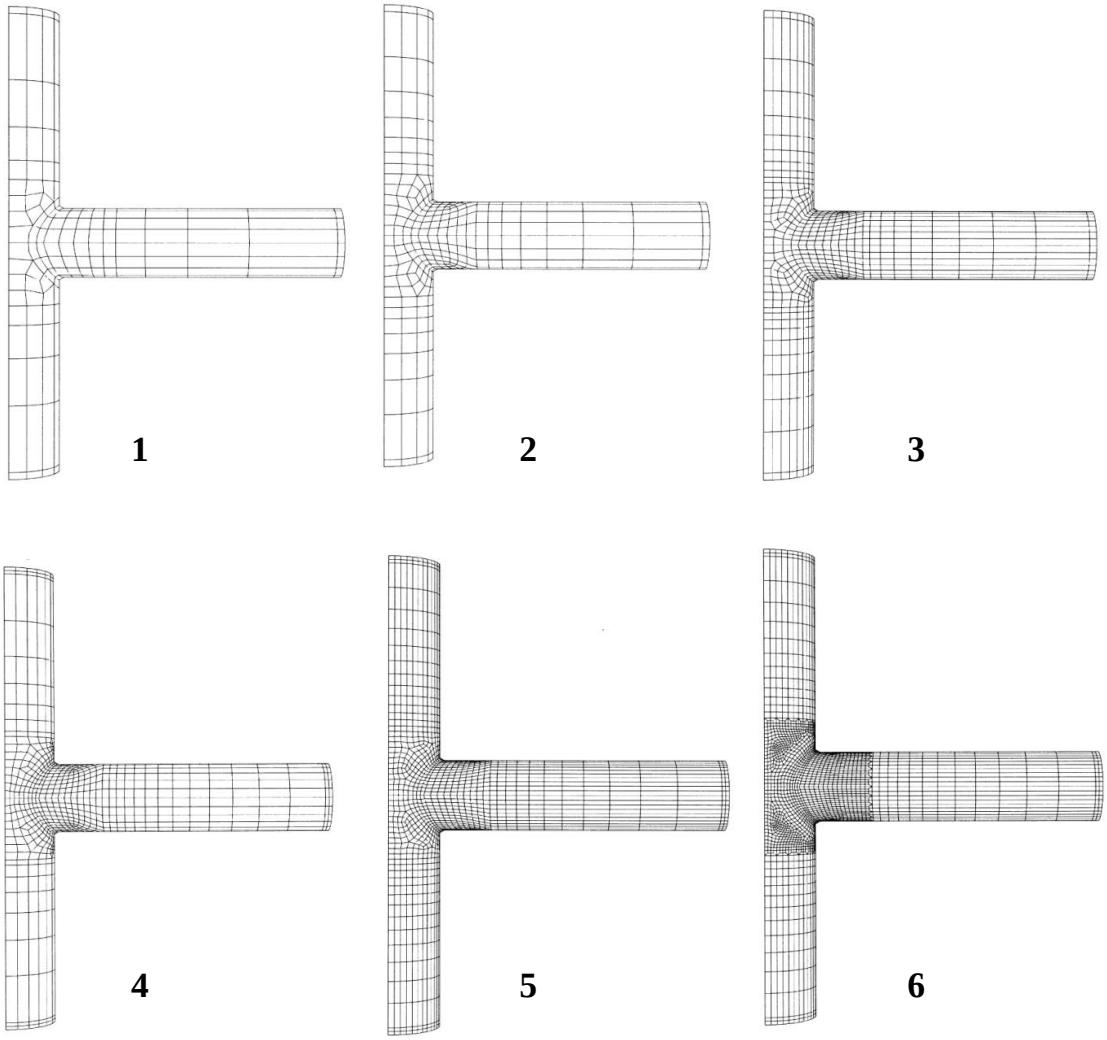

Fig. 3.4: Mesh density scheme for a typical X-joint subjected to IPB.

within 1%. Thus, mesh density type 4, with two layers of elements through the wall thickness and 12 elements along one quarter of the weld length, provides the highest efficiency and has been adopted in the following numerical investigation.

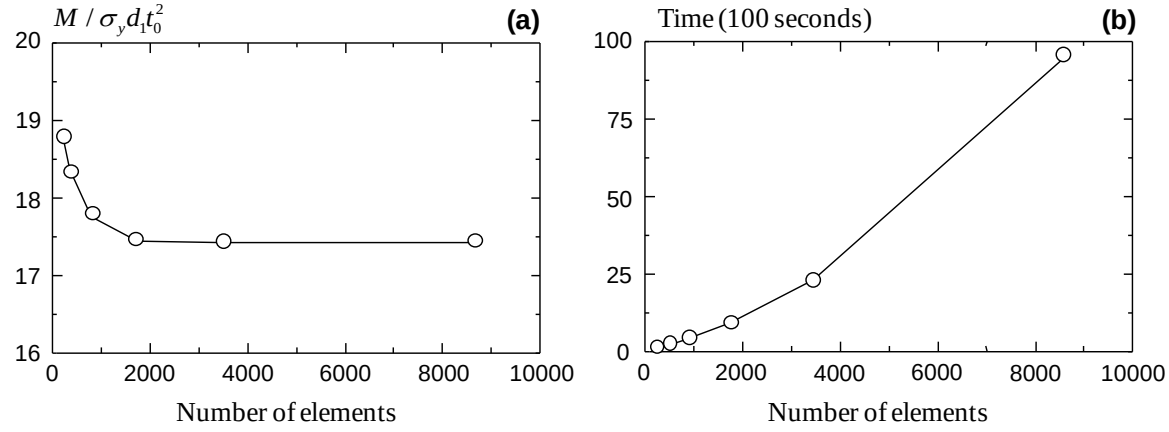

Fig. 3.5: Result of FE models in the mesh convergence study: (a) ultimate loading and (b) computational time.

3.2.3 Boundary Conditions

The symmetry in the geometry and loading conditions, for all joints analyzed, permit only a part of the joint to be modeled in order to reduce the number of elements and the computational time. Depending on the loading condition and joint type, the model mesh varies from one eighth to one half of a complete joint.

For X-joints under the axial compression or tension loading, only one eighth mesh needs to be created for the FE analysis, as shown in Fig. 3.6. Three symmetry planes follow symmetric boundary conditions with respect to X-Y, Y-Z and X-Z plane. For X-Z plane, $D_y = 0$; For X-Y plane, $D_z = 0$; For Y-Z plane, $D_x = 0$. D_x refers to the translation along X-axis. R_x denotes the rotation about X-axis. The loading acts at the brace end in a displacement or load control manner.

For X-joints under the in-plane bending or out-of-plane bending, one forth geometry

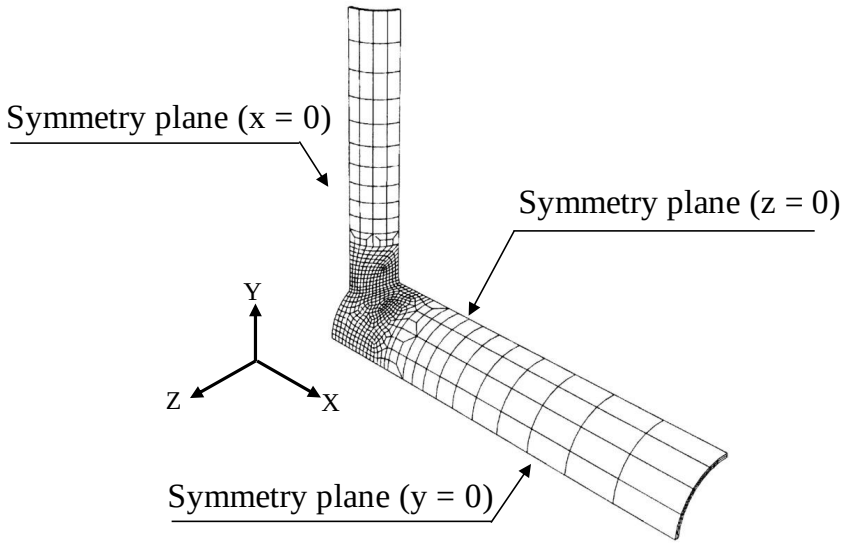

Fig. 3.6: A typical one-eighth mesh for the X-joint under the brace axial loading.

needs to be created, as shown in Fig. 3.7. The general modelling procedure employs rigid end plates at the member ends to maintain the circular shape during the loading process so that the applied boundary condition will not change due to the nonlinear deformation or the failure of the member. The modeling of rigid end plates enables the boundary condition to be applied at the central node. The thickness of the rigid end plate equals that of the corresponding member and the Young's modules E equals 100 times that of the member material. The boundary condition follows the symmetry for X-Z and X-Y planes for joints under the IPB condition and for X-Z and Y-Z planes for those under the OPB condition, respectively.

Generally, two approaches to apply the bending moment exist. The experimental procedure normally generates the brace in-plane bending through the horizontal load along the chord axis by pushing the chord or the brace, as shown in Fig. 3.8 . However, this approach may reduce the joint capacity by introducing additional shear stresses in braces. A more straightforward approach utilizes the coupled concentrated loads at the brace top, as shown in Fig. 3.9. According to Chen (2010), the shear force in braces

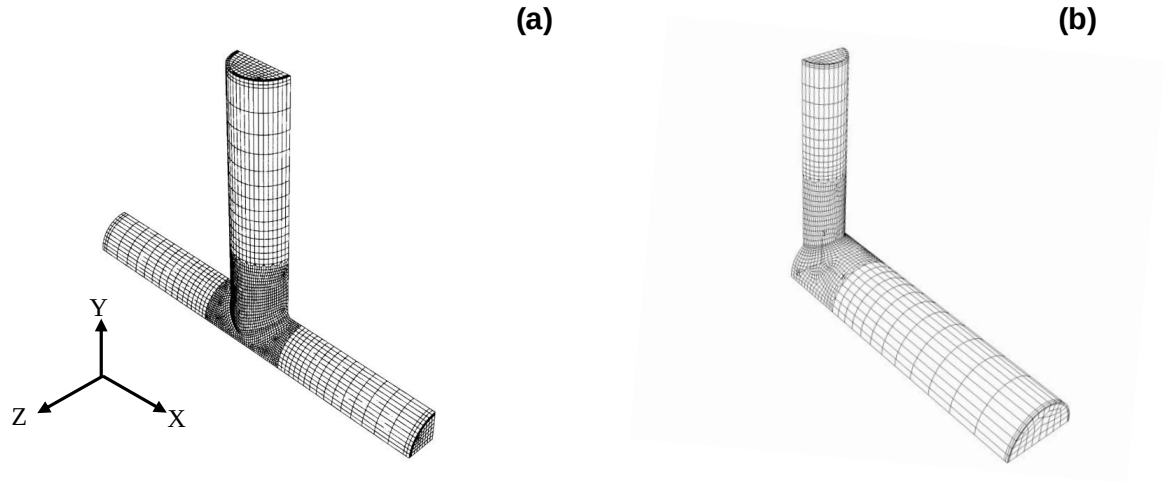

Fig. 3.7: The FE mesh for the X-joint under the brace: (a) in-plane bending (IPB) and (b) out-of-plane bending (OPB).

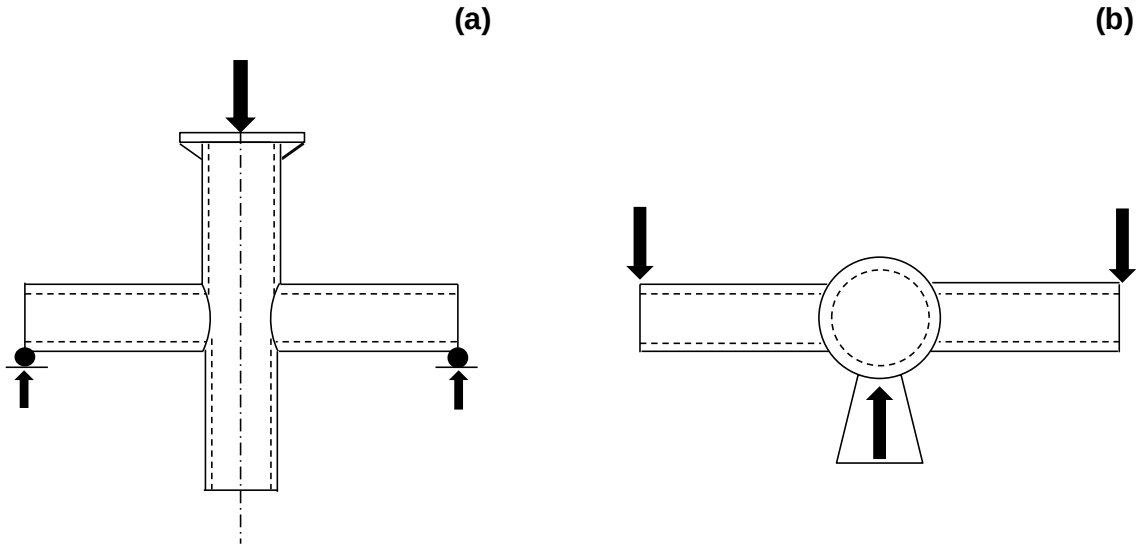

Fig. 3.8: Loading condition (front view) for the X-joint in the experiment under: (a) in-plane bending (IPB) and (b) out-of-plane bending (OPB).

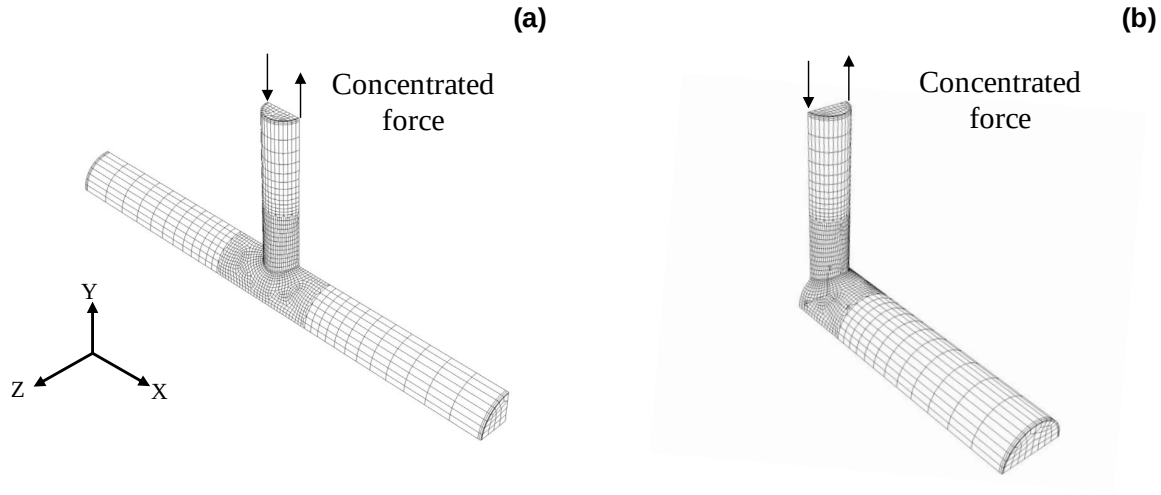

Fig. 3.9: Pure bending condition for the X-joint under: (a) in-plane bending (IPB) and (b) out-of-plane bending (OPB).

provides a negligible effect on the global behavior for CHS joints.

3.2.4 Element Type

Solid elements provide enanced accuracy in representing certain geometric shapes including weld profile, loading and contact boundary conditions (Choo *et al.*, 1998). Two types of solid elements exist: the 8-node element and 20-node element. The 8-node element (C3D8 and C3D8R in ABAQUS (2012) element library) may overestimate the joint stiffness due to the constant strain assumption throughout the element. For the higher order element, the 20-node element with 27 Gauss points (C3D20 in ABAQUS (2012) element library), the incompressibility also results in an overestimation of the real joint strength. Van der Vegte (1995) states that the use of 20-node elements would require at least 2 layers of solid elements in order to provide a representative description of the stress gradient through the chord wall thickness. The 20-node solid elements with reduced integration (C3D20R in ABAQUS (2012) element library) provides an alternative approach.

The current study analyzes a typical X-joint under the brace axial compression using

Table 3.4: Comparison of results using different element types.

Element type	No. of element	No. of node	CPU time (sec)	Ultimate load $P/\sigma_y d_0 t_0^2$
C3D20R	1430	8538	130	13.88
C3D20	1430	8538	175	14.81
C3D8	1430	2331	25	19.78
C3D8(finer mesh)	3013	4386	54	17.5
C3D8R	3013	4386	52	16.26

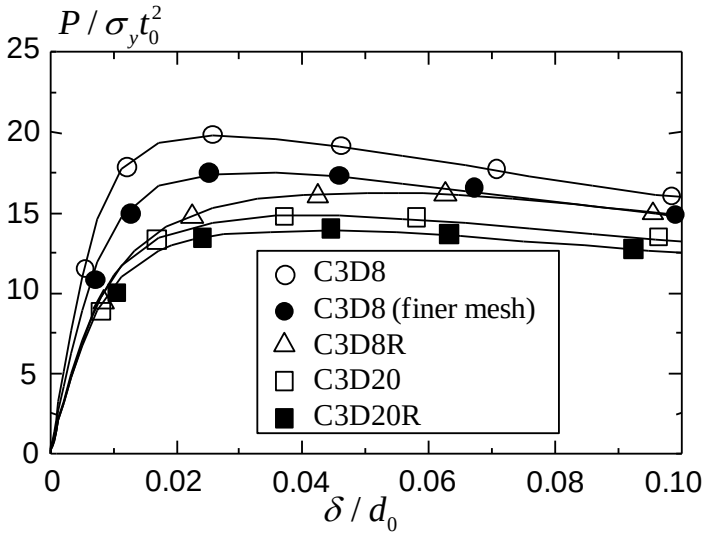

Fig. 3.10: Load deformation behavior of an X-joint under the axial compression with different element types.

different element types. The joint dimension follows Table 3.1. The analyses employ four types of solid elements: 8-node elements with full integration (C3D8), 8-node elements reduced integration (C3D8R), 20-node element with full integration (C3D20) and 20-node element with reduced integration (C3D20R) respectively, as shown in Table 3.4. The mesh density follows the mesh scheme type 4 as described in Section 3.2.2. The finer mesh scheme utilizes three layers of elements through the chord wall thickness direction and employs 8634 elements. Figure 3.10 compares different global load-deformation behaviors generated by different element types. For 8-node elements, the analysis requires less computational time but tends to overestimate the joint capacity due to the constant strain assumption even for the finer mesh. For 20-node elements with 27 Gauss points, as mentioned by van der Vegte (1995), the analysis tends to overestimate the real strength. Compared with the C3D20 element, C3D30R element employs less Gauss points therefore utilizes less CPU time. The difference between the result from C3D20R and C3D20 remains within 6%. In general, 20-node elements with reduced integration provides a good accuracy with a high efficiency. Therefore, the current study employs the 20-node solid element with reduced integration, especially for the subsequent cracked joint model.

3.2.5 Weld Profile

The brace and the chord of a typical tubular joint connect each other through the complete joint penetration groove welds. The weld size depends on the local dihedral angle between the chord and the brace outer surface, as shown in Fig. 3.11. To investigate the effect of the weld profile, the current research analyzes a typical X-joint shown in Table 3.1, under the axial compression with different weld sizes. The weld size follows three different weld profiles $L = 1.0t_1$, $L = 1.5t_1$, and $L = 2.5t_1$ respectively, where L denotes the weld length as shown in Fig. 3.12. The $L = 1.5t_1$ weld size follows the specification of the widely known AWS welding standard (AWS, 2012).

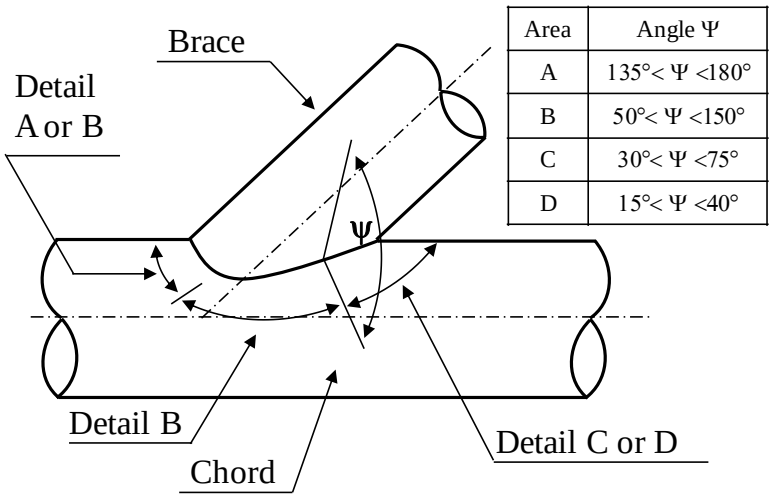

Area	Angle Ψ
A	135°< Ψ <180°
B	50°< Ψ <150°
C	30°< Ψ <75°
D	15°< Ψ <40°

Fig. 3.11: Definition of weld profile for T-, Y-, and K-tubular connections (AWS, 2012).

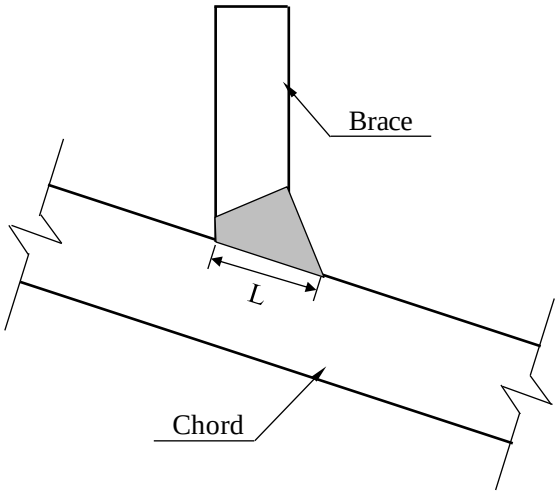

Fig. 3.12: Weld geometry parameters notation for typical tubular connections.

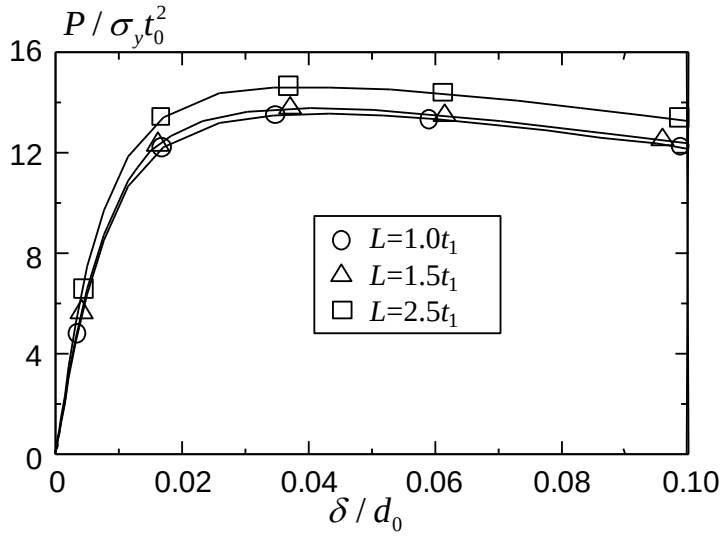

Fig. 3.13: Load deformation behavior of an X-joint under the brace compression with different weld sizes.

Figure 3.13 compares the X-joint behavior with different weld sizes. The presence of weld increases the joint capacity by only about 2% without changing the joint initial flexibility, as compared with the joint behavior without welds. However, an enlarged weld size increases about 7% of the ultimate strength and provides a higher joint stiffness by mobilizing more chord material near the brace-to-chord intersection area. Due to the sensitivity of the joint behavior to the weld size, the current FE analysis follows the specifications in AWS D1.1 (2012), which remains a widely accepted guidance for offshore engineering practice.

3.3 Verification of FE Models

This section verifies the FE analysis, based on the modelling procedure discussed in the previous sections, against different reported tests for two X-joints (Van der Vegte, 1995; Chen, 2010), one K-joint (Kurobane *et al.*, 1986) and four T-joints (Makino *et al.*, 1986).

3.3.1 X-joint

Van der Vegte (1995) and Chen (2010) report two CHS X-joint experiments, where the joints experiences the brace axial compression and in-plane bending respectively. Table 3.5 lists the geometric information for two X-joint specimens. The experimental procedure for the X-joint reported by van der Vegte (1995) generates the brace axial compression through the loading at the brace top, as shown in Fig. 3.14a. Figure 3.14b demonstrates the close agreement between the experimental load-deformation response and that computed from the FE analysis, which predicts accurately the plastic deformation around the brace-to-chord intersection as observed in the experiment.

Table 3.5: Geometric parameters of X-joints in the reported tests.

Joint	d_0(mm)	β	γ	α	τ	σ_y(MPa)
Axial	408	0.6	20.0	12.0	1	331
IPB	407	1.0	9.5	12.8	1	334

Figure 3.15a displays the experimental set-up for the X-joint subjected to the in-plane bending (Chen, 2010). A set of roller support two braces on both sides with the top end of the chord pushed down to generate IPB moments. Figure 3.15b compares the load-deformation curves between the experimental test and that computed from the FE analysis. The X-joint experiences the chord wall plastic deformation followed by the fracture failure due to the crack initiation at the weld toe. The current FE result shows good agreement with the experimental result before the crack initiation.

3.3.2 K-joint

Kurobane *et al.* (1986) report a series of tests on CHS K-joints to investigate the brace local buckling behavior. Table 3.6 lists the geometry and material property of one selected

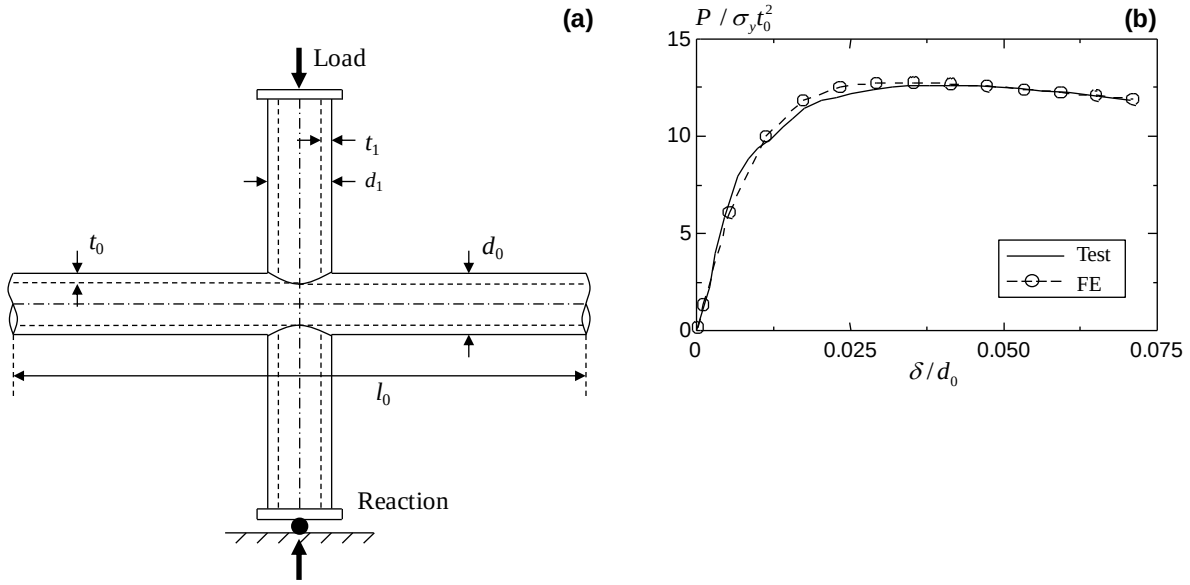

Fig. 3.14: Verification of the FE analysis for an X-joint under the axial compression : (a) test set-up and (b) FE and test results.

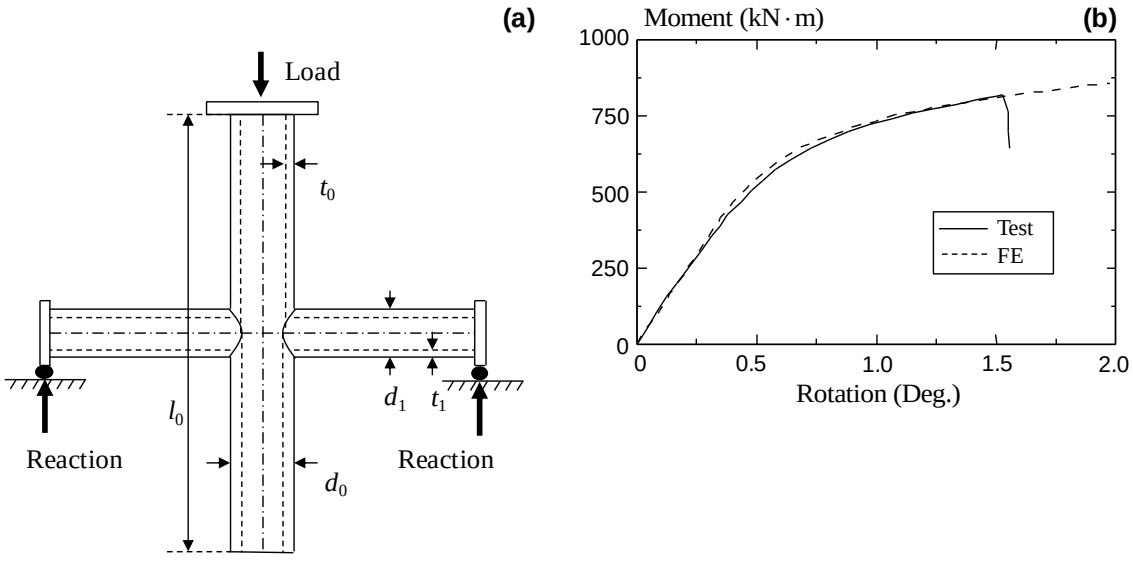

Fig. 3.15: Verification of FE analysis for an X-joint under IPB: (a) test set-up and (b) FE and test result.

gapped specimen.

Table 3.6: Geometric parameters of the K-joint in the reported test.

Joint	d_0 (mm)	β	γ	γ	τ	θ	g'	σ_y(MPa)
K-	216.4	0.76	13.7	16	0.67	60°	3.8	532

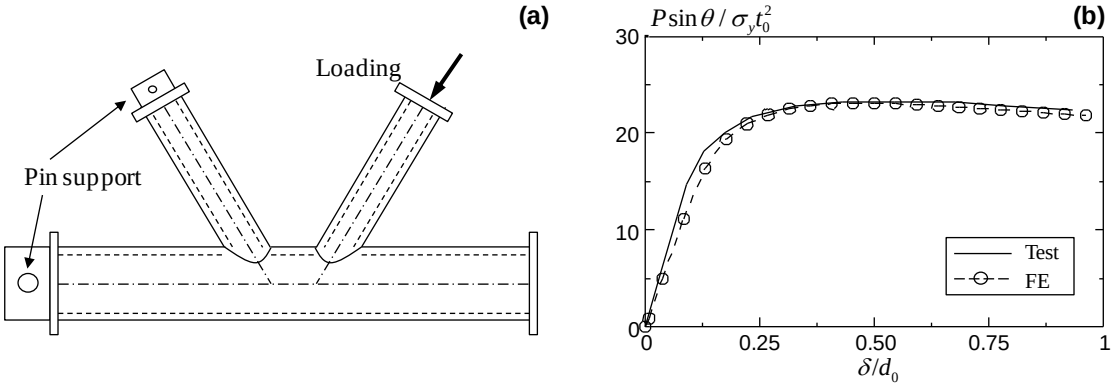

Fig. 3.16: Verification of FE analysis for K-joint under the axial loading: (a) test set-up and (b) FE and test result.

Figure 3.16a illustrates the test set-up for the gapped K-joint specimen. A test frame supports the left brace end and the left chord end by bearing pins. The K-joint experiences the axial compressive load applied on the right brace, the end of which is free to rotate in the plane of the K-joint. Figure 3.16b confirms the accuracy of the FE analysis compared to the experimental load-deformation record.

3.3.3 T-joint under Combined Loads

This section validates the FE model with a series of T-joint tests subjected to the combined out-of-plane bending and axial loading, as reported by Makino *et al.* (1986). All the T-joints share the same geometry but under different loading conditions. Table 3.7 lists the geometry and material property of the selected T-joint.

Table 3.7: Geometric information for T-specimens in the reported test.

Joint	d_0(mm)	β	γ	α	τ	σ_y(MPa)
T-	216.3	0.53	24	6.8	1	377

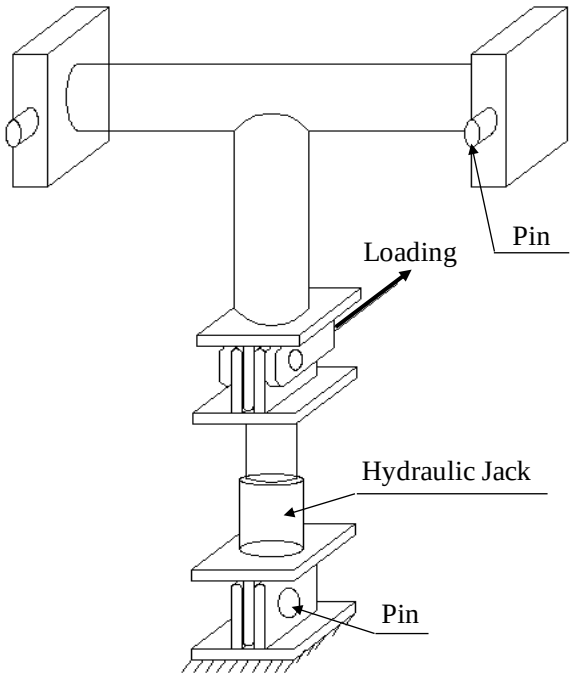

Fig. 3.17: Test set-up for the T-joint under combined brace loadings.

Figure 3.17 shows the test set-up for the T-joint. The experimental procedure applies an out-of-plane shear load and an axial load at the brace end. Four specimens experience the brace axial compression, tension, out-of-plane bending and the combined bending and compression respectively. The test employs stiff end plates, pinned to the reaction frame, at chord ends, as shown in Fig. 3.17. Figure 3.18a to 3.18c compares the load-deformation curves for T-joints under the brace axial compression, tension and out-of-plane bending. The comparisons show good agreement between FE analyses and test results.

For the combined loading condition, the experimental procedure applies the axial compressive load to one half of the maximum axial compression capacity followed by the increase of the lateral loading to generate the out-of-plane bending moment. The experiment obtains the moment by extrapolating results from strain gages, which are placed on the brace member. The current FE analysis employs two types of loading technique: the first approach utilizes the displacement control manner by increasing the out-of-plane bending moment with a fixed brace axial deformation. The second technique employs the load control manner which represents the shear load by the surface traction on the end plate and the compression by the pressure perpendicular to the end plate. Figure 3.18d compares the load-deformation behavior for the T-joint under different loading techniques. Two loading modes show small deviations compared with the experimental result.

3.4 FE Model for Cracked Tubular Joints

For tubular joints, the external force during the service life of structures, often induces cumulative fatigue damage and initiate surface cracks at hot-spot locations at the weld toe along the brace-to-chord intersection, as shown in Fig. 3.19. Therefore, failure assessment often serves as the main preoccupation during the service life of the structure. The

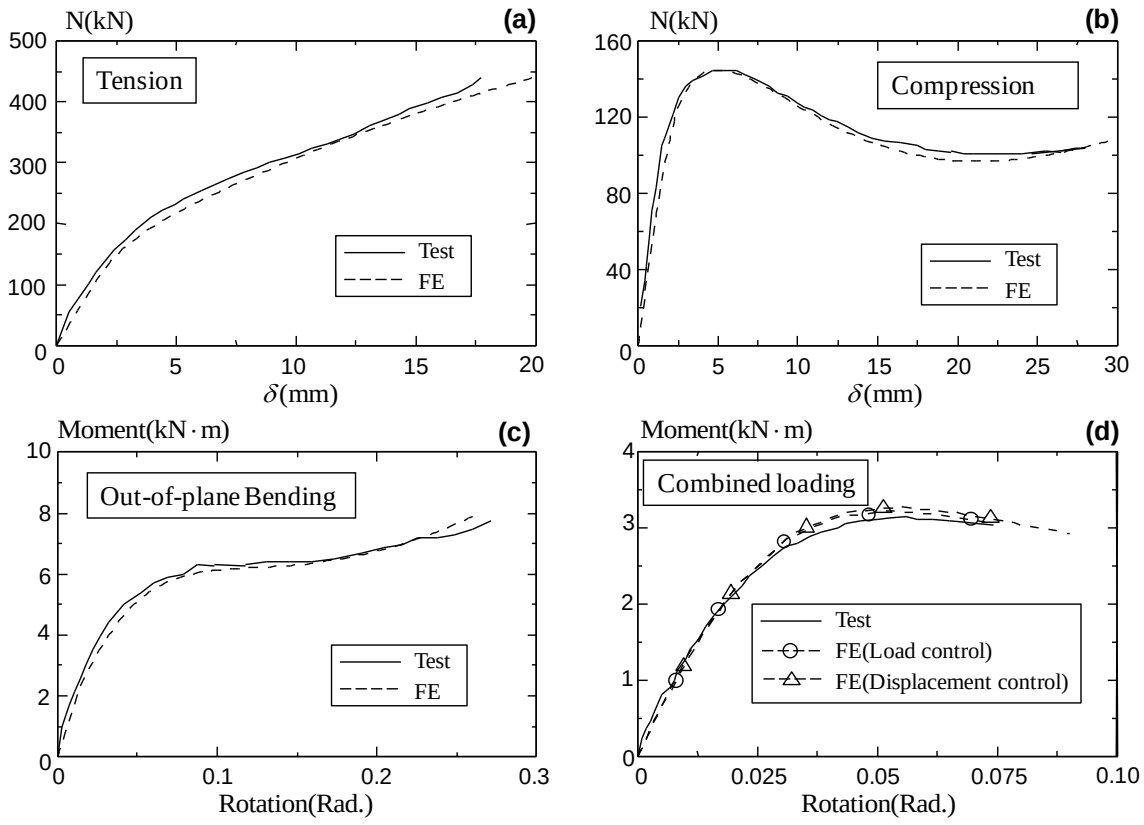

Fig. 3.18: Verification of the FE analysis for T-joints under: (a) the axial tension; (b) the axial compression; (c) the out-of-plane bending; and (d) the combined loading.

engineering failure assessment of the fatigue cracked tubular joints requires the determination of the elastic-plastic crack driving force (measured by the J-integral) for surface cracks in these connections. Due to the complexity of the CHS joint geometry, the analytical J-solutions often become intractable. Therefore, detailed FE analyses have to be performed.

Earlier researchers propose various approaches to compute the J-value for cracks located at hot-spot positions in CHS joints based on the finite element method. These approaches falls into three categories: (1) line-spring method; (2) continuous mesh method; and (3) mesh-tie method. Haswell (1991) employs line-spring elements, which approximate surface cracks with the compliance of a plane-strain, single-edge notched specimen, to compute the stress-intensity factor for the cracked tubular joint. Skallerud (1995; 1996) extends this technique to elastic-plastic J-integral analyses of tubular connections. Bowness and Lee (1995; 2002) develop a scheme to generate adequate continuous crack-front meshes with brick-type elements and calculate stress-intensity factors for surface cracks in tubular connections. Lie (2005) and Cao (1998b) introduce a similar technique to construct accurate and consistent models for cracked K- and X-joints. Qian *et al.* (2005) propose a mesh-tie procedure, which couples a global, topologically continuous mesh and a separate, local crack-front model to generate a crack near the weld toe. Bowness and Lee (1995) demonstrate the accuracy of the line-spring element for cracks with a moderate depth. This section will elaborate on the continuous mesh and mesh-tie, then compares the mesh efficiency and the result accuracy for the subsequent research.

3.4.1 Continuous Mesh Versus Mesh-tie

Continuous mesh generally consists of several complicated mapping and mesh generation processes, where many types of 3D elements including cubic elements, prism elements and pyramid elements are involved. Figure 3.20 illustrates a general procedure to model

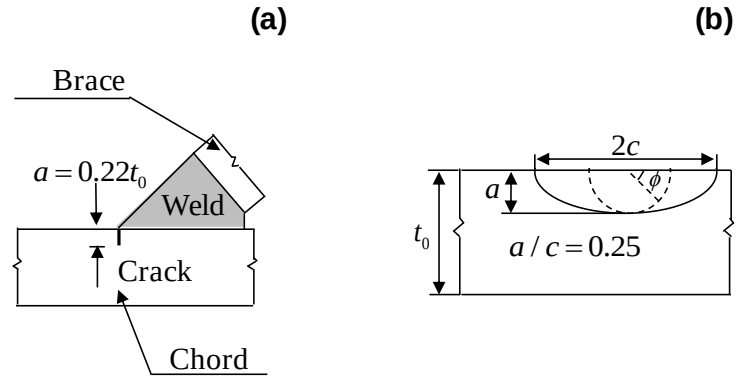

Fig. 3.19: (a) Crack at the weld toe and (b) planar view of the surface crack.

a tubular joint with a weld-toe crack, as reported by Bowness and Lee (1995).

1. The T-butt joint model in FEA CRACK software (2011) generates a focused mesh as shown in Fig. 3.20a.

2. The mapping-1 transforms the T-butt model into a 90° fan shape in the base plane while the vertical coordinate perpendicular to the base plane remains the same, as indicated in Fig. 3.20b.

3. Patran (2012) extends the base of the model in the second step to form a rectangular shape.

4. The mapping-2 transforms the base in the third step into the joint chord area by rotating nodes at the base about the axial axis of the chord member and translating the nodes above the base correspondingly along the vertical-coordinate.

5. The fifth step elongates the chord and brace length using brick elements to complete the joint modeling in Patran (2012).

The mesh-tie method for a typical X-joint with a weld-toe crack consists of two parts (Qian *et al.*, 2005): the global mesh and the local crack-front model, as shown in Fig.

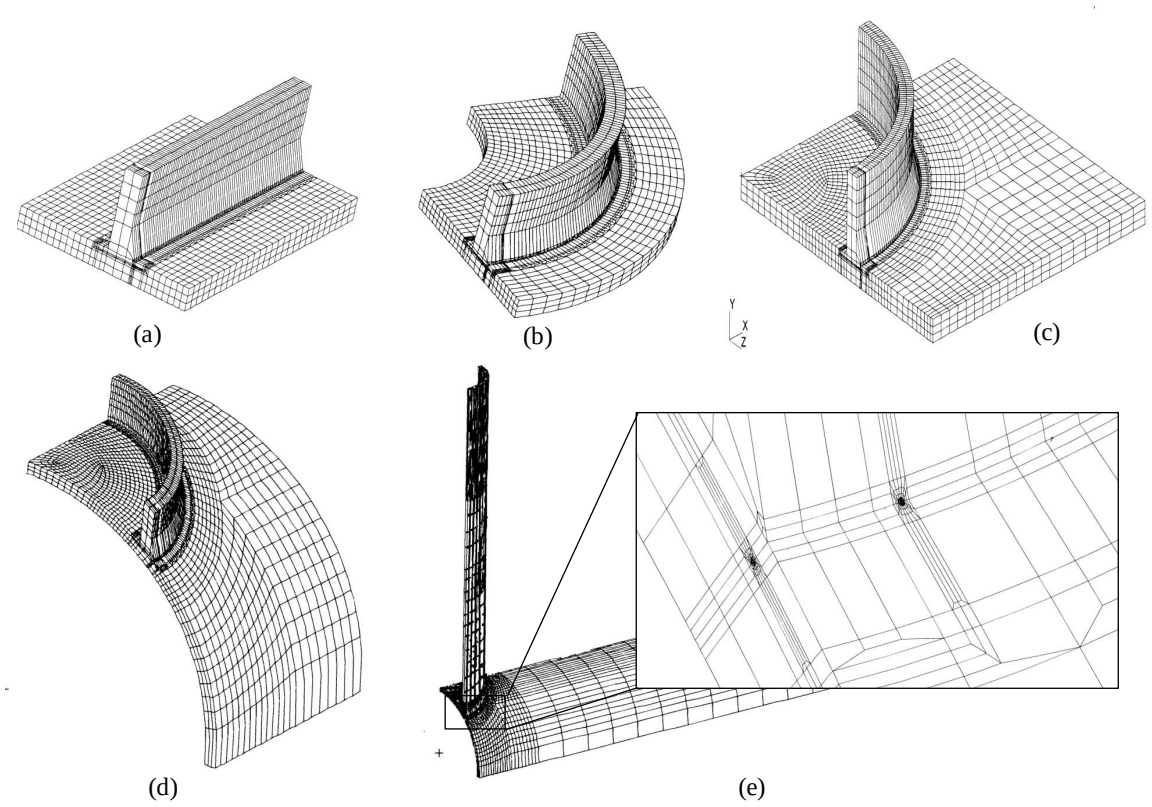

Fig. 3.20: Procedure to generate a tubular X-joint with a weld toe surface crack using the continuous mesh: (a) cracked T-butt joint generated by FEA crack (2011); (b) mapping-1; (c) mesh building in Patran (2012); (d) mapping-2; and (e) mesh building in Patran (2012).

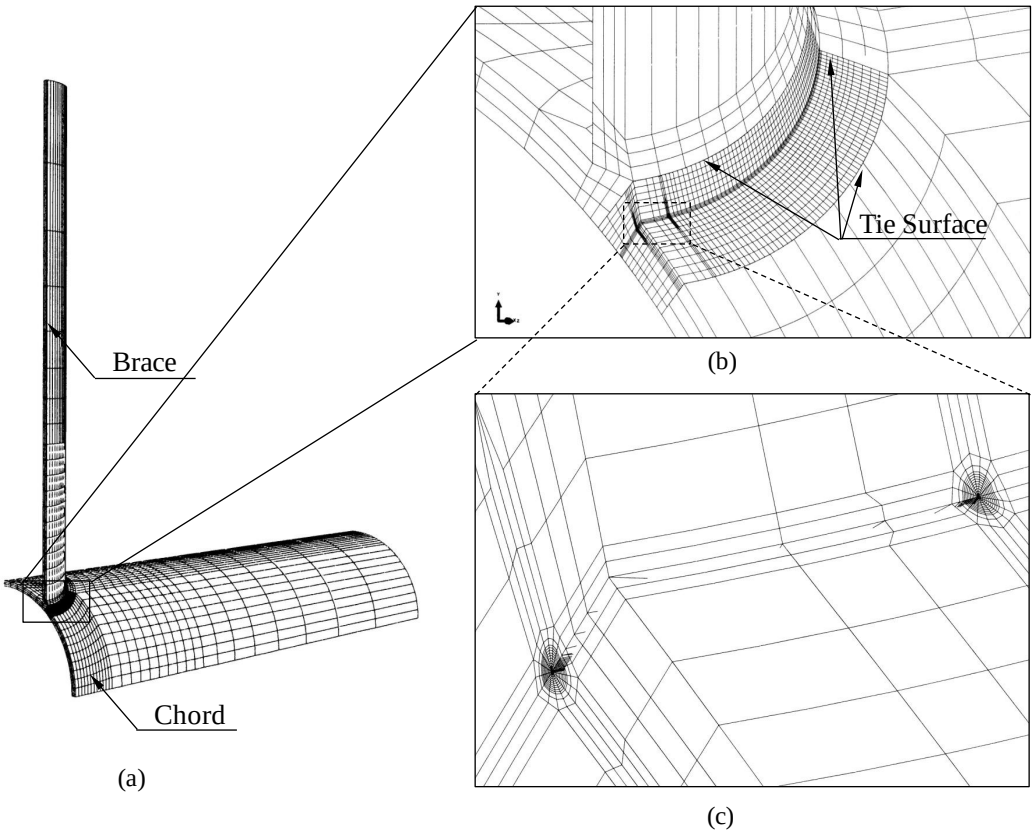

Fig. 3.21: A typical mesh-tie model for a tubular X-joint with a weld toe surface crack: (a) overall view; (b) close up view of the crack front block tied to the global model; and (c) focused mesh around the crack tip.

3.21. Patran (2012) generates the global model using twenty-node solid elements with reduced integration (C3D20R in ABAQUS element library). The local crack-front model contains a block extracted from the global model at the crown point in the tension brace weld toe, as shown in Figure 3.21a. The orientation of the crack plane follows naturally the brace-to-chord intersection curve. The "user-defined" geometry approach in the FEA CRACK software (2011) generates a focused mesh for the crack-front model within this block. The two models (global and crack-front block) are connected via the mesh-tie procedure available in the ABAQUS software (2012), as shown in Fig. 3.21b. The mesh-tie procedure ties two surfaces together for the duration of simulation and makes possible the rapid transition from a very refined crack-front model to a more coarse, global model. This procedure defines two or more geometrically identical surfaces (within a tolerance), as the master (independent) surface and the slave (dependent) surface. Each node on the slave surface, maintains the same displacement as the corresponding independent point on the master surface under the un-deformed configuration based on a set of linear, multi-point constraint equations. These multiple-point constraints remain unchanged in the subsequent analysis. Refinement of the slave surface avoids unconnected master nodes, and ensures a full tieing between the master and slave surfaces.

3.4.2 Results and Discussion

The current study analyzed one CHS X-joint with a surface crack at the weld toe using above two different mesh techniques. The joint geometry follows the description in Table 3.8, where a denotes the depth of the surface crack and c refers to one half of the crack length. Two models employ the same geometry at the crack-front location. Over the crack depth, the shallow crack remains perpendicular to the chord wall thickness. Both of FE models employ 10 rings of elements and 16 elements along the circumferential direction in each ring with a small, initially circular notch about 50 micrometers in radius at the

crack tip to enhance the numerical convergence of large deformation solutions, as shown in Figs 3.20e and 3.21c. The size of the first ring is about 3% of the crack depth. The continuous mesh model includes approximately 88,000 nodes and 18,000 elements. The mesh-tie model includes approximately 70,000 nodes and 14,000 elements.

Table 3.8: Geometric parameters of the cracked X-joint.

Joint	d_0(mm)	β	γ	α	τ	σ_y(MPa)	a/t_0	a/c
X-	406	0.6	20	12	1	355	0.2	0.25

Both FE models employ the domain-integral approach, developed by Shih *et al.* (1986) to compute the energy release rate along the curved front for the surface crack based on the displacement-strain-stress fields obtained from the finite element analyses. According to Shih *et al.* (1986), the local value of the energy release rate at a point s under a static loading condition follows the contour integral,

$$J(s) = \lim_{\Gamma \to 0} \int_{\Gamma} \left((W + T) n_1 - P_{ij} \frac{\partial u_i}{\partial X_i} n_j \right) d\Gamma \tag{3.5}$$

where Γ denotes a vanishingly small contour in the plane normal to the crack front at the point s, and n_j refers to the unit normal vector of the contour Γ, W is the strain energy density, and P_{ij} is the component of 1st Piola-Kirchhoff stress tensor. T represents the kinetic energy density. X_1 is the local coordinate along the crack depth at the point s. Equation 3.5 presents a general expression for the J-integral that includes the effects of inertial as well as inelastic material behavior.

By using a weight function, which may be interpreted as a virtual displacement field, the contour integral in Eq. 3.5 under quasistatic conditions reduces to,

$$J = \int_A \left[P_{ij} \frac{\partial u_i}{\partial X_i} - W \delta_{1i} \right] \frac{\partial q}{\partial X_i} dA \tag{3.6}$$

where q defines a virtual displacement field in the direction of crack extension and A refers to the domain enclosed by a larger contour.

For a three-dimensional crack front, the domain integral approach defines a weighted average J-value over the crack front segment ΔL as,

$$\overline{J}\Delta L = \int_{\Delta L} [J(s)q(s)]ds \tag{3.7}$$

where s denotes a position along the crack front. With the use of the divergence theorem, the numerical evaluation of $\overline{J}\Delta L$ in a local crack front coordinate system becomes,

$$\overline{J}\Delta L = \int_{V_0} \left(P_{ij} \frac{\partial u_i}{\partial X_1} \frac{\partial q_k}{\partial X_j} - W \frac{\partial q}{\partial X_1} \right) dV_0 \tag{3.8}$$

where V_0 represents the undeformed volumn of the finite domain surrounding the crack-tip. This domain-integral formulation supports finite strains and finite rotations. If the point-wise value of the J-integral does not vary appreciably over ΔL, J-integral at certain point derives from the mean-value over the whole segment,

$$J \approx \frac{\overline{J}\Delta L}{\int_{\Delta L} q(s)ds} \tag{3.9}$$

Figure 3.22 plots the non-dimensional global loads and the energy release rate for the analyzed X-joint against the non-dimensional displacement. Both techniques can simulate the plastic deformation at the brace-to-chord intersection successfully, as indicated by the Von Mises stress plot shown in Figs. 3.23 and 3.24. Following the constraint based on the un-deformed configuration of the master and slave surface, the mesh-tie model predicts a slightly stiffer behavior compared with that from the continues mesh model. However, this constraint has almost no effect on the joint load-deformation behavior. The continuous mesh model shows a softer joint behavior and a lower joint capacity due to the

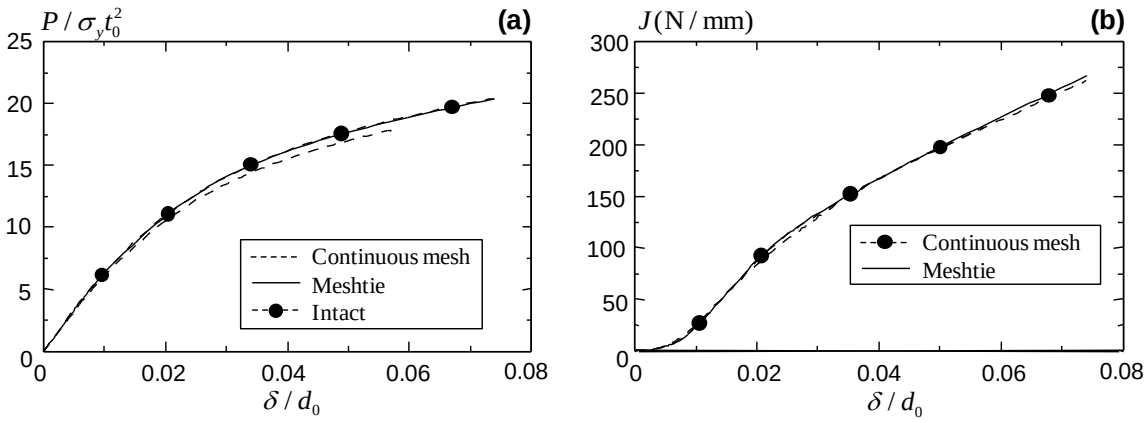

Fig. 3.22: Comparison of the continuous mesh and mesh-tie for a typical cracked X-joint: (a) load deformation curves and (b) energy release rate.

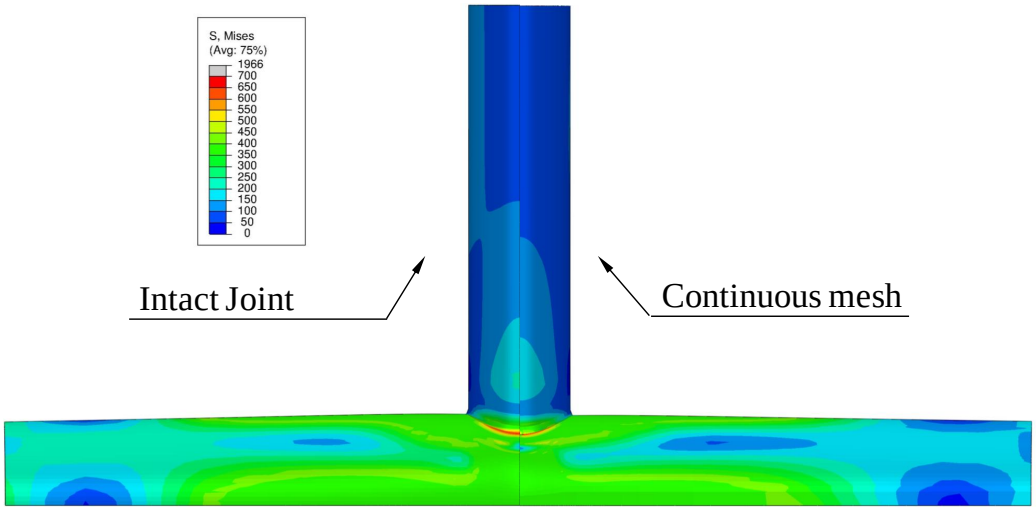

Fig. 3.23: Von Mises stress plots at displacement level $\delta/d_0 = 0.07$ for intact mesh and continuous mesh.

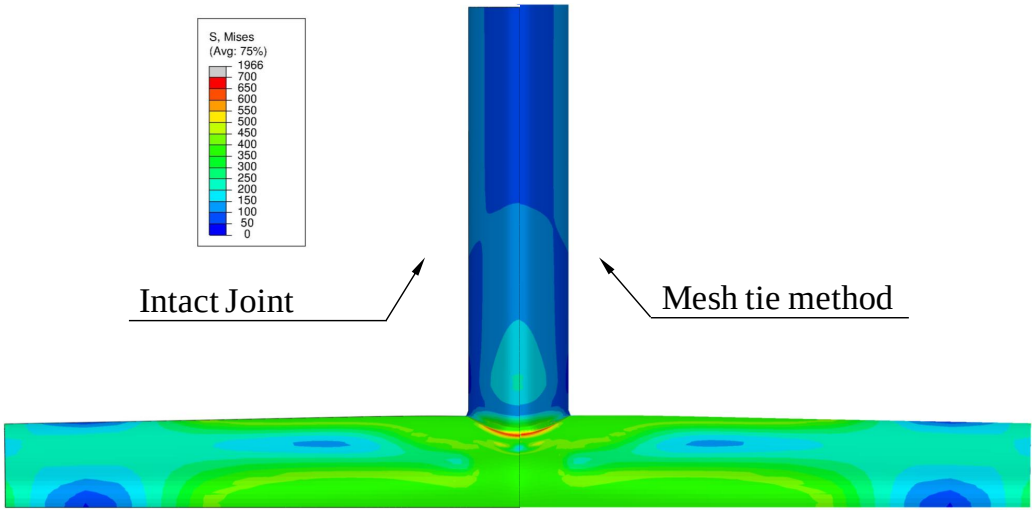

Fig. 3.24: Von Mises stress plots at displacement level $\delta/d_0 = 0.07$ for intact mesh and mesh-tie.

element distortion during the mesh transformation and mapping process. Nevertheless, two approaches show the similar stress distribution and predict successfully the trend of the energy release rate increase due to the stress concentration at the crack tip.

Without losing accuracy in the computation analysis, the mesh-tie model provides several additional advantages in the pre-processing:

- The mapping operation in the continuous mesh technique may generate irregular meshes near the crack front or the brace-to-chord intersection area which will experience a very high stress gradient at the large deformation. The element with very high aspect ratio and zero or negative volume may appear due to the node coordinate transformation. These irregular meshes may cause the computation algorithm un-converged or provide an unreliable result. The extraction of the six-face crack-front block in the mesh-tie technique introduces a regular mesh at the critical location, therefore eliminates these problems.

- The isolated local crack-front model permits a more complicated mesh for global model without considering the mesh transition with the local crack-front mesh.

Therefore, the modeling of K-, DK- and Y- joint with a crack at the weld toe becomes feasible.

- Compared with the continuous mesh model, the mesh-tie model does not involve the tedious mapping and mesh regeneration procedure.

Presumably, mesh-tie method may result in a stiffer model if more cracked are involved. However, the current research only examines single crack problems. Based on the above discussion, the subsequent research will employ the mesh-tie technique to model the cracked tubular joint specimen.

3.5 Summary

This chapter establishes a systematic procedure for the mesh generation of 3D CHS joints subjected to different types of loading. The following discussion investigates the effect of different modeling aspects on the elastic-plastic deformation for tubular joints. Comparisons against the published experimental results prove the validity of the current finite element modelling technique. A further investigation evaluates two different finite element techniques to model a semi-elliptical surface crack at the weld toe for a tubular X-joint. The study summarized above supports the following conclusions:

1. Accurate material strain hardening ensures a good estimation of the CHS joint non-linear behavior under the large deformation. The convergence analyses determine an effective mesh density with 12 elements along the brace-to-chord intersection area and 2 elements along the chord wall thickness direction to capture the accurate behavior of tubular joints. As compared with 8-node elements, 20-node elements mesh with reduced integration increases the accuracy of the analysis with the acceptable computational resources. A good representation of the weld size ensures a correct estimation of the CHS joint load-deformation curve.

2. The elastic-plastic crack driving force, denoted as the J-integral, serves as a parameter to characterize the crack tip stresses and strains for nonlinear materials, under the monotonically increasing loading. Compared with the continuous mesh technique (Bowness and Lee, 1995), the mesh-tie procedure proposed by Qian *et al.* (2005) shows advantages in accuracy and operability for tubular joints with a complex topology. The isolation of the local crack front model permits a more complicated global model. The subsequent research employs the mesh-tie technique to model the cracked tubular joint specimen.

Chapter 4

New Load Deformation Formulation for CHS X- and K-Joints in Pushover Analysis

4.1 Introduction

The extended service of steel offshore platforms beyond their initial design life of 20 years has become a common practice due to economical considerations (API, 2010). The re-assessment of such platforms requires advanced nonlinear frame analyses which should include an accurate representation of the local joint responses under overloading conditions. The rigid joint assumption in the conventional frame analysis often underestimates the deformation and over-estimates the ultimate resistance of the critical joint. The rigid joint hypothesis therefore may cause strong effects on the load-distribution and the sequence of the component failure in the structure, leading to severe deviations in the predicted frame behavior from the real structural response. However, frame analyses with rigid-joint assumptions do not always provide conservative estimations on the ul-

timate strength of the structure, since the large deformation of the joint may mobilize adjacent redundant members and lead to higher structural resistances than the prediction by rigid-joint frame analyses. Hence, improved understandings on the effect of nonlinear joint behavior on the frame response become necessary to develop a simple and calibrated engineering representation of the nonlinear joint characteristics in pushover analyses.

This chapter develops a nonlinear joint formulation which predicts closely the load-deformation responses for CHS X- and K-joints subjected to brace axial compression. This proposed formulation describes the load-deformation relationship for CHS X- and K-joints with different geometric parameters covering a brace to chord diameter ratio (β) from 0.3 to 1.0 and a chord radius to thickness ratio (γ) ratio from 7 to 25. The proposed load-deformation relationship develops from load-deformation results computed using calibrated FE analyses. The parametric formulation, proposed in the current joint representation, provides a convenient approach to characterize the load-deformation curve and eliminates the need for the elastic-plastic, large-deformation finite element analyses on CHS X- and K-joints. The nonlinear pushover analysis, performed in the numerical tool USFOS (USFOS, 2009), proves the validity of the proposed formulation by implementing the proposed formulation via spring elements between the chord and brace members in 2-D and 3-D space frames.

This chapter first develops the proposed joint formulation to represent the joint resistance increasing and decreasing with respect to the deformation due to the yielding and plasticity mobilized under the remote brace loading. The study compares the proposed joint formulation with calibrated finite element results. The following section presents the verification of the proposed formulation using experimental results reported on large-scale 2D and 3D frames. The last section summarizes the main conclusions drawn from the current study.

4.2 Joint Representation

The current work targets at developing an accurate nonlinear relationship for the load-deformation responses of CHS X- and K-joints, including both the elastic and the elastic-plastic responses. The expected function, which needs to describe such a relationship, shall entail the following characteristics. The formulation should provide highly accurate estimates on the joint response for a wide range of practical geometric parameters. The function should be at least C^1 continuous, implying that the change in the joint stiffness as the load increases should be continuous before any unstable failure occurs. The basic form of the function should remain universal for different types of joints under various loading conditions. In addition, the function should adopt a simplest possible form for curve fitting and subsequent engineering applications.

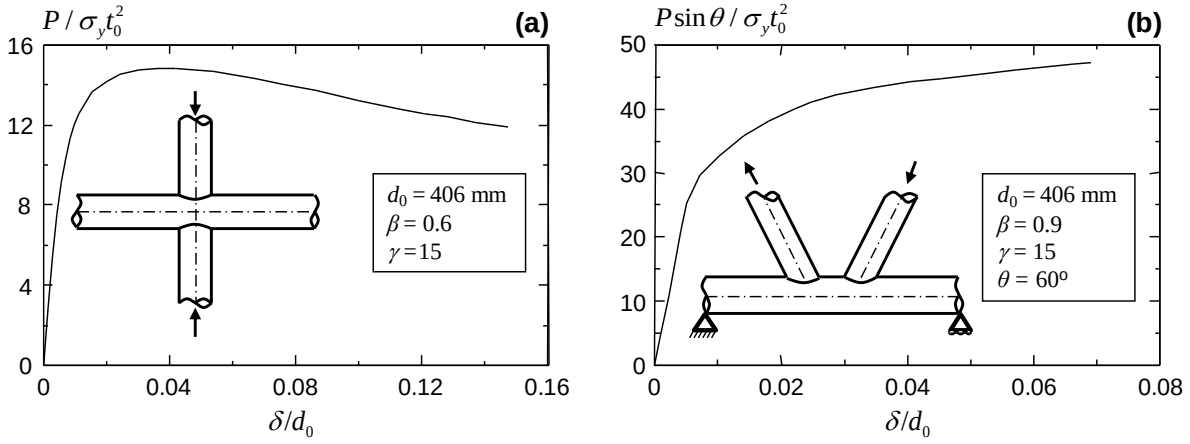

Fig. 4.1: Typical load-deformation curves for: (a) an X-joint under axial brace compression and (b) a K-joint under balanced axial brace loading.

Figure 4.1 shows the typical load-deformation curve for an X-joint under the brace axial compression and that for a gapped K-joint under balanced brace axial loads. Except for very thick-walled chords (Choo *et al.*, 2003), the X-joint under the brace axial compression often exhibits a peak load as the deformation increases. The joint resistance decreases gradually after the peak load as the plastic deformation propagates in the chord

wall. In contrast, the gapped K-joint under balanced axial loads sustains monotonically increasing loads until the joint resistance is limited by the ductility of the material, or extensive plastic deformations in the chord.

Coupling the physical response of the X- and K-joints with the requirements on the expected load-deformation function, the proposed load deformation formula follows,

$$\overline{P} = f(\overline{P_u})g(\overline{\delta}) \tag{4.1}$$

where $\overline{P}$ and $\overline{P_u}$ are the non-dimensional load and ultimate load, respectively, or,

$$\overline{P} = \frac{P \sin\theta}{\sigma_y t_0^2} \tag{4.2}$$

$$\overline{P_u} = \frac{P_u \sin\theta}{\sigma_y t_0^2} \tag{4.3}$$

where σ_y denotes the yield strength of the chord material, t_0 refers to the thickness of the chord member, and θ measures the intersection angle between the brace and the chord. The $\overline{\delta}$ parameter in Eq. 4.1 represents the non-dimensional deformation of the joint,

$$\overline{\delta} = \frac{\delta}{d_0} \tag{4.4}$$

where d_0 denotes the chord diameter. In Eq. 4.1, $f(\overline{P_u})$ is a linear function of $\overline{P_u}$ and $g(\overline{\delta})$ is a logarithmic function of $\overline{\delta}$,

$$\overline{P} = A_3\overline{P_u}\left\{1 - A_1\left[\ln\left(1 + A_2\overline{\delta}\right) - \frac{1}{\sqrt{A_1}}\right]^2\right\} \tag{4.5}$$

In Eq. 4.5, $A_3\overline{P_u}$ refers to the extreme value of the function. The derivative of the load $\overline{P}$ follows,

$$\frac{d\overline{P}}{d\overline{\delta}} = -2A_1A_3\overline{P_u}\ln\left[(1 + A_2\overline{\delta})/(e^{\frac{1}{\sqrt{A_1}}})\right]\left(\frac{A_2}{1 + A_2\overline{\delta}}\right) \tag{4.6}$$

The coefficient A_1 determines the decreasing rate of the joint strength beyond the peak load. A large value of A_1 in Eq. 4.5 creates a sharp variation in the joint resistance as the deformation increases, while a small value of A_1 generates a smooth load-deformation relationship. The value of A_1, therefore, exhibits strong dependence on the geometric parameters of the joint. The coefficient A_2 together with A_1 determines the initial stiffness of the curve. The joint displacement at the peak load derives from Eq. 4.5 by setting $\overline{P} = A_3\overline{P_u}$, or by setting Eq. 4.6 to zero,

$$\overline{\delta_u} = \frac{\delta_u}{d_0} = \frac{e^{\frac{1}{\sqrt{A_1}}} - 1}{A_2} \tag{4.7}$$

The proposed joint formulation includes four independent parameters: $\overline{P_u}$, A_1, A_2 and A_3. The current approach employs the mean strength equations in IIW (2009) for $\overline{P_u}$, which follows,

$$\overline{P_u} = 3.16(\frac{1+\beta}{1-0.7\beta})\gamma^{0.15} \tag{4.8}$$

$$\overline{P_u} = (2+16\beta^{1.6})\gamma^{0.3}\left[1+\frac{1}{1.2+(g/t_0)^{0.8}}\right] \tag{4.9}$$

Equation 4.8 defines the non-dimensional ultimate strength X-joints under the brace axial compression and Eq. 4.9 calculates that for K-joints under the balanced brace axial loading. The use of Eqs. 4.8 and 4.9 reduces the number of undetermined coefficient to three: A_1, A_2 and A_3. The value of coefficients A_1 and A_2 should remain in reasonable ranges to avoid a negative value of the dependent variable $\overline{P}$, which requires a positive value of the $g(\overline{\delta})$ function, or,

$$A_1\left[\ln(1+A_2\overline{\delta}) - \frac{1}{\sqrt{A_1}}\right]^2 < 1 \tag{4.10}$$

or,

$$e^{\frac{2}{\sqrt{A_1}}} > 1 + A_2\overline{\delta} \tag{4.11}$$

The deformation at the peak load in Eq. 4.7 should remain as a positive value, which requires $A_1 > 0$ and $A_2 > 0$.

4.3 X-Joint Formulation

The current study determines the value of A_1, A_2 and A_3 for CHS X-joints through a regression analysis of the results obtained from 30 elastic-plastic, large-deformation analysis, covering a β ratio from 0.3 to 1.0 and a γ ratio from 7 to 25.

The load-deformation characteristics of the X-joint depend significantly on the β ratio. Based on the plastic hinge model proposed by Togo (1967), plastic hinges form at the saddle point and the mid-depth point of the chord cross section when an X-joint reaches its peak capacity. For a joint with a small β ratio, the chord wall around the brace-to-chord intersection area undergoes membrane, bending and shearing actions. As the β ratio increases, the two braces become closer in locations and the load transfers from one brace to the other predominantly via the membrane action in the chord wall material between the two braces. To reflect this change, the parametric study includes six β ratios: 0.3, 0.6, 0.9, 0.93, 0.96 and 1.0 for the X-joint.

For thin-wall joints with a large γ value, the transverse shear across the chord wall thickness is negligible based on the thin-shell theory. The joint strength depends primarily on the interaction between the bending and axial stresses acting on the chord wall. Large deformations of the chord wall create strong variations in the magnitudes of these bending stresses and axial stresses, causing a pronounced change in the resistance of the joint. This sharp change in the joint resistance with increasing joint deformations yields a relatively large A_1 value. As the β ratio approaches 1.0, the membrane action becomes dominant, which leads to a much higher joint capacity than that of a joint with the same chord size under dominant bending actions in the chord wall. Therefore, the load-deformation

curve for X-joints with a large β ratio shows a smooth variation, corresponding to a small A_1 value in Eq. 4.5.

For thick-walled joints with a small γ value, the transverse shear across the chord wall contributes to the joint strength. The large bending and shear stiffness of the chord wall limits the deformation in the chord wall and leads subsequently to a small variation in the joint resistance with increasing joint deformations, as compared to thin-walled joints. This smooth variation in the load-deformation relationship for the thick-walled joint leads to a relatively small value of A_1.

The term $f(\overline{P_u}) = A_3\overline{P_u}$ in Eq. 4.5 characterizes a reference load level in the load-deformation relationship. The non-dimensional ultimate strength $\overline{P_u}$ incorporates the geometric dependence of the load resistance, while the parameter A_3 includes the effect of joint types and loading conditions. The A_3 value for CHS X-joints under brace axial compression, which often exhibits a peak in the load-deformation curve, equals to 1.0.

The curve-fitting procedure to evaluate the coefficients A_1 and A_2 consists of two steps. The first step determines the values of A_1 and A_2 for each discrete load-deformation curve obtained from the finite element analysis. The geometric-dependent formulations of A_1 and A_2 then derive from a nonlinear regression procedure (Greenwood and Nikulin, 1996) using the values of A_1 and A_2 for all joints included in the parametric study. Table 4.1 lists the corresponding formulation for A_1 and A_2, which demonstrates a close agreement with the discrete values obtained using the FE results, as shown by the small standard-deviation values.

Figure 4.2 compares the load-deformation curves predicted by the proposed joint formulation and those computed from the FE analysis for four typical CHS X-joints. The proposed load-deformation formulation agrees well with the load-deformation relationship computed from the large-deformation, elastic-plastic FE analysis.

This study compares the predictions of the critical joint deformation at the peak load

Table 4.1: Coefficients in the proposed formulation for X-joints.

Coefficient	Formulation	Proposed/FE Mean	Standard deviation	No. of data
A_1	$2.07\beta^{5.2}\gamma^{(2.5\beta^2-7.5\beta+4.3)}$	1.00	0.08	30
A_2	$(233\gamma^{3.24\beta}-40\gamma+820)\beta^{0.6}$	1.01	0.09	30
A_3	1.00	1.00	0.02	30

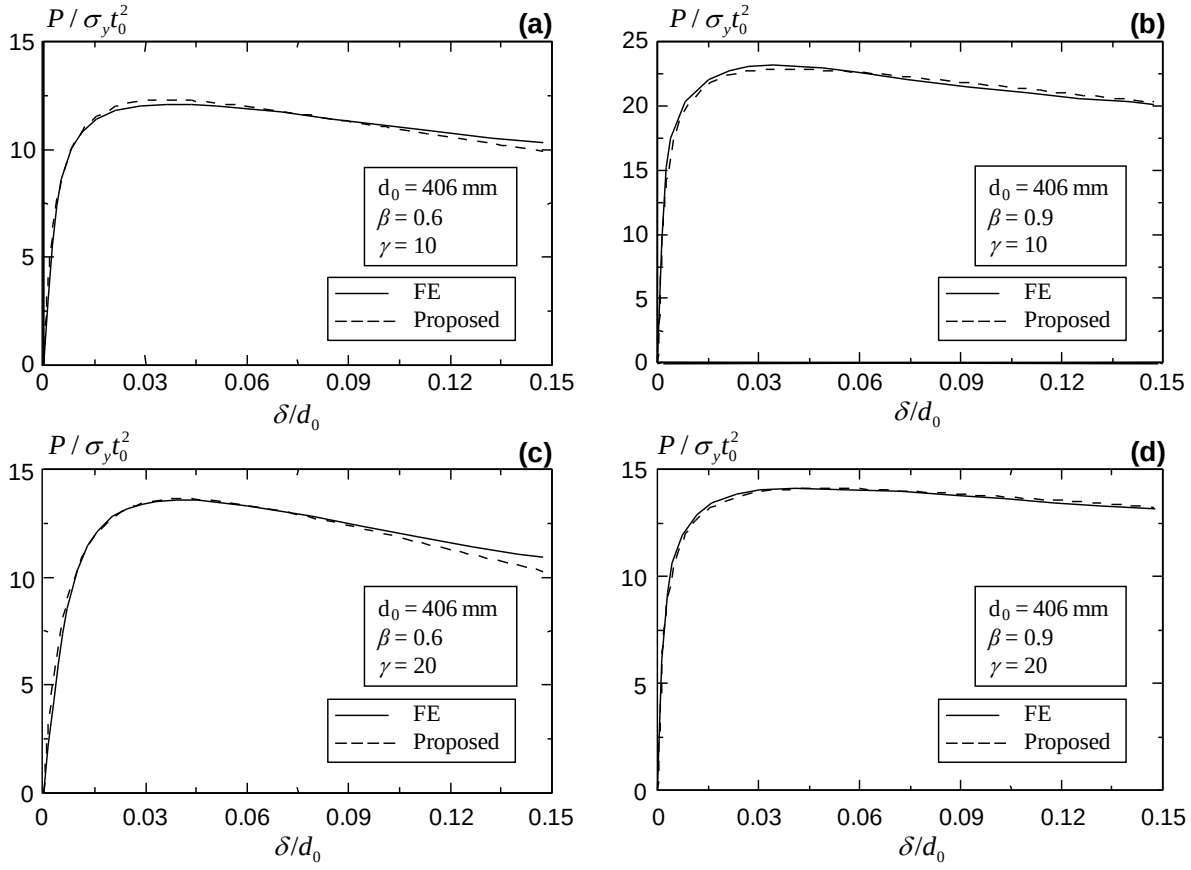

Fig. 4.2: Comparison between the proposed load-deformation formulation and FE results for CHS X-joints with: (a) $\beta = 0.6$, $\gamma = 10$; (b) $\beta = 0.9$, $\gamma = 10$; (c) $\beta = 0.6$, $\gamma = 20$; and (d) $\beta = 0.9$, $\gamma = 20$.

and the initial joint stiffness derived from the proposed joint formulation with the reported studies (Choo *et al.*, 2005; Lu *et al.*, 1994) to ensure that the proposed formulation provides reliable estimations on these important parameters. Lu's deformation limit, which corresponds to a joint deformation equal to 3% of the chord diameter (Lu *et al.*, 1994), has become a widely recognized deformation parameter to define the ultimate strength of tubular joints. The initial stiffness formulation, reported by Choo *et al.* (2005) based on an extensive numerical study, estimates the joint stiffness as,

$$k_0 = \frac{P_E}{\delta_E} = \frac{cP_u}{\delta_E} = \frac{0.8P_u}{\delta_E} \tag{4.12}$$

where the load P_E corresponds to the limit of elasticity and assumes a value of $0.8P_u$ based on the FE analysis (Choo *et al.*, 2005). The initial joint stiffness k_0, therefore, equals,

$$k_0 = 0.8\overline{P_u}/\overline{\delta_E} = 0.8A_2\overline{P_u}/(e^{(1+\sqrt{0.2/A_1})} - 1) \tag{4.13}$$

where $\overline{\delta_E}$ denotes the displacement at $0.8P_u$. Table 4.2 shows the agreement in the δ_u and k_0 values obtained from the proposed joint formulation in comparison with Lu's deformation and the k_0 results reported by Choo *et al.* (2005).

Table 4.2: Comparisons of the critical deformation at the peak load and the joint stiffness with reference studies for X-joints.

Parameters	Results from Reference	Proposed/Reference		
		Mean	Standard deviation	No. of data
δ_u/d_0	0.03 (Lu's deformation limit (1994))	1.10	0.20	30
$k_0 = \frac{P}{\delta}\frac{d_0 \sin\theta}{\sigma_y t_0^2}$	$1185\gamma^{(0.85\beta^2+0.15\beta-0.4)}$ (Choo *et al.*, 2005)	1.09	0.15	30

For X-joints under brace axial compression, a re-development of the joint strength

occurs at a large deformation level due to the direct contact of the compression braces, as observed in the BOMEL 2D and 3D frame tests (Bolt *et al.*, 1994; Bolt, 1995). Figure 4.3a shows the large deformation of the chord, which leads to the contact of two braces through the chord inner surface. This phenomenon remains uncommon in the engineering practice and only appears in the BOMEL 2D and 3D frame tests (Bolt *et al.*, 1994; Bolt, 1995). As the following research will compare the BOMEL 2D and 3d frame test results, the current joint formulation incorporates this phenomenon.

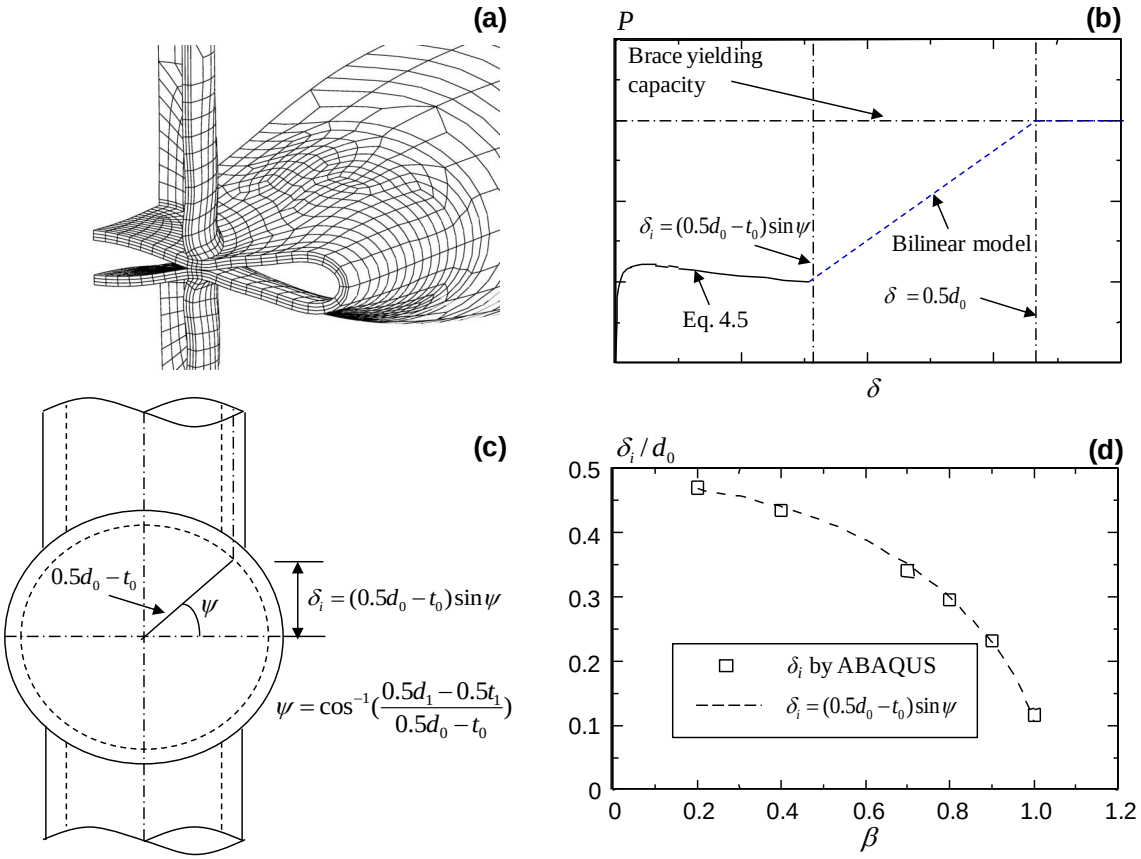

Fig. 4.3: (a) Contact of two compression braces under a large deformation level for an X-joint; (b) schematic load-deformation relationship for the X-joint with the strength re-development; (c) deformation level at the initial contact of the two compression braces; and (d) comparison of δ_i obtained from FE analyses and Eq. 4.14.

The direct contact of two brace members leads to a re-gained joint strength equal to

the axial yield strength of the brace member at a joint deformation of $\delta = 0.5d_0$. The initialization of the strength re-development depends on the β ratio, as shown in Fig. 4.3b, which defines δ_i to be the displacement corresponding to the initial contact of the two braces,

$$\delta_i = (0.5d_0 - t_0)\sin(\cos^{-1}\psi) \tag{4.14}$$

The value of δ_i corresponds to the distance between the inner surface of the chord member near the saddle point, measured along a vertical axis corresponding to the mid-thickness of the brace wall, as shown in Fig. 4.3c. Figure 4.3d shows the close agreement between Eq. 4.14 and the δ_i values obtained from the finite element analysis, which prohibits self penetration of the chord inner surface in the contact algorithm. The proposed joint formulation includes this redevelopment of joint strength for CHS X-joints under the brace axial compression through a bilinear relationship in the load-deformation relationship, as shown by the dashed line in Fig. 4.3b.

4.4 K-Joint Formulation

The load-deformation curve for the K-joint under balanced axial loads follows the response of the compression brace (Choo *et al.*, 2005). Based on the typical load-deformation curve for a gapped K-joint, which continues to sustain increasing loads beyond the Lu's deformation limit (Lu *et al.*, 1994), the K-joint formulation also follows Eq. 4.5.

The strength of the K-joint depends on the membrane, shear and bending resistance of the chord wall around the brace-to-chord intersection. In addition, the gap in the chord between the two braces transfers the load from one brace to the other and experiences bending, shear and membrane actions at large deformations. Similar to the X-joint, the transverse shear in a thick-walled chord of a K-joint also contributes to the joint strength. The shear contribution leads to a smooth load-deformation curve for the thick-walled K-

joint with a small γ ratio. Therefore, the A_1 value, which implies the rate of change in the load level, decreases as γ decreases.

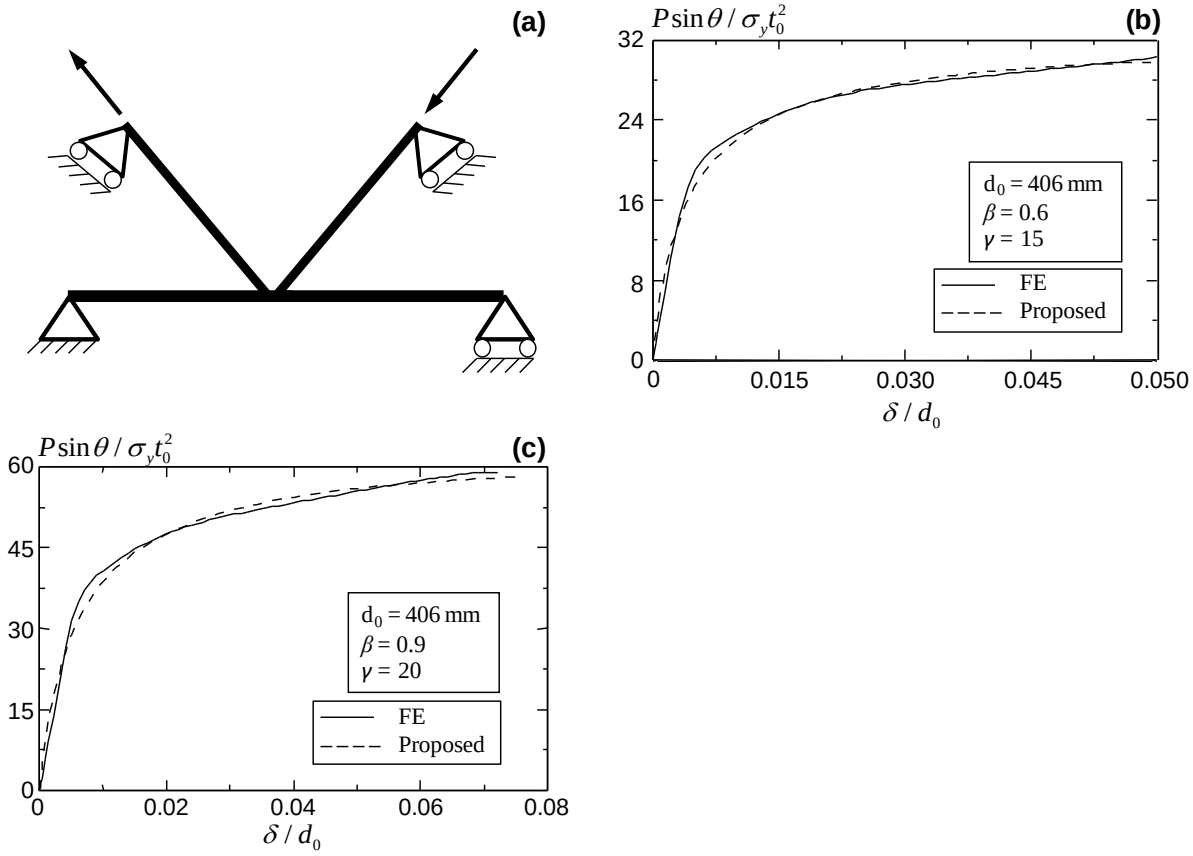

Fig. 4.4: (a) Load and boundary conditions for FE analyses of CHS K-joints; (b) the proposed load-deformation formulation for the CHS K-joint with $\beta = 0.6$, $\gamma = 15$; and (c) the proposed load-deformation formulation for the CHS K-joint with $\beta = 0.9$, $\gamma = 20$.

The determination of the coefficients A_1, A_2 and A_3 follows the same procedure as that for the X-joint. The parametric FE analysis covers a β ratio from 0.3 to 1.0 and a γ ratio from 7 to 25. The numerical analysis fixes the gap between two braces to be twice the wall thickness of the chord. The boundary conditions for the K-joint follows that shown in Fig. 4.4a, which provides a conservative representation of framing effect on the K-joint (Choo *et al.*, 2006).

Table 4.4 illustrates the formulation for A_1, A_2 and A_3 based on the nonlinear re-

Table 4.3: Coefficient in the proposed formulation for K-joints.

Coefficient	Formulation	Proposed/FE Mean	Standard deviation	No. of data
A_1	$\frac{(0.075\gamma^2-1.5\gamma+26.4)e^{(-0.0017\gamma^2+0.014\gamma+1.47)\beta}}{1000}$	1.00	0.04	16
A_2	$2267e^{-1.9\beta}$	1.00	0.05	16
A_3	1.13	1.00	0.03	16

gression analysis, which leads to a close agreement with the values determined from the FE analysis, as reflected by the mean and standard deviation values in the same table. Figures 4.4b and 4.4c sketch the load-deformation curves predicted by the proposed joint formulation and those computed from the FE analysis for two typical K-joints. The proposed joint formulation based on the IIW equation (2009) provides a close agreement with the FE results.

4.5 Validation of Joint Representation in Pushover Analysis

The current study implements the proposed joint formulation in the frame analysis performed using the nonlinear frame analysis tool, USFOS (2009). The verification study utilizes experimental results from large-scale 2D and 3D frame tests (Bolt *et al.*, 1994; Bolt, 1995; Kurobane *et al.*, 1986). The element formulation in USFOS employs the exact solution of the governing equation for beam-columns subjected to end-forces, which enables the modeling of each physical member by one element. The plastic hinges at the mid-span and at the end of the beam-column element simulate the material nonlinearity (USFOS, 2009).

4.5.1 BOMEL 2D Frames

Bolt *et al.* (1994) reports an experimental study of a series of a 2D large-scale frame tests under the scope of a joint industry project. The frame test consists of 6 double-bay X-frames and 4 single-bay K-frames. The current study compares the results of three X-braced frames, namely Frame I, Frame II and Frame III, as shown in Fig. 4.5. The design

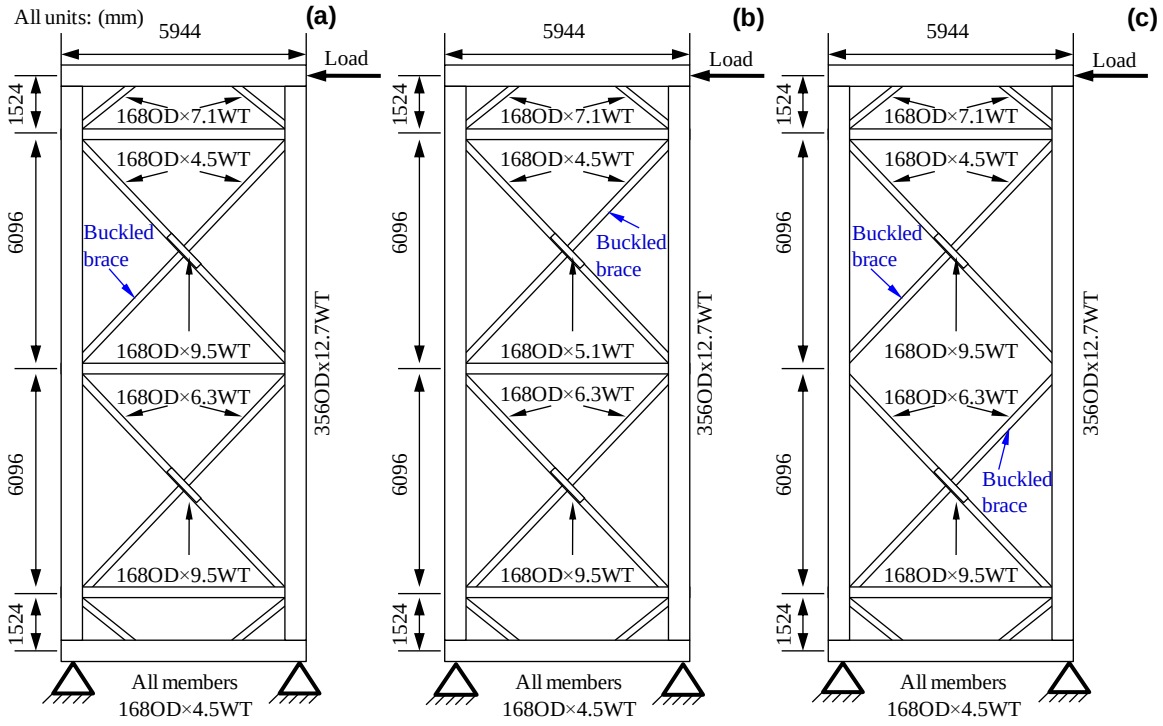

Fig. 4.5: Configuration of BOMEL 2D frames: (a) Frame I; (b) Frame II; and (c) Frame III.

of X-frames follows practical configurations representative of offshore jacket structures. Frame I has strong joint-cans at both the top and the bottom bays, together with a horizontal member in the middle of the top and the bottom bays, while frame II includes a weak joint-can at the top bay to investigate the load shedding and redistribution. Frame III remains the same as Frame I, except that the mid-horizontal member is removed. Each frame connects to a test rig through pin connections at the bottoms of the two

vertical legs, with out-of-plane pin supports provided at six primary leg joints. The test arrangement applies a horizontal load at the top of the frame until the critical joints and members deform significantly, causing pronounced reductions in the frame resistance.

The current study includes three types of joint formulation for each frame analysis:

1. the rigid joint assumption,
2. MSL joint formulation (USFOS, 2009),
3. the proposed joint formulation.

Figure 4.6a compares the numerical analysis and the test results for Frame I. In Frame I, the buckling of the top-bay compression brace (shown in Fig. 4.5a) dominates the frame strength. All three analyses predict this failure mechanism. The proposed formulation leads to a slightly better prediction on the ultimate strength of the test frame than the MSL joint formulation.

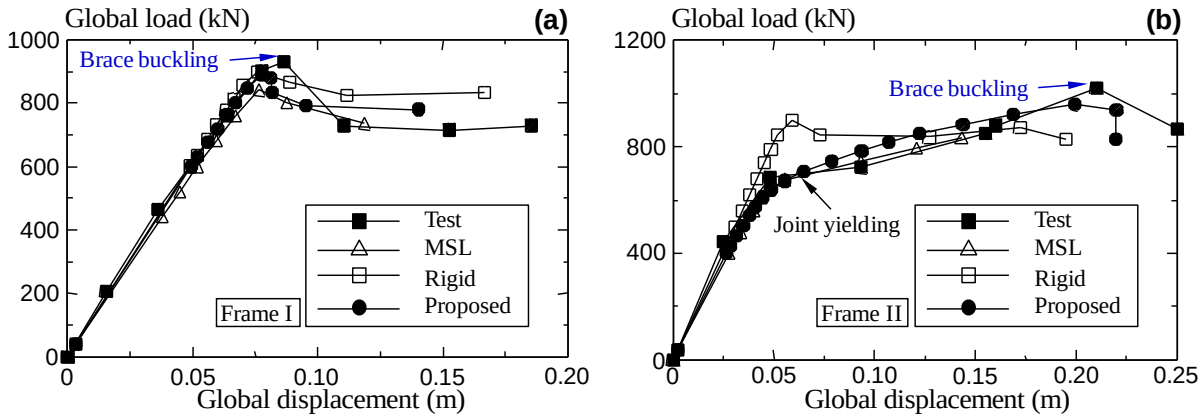

Fig. 4.6: Comparison of the global load-deformation response between numerical analyses and experimental records for: (a) Frame I and (b) Frame II.

Figure 4.6b compares the global response for Frame II, in which the top-bay X-joint is the critical structural component. This X-joint with $\beta = 1$ under brace axial compression softens gradually due to increased plastic deformations in the chord wall beyond the peak

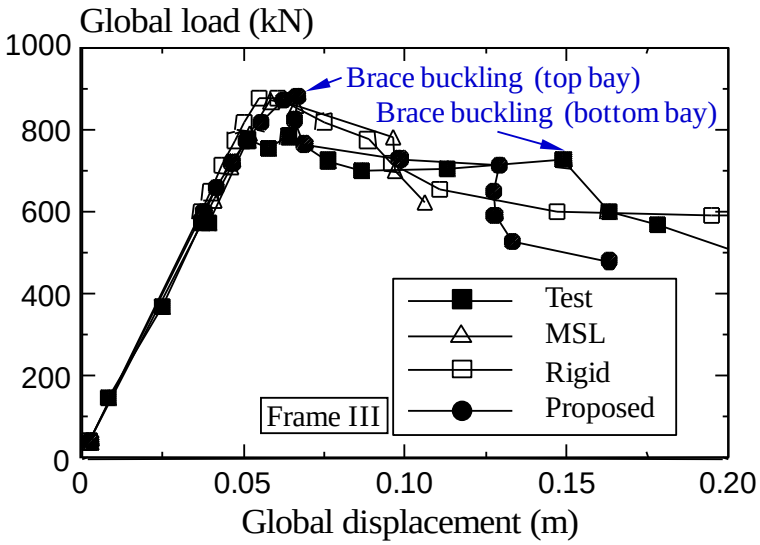

Fig. 4.7: Comparison of the global load-deformation response between numerical analyses and experimental records for Frame III.

load. The contact of two braces at a further deformation redevelops the joint strength sufficient to cause the buckling of the compression brace in the top bay. The global load applied on the frame thus increases until the buckling of that compression brace occurs. The MSL formulation shows the softening of the X-joint in line with the experimental observation. However, the MSL formulation imposes a deformation limit on the X-joint and leads to the termination of the analysis before the unstable brace buckling takes place. The proposed joint formulation predicts both the softening of the CHS joint due to plastic deformations in the chord wall and the re-strengthening of the X-joint at a large deformation level. The predicted frame response using the proposed joint formulation thus reflects correctly the buckling failure of the test frame, albeit that this brace buckling occurs at a lower load level than that observed in the test.

Without the horizontal member, Frame III shows a similar ultimate strength level compared to Frame I, as shown in Fig. 4.7. The absence of the horizontal member generates significant load re-distributions beyond the top bay brace buckling. This forces the buckling of the bottom bay brace to occur at a small global displacement level. The

frame analysis based on the proposed joint formulation provides a better prediction on the global frame response than that using the MSL formulation and that based on the rigid joint assumption.

4.5.2 Kurobane's 2D Frames

Kurobane and Ogawa (1986) summarize the cyclic tests on 15 2D frames, with six frame configurations investigated. The current study verifies the K-joint formulation based on three typical frames, as shown in Fig. 4.8. All three frames shown in Fig. 4.8 experience a vertical load at the right end of the frame, while the chord ends on the left are fixed via flange connections to a reaction wall. The test measures the rotation as the deflection of the frame divided by the length of the truss.

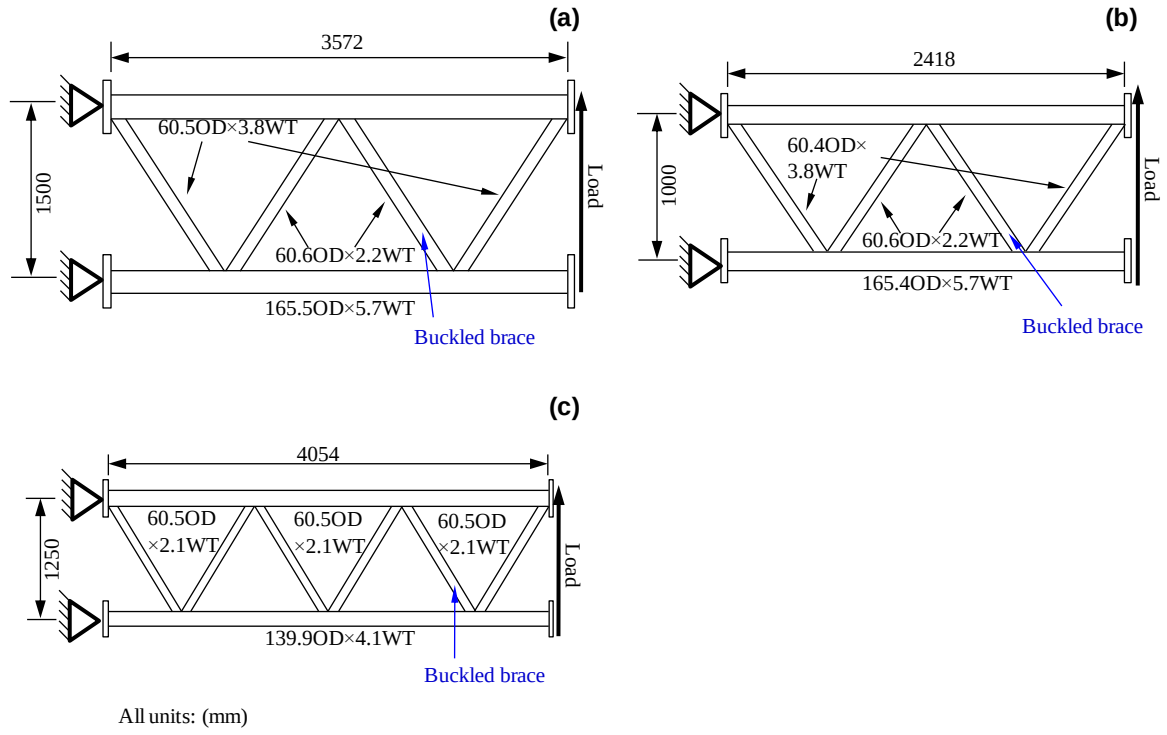

Fig. 4.8: Configuration of Kurobane's 2D frames: (1) Frame A; (b) Frame B; and (c) Frame T.

Figure 4.9 compares the numerical prediction of the frame response based on different joint formulations with the experimental results. Similar to the BOMEL 2D frames, the numerical study includes three types of joint formulation in the frame analysis. Each frame analysis includes the joint formulation for all K-joints in the frame. All three analyses (the rigid joint, the MSL formulation and the proposed formulation) predict accurately the failure mode of Frame A, which is governed by the member buckling (Figs. 4.8a and 4.9a). The proposed formulation agrees with the test results on both the frame stiffness and the ultimate frame strength. The MSL formulation predicts a more flexible frame response than the test results. A detailed examination reveals that the MSL formulation predicts a much lower joint stiffness than the proposed joint formulation does. The latter agrees with the joint stiffness obtained from a separate FE analysis for the K-joint in Frame A.

Frame B fails by the out-of-plane buckling and local buckling of the brace (Figs. 4.8b and 4.9b). The three analyses show similar strength predictions as the test, as shown in Fig. 4.9b. The MSL formulation provides a lower prediction on the frame stiffness than the test frame.

Figure 4.9c compares the numerical prediction and the experimental record on the global load-displacement response for frame T, which is governed by the buckling of the brace shown in Fig. 4.8c. The rigid joint formulation predicts a sequence of member buckling due to the stiff joint response. The MSL formulation predicts a weak joint and the frame exhibits a much lower strength and a much lower stiffness than the test results. The proposed joint formulation predicts closely the softening of the joint and agrees well with the peak strength of the test frame. After the brace buckles, the joint sustains the coupling load with axial force and in-plane-bending, which lead to the different drop between the numerical result and experimental test.

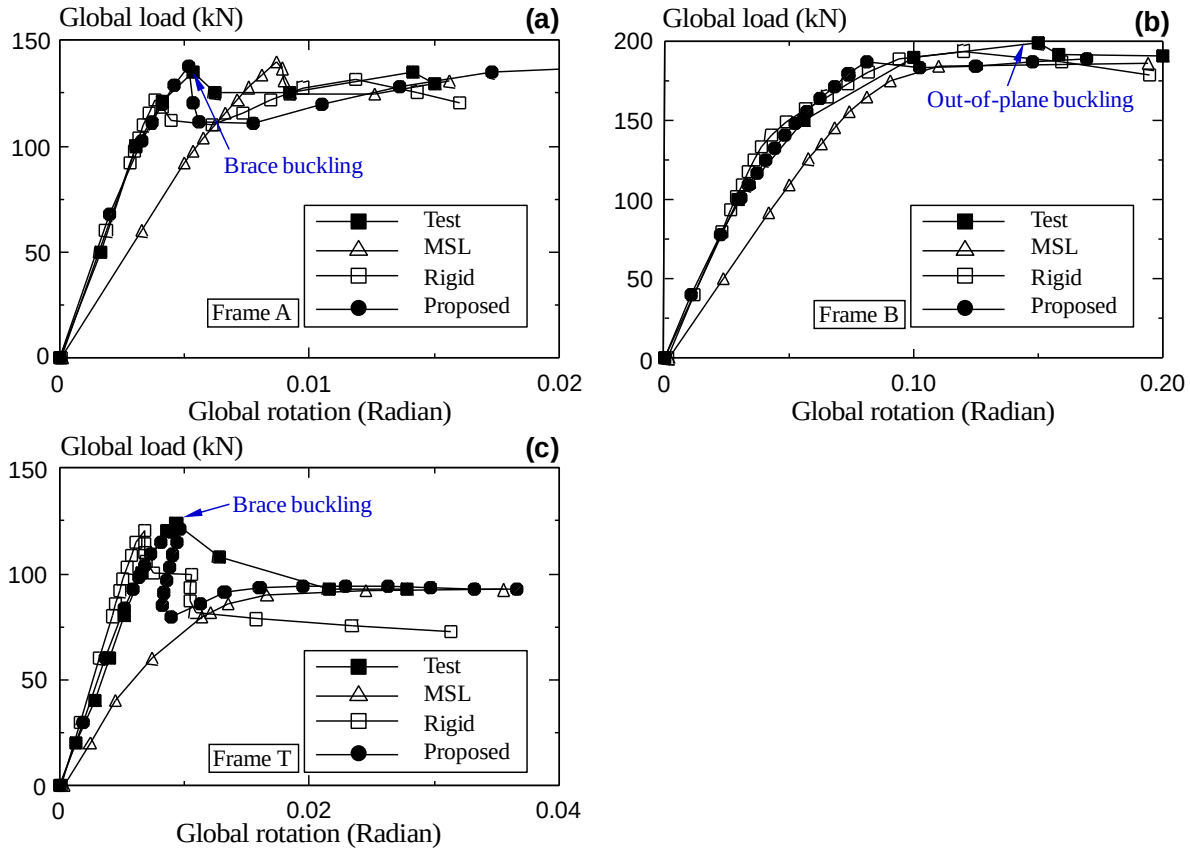

Fig. 4.9: Comparison of the global load-deformation response between the numerical analysis and experimental records for: (a) Frame A; (b) Frame B; and (c) Frame T.

4.5.3 BOMEL 3D Frames

Bolt and Billington (2000) report the large-scale 3D frame tests shown in Fig. 4.10. The double-bay test frame consists of six vertical legs. As shown in Fig. 4.10a, the structure presents a hybrid of bracing configuration typical for offshore jacket structures. The two longitudinal panels in the horizontal plane (designated as Panel A and Panel B) are X-braced. In Panel A (the bottom panel in Fig. 4.10a) the X-joints have thick joint-cans. In Panel B (the top panel in Fig. 4.10a), the two level I X-joints do not include joint-cans and the through chords run in opposite directions. The transverse panels C and D are K-braced with intermediate diamond bracing in between the two panels. In Panel C, neither of the gapped K-joints has a joint-can. The distant transverse panel E is X-braced but without a horizontal member in the middle height. The entire structure is mounted in a self-reacting frame made of I- and H- sections, as illustrated in Fig. 4.10a. The bottom of the self-reacting frame, which is parallel to Panel A, sits on a strong floor. The entire testing procedure includes three load cases, as shown in Figs. 4.10b-4.10c, in which the self-reacting frame is removed.

The testing of the 3D frame includes three load cases. In Load Case I, the front K-braced panel along Panel C is loaded vertically upwards, as shown in Fig. 4.10b. Figure 4.11a shows the comparison of three analyses with the experimental results. The weld-toe crack near the tension brace in the K-joint (Fig. 4.10b) initiates a slight decrease in the frame strength. However, this crack does not grow extensively under increasing loads. Instead, the diamond brace in level I redistributes the load to Panel D and the K-brace in Panel D buckles at the peak frame load.

None of the three types of joint formulation includes a representation on the fracture failure in tubular joints. Both the MSL and the proposed formulation predict the weakening of the joint under plastic deformation as well as the subsequent brace buckling in the frame. The proposed formulation provides a close prediction on the ultimate strength

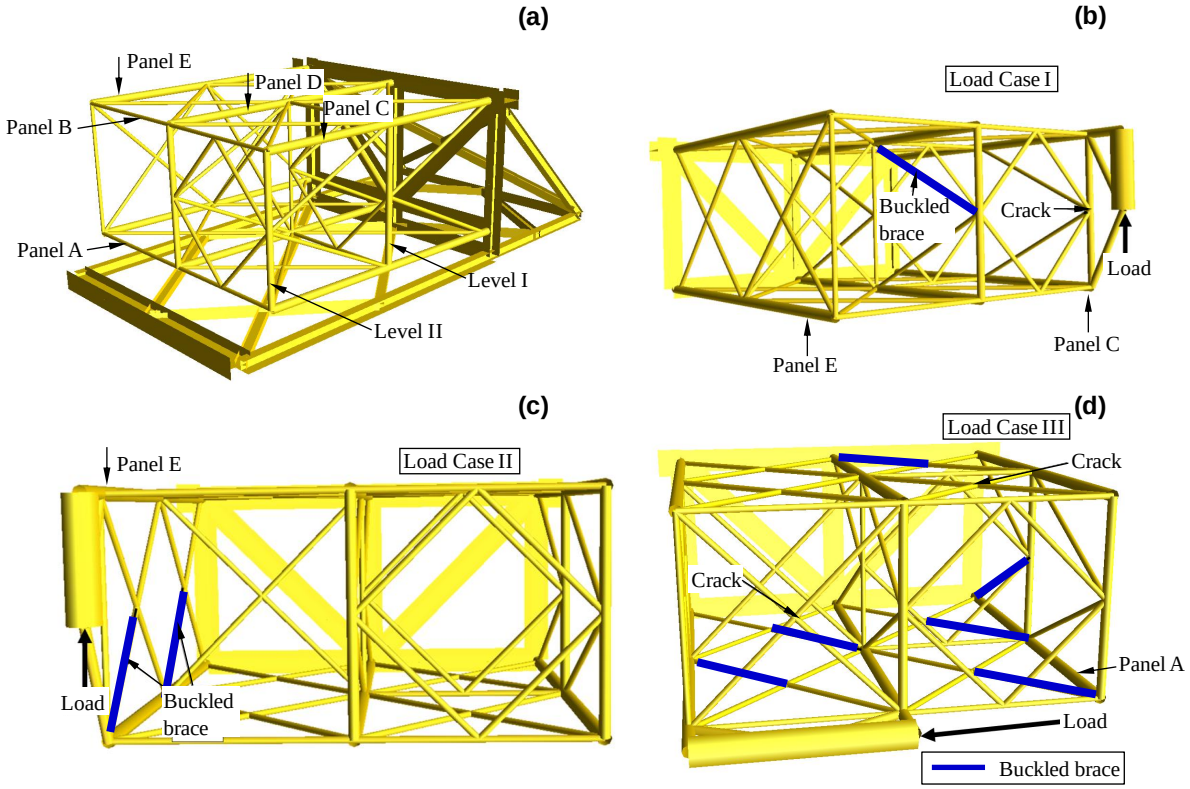

Fig. 4.10: Configuration of BOMEL 3D frame test: (a) test model; (b) Load Case I; (c) Load Case II; and (d) Load Case III.

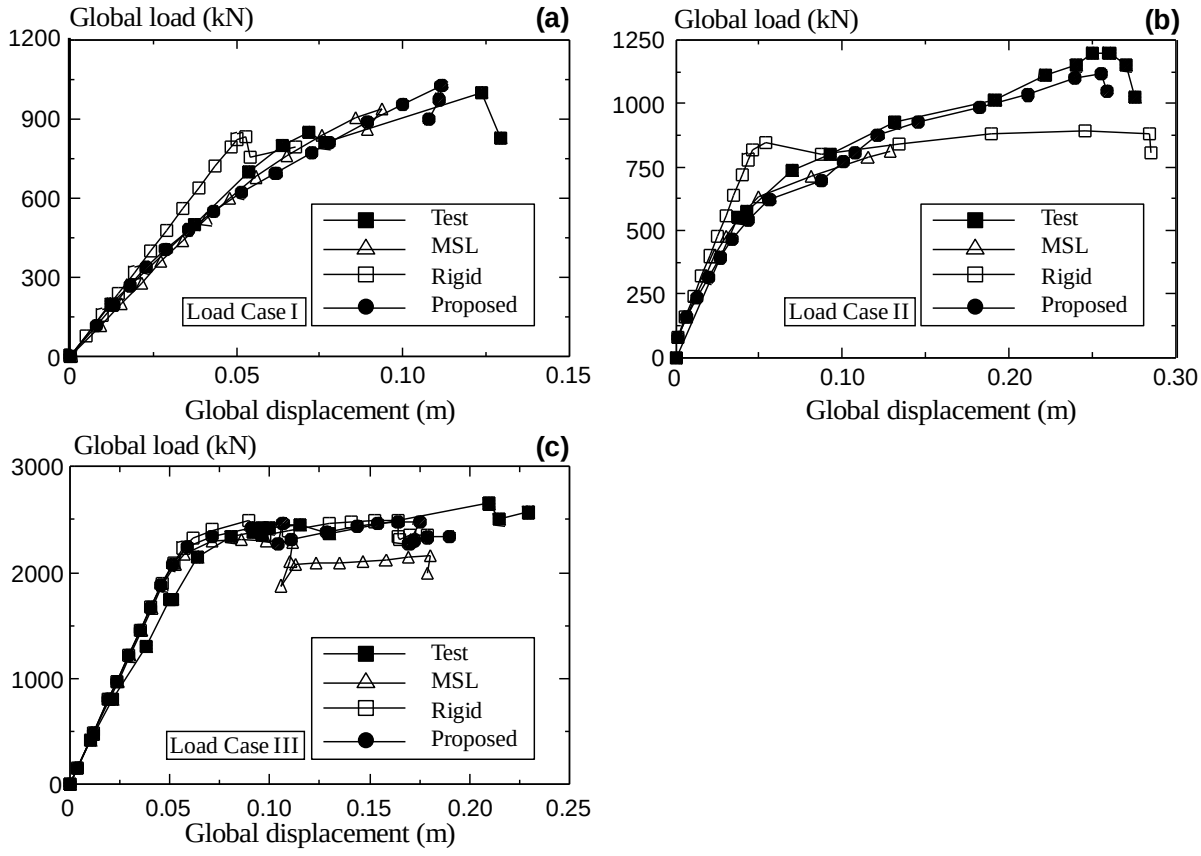

Fig. 4.11: Comparison of the global load-deformation response between numerical analysis and experimental records for BOMEL 3D test: (a) Load Case I; (b) Load Case II; and (c) Load Case III.

of the test frame.

In Load Case II, the X-braced Panel E experiences a vertical load applied in an upward direction as shown in Fig. 4.10c. The weakening of the X-joint under plastic deformation in the chord wall leads to a ductile frame response. Similar to Frame II in the BOMEL 2D frame (see Fig. 4.6b), the large deformation of the joint enables contact of the two compression braces through the inner surface of the chord. This contact leads to the redevelopment of the joint strength and causes the buckling of the compression brace. Both the MSL joint formulation and the proposed joint formulation predict the weakening of the joint, as shown in Fig. 4.11b. Similar to the Frame II (in Fig. 4.6b), the deformation limit in the MSL joint formulation terminates the frame analysis at a small deformation level, insufficient to mobilize the subsequent brace buckling. The proposed joint formulation shows a good agreement with the test results for Load case II. The rigid joint formulation estimates a relatively smaller frame capacity than the test by forcing the compression brace to buckle at a very small global deformation level.

In Load Case III, a horizontal load is applied along Panel A to the bottom X-braced panel. After all the compression braces in Panel A buckles, the horizontal braces redistribute the load to Panel B and leads to the crack in two joints shown in Fig. 4.10d. The test stops after the K-brace in Panel C buckles. Similar to Load Case I, crack initiation is not captured, which contributes to the difference between the proposed formulation and test results. Figure 4.11c shows that the proposed formulation predicts the frame ultimate strength accurately.

4.6 Summary

The current chapter develops a new load-deformation formulation for CHS X- and K-joints to describe their nonlinear load-deformation behavior in the global pushover anal-

ysis. The reference ultimate strength in the proposed joint formulation follows the latest IIW recommendations (2009). The proposed joint formulation develops through regression analyses of the FE results, which are validated against reported experimental results. The verification study of the proposed formulation on CHS X- and K-joints in the pushover analysis utilizes 2D BOMEL (Bolt *et al.*, 1994), and Kurobane frame tests (Kurobane *et al.*, 1986) as well as 3D BOMEL (Bolt, 1995) frame experiments. The study summarized above supports the following conclusions:

1. The proposed joint formulation provides a convenient approach to estimate the load-deformation relationship for CHS X- and K-joints. The parametric formulation based on the joint geometry and loading conditions eliminates the need for the elastic-plastic, large-deformation finite element analyses on CHS X- and K-joints. The verification based on the reported experimental study proves the accuracy of the proposed formulation.

2. The comparison between the frame analyses with various joint formulations and the experimental data demonstrates the significance of the nonlinear load-deformation joint behavior in the frame response, especially for simple 2-D frames with low redundancy. The rigid joint assumption leads to completely different failure modes in a frame with weak joints. The proposed formulation, implemented as joint-spring elements in the frame analysis, provides close predictions on both the failure modes and the ultimate strength for 2-D and 3-D tested frames.

Chapter 5

An Eta-Approach to Evaluate the Elastic-Plastic Energy Release Rate for Weld-Toe Cracks in Tubular X- and K-Joints

5.1 Introduction

Circular hollow sections (CHSs) often serve as the primary structural component for steel offshore platforms. During the transportation, installation or operation, the offshore platform often experiences ineluctably variable-amplitude environmental loads, including waves, currents and winds (API, 2010; DNV, 2011). The significant stress variation caused by these environmental actions may induce cumulative fatigue damage and initiate surface cracks at hot-spot locations at the weld toe along the intersection of two or more CHS members, as shown in Fig. 5.1. The engineering failure assessment of the fatigue cracked tubular joints requires a convenient and accurate approach to determine

the elastic-plastic crack driving force (measured by the J-integral) for surface cracks in these connections with a complex topology, for which analytical solutions often become intractable. The energy-based η approach, which calculates the energy release rate based on the area under the load versus the load-line displacement curve for simple fracture specimens with a through-thickness crack, provides a theoretically validated framework to determine the elastic-plastic energy release rate for fatigue cracks in 3-D structural components.

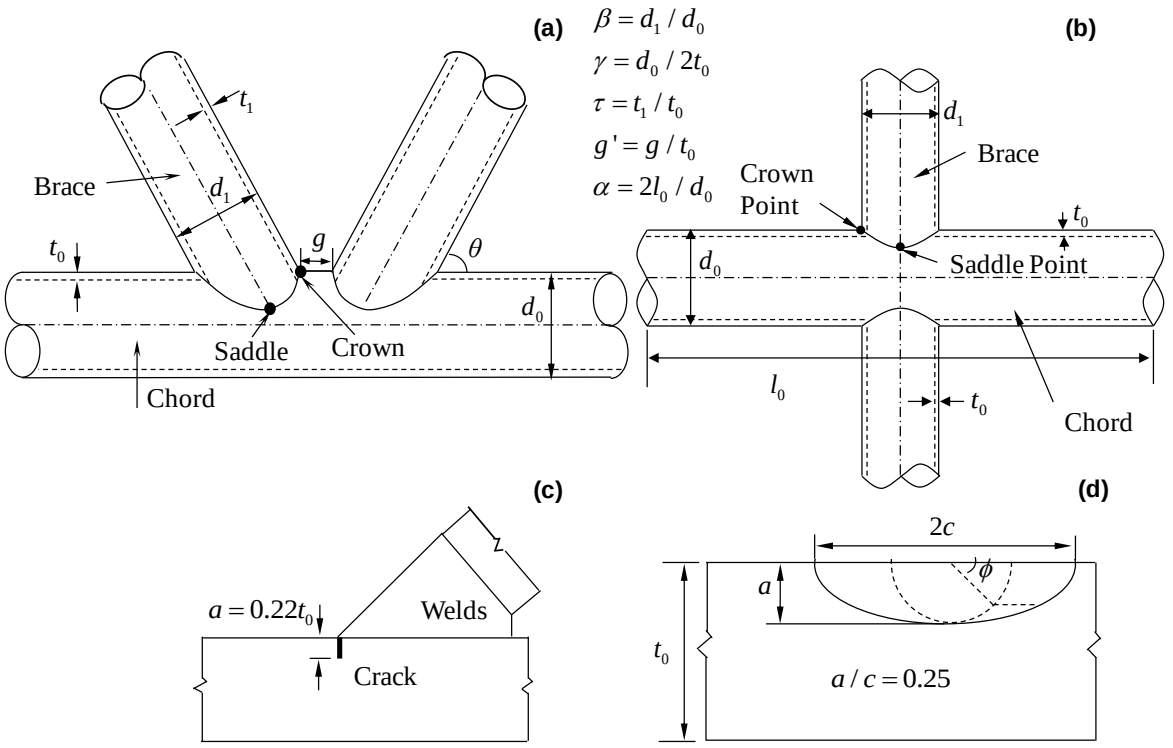

Fig. 5.1: Geometric configuration of a typical CHS joint: (a) front view of a K-joint; (b) front view of an X-joint; (c) a surface crack at the weld toe; and (d) planar view of the surface crack.

Earlier researchers propose various approaches to compute the J-value for cracks located at hot-spot positions in CHS joints based on the finite element method, as described in Section 3.4. All these J-integral evaluation methods involve complex pre-processing work and require substantial computational resources. The η approach, originally pro-

posed by Rice *et al.* (1973), provides an energy-based method to estimate the J-integral value for standard fracture specimens using the area under the load versus the load-line displacement record. Sumpter and Turner (1976) extend the η approach by decomposing the J-integral value into an elastic and a plastic component. The plastic work factor η_{pl}, a dimensionless parameter, relates the plastic component of the J-integral with the plastic work under the load versus the load-line displacement curve. Previous researchers introduce various plastic η factors (Turner, 1981; Paris *et al.*, 1980; Merkle and Corten, 1974; Clarke and Landes, 1979; Sumpter, 1987), focusing on standard fracture specimens, *e.g.*, the compact tension, C(T), specimen and the single-edge-notched bend, SE(B), specimens used in ASTM E-1820 (2011). The available literature has not yet reported any study on the η approach for surface cracks in 3-D structural components with a complex topology.

The current study extends the plastic η approach to estimate the energy release rate for surface cracks in CHS X- and K-joints. The η approach presents a close prediction of the J-value compared to the domain-integral approach. This proposed method demonstrates a linear relationship between the external plastic work and the elastic-plastic crack driving force and provides a convenient approach to evaluate the elastic-plastic crack driving force before significant plastic deformations develop in the adjacent chord material for cracked joints under monotonically increasing brace axial loads.

This chapter starts with an introduction of the derivation of the plastic η approach for the SE(B) specimen. The next section discusses the variation of the crack driving force along the front of shallow surface cracks located at weld-toes of the chord crown point near the tension brace in K-joints calculated from the domain-integral method. The following section evaluates the J-integral along the front of shallow surface weld-toe cracks located at the saddle point for X-joints under brace axial tensile loads. The subsequent section proposed the plastic η approach for weld toe cracks in tubular joints.

The last section summarizes the main conclusion drawn from the current study.

5.2 The η Approach

The derivation of the η approach follows a dimensionless analysis (Turner, 1981; Paris *et al.*, 1980) performed for fracture specimens with a through-thickness crack. Figure 5.2a plots a typical SE(B) specimen, where a denotes the depth of the crack and b refers to the length of the remaining ligament. For the displacement-controlled condition, the J-integral follows,

$$J = -\frac{\partial U}{B\partial a} = -\frac{1}{B}\int_0^{\Delta}\left(\frac{\partial P}{\partial a}\right)_{\Delta_{LLD}} d\Delta_{LLD} \tag{5.1}$$

where U denotes the strain energy stored in the fracture specimen and equals the area under the load versus the load-line displacement curve, P is the applied external loading, B refers to the thickness of the specimen and Δ_{LLD} measures the load-line displacement. Under large deformations, the specimen deforms into a plastic-hinge mechanism with two rigid bars, as shown in Fig. 5.2b. The plastic rotation θ_{pl} can be assumed as a dimensionless function f, which depends on the applied loading, geometry and material properties,

$$\theta_{pl} = f(\frac{M_P}{\sigma_y b^2 B}, \frac{E}{\sigma_y}, n) \tag{5.2}$$

where M_P denotes the moment at the plastic hinge induced by the load P, σ_y refers to the material yield strength, and n is the strain-hardening exponent in the Ramberg-Osgood relationship,

$$\varepsilon = \frac{\sigma}{E} + \alpha\frac{\sigma_y}{E}(\frac{\sigma}{\sigma_y})^n \tag{5.3}$$

For a typical structural steel material,

$$\alpha\frac{\sigma_y}{E} = 0.002 \tag{5.4}$$

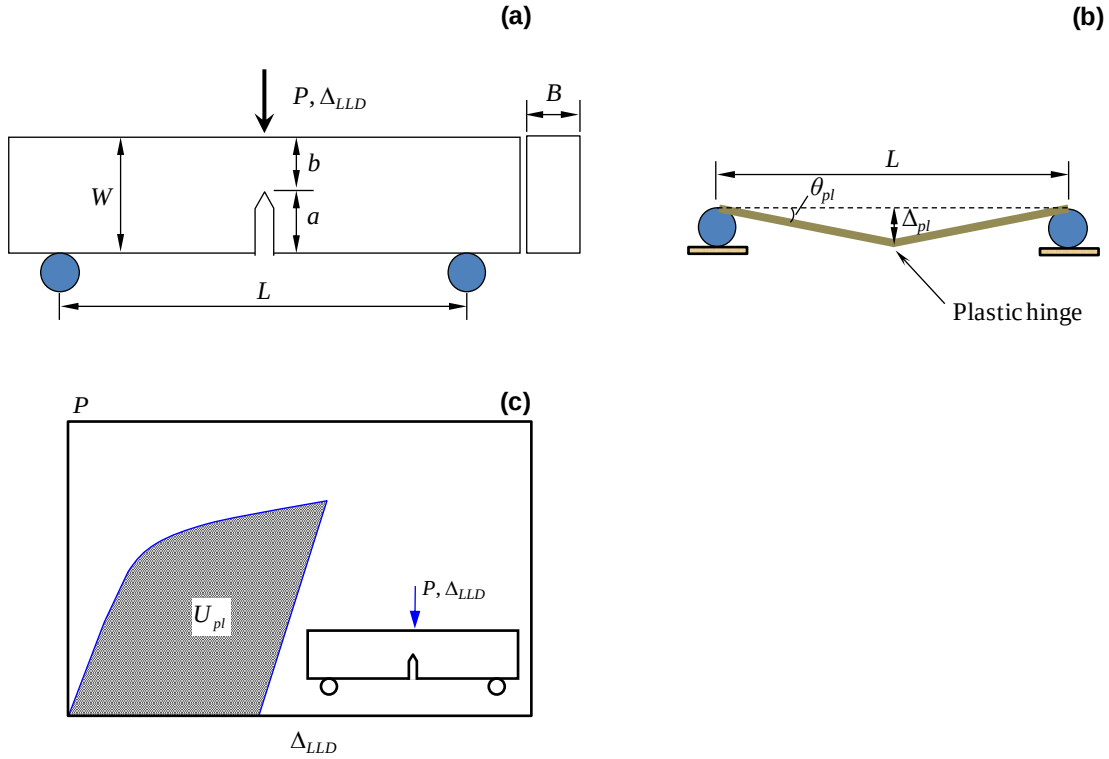

Fig. 5.2: (a) Geometric configuration of a SE(B) specimen; (b) plastic-hinge mechanism for a SE(B) specimen; and (c) schematic plot of the load versus the load-line displacement for a fracture specimen.

In Eq. 5.2, M_P and θ_{pl} follow a linear function of P and Δ_{pl}, respectively,

$$M_P = \frac{PL}{4} \tag{5.5}$$

$$\theta_{pl} = \frac{\Delta_{pl}}{L/2} = \frac{2\Delta_{pl}}{L} \tag{5.6}$$

where L denotes the length of the specimen. By reversing Eq. 5.2, M_P follows,

$$M_P = Bb^2\sigma_y h(\theta_{pl}, \frac{E}{\sigma_y}, n) \tag{5.7}$$

where h is a dimensionless function depending on the plastic rotation and material properties. The combination of Eqs. 5.5, 5.6, and 5.7 provides the expression for P,

$$P = \frac{4Bb^2\sigma_y}{L} h\left(\frac{2\Delta_{pl}}{L}, \frac{E}{\sigma_y}, n\right) \tag{5.8}$$

By substituting Eq. 5.8 into Eq. 5.1, the J-integral becomes,

$$J = -\frac{1}{B}\int_0^{\Delta}\left(\frac{\partial P}{\partial a}\right)d\Delta = \frac{1}{B}\int_0^{\Delta}\left(\frac{\partial P}{\partial b}\right)d\Delta = \frac{1}{B}\int_0^{\Delta}\left[\frac{8Bb\sigma_y}{L} h\left(\frac{2\Delta_{pl}}{L}, \frac{E}{\sigma_y}, n\right)\right]d\Delta \tag{5.9}$$

$$J = \frac{1}{B}\int_0^{\Delta}\frac{2P}{b}d\Delta = \frac{2}{Bb}\int_0^{\Delta} Pd\Delta \tag{5.10}$$

The above leads to the development of a more general form for other types of fracture specimens and structural components with through-thickness cracks,

$$J = \frac{\eta}{Bb}\int_0^{\Delta} Pd\Delta = \frac{\eta U}{Bb} \tag{5.11}$$

where the η factor, replacing the constant 2 in Eq. 5.10, denotes a non-dimensional parameter relating the J-integral with the work U. Sumpter and Turner (1976) further

decompose the total J-integral into the elastic and plastic components,

$$J = J_{el} + J_{pl} \tag{5.12}$$

where J_{el} denotes the elastic component of J given by,

$$J_{el} = \frac{K_I^2}{E'} \tag{5.13}$$

and J_{pl} refers to the plastic component of J given by,

$$J_{pl} = \eta_{pl} \frac{U_{pl}}{A_{lig}} \tag{5.14}$$

In Eq. 5.13, K_I denotes the mode I stress-intensity factor and E' refers to the effective modulus of elasticity which equals the Young's modulus E for a plane stress condition and $E/(1-\upsilon^2)$ for a plane strain condition. In Eq. 5.14, U_{pl} denotes the plastic work under the load versus the load-line displacement curve, as shown in Fig. 5.2c and A_{lig} refers to the un-cracked cross-sectional area. The η_{pl} remains as a dimensionless factor varying with the specimen type, the crack depth ratio and the material strain hardening exponent. For the middle tension, M(T), specimen made of a rigid plastic material, $\eta_{pl} = 1$. For compact tension and disk compact tension specimens (ASTM E1820, 2011),

$$J_{pl} = 2 + 0.522 \frac{b}{W} \tag{5.15}$$

Numerous finite element analyses prove the accuracy of the η approach at large plastic deformations (Paris *et al.*, 1980; Sumpter, 1987).

5.3 Elastic-Plastic Crack Driving Force for CHS K-Joints

This section introduces the finite element procedure for CHS K-joints and discusses the variation of crack driving forces with respect to geometric parameters for tubular K-joints.

5.3.1 K-Joint Geometry and FE Modeling

Figure 5.1a shows the typical configuration of a typical CHS K-joint, fabricated by profiling and welding the branch members (the brace) to the main member (the chord). The weld geometry follows the AWS specification (2012). The cyclic loading often nucleates fatigue surface cracks at the hot-spot positions (Karamanos *et al.*, 2000) located at the chord crown point near the tension brace. The surfaces of the fatigue cracks remain perpendicular to the chord outer surface, as shown in Fig. 5.1c. The current finite element model omits the material in the weld-grinding profile to avoid highly distorted elements around the brace-to-chord intersection (Qian *et al.*, 2007).

The current study investigates the crack driving force corresponding to different geometric parameters with four β ratios ($\beta = 0.3$, 0.6, 0.9, 1.0), three γ ratios ($\gamma = 15$, 20, 25) and three gap ratios ($g' = 2$, 6, 10). The chord outer diameter for all models remains fixed at 406 mm, with the brace-to-chord intersection angle equal to $\theta = 60°$. The τ ratio remains as a constant, or $\tau = 1.0$, and defines the same wall thickness for the brace and the chord. The α value is kept at 16 to avoid the constraining effect of the chord ends. Similarly, the brace has a length equal to four times the brace outer diameter. The crack geometry, $a/t_0 = 0.2$ and $a/c = 0.25$, represents a realistic size and depth for shallow surface flaws.

The material Poisson's ratio equals 0.3 for the steel materials and the welds considered in this study. The elastic-plastic material property, following the uni-axial stress-strain

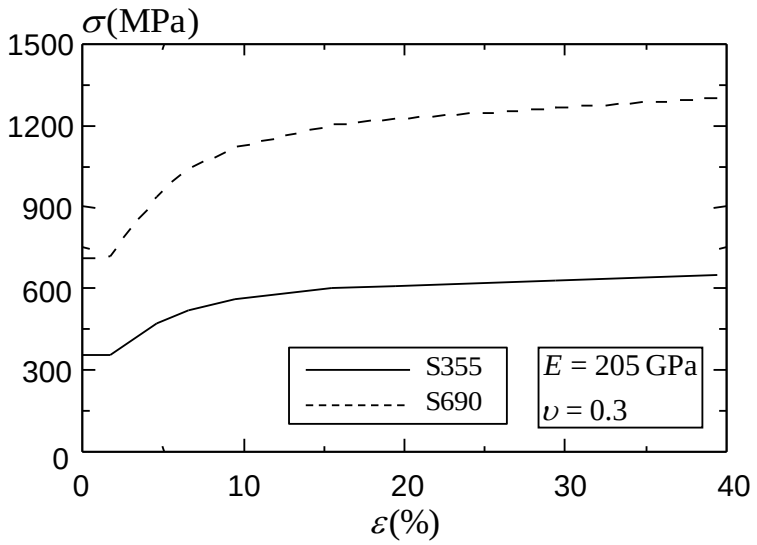

Fig. 5.3: Uni-axial true stress-true strain relationship for the chord, weld and brace materials in modeled CHS joints.

relationship of a typical steel S355, as plotted in Fig. 5.3, remains the same for chord, brace and weld materials. The yield strength and ultimate strength are 355 MPa and 450 MPa, respectively.

The FE mesh for a typical K-joint with a weld-toe crack consists of two parts: the global mesh and the local crack-front model, as shown in Fig. 5.4. The current research employs an automatic procedure developed in the Patran Command Language (Qian *et al.*, 2002) to generate the global model. The adoption of twenty-node solid elements with reduced integration (C3D20R in ABAQUS element library) allows an accurate representation of the weld profile which follows the specifications in AWS (2012). Symmetry about the $z = 0$ plane permits the use of a half model (see Fig. 5.4a). The numerical model utilizes a rigid plate at the end of the CHSs, with its thickness equal to the wall thickness of the corresponding member, and Young's modulus equal to 100 times that of the corresponding member. The boundary condition imposed on the center node of the rigid plate follows that shown in Fig. 5.4d, which provides a conservative representation of the framing effect on the K-joint by adjacent structures (Choo *et al.*, 2006).

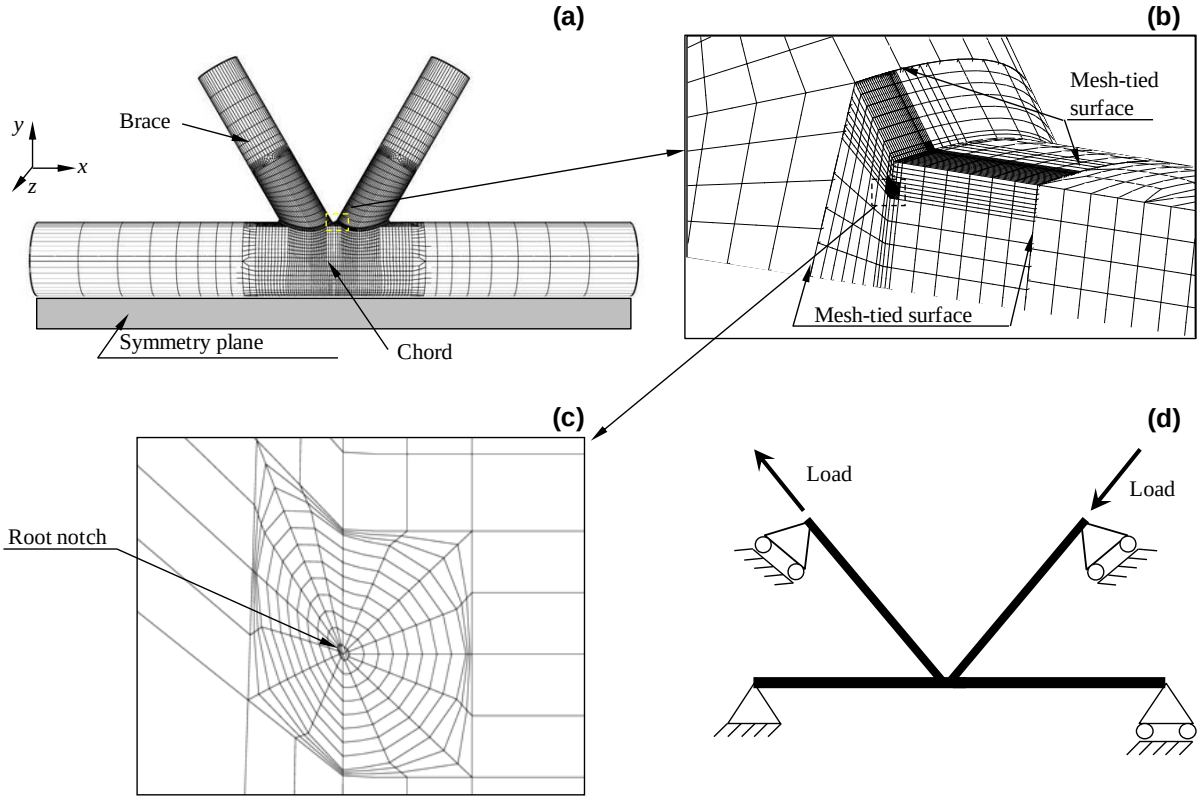

Fig. 5.4: Typical FE details for a CHS K-joint with a surface crack at the crown point near the tension brace: (a) global model; (b) mesh-tieing between the local crack-front mesh and the global model; (c) crack-tip mesh; and (d) loading and boundary conditions.

The balanced loading condition also develops a higher value of the elastic-plastic driving force, as the brace-chord intersection of a K-joint undergoes more severe, localized plastic deformation under the large remote loading (beyond the elastic limit) (Qian *et al.*, 2007).

The local crack-front model contains a block extracted from the global mesh at the crown point near the tension brace, as shown in Fig. 5.4b. The orientation of the crack plane follows naturally the brace-to-chord intersection curve, consistent with the real fatigue cracks observed in test specimens (Bowness and Lee, 1995). The "user-defined" geometry approach in the FEA CRACK software (2011) generates a focused mesh for the crack-front model within this block. At each crack-front location, the current FE model employs 8 rings of elements and 16 elements along the circumferential direction in each ring with a small, initially circular root notch about 50 micrometers in radius at the crack tip to enhance the numerical convergence at large deformations, as shown in Fig. 5.4c. The size of the first ring is about 3% of the crack depth. A typical FE mesh shown in Fig. 5.4a includes approximately 160,000 nodes and 32,000 elements. The two models (global and crack-front block) are connected via the mesh-tie procedure available in the ABAQUS software (2012), as shown in Fig. 5.4b.

5.3.2 Results and Discussion

The current study employs the domain-integral approach (Shih *et al.*, 1986), as discussed in Section 3.4, to compute the energy release rate along the curved front of the surface crack. The finite element analysis employs the incremental theory of plasticity and the finite-strain formulation to compute the elastic-plastic J-value along the front of surface cracks in CHS K-joints. Qian *et al.* (2006) demonstrate that the largest crack driving force exists at the deepest point ($\phi = \pi/2$) along the front for the crack ($a/t_0 = 0.2$ and $a/c = 0.25$) located at a distance of 5mm from the weld toe in the thick-walled CHS K-joint.

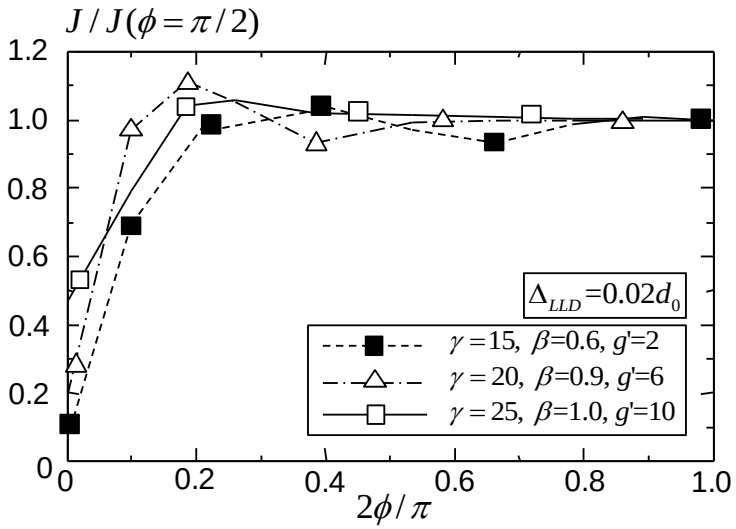

Fig. 5.5: Variation of the non-dimensional J-values along the crack front for different K-joint geometries.

Figure 5.5 plots the variation of the non-dimensional J-value along the front of the crack located at the crown point near the tension brace for three typical CHS K-joints with different β, γ, and gap ratios g'. The J-value, corresponding to the large axial brace deformation $\Delta_{LLD} = 0.02d_0$, exhibits a nearly even distribution for $2\phi/\pi > 0.3$. Therefore, the elastic-plastic crack driving force analyzed in the current study refers to the value at $\phi = \pi/2$ in the 8th domain.

Figure 5.6a indicates a clear distinction in the J-Δ_{LLD} relationships for K-joints with $\gamma = 20$ and $g' = 2$ corresponding to different β ratios. The bending action between two crown points in the chord wall increases significantly as the brace axial load applied on a K-joint increases. The decrease of the β ratio reduces the local dihedral angle near the saddle point and promotes the local bending and shearing action in the chord wall along a shorter weld length. Therefore, the increased intensity of the plastic deformation near the crack surface for a small β ratio induces a higher crack driving force than that for a lager β ratio. For the joint with a small β and g' ratio, the crack driving force increases initially and reaches a plateau as the displacement imposed at the brace end increases, as

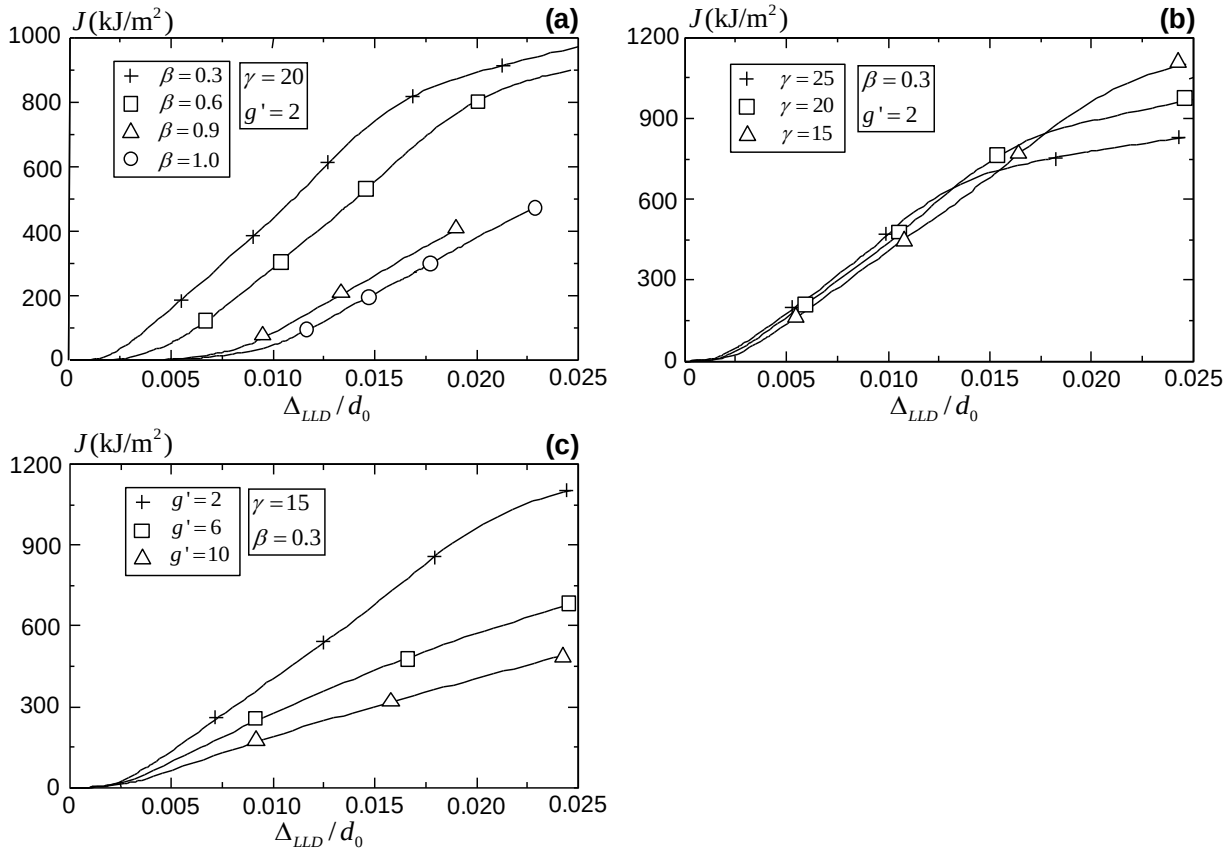

Fig. 5.6: Elastic-plastic J-values for K-joints with (a) $\gamma = 20$, $g' = 2$; (b) $\beta = 0.3$, $g' = 2$; and (c) $\gamma = 15$, $\beta = 0.3$.

shown in Fig. 5.6a for $\beta = 0.3$. The plastic deformation, in the welds and the adjacent brace material away from the crack location, absorbs the remotely imposed displacements at the brace end, and thereby shields the crack-front material in the chord wall. This shielding phenomenon does not occur in joints with higher β ratios ($\beta > 0.6$) or higher g' ratios ($g' > 6$). For joints with a large β ratio, the increased brace diameter and weld volume prevents extensive plastic deformations in the brace and welds, and constrains the plastic deformation in a localized volume of material near the crown point.

The change in γ ratios varies the chord wall thickness, thus the bending action in the chord material for joints with the same chord outer diameter d_0 and the same τ ratio. The decrease of the γ ratio introduces a larger chord wall thickness and a larger magnitude of brace loading, and thus produces a higher value of the J-integral. In contrast, a decrease in the γ ratio reduces the chord wall compliance against bending, and generates lower values of the elastic-plastic J-integrals. The combination of these two effects reduces the variation of the elastic-plastic driving force with respect to the γ ratio, as shown in Fig. 5.6b. For joints with a small γ ratio, the large wall thickness postpones the plastic deformation in the welds and the adjacent brace material near the crack surface, and leads to a continuous increase in the crack driving force as compared to the thin-walled joint with a larger γ ratio.

Figure 5.6c plots the variation of the elastic-plastic J-value for different gap ratios (g') ranging from 2 to 10 for a specific β ratio and γ ratio. The chord wall between the two crown points experiences bending, shearing and membrane actions at large deformation levels. The lower gap ratio reduces the length of the chord wall between two crown points, and thus causes the concentration of bending and shearing actions near the crack surface. Therefore, the crack located at the weld toe in a joint with a smaller gap experiences a higher crack driving force at large deformation levels. For larger gap ratios, the adjacent chord material prevent the sharp force transition between the two crown points, and thus

leads to a smaller crack driving force.

5.4 Elastic-Plastic Crack Driving Force for CHS X-Joints

Following the finite element procedure for CHS K-joints, this section investigates the variation of crack driving forces along a surface crack located at the chord weld toe near the saddle point with respect to different geometric parameters for tubular X-joints under the brace tensile loads.

5.4.1 X-Joint Geometry and FE Modeling

The fatigue surface cracks for CHS X-joints often forms at the hot-spot positions located at the chord saddle point near the tension brace (Chang and Dover, 1999). The surfaces of the fatigue cracks remain perpendicular to the chord outer surface, as shown in Fig. 5.1c. The finite element models employs the similar computational procedure as that for CHS K-joints. The mesh-tie procedure couples the displacement field between a relatively coarser master surface on the global model and a relatively finer slave surface in the local crack front mesh, as shown in Fig. 5.7. The symmetry permits the use of one-eighth model mesh with all nodes on the symmetry plane constrained in the perpendicular DOF.

All the X-joint models employ a fixed chord outer diameter (d_0 = 406 mm) but different geometric parameters with four β ratios (β = 0.3, 0.6, 0.9, 0.95) and four γ ratios (γ = 10, 15, 20, 25). The brace-to-chord intersection angle equals to $\theta = 90°$. This study considers the steel S355 as the base material, whose true stress-true strain curve is plotted in Fig. 5.3. For relatively thicker (γ = 10, 15) CHS X-joints with large β ratios (β = 0.9, 0.95), the current analysis employs a high strength steel S690 for the brace material to avoid the brace yielding under the large deformation. Figure 5.3

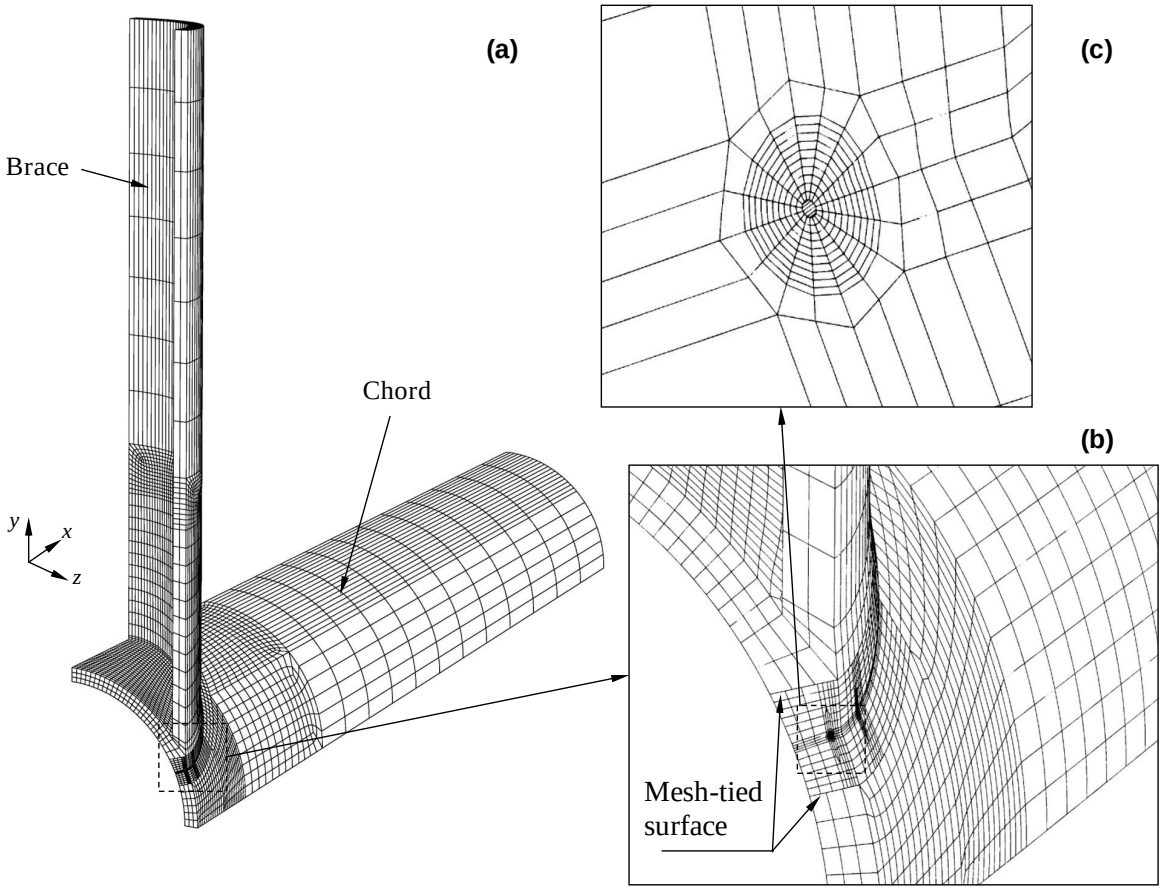

Fig. 5.7: Typical FE details for a CHS X-joint with a surface crack at the chord saddle point near the tension brace: (a) global model; (b) mesh-tie between the local crack-front mesh and the global model; and (c) crack-tip mesh.

illustrates the uniaxial true stress-true strain curve for the S690 steels obtained from tension tests. The local crack model, with an $a/t_0 = 0.2$ and $a/c = 0.25$ semi-elliptical surface crack, contains 16 rings of element around each crack front location. The total number of elements for X-joints ranges from 7,500 to 15,000, with the number of nodes ranging from 35,000 to 78,000.

5.4.2 Results and Discussion

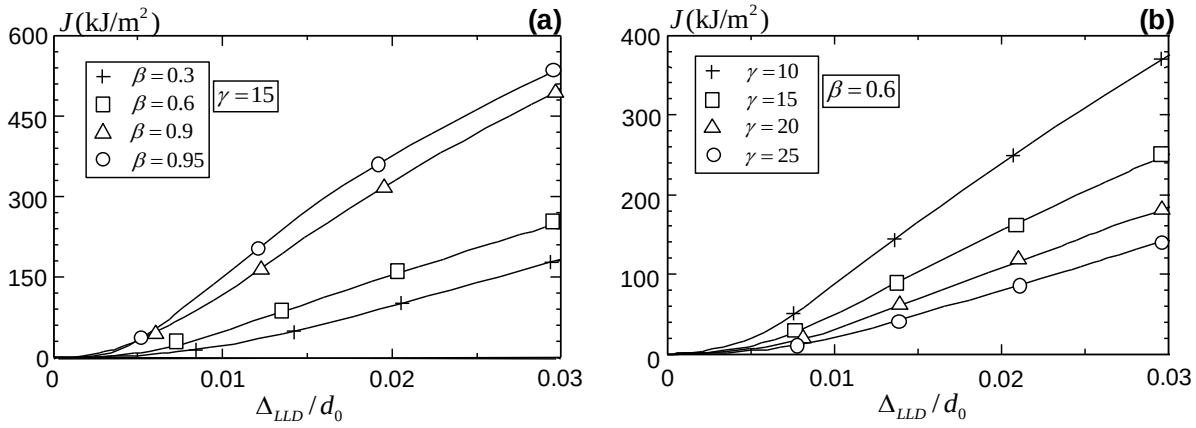

Fig. 5.8: Elastic-plastic J-values for X-joints with (a) $\gamma = 15$ and (b) $\beta = 0.6$.

Figure 5.8a plots the variation of the J-Δ_{LLD} relationship for X-joints with $\gamma = 15$ corresponding to different β ratios. The welds at the brace-to-chord intersection experience primarily axial tension under remotely applied displacement at brace ends. For joints with high β ratios, the chord wall between the two braces mainly sustains membrane action, coupled with the small amount of bending stresses induced by the eccentricity between the brace wall and the chord wall. As β decreases, the large bending stress becomes predominate in the chord wall near the saddle point. The change of the load path leads to the clear distinction in the J-Δ_{LLD} relationship between the high β ratio joints and joints with β ratios lower than 0.6. The large variation of the local dihedral angle along the brace-to-chord intersection induced by large β ratios localizes the

membrane action and bending action at the chord material between two saddle points, there produces a higher crack driving force in spite of a longer weld length. Therefore, the variation of the J-Δ_{LLD} relationship for X-joints with different β ratios shows an opposite trend against that for K-joints (Fig. 5.6a). On the other hand, a larger β ratio provides a large brace axial loading by mobilizing more chord material at the brace to chord intersection area. As the β increases, the plastic bending in the chord wall near the symmetry plane ($y = 0$) dissipates part of the applied brace displacement, therefore indicates a slowing rate of increase of the J-value at large deformations, as indicated in Fig. 5.8a.

The change in γ ratios varies the membrane and bending capacities of the chord wall. For joints with the same chord outer diameter d_0 and β ratio, the decrease of the γ ratio introduces a larger magnitude of the brace loading under the same remotely applied displacement at the brace end. The reduction of the chord wall compliance does not contribute as much as that for K-joints due to the additional membrane action of the chord material between two braces. Therefore, the change of the γ ratio produces a clear distinction in the J-Δ_{LLD} relationship for X-joint under the brace axial loading. The increase of the brace loading becomes predominant and leads to a higher value of the J-integral for X-joints with higher γ ratios, as shown in Fig. 5.8b.

5.5 Application of the η Approach to Cracked Joints

This section firstly derives the plastic η approach for CHS joints with a surface crack located at the hot-spot location. The following discussion proposes a series of B_{eff} based on FE results obtained in the previous section. The proposed η approach shows a close agreement with J-values computed from the domain-integral approach.

5.5.1 Plastic η Approach for Cracked Joints

The derivation of the plastic η approach for cracked joints follows the similar procedure as mentioned in Section 5.2. The elastic-plastic crack driving force J-integral, which represents the energy release rate in the joint with a surface crack, follows,

$$J = -\frac{1}{B}\int_0^{\Delta}\left(\frac{\partial P}{\partial a}\right)_{\Delta} d\Delta = -\int_0^{\Delta}\frac{\partial P}{B\partial a}d\Delta = -\int_0^{\Delta}\frac{\partial P}{\partial A_{crack}}d\Delta \tag{5.16}$$

where A_{crack} denotes the surface crack area. The present study assumes that the change of the axial brace loading follows,

$$P = \frac{\sigma_y t_0^2}{\sin\theta} m A_{lig}^{\eta_{pl}} F\left(\frac{\Delta_{LLD}}{d_0}, \beta, \gamma, \alpha, n, \frac{\sigma_y}{E}\right) \tag{5.17}$$

where m and η_{pl} are two non-dimensional constants, F denotes a dimensionless function, describing the change of the external axial loading with respect to the axial brace displacement, geometric parameters and material properties. The dimensionless function F assumes independence of the crack area or the remaining ligament area, consistent with the previous efforts to quantify the cracked joint strength through an area reduction factor (Stacey *et al.*, 1996; Burdekin *et al.*, 1998). The parameter A_{lig} refers to the remaining un-cracked area, which satisfies $\partial A_{crack} = -\partial A_{lig}$. Thus,

$$-\frac{\partial P}{\partial A_{crack}} = -\frac{\partial P}{\partial A_{lig}} = \frac{\sigma_y t_0^2}{\sin\theta} m\eta_{pl} A_{lig}^{\eta_{pl}-1} F\left(\frac{\Delta_{LLD}}{d_0}, \beta, \gamma, \alpha, n, \frac{\sigma_y}{E}\right) = \frac{\eta_{pl} P}{A_{lig}} \tag{5.18}$$

$$J = -\frac{\partial U}{\partial A_{crack}} = \frac{\eta_{pl}}{A_{lig}}\int_0^{\Delta} P d\Delta \tag{5.19}$$

A more general form follows Eq. 5.12,

$$J = J_{el} + J_{pl} = \frac{K_I^2}{E'} + \frac{\eta_{pl} U_{pl}}{A_{lig}} \tag{5.20}$$

Under a large axial displacement, the large plastic deformation occurs around the brace-to-chord intersection area. Figure 5.9 plots the variation of the elastic component of the J-integral with respect to the non-dimensional load-line displacement. The elastic component J_{el} contributes to less than 5% of the total J-value at large deformations ($\Delta_{LLD}/d_0 > 0.015$). The current study thus neglects the elastic portion of the J-integral due to its small contribution.

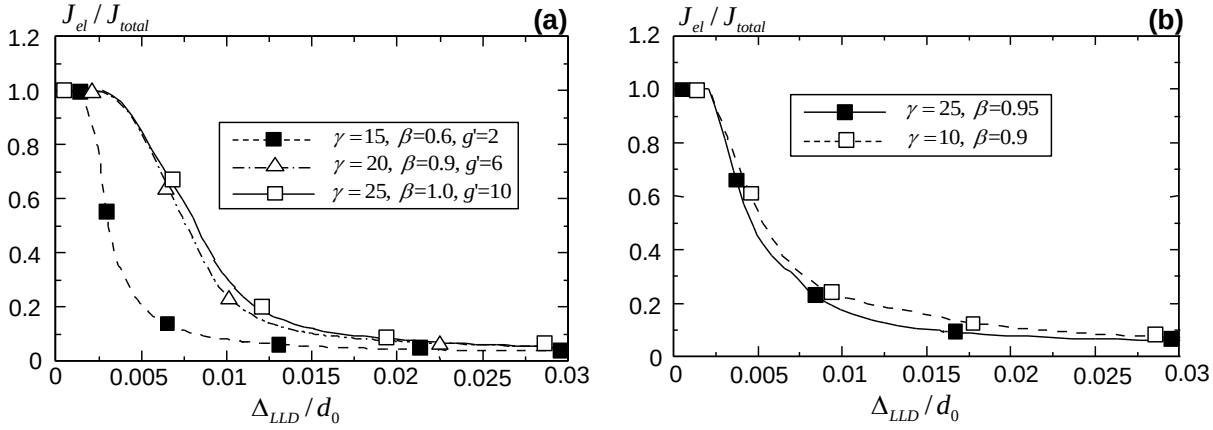

Fig. 5.9: Variation of the elastic component of the J-value over the total J for different geometries: (a) K-joints and (b) X-joints.

This study assumes a proportional relationship between the axial load resistance and the ligament area, as observed in previous experimental (Burdekin *et al.*, 1998; Talei-Faz *et al.*, 2004) and numerical investigations (Wang *et al.*, 2011) on tubular joints with a surface crack. These investigations prove that the ratio of the cracked joint strength over the intact joint strength varies linear with the crack area for CHS joints with surface cracks, or,

$$P_{crack} = P_{intact}\left(1 - \frac{A_{crack}}{L_w t_0}\right) \tag{5.21}$$

This assumption leads to a unity value for η_{pl} in Eq. 5.17. Equation 5.20 thus becomes,

$$J = \frac{U_{pl}}{A_{lig}} \tag{5.22}$$

In Eq. 5.22,

$$J = J_{ave} = \left(\sum_{i=1}^{n} J_i \Delta B_i \right) \Big/ \sum_{i=1}^{n} \Delta B_i \tag{5.23}$$

where J_{ave} refers to the average J-value along the crack front, J_i and ΔB_i denote the J-integral at a local crack-front point and the length of a segment enclosing this crack-front point, respectively. The current study assumes a constant J_i along the crack front. In Eq. 5.23,

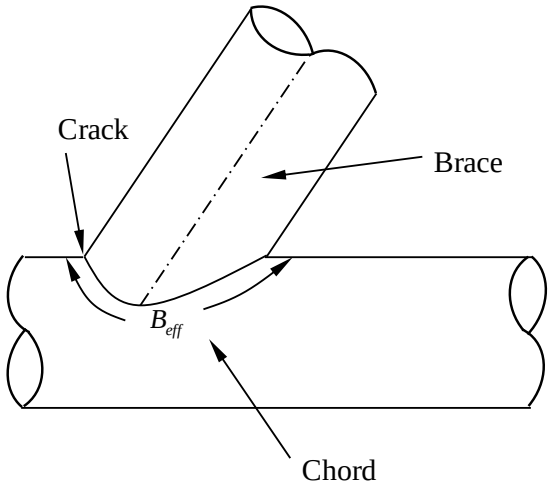

Fig. 5.10: Schematic view of the effective width B_{eff} for a K-joint with a crack located at the crown point near the tension brace.

$$A_{lig} = (2c + B_{eff})t_0 - \frac{\pi ac}{2} \tag{5.24}$$

where c is the half length of the semi-elliptical crack, the second term $\pi ac/2$ calculates the area of a semi-elliptical crack. B_{eff} denotes the effective width along the brace-to-chord intersection area, as illustrated in Fig. 5.10 for a K-joint with a crack located at the crown point near the tension brace.

5.5.2 *J*-Estimation Using the Plastic η Approach for Cracked K-Joints

The current study determines the value of B_{eff} for CHS K-joints with semi-elliptical surface cracks located at the crown point near the tension brace based on the results obtained from 36 elastic-plastic, large-deformation analyses in Section 5.3, covering a β ratio from 0.3 to 1.0, a γ ratio from 15 to 25, and a gap ratio from 2 to 10. The study calculates A_{lig} in Eq. 5.22 for each joint through a regression analysis based on the linear portion of the J versus the applied displacement curve (see Fig. 5.6), followed by Eq. 5.24 to determine the value of B_{eff}.

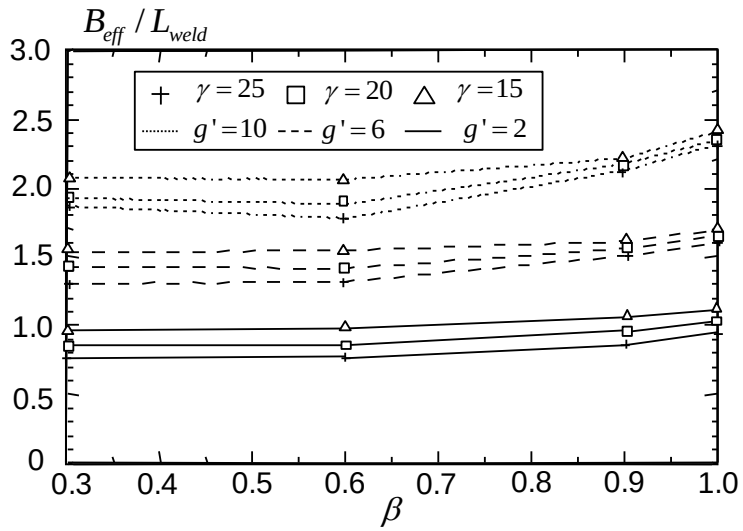

Fig. 5.11: Variation of the non-dimensional effective width B_{eff} for cracked K-joints with different geometries.

Figure 5.11 plots the variation of the non-dimensional effective width, B_{eff}/L_{weld}, corresponding to different CHS K-joints. The calculation of the weld length (Qian, 2013), L_{weld}, follows,

$$L_{weld} = 2\beta d_0 \int_0^{\pi/2} \left(\frac{\sin^2 \omega}{\sin^2 \theta} + \frac{\cos^2 \omega}{1 - \beta^2 \sin^2 \omega} \right)^{0.5} d\omega \tag{5.25}$$

where ω is an angle defining the position on the brace-to-chord intersection length mea-

sured in a plane perpendicular to the longitudinal axis of the brace. Similar to the variation of the elastic-plastic driving force, the effective width B_{eff} shows a small variation with respect to the γ ratio. As mentioned previously, for a smaller γ ratio, the increase in the J-value due to a larger remote loading counterbalances the decrease in the J-value due to the lower chord wall compliance. For higher β ratios, the effective width B_{eff} shows an increasing value due to the larger brace-to-chord intersection length. With a larger transition area between the two crown points, the increasing gap ratio leads to a higher effective width B_{eff}.

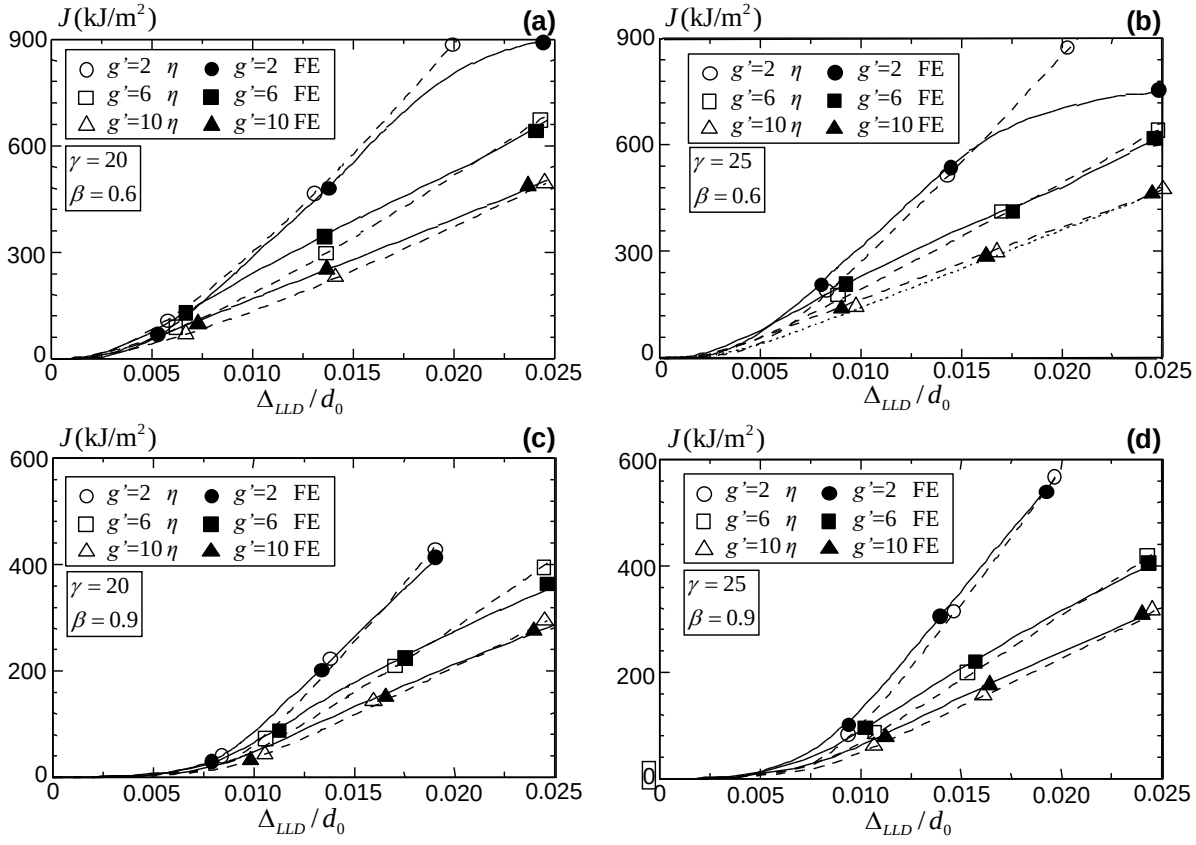

Fig. 5.12: Comparison of the elastic-plastic J-values estimated using the proposed η approach and the FE analyses for K-joints with: (a) $\gamma = 20$, $\beta = 0.6$; (b) $\gamma = 25$, $\beta = 0.6$; (c) $\gamma = 20$, $\beta = 0.9$; and (d) $\gamma = 25$, $\beta = 0.9$.

Figures 5.12, 5.13 and 5.14 compare the crack driving force predicted by the proposed

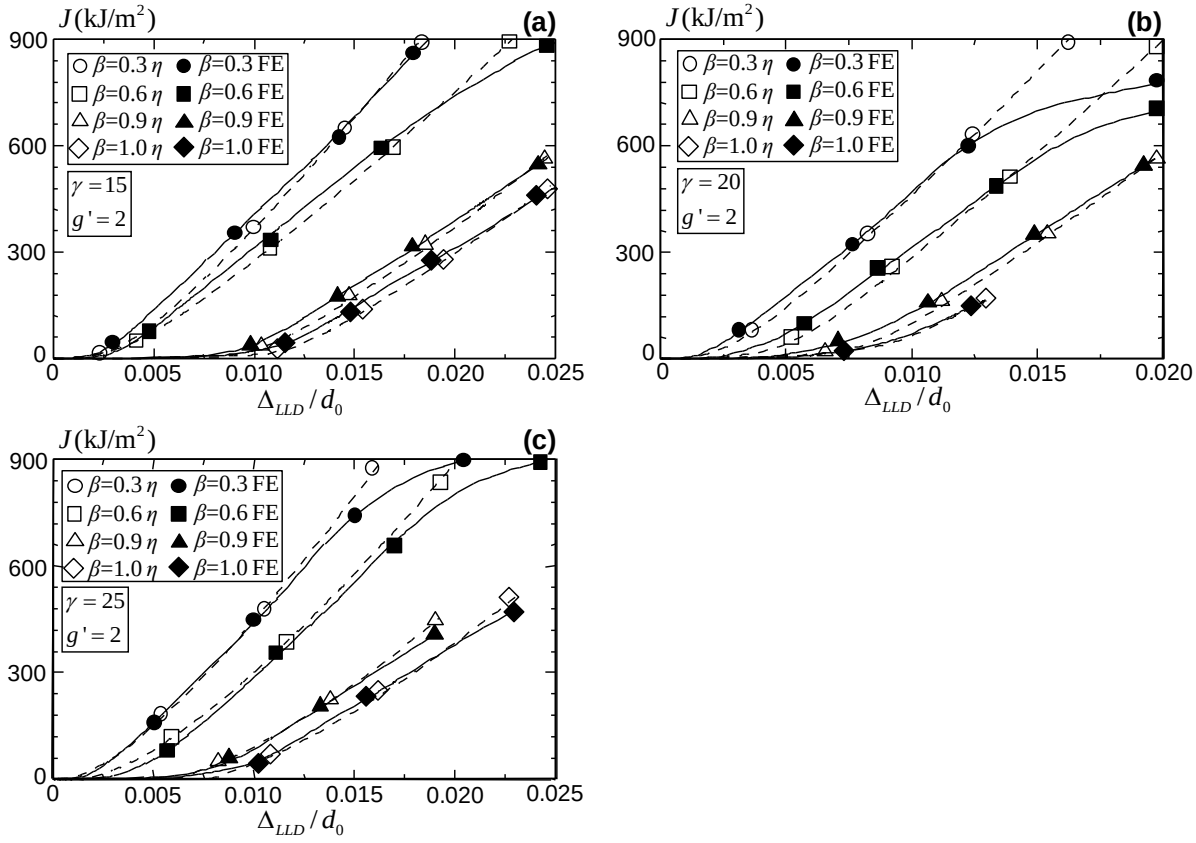

Fig. 5.13: Comparison of the elastic-plastic J-values estimated using the proposed η approach and the FE analyses for K-joints with: (a) $\gamma = 15$, $g' = 2$; (b) $\gamma = 20$, $g' = 2$; and (c) $\gamma = 25$, $g' = 2$.

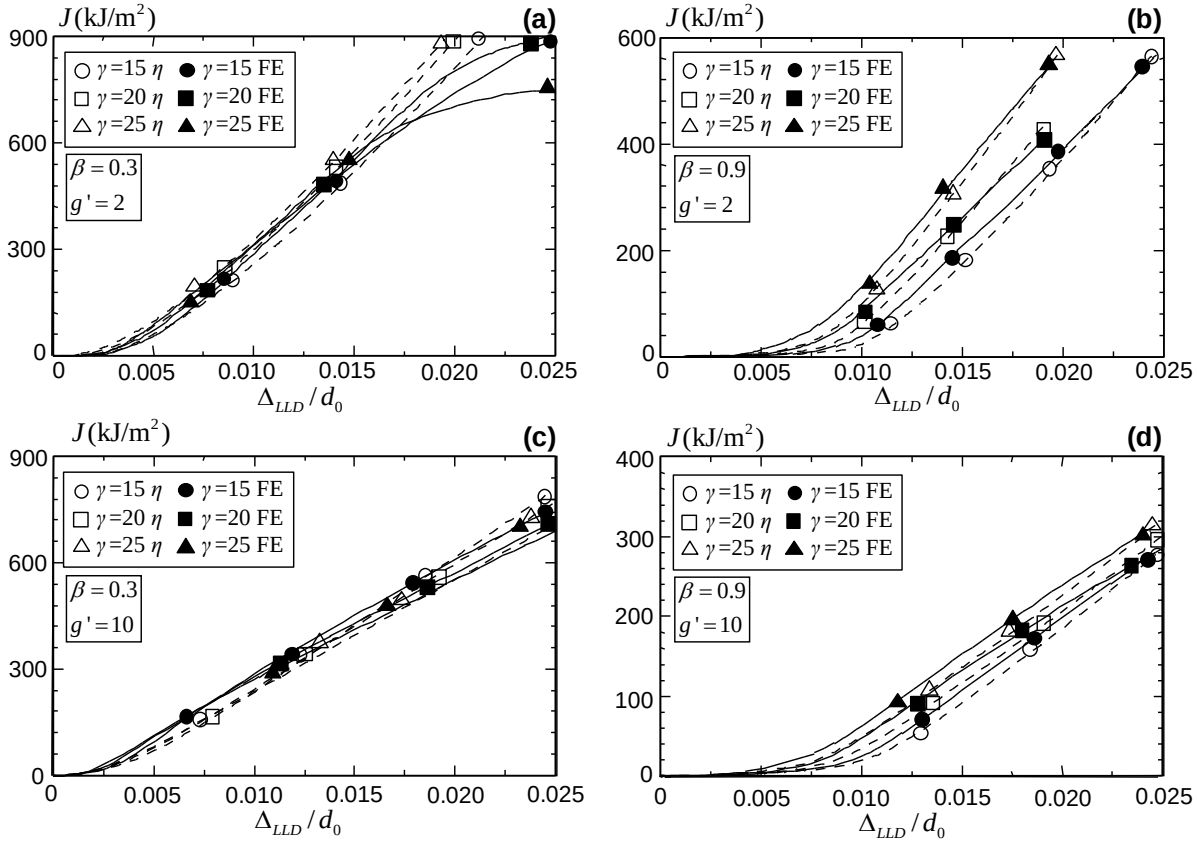

Fig. 5.14: Comparison of the elastic-plastic J-values estimated using the proposed η approach and the FE analyses for K-joints with: (a) $\beta = 0.3$, $g' = 2$; (b) $\beta = 0.9$, $g' = 2$; (c) $\beta = 0.3$, $g' = 10$; and (d) $\beta = 0.9$, $g' = 10$.

η approach against the J-values computed from the domain-integral approach presented in the previous section. The proposed B_{eff} predicts closely the increase in the J-integral as the remote loading increases for high β ratios. For small β ratios at large deformations, the plastic deformation in the welds and the brace absorbs effectively the imposed remote displacement, which leads to a larger effective width. The proposed η approach does not capture this shielding effect and exhibits a conservative, over-prediction for K-joints with a small β ratio.

5.5.3 *J*-Estimation Using the Plastic η Approach for Cracked X-Joints

Figure 5.15 plots the variation of the non-dimensional effective width B_{eff}, corresponding to different X-joint geometries. Following the procedure to determine the effective width B_{eff} as described in Section 5.5.2, the 16 elastic-plastic, large-deformation X-joint models employ a β ratio from 0.3 to 0.95, a γ ratio from 10 to 25. The derivation of the non-dimensional effective width B_{eff} diminishes the effect of the remote brace loading on the crack driving force while closely reflects the change of the J-value with respect the surrounding material. Different from the variation of the elastic-plastic driving force corresponding to the γ ratio (as shown in Fig. 5.8b), the effective width B_{eff} shows small variation with respect to the γ ratio. The difference demonstrates the strong correlation of the J-value increase for high γ ratio joints with respect to the larger remote brace loading. The concentration of the load transition area at the chord area between the two saddle points due to the localization induced by the large variation of the dihedral area generates a small magnitude of non-dimensional effective width B_{eff} for X-joints with higher β ratios. Therefore, the non-dimensional effective with B_{eff} shows a decreasing trend corresponding to a larger β ratio.

Figures 5.16 and 5.17 plots the crack driving force predicted by the proposed η ap-

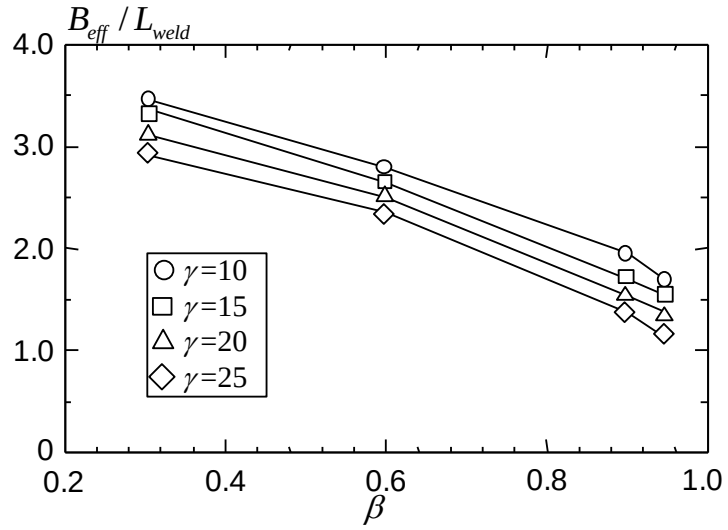

Fig. 5.15: Variation of the non-dimensional effective width B_{eff} for cracked X-joints with different geometries.

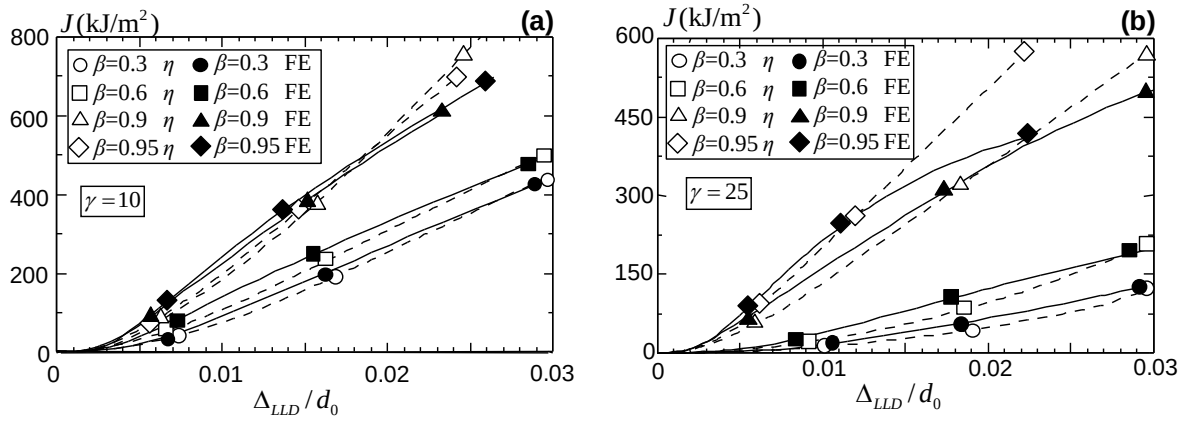

Fig. 5.16: Comparison of the elastic-plastic J-values estimated using the proposed η approach and the FE analyses for X-joints with: (a) $\gamma = 10$ and (b) $\gamma = 25$.

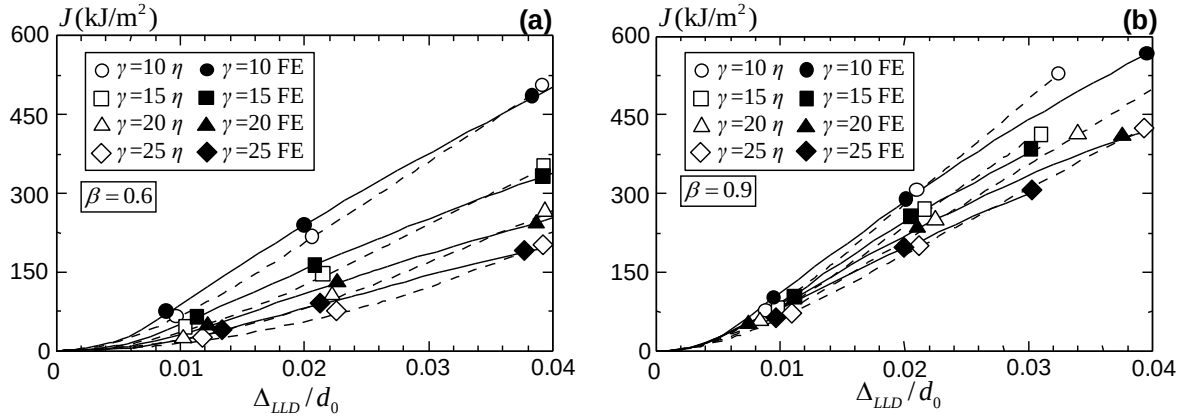

Fig. 5.17: Comparison of the elastic-plastic J-values estimated using the proposed η approach and the FE analyses for X-joints with: (a) $\beta = 0.6$ and (b) $\beta = 0.9$.

proach against the J-values computed from the domain-integral approach presented in the previous section for cracked X-joints. The proposed B_{eff} predicts closely the increase in the J-integral as the remote loading increases for lower β ratios. For larger β ratios at large deformations, the plastic deformation in the brace and welds absorbs effectively the imposed remote displacement, which leads to a change of the increasing rate in the crack driving force. The proposed η approach does not capture this shielding effect and exhibits a conservative, over-prediction for X-joints with larger β ratios.

5.5.4 Sensitivity Study of the Material Yield Strength and the Strain Hardening Component

A further investigation studies the effect of the material properties, *e.g.*, the material yield strength, σ_y, and the strain-hardening exponent, n, on the proposed effective width B_{eff}. Figure 5.18 plots the variation of the elastic-plastic crack driving force corresponding to different material properties with two strain-hardening exponents $n = 5$ and $n = 10$, and three different yield strengths of 275 MPa, 355 MPa and 460 MPa. A lower strain-hardening ratio constrains the plastic deformation within the materials near the crack

front, which leads to a continuously increasing J-integral as the remote load increases. A higher material yielding strength leads to a higher J-integral at a large deformation. The dimensionless function F in Eq. 5.18 considers these material effects and includes them in the plastic work U_{pl}. Without changing the effective width, the proposed η approach predicts closely the increase in the J-values before the shielding effect on the crack-front material, caused by the large plastic deformation in materials away from the crack, occurs.

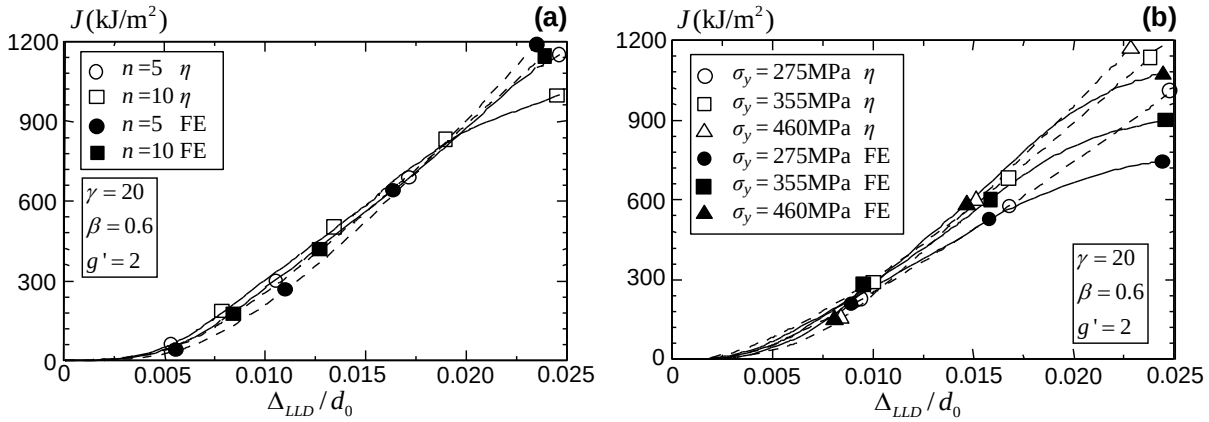

Fig. 5.18: Comparison of the elastic-plastic J-value between the proposed η approach and the FE results for K-joints with $\gamma = 20$, $\beta = 0.6$ and $g' = 2$ corresponding to: (a) different material strain hardening exponents $n = 5$ and $n = 10$; and (b) material yielding strength $\sigma_y = 275$MPa, $\sigma_y = 355$MPa, and $\sigma_y = 460$MPa.

5.6 Summary and Conclusion

This chapter investigates the elastic-plastic crack driving force for CHS K- and X-joints with a semi-elliptical surface crack located at the crown point near the tension brace through a mesh-tie procedure. Following a dimensionless analysis, the current study extends the conventional plastic η approach for simple 2-D fracture specimens with through thickness cracks to large-scale 3-D tubular joints with surface cracks. The close agreement

in the J-values estimated using the η approach and those computed from the domain-integral method proves the validity of the plastic η approach with the proposed effective width. The study summarized above supports the following conclusions:

1. For CHS K-joints, the elastic-plastic crack driving force increases with reduced β ratios due to the decreasing weld length and the higher bending effect in the chord wall material. The J-value shows a small variation with respect to γ ratios due to the balance between the chord wall compliance and the remote loading. For joints with small gap ratios, the limited chord material between crown points constrains the plastic deformation within a localized region near the crack surface and leads to a higher crack driving force. For K-joints with lower β ratios and small gap ratios, the plastic deformation in the welds absorbs the imposed remote displacement near the crack surface at large deformation levels. Thus, the crack driving force increases initially and then approaches a plateau as the remote load increases.

2. For CHS X-joints, the elastic-plastic crack driving force increases with respect to the increased β ratios due to the concentration of the load transition area at the saddle point of the chord material between two tensile braces. Smaller γ ratios with a larger wall thickness generate the larger J-value through an increased remote brace loading under the same applied displacement.

3. The current study shows that the η_{pl} value equals 1 based on the linear dependence of the cracked joint strength on the remaining intact area established by previous experimental and numerical investigations for surface cracked tubular joints. The plastic η approach with the proposed effective width B_{eff}, shows a close prediction of the elastic-plastic crack driving force compared with the domain-integral J-values. The plastic η approach provides a convenient alternative to estimate the J-values for cracked tubular K and X-joints using solely the load versus the load-line

displacement curve.

4. Previous research employs the plastic limit work approach to define the thick-walled joint strength where the joint shows an increasing resistance until the material ductility limit (Choo *et al.*, 2003). The strong correlation between the elastic-plastic crack driving force and the joint plastic work under the load versus load-line displacement curve provides a theoretical base for the plastic limit approach and proves the plastic work as a possible criterion for establishing a deformation limit.

5. The plastic η approach does not reflect the shielding effect on the crack-front material caused by the plastic deformation in the brace and weld materials away from the crack location under large deformations. The shielding effect causes a gradual reduction in the increasing rate of the J-value with respect to the applied displacements. The η approach thus conservatively over-predicts the elastic-plastic crack driving force at large load levels.

Chapter 6

A Phenomenological Fracture Formulation Coupled with *J-R* Curve for Tubular Joints

6.1 Introduction

Circular hollow sections (CHSs) have become the primary structural component for steel platforms in offshore applications. The reassessment of aging steel offshore platforms beyond their design life requires advanced nonlinear frame analyses which should include an accurate description of the local joint response under overloading conditions. Crack initiation and extension, followed by unstable fracture failure, around the brace-to-chord intersection often emerge as the predominant failure mechanism for tubular joints subjected to monotonically increasing tension (Makino *et al.*, 1995). The representation of such failure for tubular joints influences the ultimate and the post-ultimate frame behavior significantly (Qian, 2005).

Conventional wisdoms (Van der Vegte *et al.*, 2002; Dexter and Lee, 1999) in addressing

the ductile fracture failure in tubular joints often utilize an empirical tensile plastic strain of 20%, inferred from the typical elongation values in standard uniaxial tension tests for steels, as the failure criterion to represent the onset of ductile tearing in materials near the weld toe of the tension brace. Beyond this strain limit, the load-deformation behavior obtained from the finite element (FE) analysis, where no crack or damage model is involved, becomes potentially un-conservative. However, the significant mesh dependence and the low elongation strains for high strength steels often complicate the extraction of the 20% tensile plastic strain from the finite element model and limit the application of this failure criterion (Skallerud and Amdahl, 2002). Besides the tensile plastic strain, the accumulated plastic strain and the stress triaxiality can impose strong effects on the macrocrack initiation. The widely used integrity assessment standard BS7910 (2005) provides a series of failure assessment diagrams (FAD) to assess the acceptability of a flaw in metallic structures. However, these FADs do not lead directly to a load-deformation relationship for tubular joints with an extending crack.

Macroscopic joint models often describe the joint fracture failure by limiting the joint deformation in the load-displacement relationship. The American Petroleum Institute (API) recommends a deformation limit equal to 5% of the chord diameter for the brace axial deformation to define the crack initiation (USFOS, 2009). The joint capacity decreases linearly to zero when the brace axial deformation increases to 10% of the chord diameter. The MSL joint formulation (Dier and Hellan, 2002), developed through a joint industry-university project, incorporates the joint fracture behavior by limiting the deformation to a fraction of the chord diameter based on the mean value of a series of experimental results. Beyond this limit, the joint capacity decreases to a small magnitude to represent the unstable fracture failure. A piece-wise linear joint model, developed by Choo *et al.* (2005), employs a deformation limit of 10% of the chord diameter for the crack initiation and 30% of the joint ultimate capacity as the residual resistance for the

cracked joint. However, all these joint fracture formulations remain empirical in nature and lack strong theoretical foundations, which limit their transferability to a wide range of joint geometry, material and loading conditions foreseeable in real offshore platforms.

The present work proposes a new fracture formulation to describe the nonlinear joint load-deformation characteristics caused by the plastic deformation, ductile tearing and consequently the unstable fracture failure in tubular joints under monotonically increasing brace tension. This formulation integrates, for the first time, the material fracture resistance curve (the J-R curve), into the load-displacement formulation of a tubular joint. The proposed joint formulation determines the deformation level at the initiation of ductile tearing as the crack driving force in an assumed, initial shallow crack reaches the material fracture toughness. The derivation of the load-displacement relationship during the ductile tearing process integrates an experimentally measured J-R curve with the crack driving force computed from a detailed elastic-plastic, large deformation 3D finite element analyses, and an area reduction factor for the cracked joints. The comparison of the above procedure against the experimentally measured joint response validates the material fracture J-R curve as a basis to quantify the joint resistance against ductile crack extension.

This chapter reviews firstly the existing approaches to describe the fracture failure in tubular joints under large plastic deformations. The next section describes the joint fracture failure in both macroscopic and microscopic scales. The discussion then focuses on the effect of a pre-existing crack on the load-deformation behavior of tubular joints. The physical response of the tubular joint discussed herein leads to the proposed fracture formulation to describe the joint behavior inflicted with fracture failure. The fifth section validates the proposed joint fracture formulation based on a series of tubular joint tests. The last section summarizes the main conclusion drawn from the current study.

6.2 Ductile and Unstable Fracture in Tubular Joints

All engineering metals and alloys contain inclusions and second-phase particles (Gurson, 1985). Ductile materials often fail as a consequence of nucleation, growth and coalescence of the microscopic voids that initiate at these inclusions and second phase particles. Without a member failure, a tubular joint under axial tension often sustains monotonically increasing loads until the joint resistance is limited by the ductility or the plasticity in the chord material.

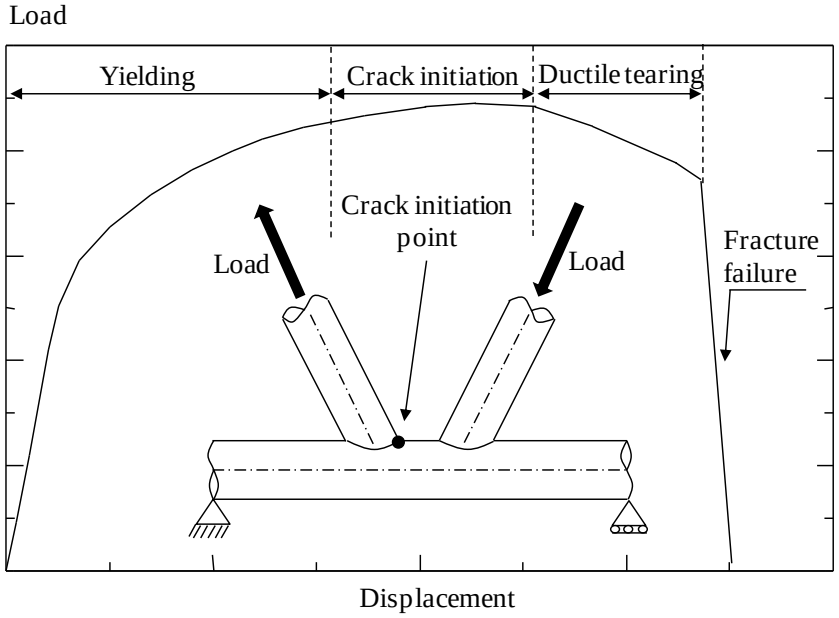

Fig. 6.1: Typical load-deformation behavior of a CHS K-joint under balanced brace axial loads.

Figure 6.1 shows a typical gapped tubular K-joint sustaining a monotonically increasing balanced axial loading with a pin-support at the chord left end and a roller-support at the chord right end. The experimental study (Bolt, 1995) often observes the overall joint load-deformation behavior in four phases:

1. Yielding firstly occurs around the hot spot location, *i.e.*, the crown point, at the chord side near the tension brace weld toe as shown in Fig. 6.1. The plasticity

spreads along the brace-to-chord intersection area with an increasing applied load. The growing plasticity forces the load-displacement curve to deviate from the initial elastic response in the elastic-plastic stage. At the microscopic scale, a free surface may form around an inclusion or second phase particle by either the interface decohesion or the particle cracking under large hydrostatic stresses (Anderson, 2004) as experienced by the chord material near the weld toe. However, no cracks visible to naked eyes exist at this stage.

2. With increasing plastic strains and hydrostatic stresses, the void formed inside the chord material grows around the particle. The growing void combines with adjacent voids to form a macroscopic flaw gradually. The eye-visible crack initiates at the crown point of the tension brace weld toe. However, the small crack area at this stage does not form a critical failure in the joint load path. The low crack tip constraint dissipates the applied energy through plastic deformations in the nearby materials around the very shallow crack tip. The joint does not indicate noticeable deterioration in its load resistance.

3. As the crack extends along the brace-to-chord intersection, the increasing crack size grows to a significant portion of the brace-to-chord intersection area. A sufficiently large crack begins then to reduce the joint capacity by evolving into a deep crack during the ductile tearing.

4. With the growing plastic deformation, the joint has fully utilized the energy dissipating mechanism available in the material. The continued increase in the remote brace displacement requires the energy to be dissipated through the crack extension. In addition, the crack size has become large enough such that the near-tip stress grows sufficiently large to overcome the cohesive strength of the material. The change in the applied energy per unit crack extension has become much larger than

the variation of the available energy release rate per unit crack extension locked in the material. The cracked section is thus no longer able to sustain the applied load, causing unstable crack extensions with a sudden loss of the joint resistance.

6.3 Presence of Surface Cracks on Joint Response

The crack initiation and growth violate the continuity and integrity of the material and geometry, based on which the conventional finite element method is formulated. Fracture mechanics provides a convenient approach to analyze the energy and load levels required to initiate and grow an existing crack in a structure detail. The unique relationship between the near-tip energy driving the crack extension and the load level sustained by the structural detail bridges the ductile tearing process with the remotely applied loading. Wang *et al.* (2011) demonstrate the marginal effect of a shallow surface near-toe crack on the global behavior of thick-walled X-joints under the axial tensile loading.

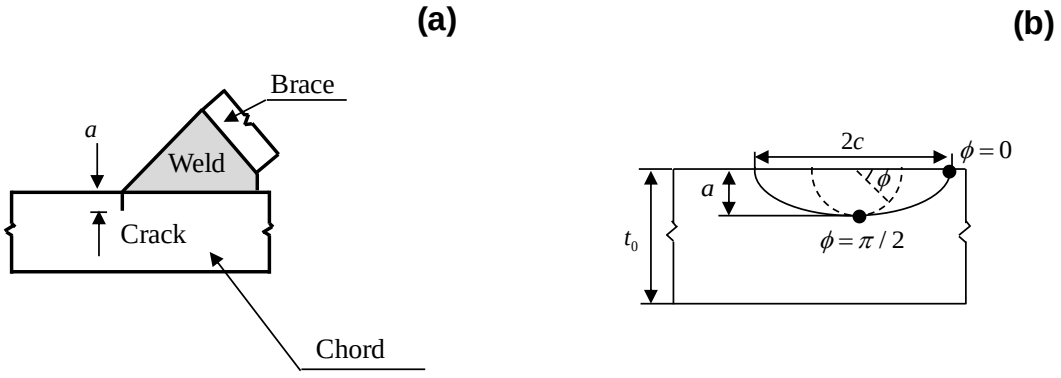

Fig. 6.2: Cracks located at the weld toe for CHS K-joints: (a) location and (b) profile.

The current study investigates the effect of a pre-existing surface crack to the load deformation behavior of K-joints subjected to the balanced axial loading. Surface cracks remain stationary under increasing remote loadings. The large-deformation, elastic-plastic finite element analysis includes 42 models with various joint geometries and crack sizes,

as listed in Table 6.1. Figure 6.2 shows the geometric configuration of a surface crack located at the crown point of the tension brace weld toe for a typical CHS K-joint. The chord outer diameter (β) for all FE models remains fixed at 406 mm, while the brace outer diameter (d_1) to the chord outer diameter ratio (d_0), ranges from 0.3 to 0.9, the chord outer radius to the chord wall thickness ratio (γ) varies from 15 to 25, and the gap between the two brace weld toes over the chord wall thickness ratio (g') changes from 2 to 10. The brace wall to the chord wall thickness ratio (τ) is kept at 1.0, indicating the same wall thickness for both braces and the chord. All the FE models include a surface crack located at the crown point of the tension brace weld toe, which sustains significant tensile and shear stresses under the balanced axial loading condition. The crack surface, as shown in Fig. 6.2, follows the curved weld line along the brace-to-chord intersection (Bowness and Lee, 1998), to represent a typical fatigue crack observed in tubular connections. The FE models assume four different crack-depth ratios, $a/t_0 = 0$ (intact joint), 0.2, 0.5, and 0.7, while the crack aspect ratio (a/c) remains fixed at 0.25 for all crack depth ratios. Table 6.1 lists the geometric information of FE models employed in the current study, where $A_{crack}\%$ refers to the crack area normalized by the brace-to-chord intersection area,

$$A_{crack}\% = \frac{A_{crack}}{A_w} = \frac{A_{crack}}{L_w t_0} \tag{6.1}$$

The mesh-tie procedure (Qian *et al.*, 2007) couples a local crack-front model built in FEA-Crack (2011) and the global continuous model generated in Patran (2012). The symmetry in both the geometry and loading conditions leads to a one-half symmetric FE model, as shown in Fig. 6.4. The boundary condition follows Fig. 6.1, with the end plates employed for the chord and braces to maintain a circular shape under large deformations. This boundary condition reflects the typical constraints experienced by a K-joint within a global frame (Choo *et al.*, 2006). The elastic-plastic material properties for members and welds follow the true stress-true strain relationships of S355 and S690

steels respectively, as shown in Fig. 6.3.

Table 6.1: K-joints with different surface crack sizes investigated in the FE study.

Joint	γ	β	g'	a/t_0	A_{crack}%
K1	15	0.3	6	0	0%(intact)
				0.2	1.0%
				0.5	4.0%
				0.7	9.4%
K2	20	0.6	2	0	0%(intact)
				0.2	0.25%
				0.5	1.5%
				0.7	3.5%
K3	25	0.9	10	0	0%(intact)
				0.2	0.10%
				0.5	0.91%
				0.7	1.8%

Figure 6.5 and 6.6 compares the non-dimensional load-deformation curves of K-joints with and without the weld-toe crack. In the gapped K-joints, the chord material within the gap between the two crown weld toes experiences significant bending stresses under large brace axial loads. The chord material near the crack surface experiences plastic deformation at a very low load level due to the significant stress concentration at the weld toe. As the deformation increases, the plastic flow redistributes stresses to materials along the brace-to-chord intersection, assuming a stationary, non-growing crack. Therefore, the presence of a shallow surface crack shows a marginal effect on the global joint stiffness. With increasing load, however, the large plastic deformation within the gap material combined with a sharp local dihedral angle at the crown point, develops a hinge-like mechanism to resist the applied brace load. The presence of a surface crack at the crown point deviates the load-displacement curve of the cracked joint from that of an intact joint. Nevertheless, an increase of the crack depth from $a/t_0 = 0.2$ to $a/t_0 = 0.7$ does not

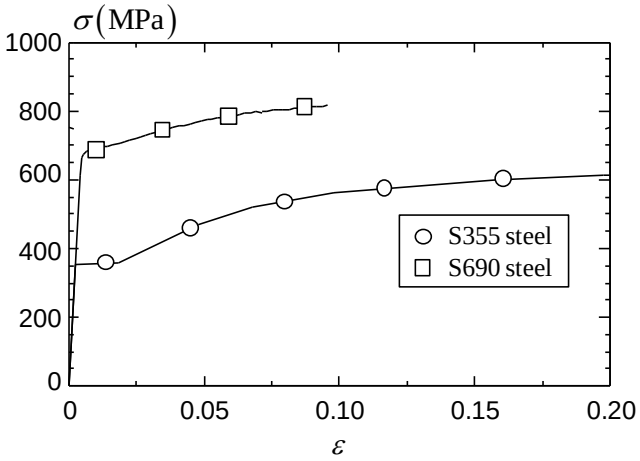

Fig. 6.3: Uniaxial true stress-true strain curve for S690 and S355 steels.

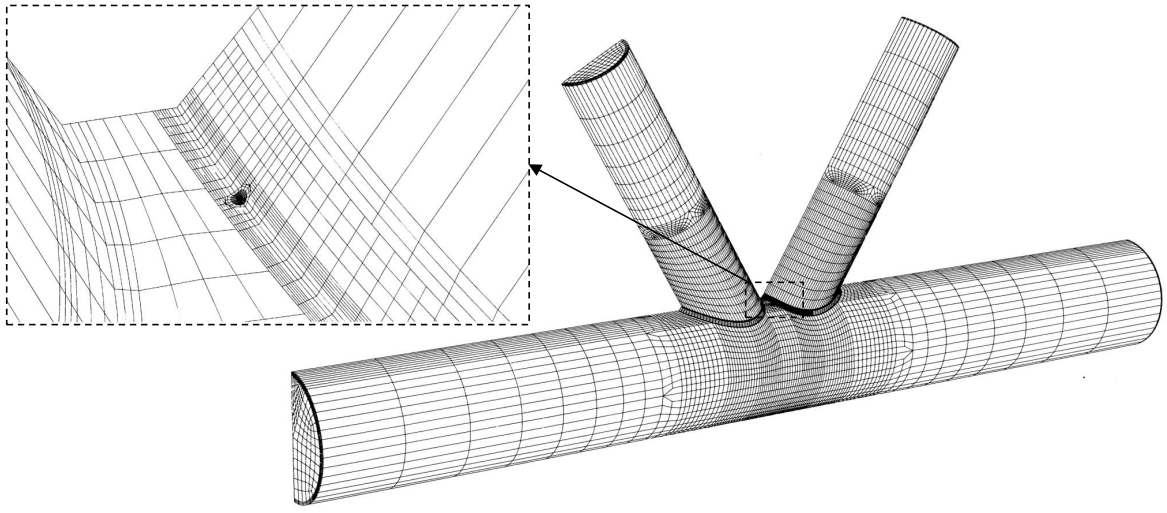

Fig. 6.4: Finite element mesh with mesh-tie for a CHS K-joint.

introduce significant reductions in the joint resistance, as revealed in Figs. 6.5 and 6.6.

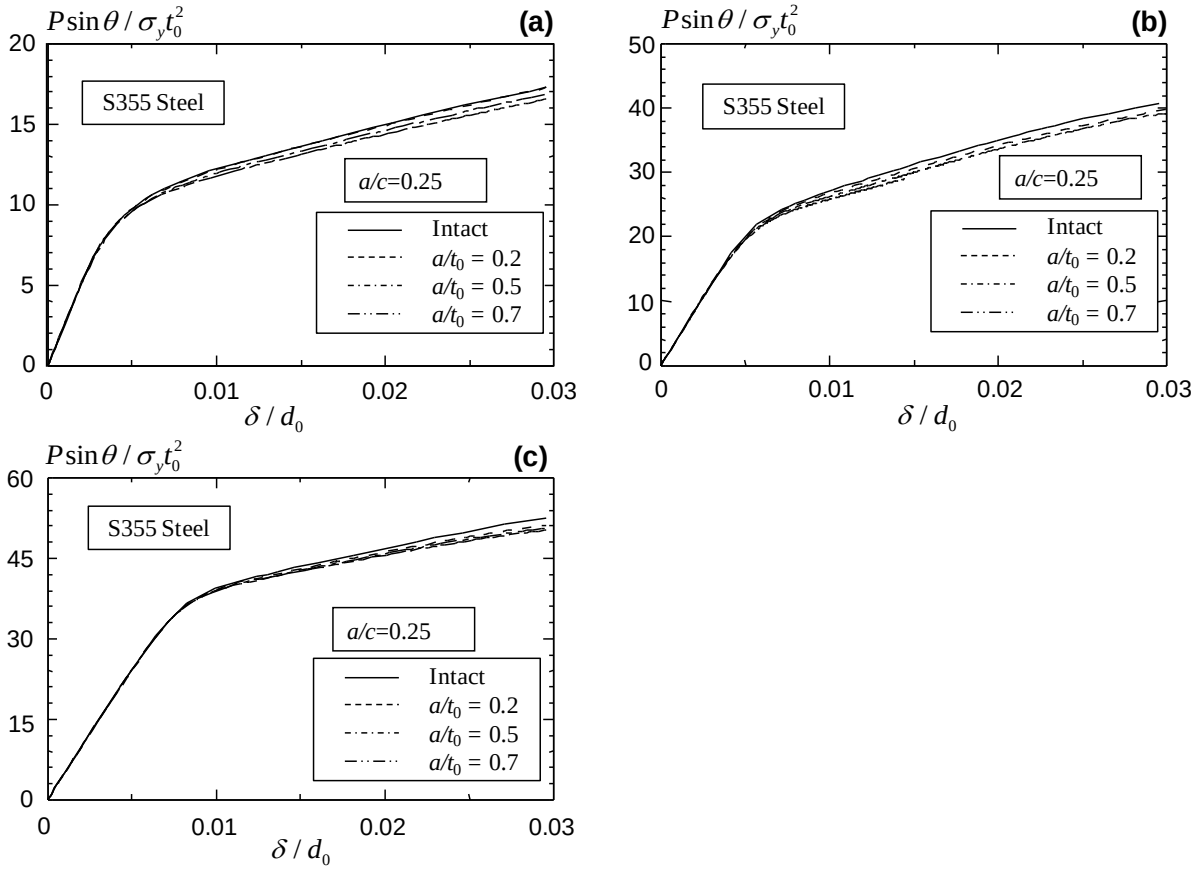

Fig. 6.5: Non-dimensional load-deformation curves of S355 K-tubular joints with and without the weld-toe crack: (a) $\gamma = 15$, $\beta = 0.3$, $g' = 6$; (b) $\gamma = 20$, $\beta = 0.6$, $g' = 2$; and (c) $\gamma = 25$, $\beta = 0.9$, $g' = 10$.

Figure 6.7 plots the non-dimensional crack driving force along the crack front corresponding to different deformations computed from the K-joint with $\gamma = 20$, $\beta = 0.6$, $g' = 2$. For all three crack depths, the crack tip at locations near the free surface ($\phi \to 0$), experiences a higher crack driving force at the small deformation due to the geometric constraint at the chord material surface. However, the normalized crack driving force at locations $\phi \to 0$ decreases as the remote load increases due to the loss of the surface constraint at the large deformation, which redistributes more crack tip energy towards the deepest point $2\phi/\pi = 1$ of the crack front.

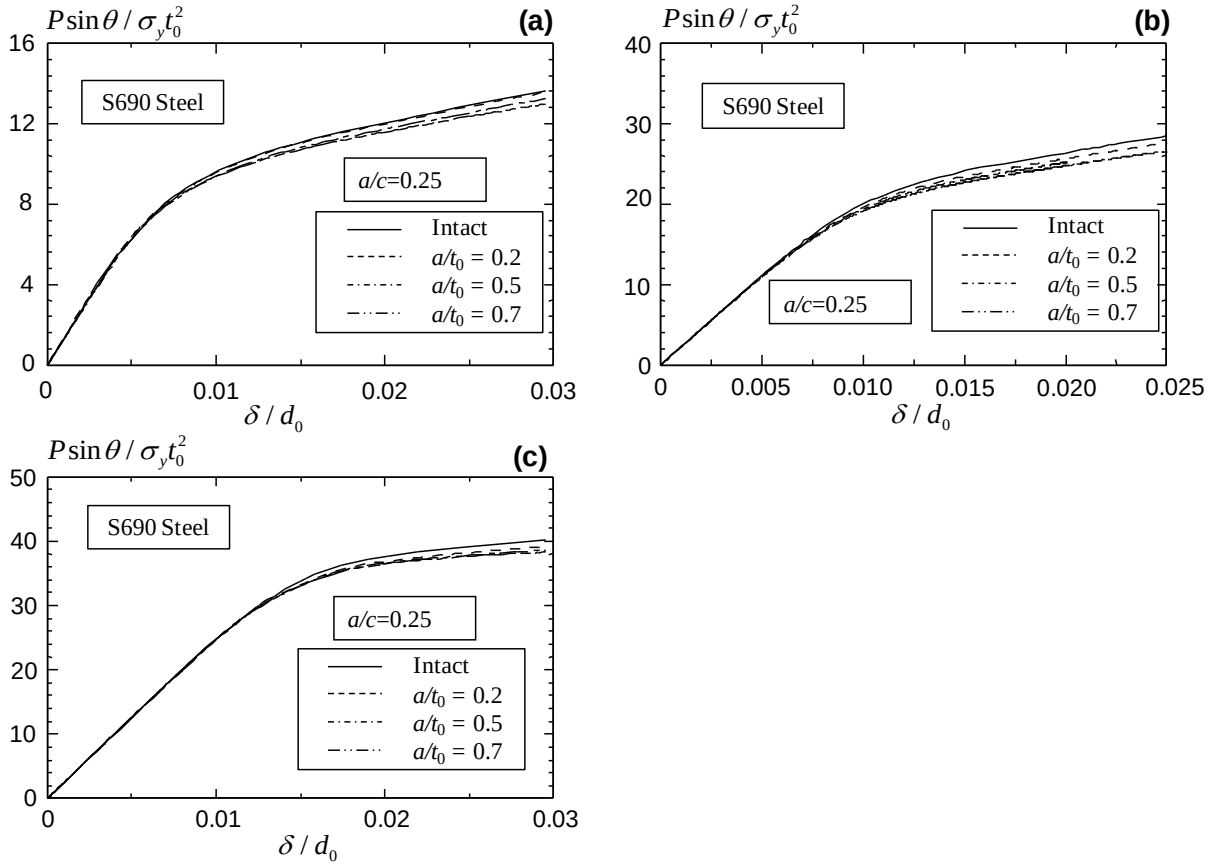

Fig. 5: Load deformation for S690

Fig. 6.6: Non-dimensional load-deformation curves of S690 K-tubular joints with and without the weld-toe crack: (a) $\gamma = 15$, $\beta = 0.3$, $g' = 6$; (b) $\gamma = 20$, $\beta = 0.6$, $g' = 2$; and (c) $\gamma = 25$, $\beta = 0.9$, $g' = 10$.

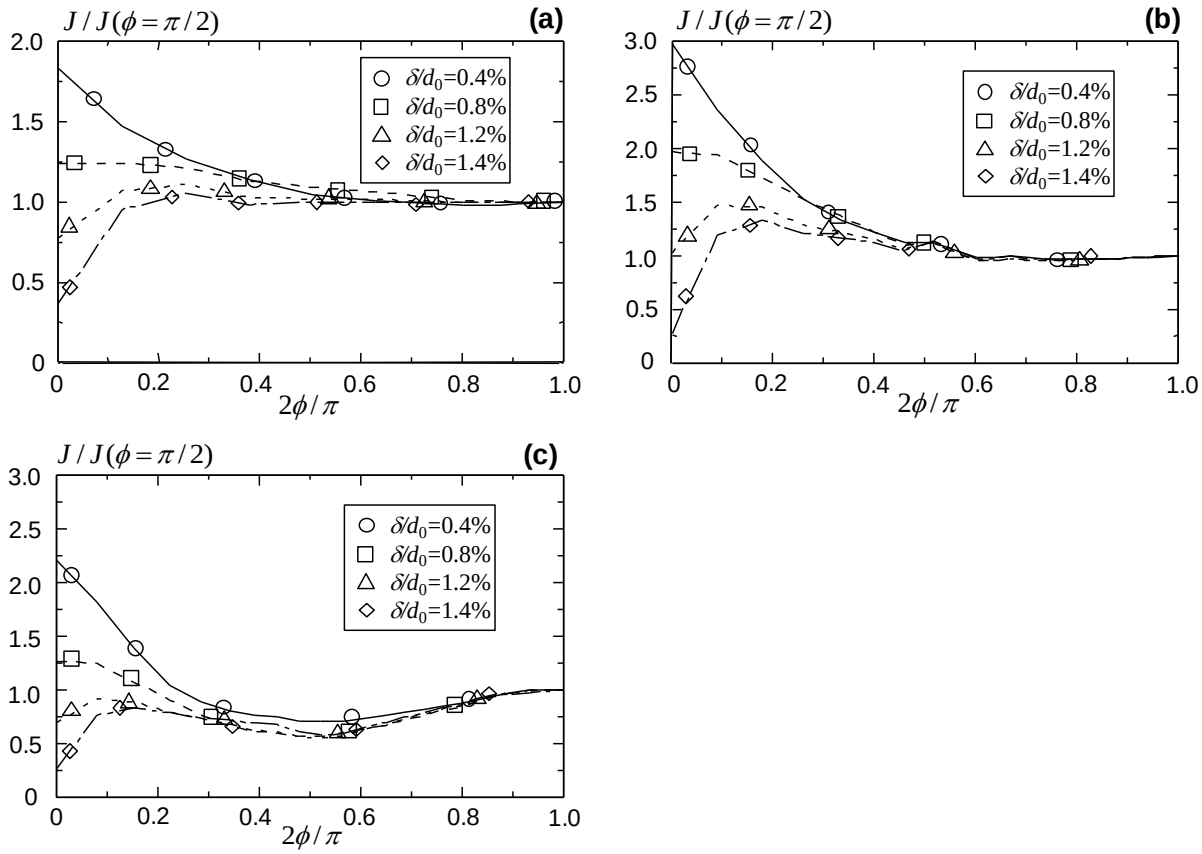

Fig. 6.7: Non-dimensional crack driving force along the crack front for the S355 K-joint $\gamma = 20$, $\beta = 0.6$, $g' = 2$ with different crack depths: (a) $a/t_0 = 0.2$; (b) $a/t_0 = 0.5$; and (c) $a/t_0 = 0.7$.

Table 6.2: K-joints with different surface crack aspect ratios but the same crack area.

Joint	a/t_0	a/c	A_{crack}%
K1	0.5	0.07	16%
	0.6	0.11	16%
	0.7	0.14	16%
K2	0.5	0.03	10%
	0.6	0.04	10%
	0.7	0.06	10%
K3	0.5	0.03	9%
	0.6	0.04	9%
	0.7	0.05	9%

A further study investigates the effect of the crack aspect ratio on the global joint behavior using different crack aspect ratios for the same crack area, as shown in Table 6.2. Figure 6.8 plots the normalized load-deformation behavior of CHS K-joints corresponding to different crack aspect ratios. The load-displacement of the K-joints exhibits insensitive dependence on the different crack aspect ratios. Figure 6.8 confirms that the load-displacement response of a K-joint under balanced brace axial loads depends on the crack area. For a K-joint with a continuously growing crack front, the crack driving force at the most critical location, coupled with an experimentally determined J-R curve, thus governs the amount of crack extension and consequently the area of the extended crack. The area of the extended crack enables the determination of the strength of the cracked K-joint using an established area reduction factor (Burdekin *et al.*, 1998) for tubular joints. The current study therefore entails two assumptions in the proposed fracture formulation: 1) the most critical location along the crack front lies at the deepest crack front point $2\phi/\pi = 1$ (Qian *et al.*, 2007); and 2) the crack aspect ratio remains constant as the crack extends.

Figure 6.9 compares the elastic-plastic crack driving force, at the deepest crack-front point $2\phi/\pi = 1$ against the non-dimensional displacement for the K-joints in Table 6.1 made of S355 steels. For K-joint with a small gap ratio ($g' = 2$) in Fig. 6.9a, the limited chord material between two crown points causes the concentration of the bending and shear actions near the crack surface. Thus, the crack driving force increases rapidly for the deep-crack joint ($a/t_0 = 0.7$). For the deep surface crack ($a/t_0 = 0.7$) in the K-joint with a lager gap ratio ($g' = 6$ and 10), the larger constraint (as indicated in Figs. 6.10a and 6.10b) from the surface at $\phi = 0$ attracts more plasticity and generates a lower initial crack driving force at $2\phi/\pi = 1$ under the small deformation due to the yielding in the nearby welds. However, under large deformations, the loss of the constraint at the location $\phi = 0$ induces a rapid growth in the crack driving force at the location $2\phi/\pi = 1$.

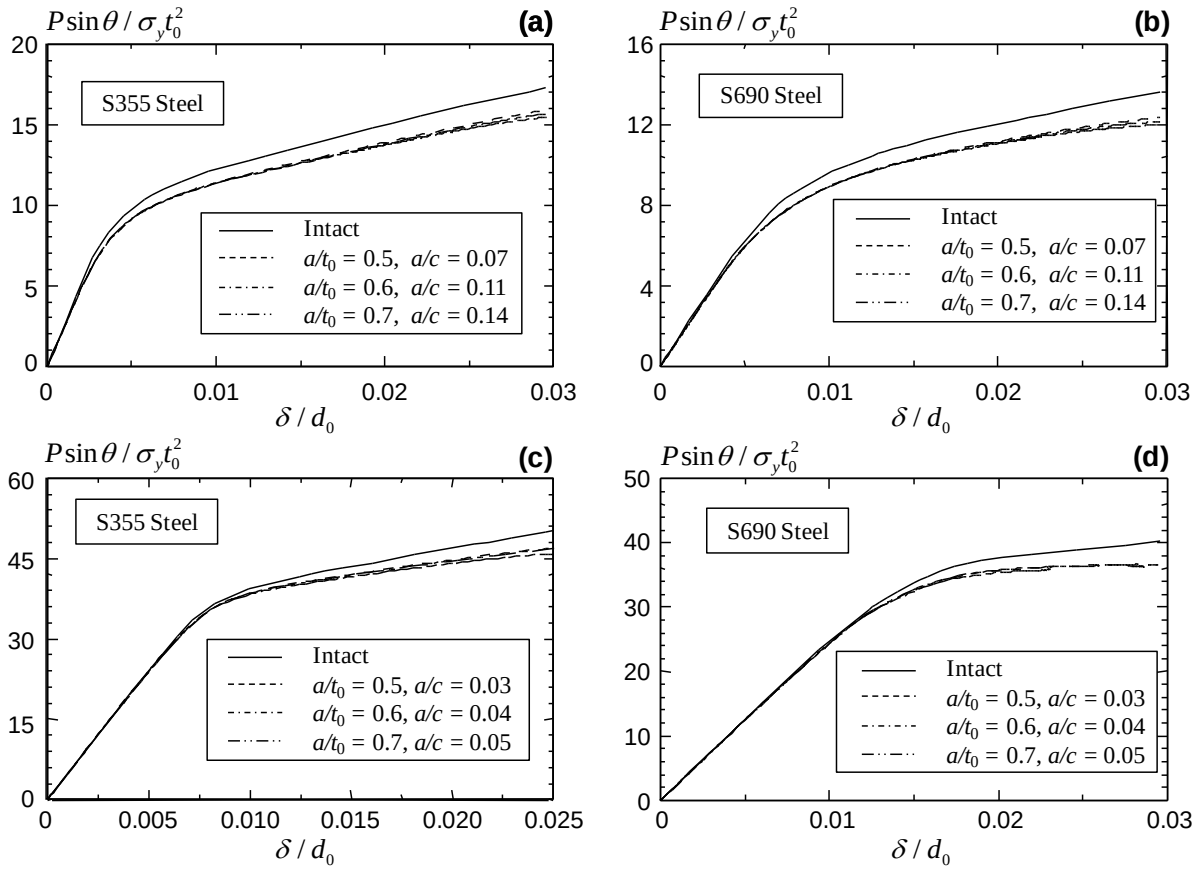

Fig. 6.8: Non-dimensional load-deformation curves of tubular K-joints with same crack area but different crack aspect ratios: (a) $\gamma = 15$, $\beta = 0.3$, $g' = 6$, $\sigma_y = 355$MPa; (b) $\gamma = 15$, $\beta = 0.3$, $g' = 6$, $\sigma_y = 690$MPa; (c) $\gamma = 25$, $\beta = 0.9$, $g' = 10$, $\sigma_y = 355$MPa; and (d) $\gamma = 25$, $\beta = 0.9$, $g' = 10$, $\sigma_y = 690$MPa.

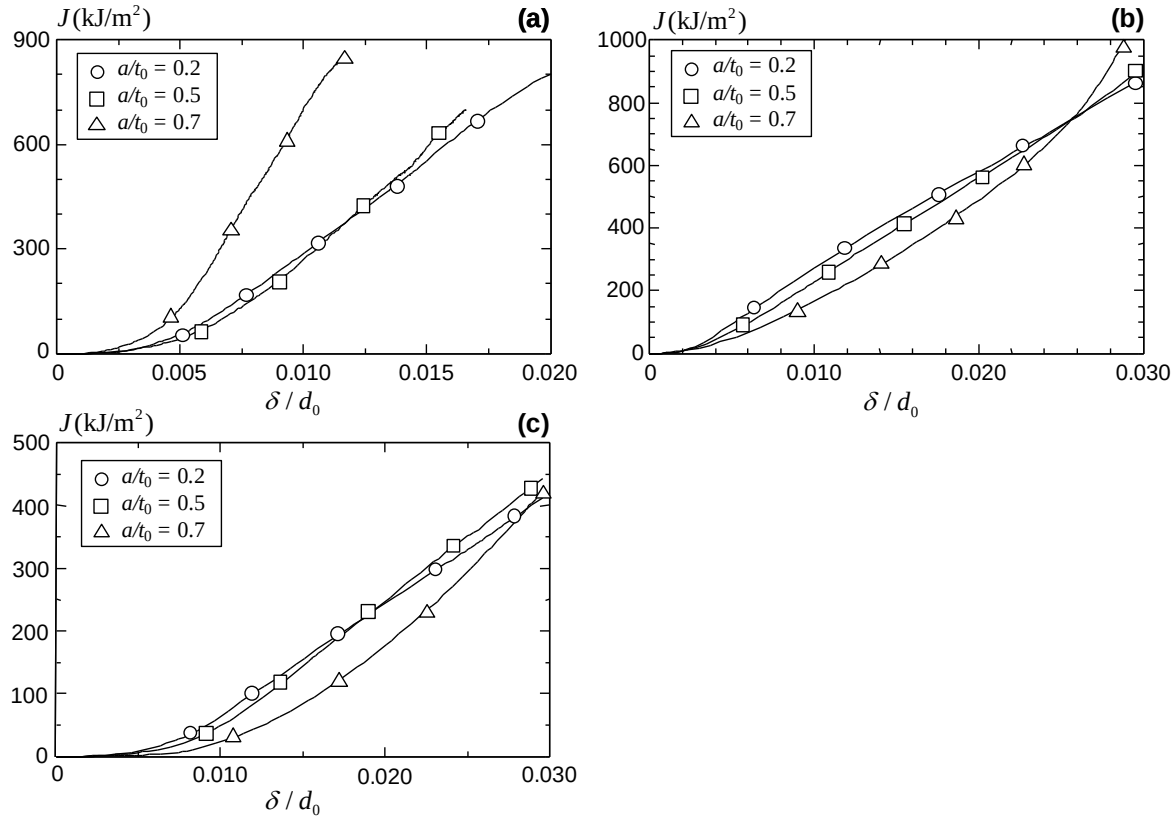

Fig. 6.9: Evolution of the elastic-plastic J-value versus the applied displacement for K-joints with different crack depths: (a) $\gamma = 20$, $\beta = 0.6$, $g' = 2$, $\sigma_y = 355$MPa; (b) $\gamma = 15$, $\beta = 0.3$, $g' = 6$, $\sigma_y = 355$MPa; and (c) $\gamma = 25$, $\beta = 0.9$, $g' = 10$, $\sigma_y = 355$MPa.

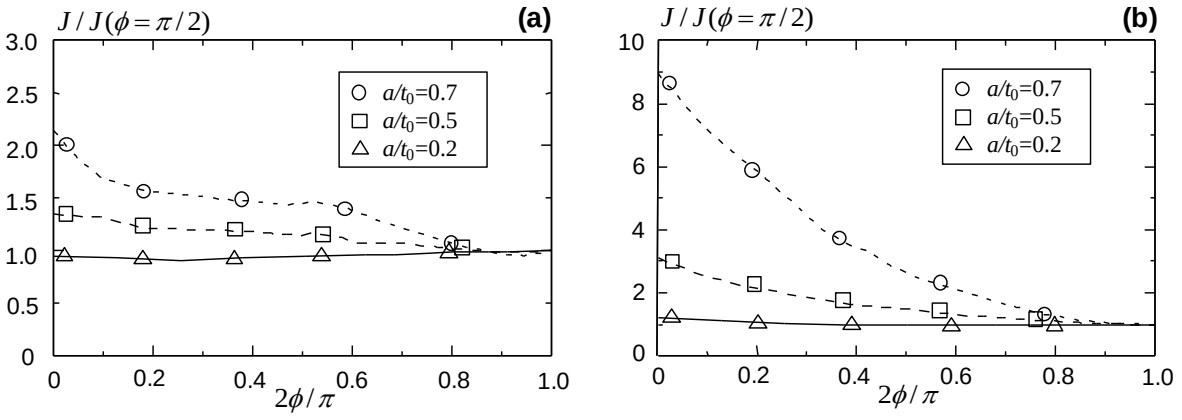

Fig. 6.10: Surface constraint effect at the small deformation for a surface crack in tubular K-joints corresponding to different crack depths: (a) $\gamma = 15$, $\beta = 0.3$, $g' = 6$, $\sigma_y = 355$MPa and (b) $\gamma = 25$, $\beta = 0.9$, $g' = 10$, $\sigma_y = 355$MPa.

For the shallow surface crack ($a/t_0 \leq 0.5$), the balance between the surface constraint and the crack depth induces an insensitive effect of the crack depth on the variation of the crack driving force at the governing location ($2\phi/\pi = 1$). The increasing gap in a K-joint allows the applied stresses to be distributed in the intact material near the cracked location. The crack driving force for the deep cracks in K-joints with $g' = 6$ and 10 therefore does not indicate a strong increase as the load increases. Nevertheless, the crack driving force remains insensitive with respect to the shallow crack size ($a/t_0 \leq 0.5$) for all three different gap ratios.

6.4 Proposed Joint Fracture Formulation

The current study employs the elastic-plastic crack driving force measured by the domain J-integral, coupled with an experimentally determined J-R curve from a deep-crack fracture specimen, to describe phenomenologically the load-displacement response of a tubular joint which experiences ductile tearing followed by the unstable fracture failure.

6.4.1 Material Fracture Resistance *J-R* Curve

In the ductile tearing process, the metal material often shows a rising resistance curve, where the fracture toughness increases with the crack growth. Figure 6.11 schematically illustrates a typical J resistance curve for a ductile material. The small amount of apparent crack growth due to blunting in the initial stage of the deformation produces a nearly vertical R curve. As the applied load increases, the material at the crack tip fails locally and the crack extends further when:

$$J > J_{IC} \tag{6.2}$$

where J_{IC} refers to the fracture toughness measured from a standard fracture specimen satisfying the size requirement in ASTM E-1820 (2011). A plastic zone at the crack tip forms and increases in size as the crack grows. The growing plastic zone requires an increasing crack driving force to maintain the stable crack growth. During steady-state crack growth, a plastic zone of approximately the same size sweeps through the material, leaving a plastic wake (Anderson, 2004). The required elastic-plastic crack driving force, or the resistance, increases asymptotically towards J_{max}, which refers to the J-value at the intersection between the J-R curve and the 1.5 mm offset line in the J-R curve test, as illustrated in Fig. 6.11. The J_{max} value represents a limit of the measurable J-resistance, beyond which the substantial crack growth leads to the severe unloading in the near-tip material and violates the fundamental assumption in the J similitude concept. The similitude concept ensures the same stress/strain/displacement fields near two crack tips (with the same driving force J) in two different structures subjected to completely different loadings. If the crack driving force induced by the external loads exceeds J_{max} or becomes tangent to the J-R curve, the proposed joint formulation assumes the onset of the unstable fracture failure. The J_{max} value thus determined should remain smaller than the maximum J-value ($= b_0\sigma_y/10$ or $B\sigma_y/10$) dictated by the size of the fracture specimen as prescribed in ASTM E-1820 (2011).

6.4.2 General Description of the Proposed Joint Fracture Formulation

Figure 6.12 illustrates the proposed joint fracture formulation presented in the J-L_r space. The load ratio L_r defines the ratio between the available joint strength over the ultimate strength of the intact joint. The proposed joint model assumes that the joint sustains an ultimate load resistance before ductile tearing initiates in the steel material. Figure 6.13 translates the fracture model shown in Fig. 6.12 into a characteristic load-deformation

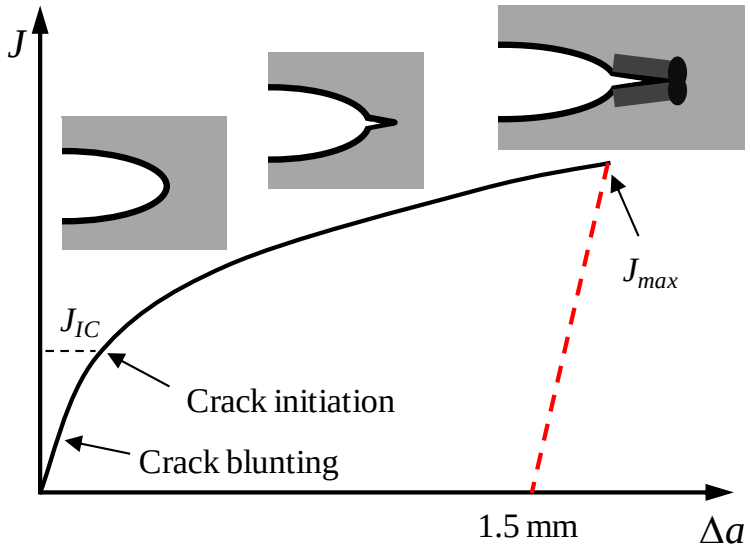

Fig. 6.11: Schematic J resistance curve for a ductile material.

response of a tubular joint. The translation from Fig. 6.12 to Fig. 6.13 requires a relationship between the joint resistance and the remote displacement for a tubular joint with an extending crack.

The load-deformation behavior before the initiation of ductile tearing follows the conventional FE analysis without any damage model involved. With the negligible effect of the shallow surface cracks on the joint resistance demonstrated in Fig. 6.9, the current joint model assumes an initial shallow surface crack to determine the displacement level when ductile tearing initiates, *i.e.*, the displacement level at which,

$$J = J_{IC} \tag{6.3}$$

Section 6.4.3 examines the sensitivity of the assumed initial crack size in the proposed joint formulation. The load level at which the ductile tearing initiates depends on the

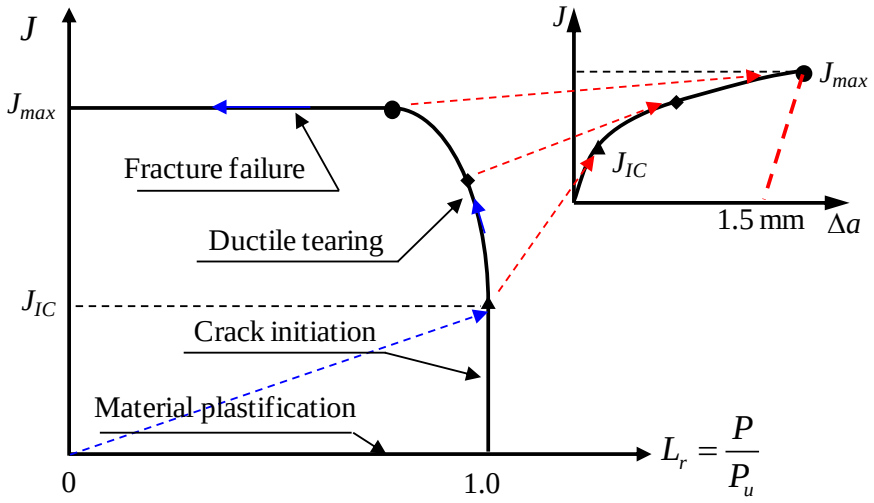

Fig. 6.12: J versus the load ratio for an extending crack in a tubular joint.

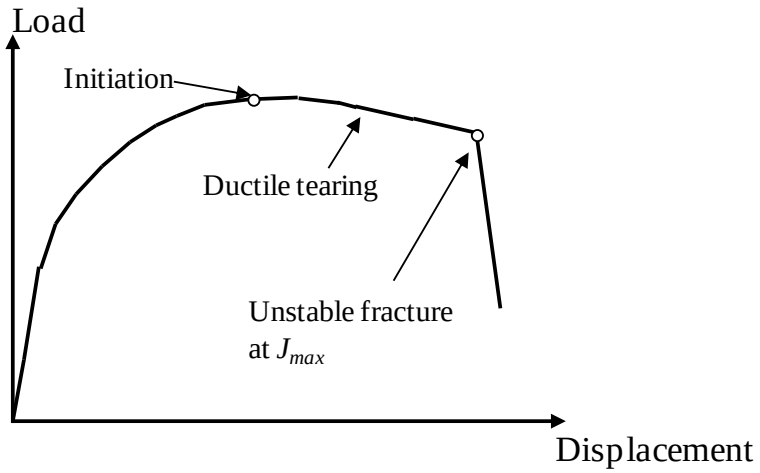

Fig. 6.13: Schematic load-deformation curve for tubular joints based on the proposed fracture representation in Fig. 6.12.

size of the initial crack assumed, or,

$$P_{u,crack} = P_u A_{RF} \tag{6.4}$$

where A_{RF} defines the area reduction factor,

$$A_{RF} = \left(1 - \frac{A_{crack}}{L_{weld} t_0}\right)\left(\frac{1}{Q_\beta}\right)^m \tag{6.5}$$

and Q_β denotes a geometric parameter depending on β,

$$Q_\beta = \begin{cases} 1 & \beta \leq 0.6 \\ \frac{0.3}{\beta(1-0.833\beta)} & \beta > 0.6 \end{cases}$$

The area reduction factor with $m = 1$ provides conservative strength estimations (Wang *et al.*, 2011) for cracked joints. The current study assumes $m = 0$, which provides an accurate estimation of the surface cracked tubular joints (Wang *et al.*, 2011).

Upon the initiation of the ductile tearing, the proposed fracture model allows a small amount of crack extension. During the stable ductile tearing process, the relationship between the crack driving force and the amount of crack extension at the deepest crack-front location follows the experimentally measured J-R curve. For a crack to remain stable while extending (by a short amount of $\Delta_a < \Delta a_{max} \approx 2mm$ based on the 1.5 mm offset line in a typical J-R curve test), the crack driving force versus the corresponding crack extension shall match the resistance of the material against fracture.

The small-scale yielding requirement in obtaining a valid J-R curve from the standard fracture specimens imposes a strict requirement on the transferability of the same J-R curve when applied to assess a realistic flaw in a structural component. The structural component should entail a well-contained crack front with high plasticity constraints

to satisfy the J similitude requirement. The requirement of the J-integral value as a valid crack-tip parameter also limits its application to the ductile tearing process with a large amount of crack extension. The proposed joint fracture formulation employs J_{max} from the fracture test as a threshold, beyond which unstable fracture occurs in the joint and causes the complete loss of the joint capacity, as shown in Fig. 6.13. The plastic deformation in the adjacent weld or brace material away from the crack location absorbs the remotely imposed displacements at the brace end, and thereby shields the crack-front material in the chord wall at large deformations (Qian *et al.*, 2007). Without considering this shielding effect, the proposed fracture formulation provides a conservative estimation on the load-displacement relationship for a tubular joint with ductile tearing and subsequently unstable fracture.

In summary, the proposed load-displacement formulation to represent ductile crack extension followed by unstable fracture in a tubular joint consists of the following steps,

- Step 1: the load-displacement relationship for the initially intact tubular joint follows from the results finite element analysis firstly.

- Step 2: the proposed approach assumes an initial shallow surface crack to determine the displacement level at which ductile crack extension initiates. At this displacement level, the computed energy release rate at the deepest crack-front location reaches the material fracture toughness, J_{IC}. The corresponding load capacity derives from Eq. 6.4. Figure 6.5 and 6.6 demonstrate the insignificant effect of the shallow cracks on the strength of the tubular K-joints. Section 6.4.3 examines the assumed initial crack sizes on the derived load-displacement relationship for X- and K-joints.

- Step 3: beyond the crack initiation, the proposed formulation assumes that the J-Δa relationship during the ductile tearing in a tubular joint adheres to the J-R

curve measured from a high-constraint fracture specimen before J_{max} is reached. The amount of crack extension determined by the J-R curve enables an estimation of the joint strength with an extending crack, using the area reduction factor in Eq. 6.5.

- Step 4: the ductile tearing continues until the amount of crack extension reaches Δa_{max}, determined by the 1.5 mm offset line in the J-R curve test. The 1.5 mm offset line represents a limit beyond which severe local unloading occurs near the crack tip and impinges on the fundamental assumption in the J similitude concept. The short Δa_{max} thus represents a limit of the transferability of the J-R curve from the small-scale fracture specimen to the large-scale tubular joints. As the amount of crack extension exceeds Δa_{max}, the proposed formulation assumes the total loss of the joint capacity.

6.4.3 Sensitivity of the Initial Crack Size

The proposed joint formulation assumes an initial crack size to determine the initiation of the ductile tearing and the corresponding load and deformation levels. The numerical study examines the effect of the initial crack size assumed in two CHS K-joints under the balanced axial loading and two CHS X-joints under the brace axial tension. The initial crack sizes considered include $a/t_0 = 0.2$, 0.3 and 0.5 with the crack aspect ratio fixed at $a/c = 0.25$ for all crack sizes. This sensitivity analysis employs a typical J-R curve for the structural steel S350 (to be discussed in Section 6.5). Figure 6.14 and 6.15 manifest the normalized load-deformation behavior obtained for CHS K-joints and X-joints. The variation of the initial crack size shows a marginal effect on the load-deformation curve for X- and K-joints due to the insensitivity of both the crack driving force and the ultimate strength with respect to the shallow crack size. Therefore, the current study assumes an initial crack size of $a/t_0 = 0.2$ and $a/c = 0.25$ to evaluate the change of the crack driving

force at the hot-spot region for joints under axial tension.

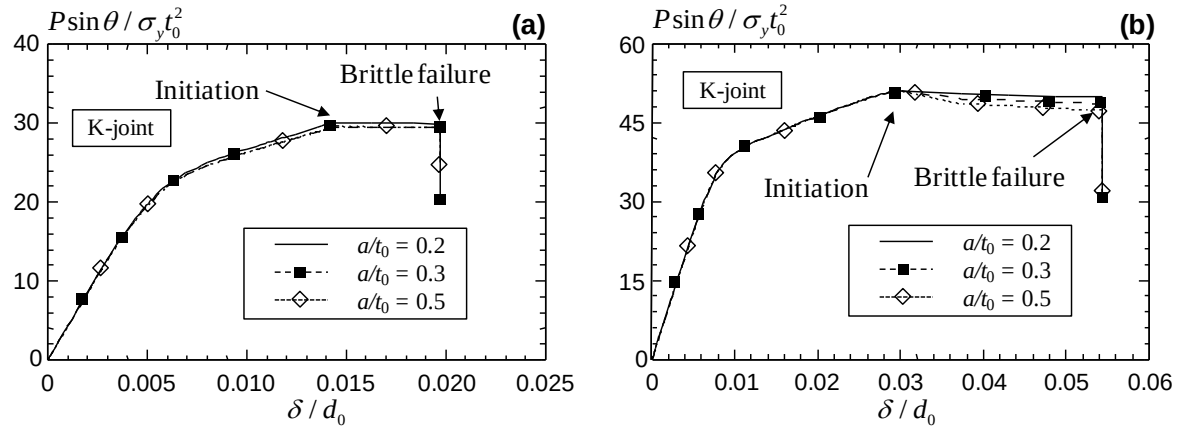

Fig. 6.14: Sensitivity of the initial crack size for the proposed joint fracture formulation in K-joints: (a) $\gamma = 20$, $\beta = 0.6$, $g' = 2$ and (b) $\gamma = 25$, $\beta = 0.9$, $g' = 10$.

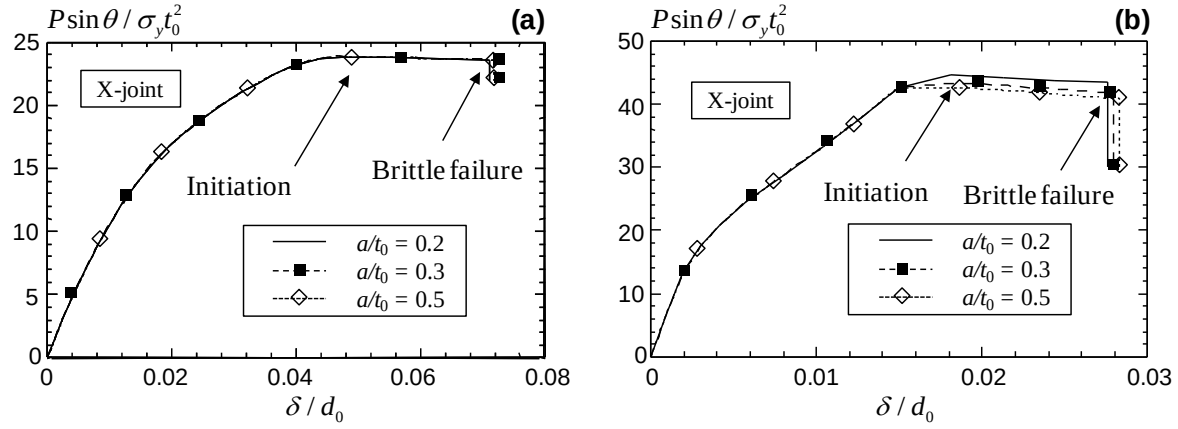

Fig. 6.15: Sensitivity of the initial crack size for the proposed joint fracture formulation in X-joints: (a) $\gamma = 25$, $\beta = 0.6$ and (b) $\gamma = 20$, $\beta = 0.9$.

6.5 Verification of the Proposed Joint Fracture Formulation with Experimental Tests

This section verifies the proposed joint formulation based on the experimentally measured load-deformation responses of three cracked X-joint specimens (Qian *et al.*, 2012, 2013) and one intact KK joint (Wang *et al.*, 2000). The comparison proves the validity of the J-integral as the criteria to characterize the initiation of the ductile tearing, the corresponding strength reductions, and the final unstable fracture failure.

6.5.1 XN Joint

Qian *et al.* (2013) report an experimental investigation of a fatigue-cracked, pre-notched CHS X-joint (denoted as XN joint) fabricated from high strength steels (S690) subjected to the brace in-plane bending. The geometry of the high strength steel thick-walled X-joint follows $\beta = 0.69$, $\gamma = 6.4$ and $\tau = 0.86$. The test setup generates the brace in-plane bending by applying a vertical compression on the top end of the chord member, while two ends of the brace members sit on two saddle supports, one of which rests on a roller support and the other on a pin support, as indicated in Fig. 6.16. Figure 6.17a plots the true stress versus true strain curve measured from coupon specimens for both brace and chord materials. The circular hollow section X-joint entails a prefabricated V-notch near the weld toe at the crown position of the chord side, as shown in Fig. 6.16. The experimental procedure consists of two loading stages, a fatigue pre-cracking cyclic load to generate a sharp fatigue surface crack along the root of the prefabricated notch followed by a monotonic brace in-plane bending. Figure 6.17b plots the profile of the semi-elliptical fatigue crack, a_0, measured by the post-test sectioning of the cracked specimen. Their study also reports the J-R curve measured by several side-grooved compact tension, C(T) specimens (ASTM E1820, 2011), fabricated from the chord material. Figure 6.17c plots

one of the measured fracture resistance J-R curve employed in the current study.

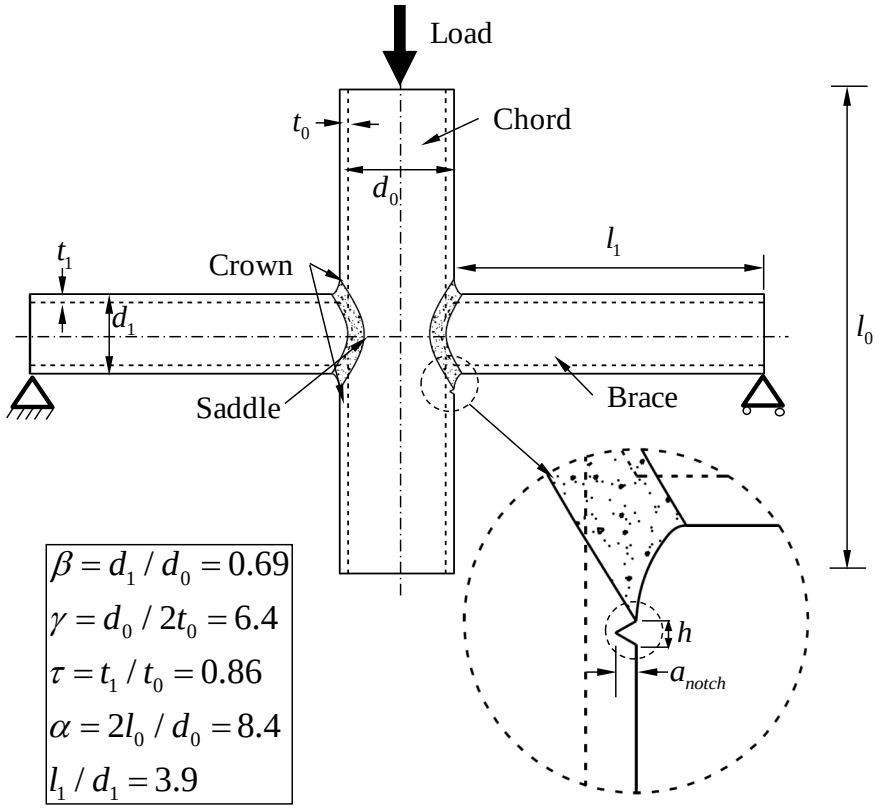

Fig. 6.16: Geometric configuration of XN joint (Qian *et al.*, 2013).

The symmetry of the joint geometry and the loading condition permits the current study to model the specimen using one quarter finite element mesh for the numerical analyses. The mesh-tie procedure couples the local crack front model, built in FEA (2011) with a global continuous model generated in Patran (2012). Figure 6.18a compares the elastic-plastic crack driving force (J-value) computed from a large deformation, finite element analysis and the η approach as described in Chapter 5. The close agreement demonstrates the strong linear relationship between the global plastic work and the energy release rate at the deepest crack front for the high strength steel X-joint, before extensive yielding occurs in the welds and braces. Figure 6.18b compares the joint response predicted by the numerical analysis with the test result. During the experiment,

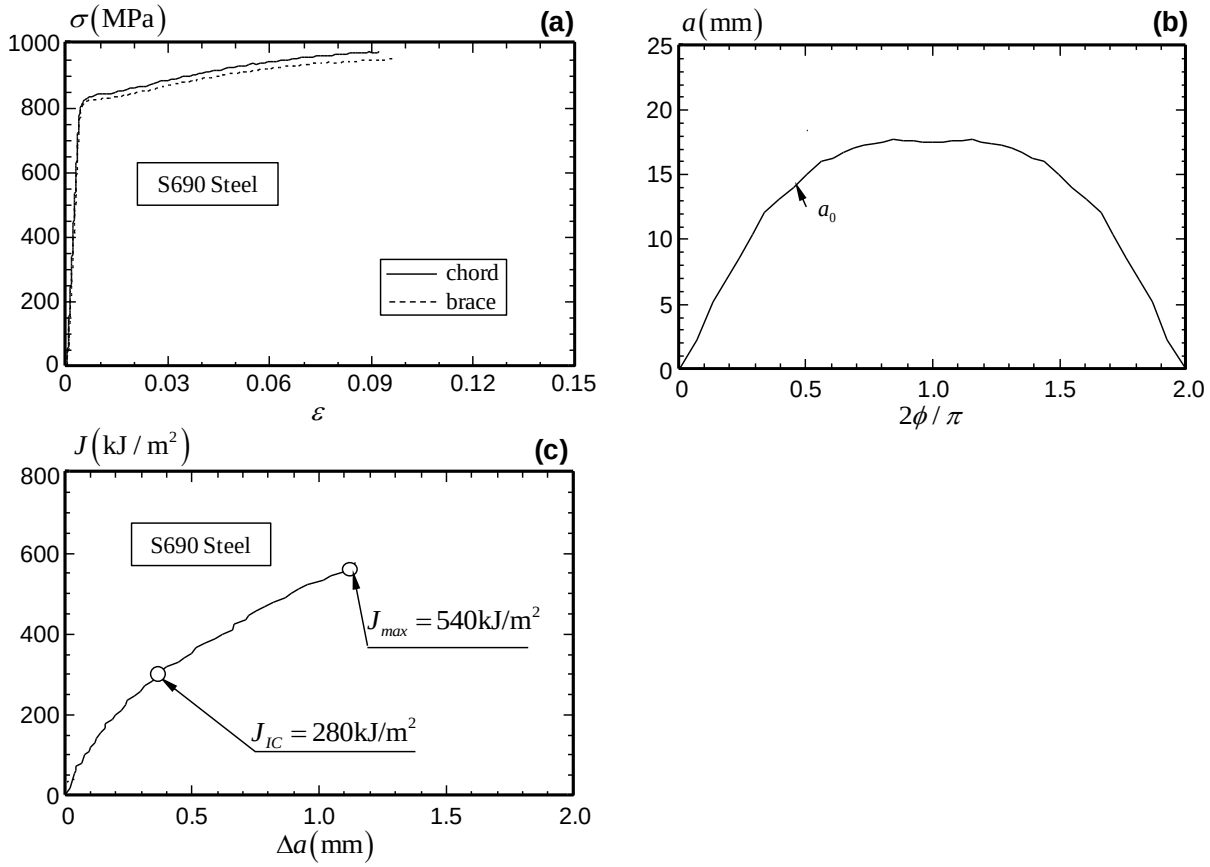

Fig. 6.17: Material property for XN joint: (a) uni-axial true stress-true strain relationships for the chord and brace material and (b) crack front profile before the ductile tearing; and (c) fracture resistance J-R curve for the chord material.

the X-joint experiences a maximum load of 1864kN, beyond which a brittle failure occurs. The deformation limit at the brittle failure corresponds to a brace rotation of 0.053 radian far below Lu's deformation limit (1994). Without a material damage model to simulate the crack extension, the finite element analysis predicts a continuously increasing joint resistance which deviates from the experimental load versus load-line displacement curve at large deformations. The proposed joint fracture formulation predicts closely the unstable fracture failure in the joint corresponding to the deformation where $J = J_{max}$.

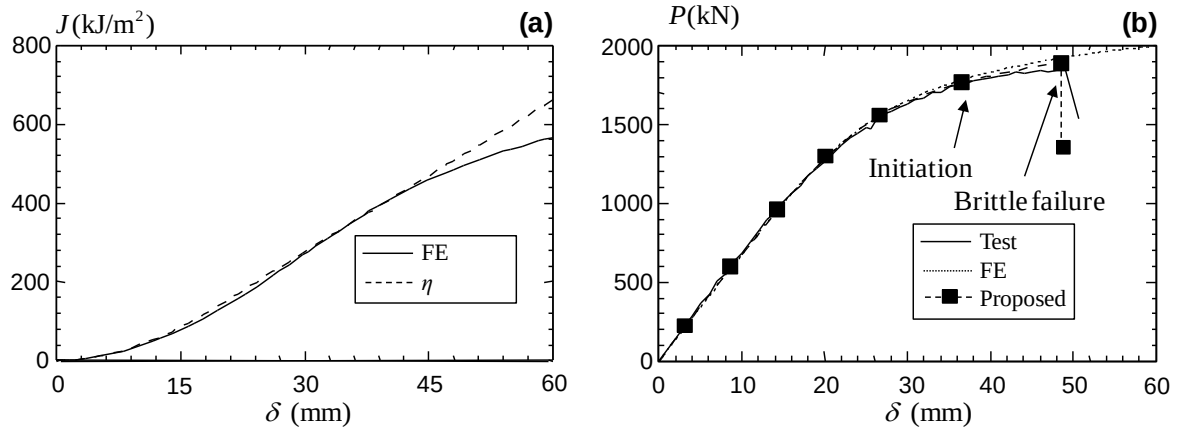

Fig. 6.18: (a) Evolution of the elastic-plastic J-value at the deepest crack-front for XN joint and (b) comparison of the experimental load-displacement curve with the FE results and the proposed fracture formulation for XN joint.

6.5.2 PJP+ Joint

Qian *et al.* (2012) summarize a series of cyclic tests on CHS X-joints with partial joint penetration plus welds (denoted as PJP+ joint) subjected to the brace in-plane bending moment. The current study verifies the proposed joint fracture formulation based on two selected joints, J1-1F and J1-2F, as described in Table 6.3. Figure 6.19 shows the typical configuration of the test setup. Both joints experience a vertical load applied at the top loading fixture, while the two brace ends rest on two supports. The experimental

procedure firstly generates a fatigue crack at the hot spot location by the cyclic loading followed by a monotonic brace in-plane bending to obtain the ultimate strength of the cracked joint specimen. Figure 6.20a plots the true stress-true strain curve of the chord and brace material employed for all the joint specimens. Figure 6.20b shows the fracture toughness J-R curve for the brace material measured by the side-grooved compact tension, C(T) specimens (ASTM E1820, 2011), cut from the joint material after the test. The brace material provides an increasing fracture toughness as the crack extends. The chord material exhibits a very high fracture toughness which exceeds the maximum J-value limited by the small-scale yielding requirement in fracture specimens.

Table 6.3: Geometrical information for PJP+ joints.

Joint	d_0(mm)	β	γ	α	τ	Major fatigue crack position
J1-1F	750	0.54	15	4.67	0.5	left brace crown point
J1-2F	750	0.54	15	4.67	0.5	left chord crown point

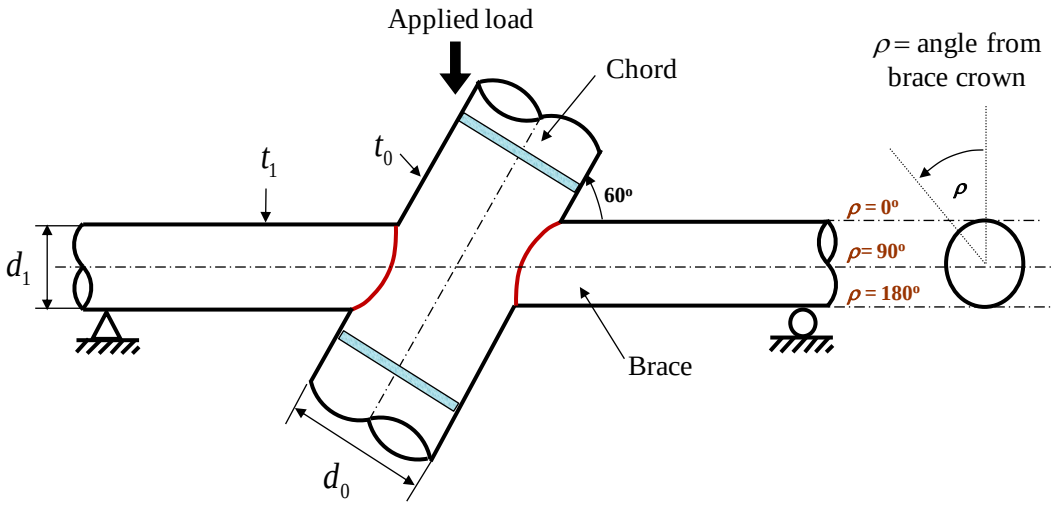

Fig. 6.19: Geometric configuration of the PJP+ CHS X-joints.

Figure 6.21a shows the crack-front profile of the fatigue crack located in the brace

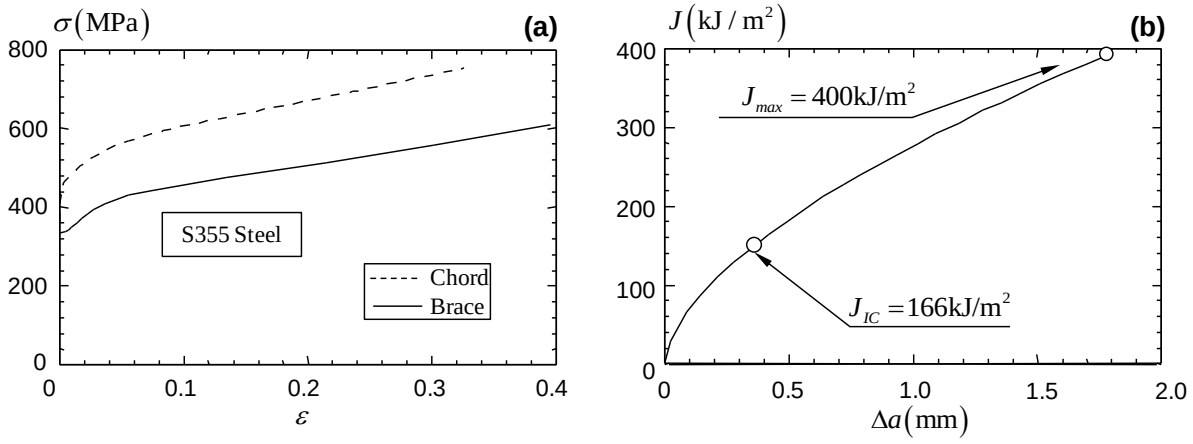

Fig. 6.20: Material property of the PJP+ CHS X-joints: (a) uni-axial true stress-true strain curves for the chord and the brace materials and (b) fracture resistance J-R curve for the brace material.

material near the weld toe for the specimen J1-1F joint, prior to the monotonic loading test, where the angle ρ denotes the position along the brace-to-chord intersection measured from the top of the brace in a counter-clockwise direction when viewed from the right side of the joint, as shown in Fig. 6.19. The current study follows the similar finite element technique as that for XN joint. Figure 6.21b demonstrates the strong relationship between the joint global plastic work and the elastic-plastic crack driving force at the deepest crack-front location, evidenced by the close agreement in the J-values predicted by the η approach and those computed using domain integrals. Figure 6.21c compares the prediction using the proposed joint fracture formulation with the test result. The J1-1F joint experiences a limited amount of ductile tearing followed by an unstable fracture failure in the brace. Without considering shielding effect of the plastic deformation mobilized in the adjacent welds and braces, the proposed joint formulation predicts a conservative estimation on both the strength and ductility of the specimen.

The experiment for J1-2F joint generates a fatigue crack at the crown point of the chord weld toe. Figure 6.22 shows the increase of the crack driving force against the

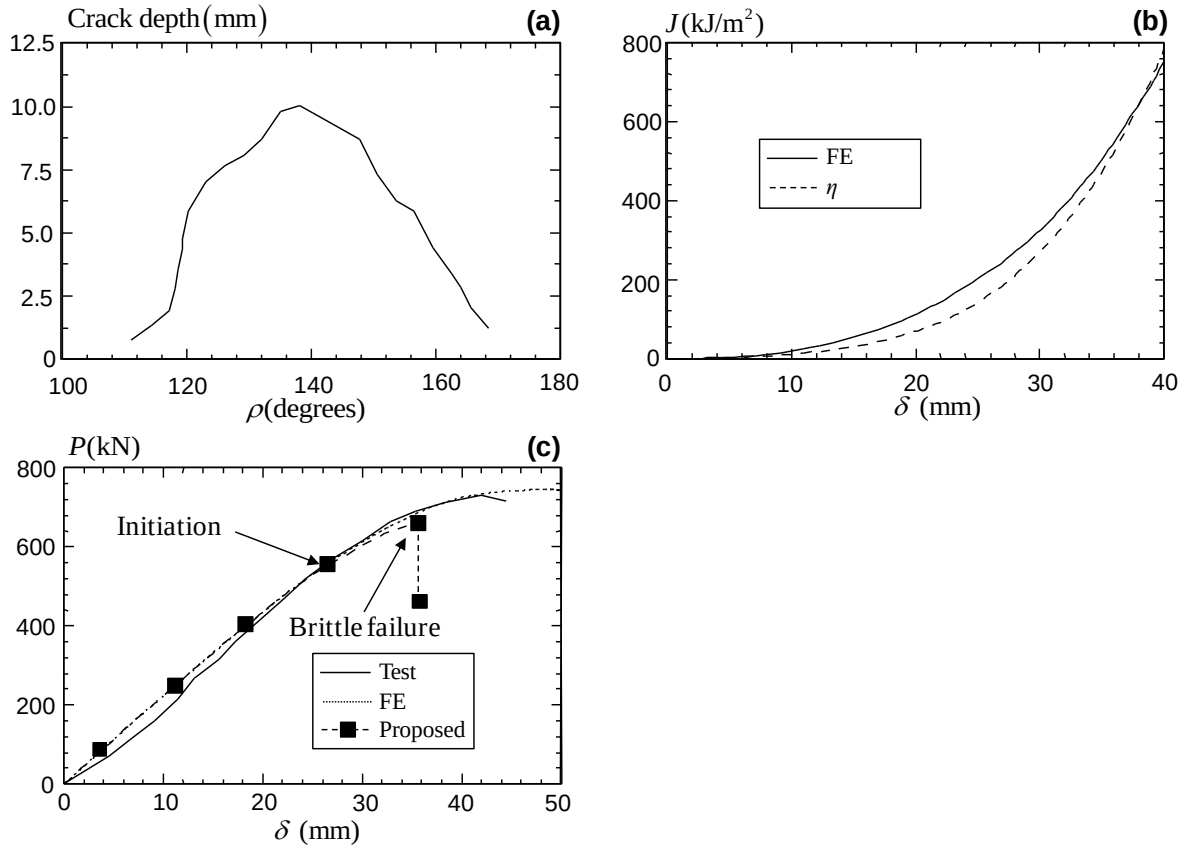

Fig. 6.21: (a) Fatigue crack profile for PJP+ X-joint J1-1F; (b) evolution of the elastic-plastic J-value at the deepest crack-front for J1-1F joint; and (c) comparison of the experimental load-displacement curve with the FE results and the proposed fracture formulation for J1-1F.

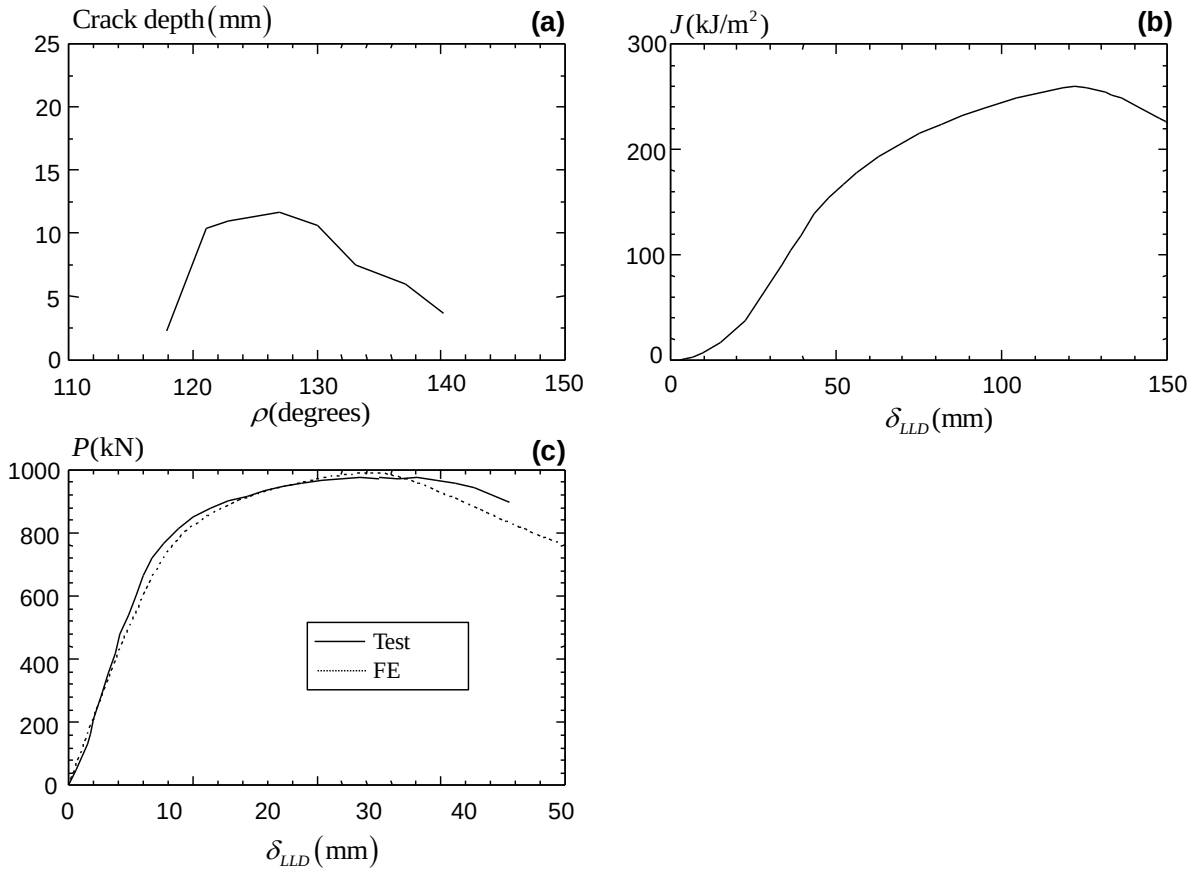

Fig. 6.22: (a) Fatigue crack profile for PJP+ X-joint J1-2F; (b) evolution of the elastic-plastic J-value at the deepest crack-front for J1-2F joint; and (c) comparison of the experimental load-displacement curve with the FE results for J1-2F.

load-line displacement, produced from the finite element analysis. As the elastic-plastic crack driving force remains far below the crack initiation fracture toughness (J_{IC}), the joint fails due to the brace local buckling at the compression side instead of the unstable fracture failure.

6.5.3 KK Joint

Wang *et al.* (2000) report a CHS uni-planar intact KK-joint without any machined notch or fatigue crack, as shown in Fig. 6.23. The KK-joint specimen experiences the anti-symmetric, monotonically increasing axial loads while two chord ends remain pinned on two supports. Figure 6.24a plots the uniaxial true stress-true strain curves for the chord and brace, with the yield strength σ_y = 342MPa and 366 MPa respectively. Due to the unavailable fracture resistance curve for the steel material used in the test, the current study employs the J-R curve, as shown Fig. 6.24b, for a similar steel grade S350 available in the local market in formulating the phenomenological representation of the joint. The test process observes the crack initiation on the chord surface near the weld toe between the tension brace and the chord before the joint reaches the ultimate capacity. As the remote brace loading increases, the joint specimen experiences ductile tearing until it reaches the ultimate capacity.

The current study assumes a shallow surface crack located at the chord surface near the tension brace weld toe to characterize the ductile tearing and final unstable fracture failure as in the proposed joint fracture formulation. The experimental procedure observes a sudden load reduction after some amount of ductile tearing, as indicated in Fig. 6.25. Similar to the previous results, the FE analysis without a material damage model predicts the yielding of the joint followed by a very ductile response. The proposed joint formulation predicts a slightly conservative estimation of the joint unstable fracture.

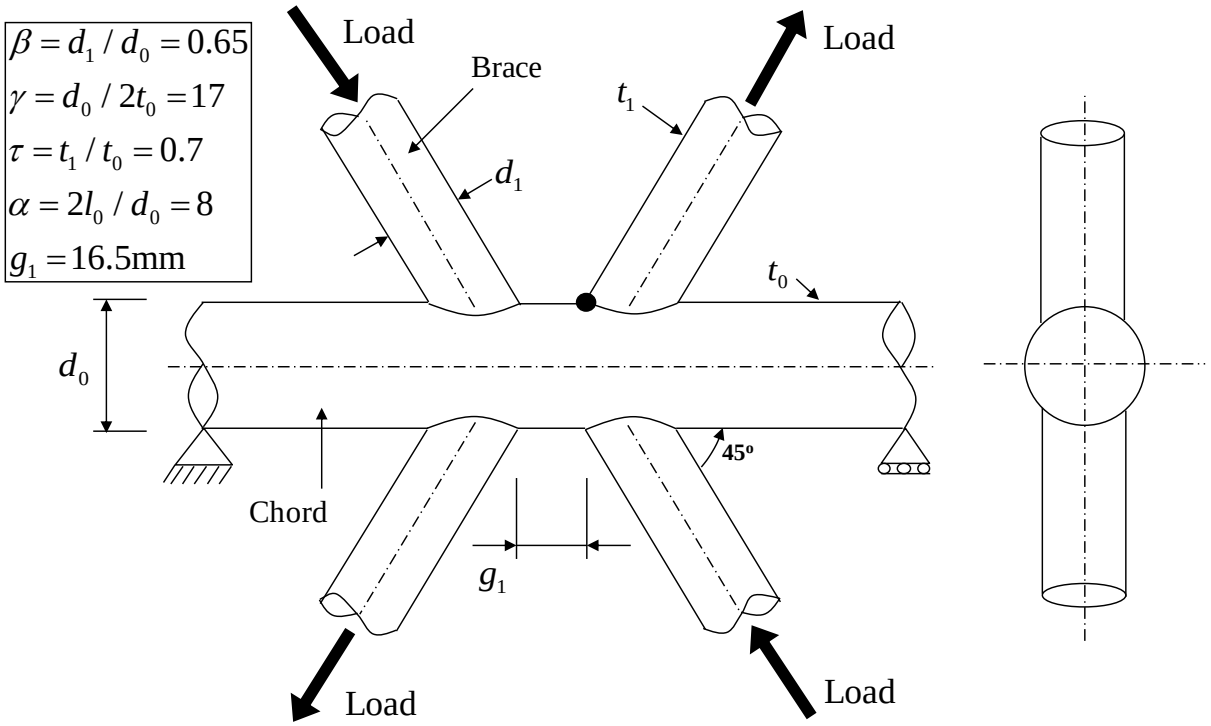

Fig. 6.23: Geometric configuration of CHS KK-joint.

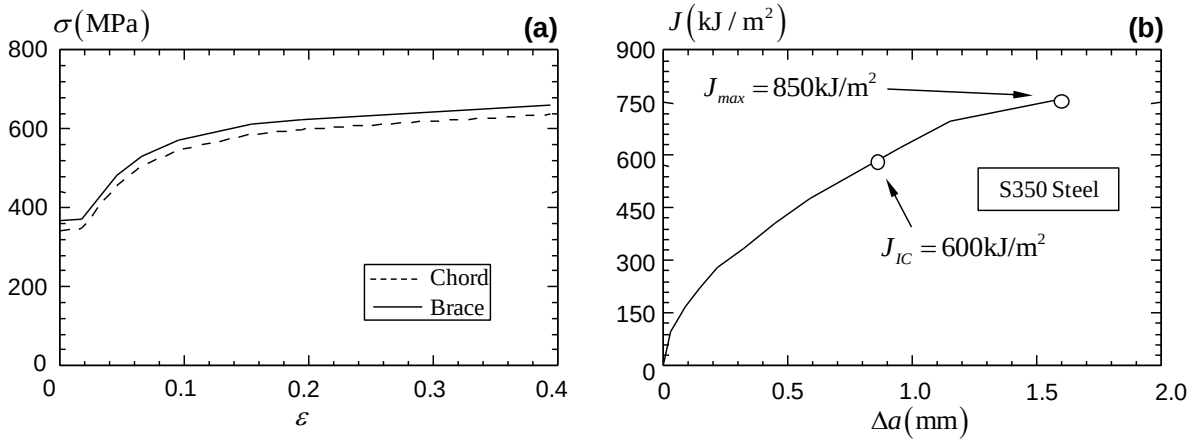

Fig. 6.24: Material property of CHS KK-joints: (a) uni-axial true stress-true strain curves for the chord and the brace materials and (b) fracture resistance J-R curve for the chord material.

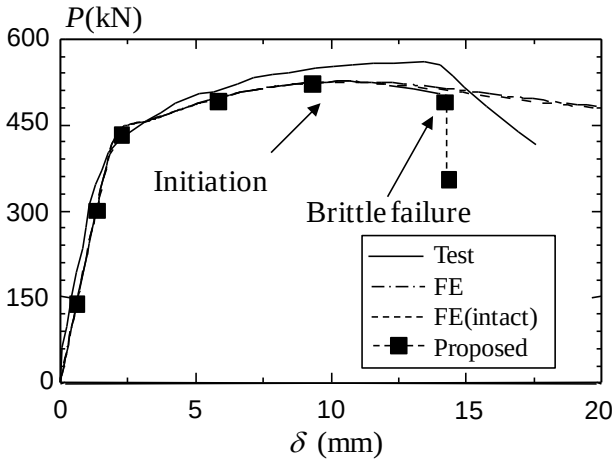

Fig. 6.25: Comparison of the experimental load-displacement curve with FE results and the proposed fracture formulation for KK-joint.

6.6 Conclusion

The current study proposes a new joint fracture formulation to describe the weakening of the joint resistance caused by the ductile crack extension, as well as the significant loss in joint strength invoked by unstable fracture failure. The proposed joint fracture formulation employs the elastic-plastic crack driving force, J-integral, computed from the the large deformation, finite element analyses to characterize the initiation of the ductile tearing and the subsequent fracture failure after a limited amount of crack extension. The close agreement in the load-deformation behavior with the reported joint proves the validity of the proposed joint fracture formulation. The study summarized above supports the following conclusions:

1. The proposed joint formulation assumes an initial crack size to determine the onset of ductile crack extension at $J = J_{IC}$. The load-deformation responses thus derived demonstrate clear independence of the load-displacement relationship on the assumed initial crack size and the crack aspect ratio.

2. The joint resistance during the stable ductile tearing process follows the joint ca-

pacity coupled with an area reduction factor A_{RF}. The A_{RF} value derives from the cracked area, assuming a constant crack aspect ratio, a/c, for the extending crack in the tubular joint. Consequently, the crack area depends on the amount of the crack extension at the deepest crack-front location. During the crack extension, the crack driving force versus the crack extension relationship at the deepest crack-front location adheres to the J-R curve measured from a high-constraint fracture specimen. This approach estimates closely the deterioration in the joint strength as the crack extends, as demonstrated by the comparison against the experimental results on tubular joints.

3. The proposed joint formulation assumes the occurrence of the joint unstable brittle failure at $J = J_{max}$ with a total loss of the joint resistance. The employment of J_{max} provides a conservative fracture threshold, which satisfies the transferability requirement for the J-R curve from the standard fracture specimen to a realistic flaw in a structural component. The verification of the proposed joint formulation based on the joint behavior demonstrates the validity of the J-integral in representing the onset of ductile tearing and the joint unstable failure.

Chapter 7

Frame Study

7.1 Introduction

Past decades have observed tremendous offshore jacket structures used in petroleum activities. Improvements in the possible oil recovery from several fields have increased the interest for using these platforms beyond their initial 20-year design life. Thus, Structural Integrity Management (SIM) serves as an important process for ensuring the continued fitness-for-purpose of offshore structures. The traditional design of the steel offshore jacket determines the distribution of the force through the structure subject to specified design environmental loads based on the elastic frame analysis. During SIM process, the seabed subsidence and the revised design wave crest both lead to the increased risk of the inundation of the platform deck, which will generate a large wave-in-deck force far beyond the initial design loading. However, the jacket may exhibit the reserve strength beyond the required design resistance due to the material nonlinearity and the structural redundancy. Therefore, accurate predictions of the static collapse and push-over analyses of jacket structures exhibit an increasing importance.

The accuracy of frame analyses depends mainly on the accurate prediction of the

member behavior, the proper modeling of the joint behavior and the joint-frame interaction. Previous research has developed elements to capture accurately the nonlinear member behavior (Hellan, 1995). Different researchers (Dier and Hellan, 2002; USFOS, 2009; Choo *et al.*, 2005) also propose different joint formulations to simulate the CHS joint behavior based on either experimental or numerical data. However, the approach to characterize the nonlinear joint behavior, especially the joint load-deformation response under the excessive tensile loads, still requires further investigation.

The current study proposes an integrated load-deformation formulation for CHS K-joints under monotonically increasing balanced brace axial loads based on the synthesization of previous chapters. The joint load-deformation formulation incorporates the nonlinear joint representation proposed in Chapter 4 and the fracture formulation discussed in Chapter 6 through the η approach described in Chapter 5. The joint formulation, implemented as a nonlinear joint spring in USFOS (2009), proves to be a convenient approach to simulate the joint behavior and the joint-frame interaction for tubular K-frames in pushover analyses.

This chapter discusses firstly the fracture toughness test for the grade S260 steel material, from which the selected verification frames are fabricated. The fracture resistance J-R curve obtained provides the specific information to characterize the overall load deformation behavior of the K-joint under the potential fracture failure. The next section demonstrates the accuracy of the proposed joint formulation, implemented as nonlinear joint springs in the pushover analysis for 2D K-frames. The following section extends the application of the proposed K-joint formulation to a realistic offshore jacket and discusses the effect of the joint fracture failure on the global structure behavior.

7.2 Evaluation of Steel Properties in BOMEL Frames

Bolt *et al.* (1995) report an experimental study of two series of 2D large-scale frames under the monotonically increasing loading. The current study focuses three single-bay 2D K-frames, which are designed with gapped K-joints and experiences unstable fracture failures during the test. The proposed joint fracture formulation, as described in Chapter 6, requires the fracture toughness J-R curve for the steel material used in the K-frames. The investigation reported by Bolt *et al.* (1995), however, did not present any fracture resistance curves for the steel pipe BS3602-430ERW, from which the K-frames are fabricated. The current study thus performs a J-R curve test on a closest steel material available, with similar chemical compositions and mechanical properties.

This section shows the setup and the experimental observation of the fracture toughness test conducted for the steel material. The overall experimental program includes two types of tests, the uniaxial tensile test (ASTM E8/E8M, 2011) and the fracture resistance test (ASTM E1820, 2011) using the single-edge-notched bend, SE(B), specimens with two different thicknesses.

7.2.1 Uniaxial Tension Test

Axial tensile tests determines the yield strength, tensile strength, elongation, and area reduction of metallic materials at the room temperature (ASTM E8/E8M, 2011). The current test employs the grade S260 steel material cut from a hot rolled steel plate. The chemical composition of the selected steel material satisfies the material requirement prescribed for the steel pipe BS3602-430ERW, as shown in Table 7.1. Figure 7.1 shows the geometric configuration of the specimens for the experiments, tested under a displacement controlled loading. Figure 7.2a represents the engineering stress-strain curve obtained from the uni-axial tension test, which consists of three duplicate coupon speci-

mens fabricated from the same material. Figure 7.2b shows the coupon specimens after the experiment, which indicate significantly necked sections at the rupture zone. The fracture surface shows a typical cup and cone shape, as indicated in Fig. 7.2c, due to the stress triaxiality at the center and the plasticity mobilized near the surface. Table 7.2 lists the Young's modulus, the yield strength, the ultimate tensile strength and the elongation measured from the coupon specimens. The steel material used in 2D K-frames has a reported yield strength of 275MPa, a Young's modulus of 207GPa and an elongation of 36%, as shown in Table 7.2.

Table 7.1: Comparison of the chemical composition between the selected steel and the steel in K-frames.

Chemical composition	C (%)	Si (%)	Mn (%)	P (%)	S (%)
BS3602-430ERW	0.21(max)	0.35(max)	0.4-1.2	0.04(max)	0.04(max)
Selected steel S260	0.19	0.24	1.09	0.009	0.007

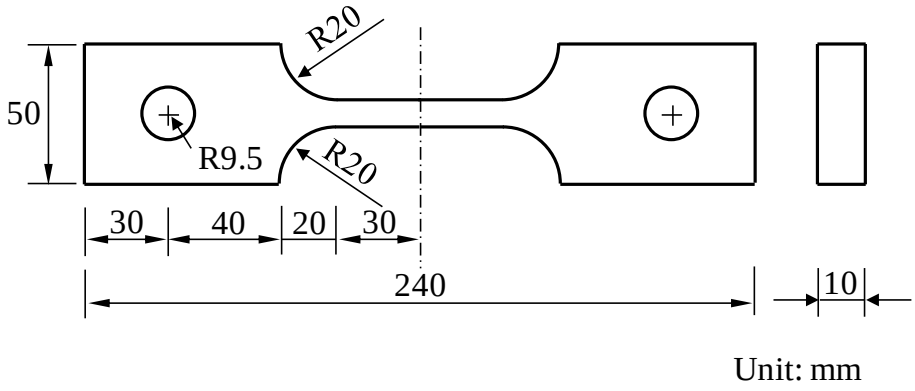

Fig. 7.1: Configuration of the uniaxial tension specimen for the S260 material.

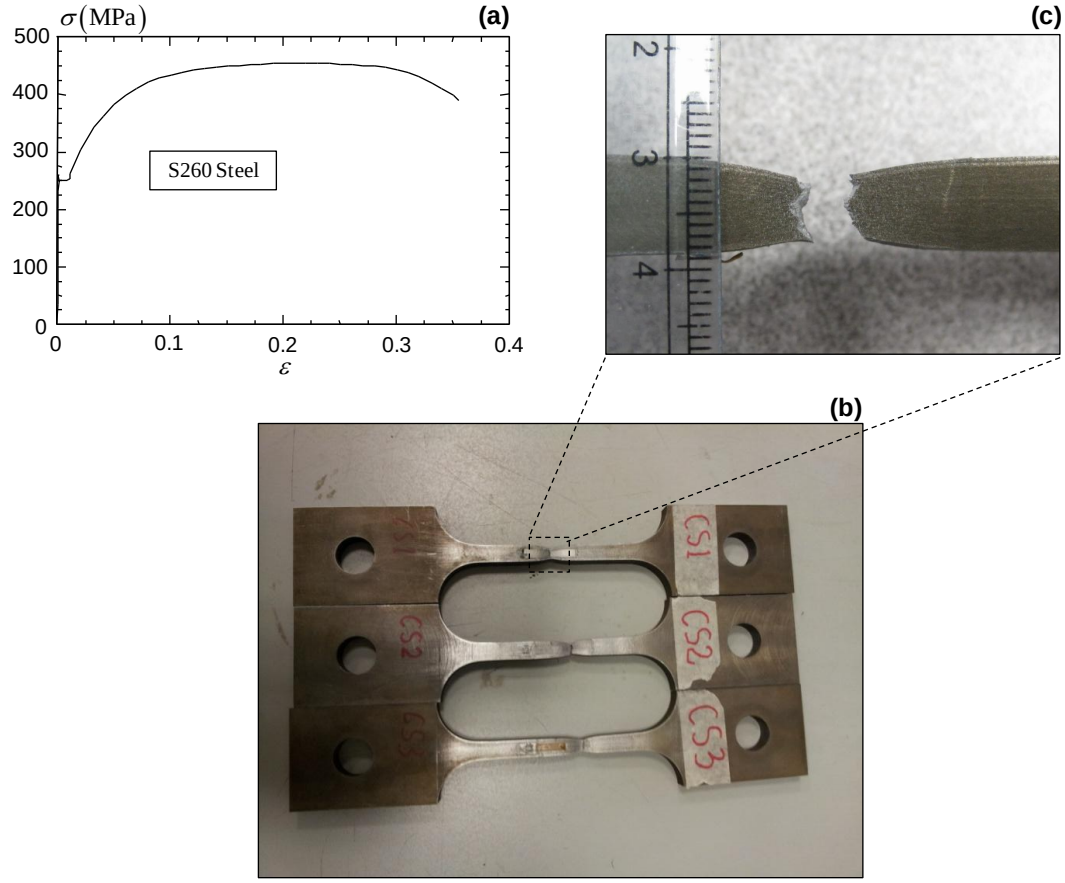

Fig. 7.2: (a) Uni-axial engineering stress-strain relationship for the S260 material; (b) tension specimens after the coupon test; and (c) close-up view of the necked section.

Table 7.2: Comparison of the mechanical properties of the selected steel material and the steel in K-frames.

Steel	E (GPa)	Yielding strength (MPa)	Tensile Strength (MPa)	Elongation
BS3602-430-ERW	207	275	-	36%
Selected steel S260	207	254	456	35%

7.2.2 Fracture Resistance *J-R* Curve Test

The fracture resistance J-R curve test measures a continuous fracture toughness J-value versus crack-extension relationship (ASTM E1820, 2011) for the steel material. The test requires continuous measurement of force versus load-line displacement or crack mouth opening displacement. A J-R curve will form if any stable tearing response occurs. The specimen firstly experiences a cyclic loading to generate a natural sharp crack. The test then utilizes the elastic-compliance method, where multiple points are determined from a single specimen. The elastic-compliance performs an unload/reload sequence during the test and measures the compliance to estimate the corresponding crack size. Each point represents a J-Δa pair at each unload/reload step, where J-value derives from the summation of the elastic component J_{el} and the plastic component J_{pl} while Δa refers to the difference between the current crack size and the original crack size. The post-test analysis constructs the J-R curve using a regression line based on qualified data-points.

Past research observes a conservative result from the single-edge-notched bend, SE(B), specimen compared to those from tensile loading configurations. The current fracture toughness test consists of four single-edge-notched bend, SE(B), specimens, fabricated from the same plate with the axial tension specimens. All the SE(B) specimens follow the same rolling direction to maintain the consistent material mechanical property. Figure 7.3 illustrates the configuration of the SE(B) specimen. The SE(B) specimens tested include two different thicknesses, $B = 25.4$ mm (1 inch) and $B = 50.8$ mm (2 inches), with the width to the thickness ratio, W/B, of 2.0 and 1.5 respectively. The length to the width ratio, L/W equals 4.5 for all specimens. Each geometry contains two duplicate specimens. The side groove in the SE(B) specimen reduces the net thickness B_N to 80% of the original thickness B to facilitate uniform crack extensions across the thickness. All the specimens tested have a prefabricated notch, $a_{notch}/W = 0.4$, with machined knife edges (see Fig. 7.3) at the crack mouth to host the displacement gage during the

experiment.

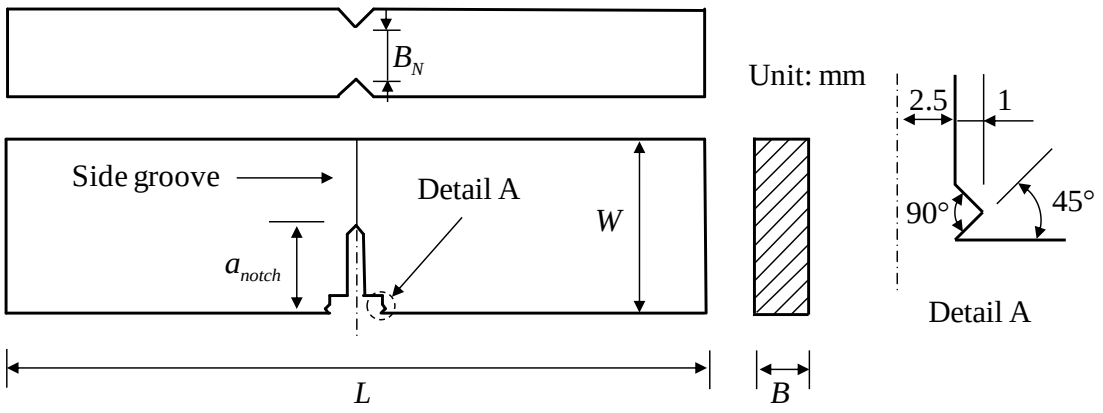

Fig. 7.3: Configuration of the single-edge-notched bend, SE(B) specimen.

The test setup, as indicated in Fig. 7.4, applies a vertical load at the middle of the specimen, while two ends sit on two support rollers. The experimental procedure utilize a cyclic fatigue pre-cracking loading to produce the sharp fatigue crack. The description outlined in ASTM E-1820 (2011) limits the maximum stress intensity factor applied to the specimen during the fatigue precracking process by:

$$K_{MAX} = 0.063\sigma_y \text{MPa}\sqrt{\text{m}} \tag{7.1}$$

In Eq. 7.1, σ_y refers to the material yield strength in MPa. Table 7.3 lists the information about the cyclic loading for two sets of specimen. The final crack length remain between 0.45 and $0.70W$ for J determination, as described in ASTM E-1820 (2011). After the fracture resistance test, each specimen experiences the heat tinting at about 300°C for 30 min to mark the ductile tearing crack, followed by the careful breaking to expose the fracture surface under a subzero temperature.

Figure 7.5 represents the load versus the crack opening displacement (COD) curve, recorded during the experiment, for the tested specimens with two different thickness. The experiment for the thin specimen with the thickness $B = 25.4$ mm observes a stable

Table 7.3: Information for the cyclic loading during the fracture toughness test.

Specimen	Cyclic loading range	Frequency	Fatigue crack length	NO. of cycles
25.4 mm (1 inch)	$1 \sim 11$kN	5HZ	11.5 mm	350,000
50.8 mm (2 inches)	$14 \sim 26$kN	5HZ	8.5 mm	130,000

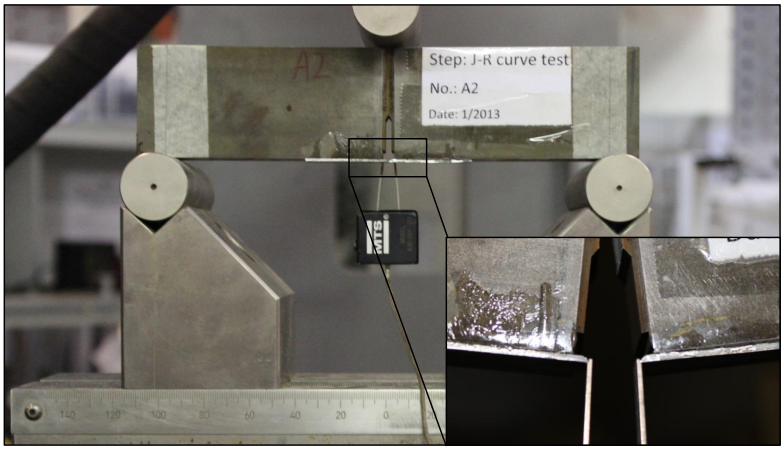

Fig. 7.4: Test set-up for the single-edge-notched bend, SE(B) specimen.

ductile tearing, as indicated in Fig. 7.6a by the crack surface after the specimen breaking. The test for the thick specimen records a combination of the ductile tearing followed by the brittle fracture. The crack propagates stably beyond the peak load under the displacement controlled loading, followed by a brittle fracture with a fast crack propagation along the original crack front accompanied with a loud sound. The test continues to increase the applied displacement until the COD gauge becomes out of range. The specimen shows the second stage of the ductile tearing, as indicated in Fig. 7.6b by the smooth surface after the coarse surface induced by the brittle fracture.

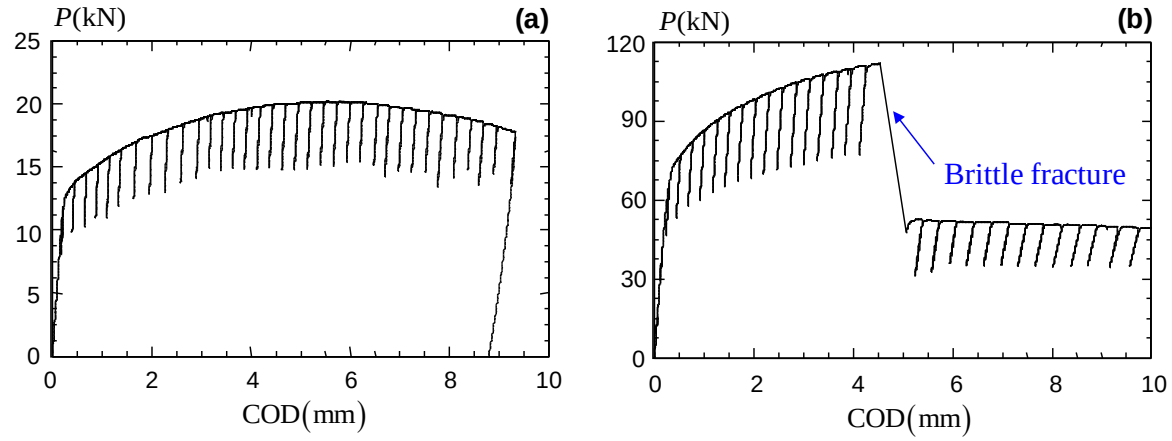

Fig. 7.5: Load versus crack opening displacement (COD) curve of the tested SE(B) specimen with the thickness: (a) $B = 25.4$ mm and (b) $B = 50.8$ mm.

The exposure of the crack surface after the specimen breaking, as shown in Fig. 7.6, shows different surface characteristics corresponding to specific crack formation process. The fatigue pre-crack surface exhibits a quite flat plane in the macroscopic scale due to the small magnitude of cyclic loads. The stable ductile tearing generates a macroscopically flat and opaque surface which is full of dimples due to the growth of microvoids (Anderson, 2004). The fast unstable fracture leaves a macroscopically rough but reflective plane which indicates the tiny flat surface in the microscopic scale.

Figure 7.7 represents the measured fracture resistance J-R curve in the current test,

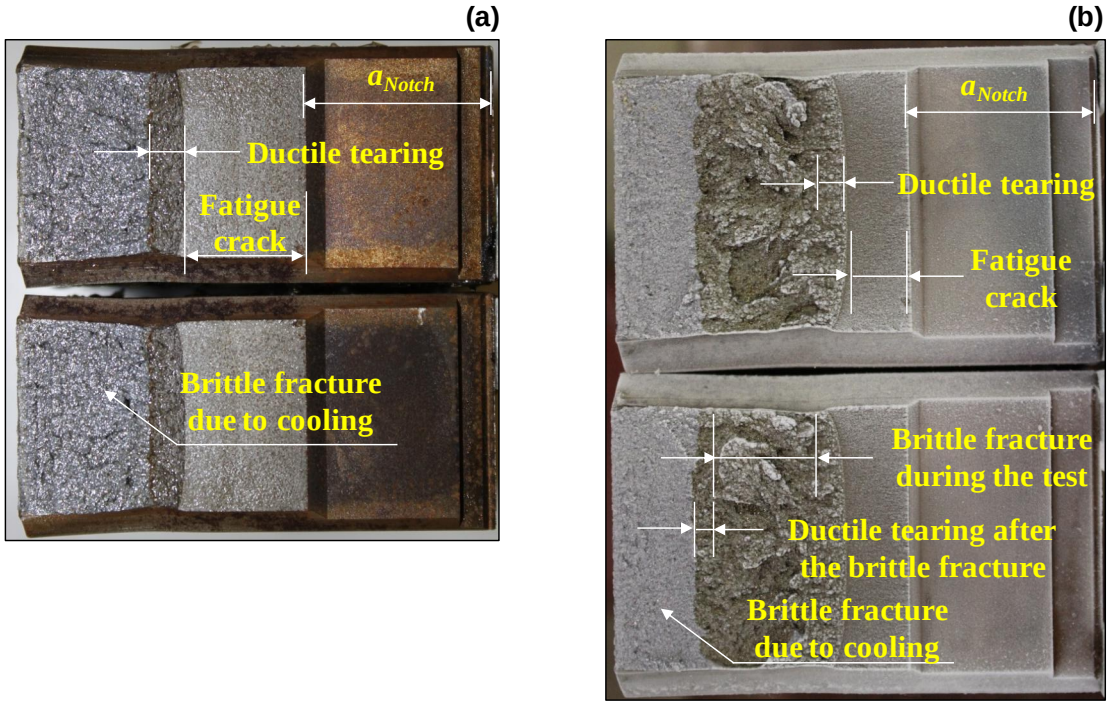

Fig. 7.6: Fracture surface after the breaking under the subzero temperature for the SE(B) specimen with the thickness: (a) $B = 25.4$ mm and (b) $B = 50.8$ mm.

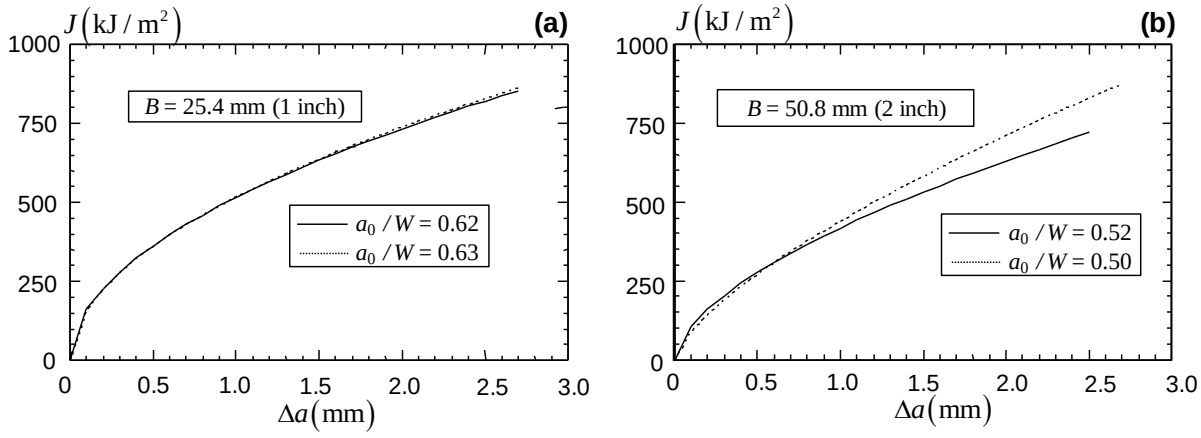

Fig. 7.7: Fracture resistance curve obtained from the SE(B) specimen with thickness: (a) $B = 25.4$ mm and (b) $B = 50.8$ mm.

where different fatigue pre-crack lengths induce slightly different a_0/W ratios. The J-Δa curves in Fig. 7.7a exhibit close agreement in the initial and rising portion between two specimens with the same thickness $B = 25.4$ mm. For the thick specimens, $B = 50.8$ mm, the current study employs the load versus COD curve before the brittle fracture occurs (as in Fig. 7.5b). The deviation of the J-Δa curves between two thick specimens becomes larger as the crack extension increases, as shown in Fig. 7.7b. Table 7.4 lists the critical fracture toughness, J_{IC} values, obtained from the 0.2 mm offset line, following the procedures outlined in ASTM E-1820 (2011). The J-R curve obtained from the $B = 50.8$ mm specimens shows reduced fracture resistances with the crack extension, as indicated by a lower value of J_{IC} in Table 7.4. Table 7.4 also shows the J_{max} value, corresponding to the 1.5 mm offset line, beyond which the J-Δa curve violates the small-scale yielding assumption and becomes invalid (ASTM E1820, 2011).

Table 7.4: Measured fracture toughness J_{IC} in the SE(B) specimen for S260 steels.

Specimen	B(mm)	a_0/W	J_{IC}(kJ/m^2)	$J_{\Delta a=1.5\text{mm offset}}$(kJ/m^2)
A1	25.4	0.62	485	855
A2	25.4	0.63	486	865
B1	50.8	0.52	330	723
B2	50.8	0.50	332	860

7.3 Verification of the Proposed Joint Representation for BOMEL K-Frames

Bolt *et al.* (1995) report an experimental test on the behavior of 2D large-scale K-braced frames under static loading. Figure 7.8 sketches the detail dimensions for three of the tested frames (Frame VII, VIII, and X), which employ similar frame geometries

but different local joint geometries. All the frames incorporate an intact weak gapped K-joint with an increasing gap ratio from Frame VII to Frame X. During the loading procedure, the frame remains pin connected at the base to a triangulated test rig. The experimental procedure applies a monotonically increasing horizontal load at the top of the frame until the critical joints and members deform significantly and the residual strength of the overall frame is obtained. For all the three frames shown in Fig. 7.8, the unstable fracture failure in the K-joint proves to be the dominant failure mode and leads to significant reductions in the frame resistance.

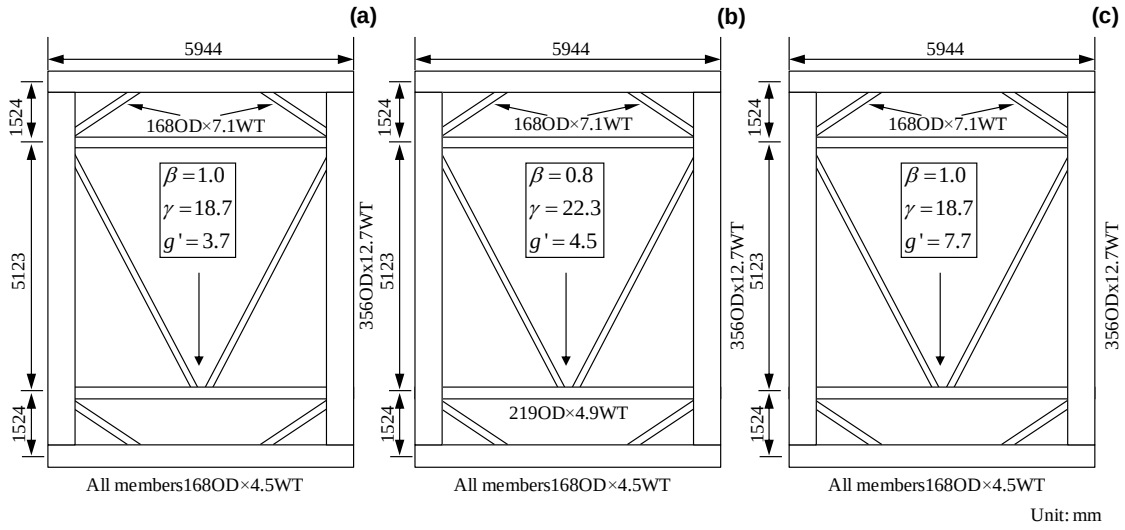

Fig. 7.8: Configuration of 2-D K-frames: (a) Frame VII; (b) Frame VIII; and (c) Frame X.

The current study proves the robustness of the proposed joint formulation through the nonlinear pushover analysis by coupling the fracture toughness obtained from the above section with the joint fracture formulation. The K-joint load-deformation behavior under the balanced brace axial loading in the integrated joint formulation follows the nonlinear joint representation described in Chapter 4, before the initiation of the ductile tearing corresponding to which the joint has experienced sufficient crack extension to trigger apparent reductions in the joint capacity. The load-deformation characteristics during

the ductile tearing derives from the joint fracture formulation (as mentioned in Chapter 6), which defines a unique relationship between the energy release rate level and the joint resistance level through the fracture resistance J-R curve of the joint chord material. The current study utilizes the critical fracture toughness, J_{IC}, for the thin specimen with the thickness $B = 25.4$ mm, and employs the $J_{\Delta a=1.5\text{mm offset}}$ as J_{max} in the joint fracture formulation. The η approach, as proposed in Chapter 5, estimates the energy release rate level purely based on the joint load versus the load-line displacement curve.

The pushover analysis, performed in the current study, employs USFOS (2009) to incorporate the nonlinear joint behavior as user-define nonlinear spring elements between the brace member and the chord member. By representing each individual member based on the exact solution of the beam-column governing equation subjected to end-forces, USFOS allows accurate representations of each physical member with a single element. The calibration process contains four types of joint formulation:

1. rigid joint analysis,
2. default MSL joint formulation (available in USFOS (2009)),
3. MSL joint crack formulation (available in USFOS (2009)),
4. the proposed joint formulation.

The default MSL formulation derives from parametric investigations benchmarked against the load-shedding behavior for the single joint in Frame VII (MSL, 2000). Based on the curve fitting of the global frame behavior, the default MSL joint formulation employs a ductility limit of $0.06d_0$ and 33% of joint capacity as the residual joint strength (MSL, 2000). The MSL crack formulation, on the other hand, limits the joint axial displacement by,

$$\frac{\delta}{d_0} = 0.026 \tag{7.2}$$

which prescribes a CHS K-joint fracture criterion solely proportional to the chord diameter while ignoring the effect from the chord wall thickness and the joint gap region.

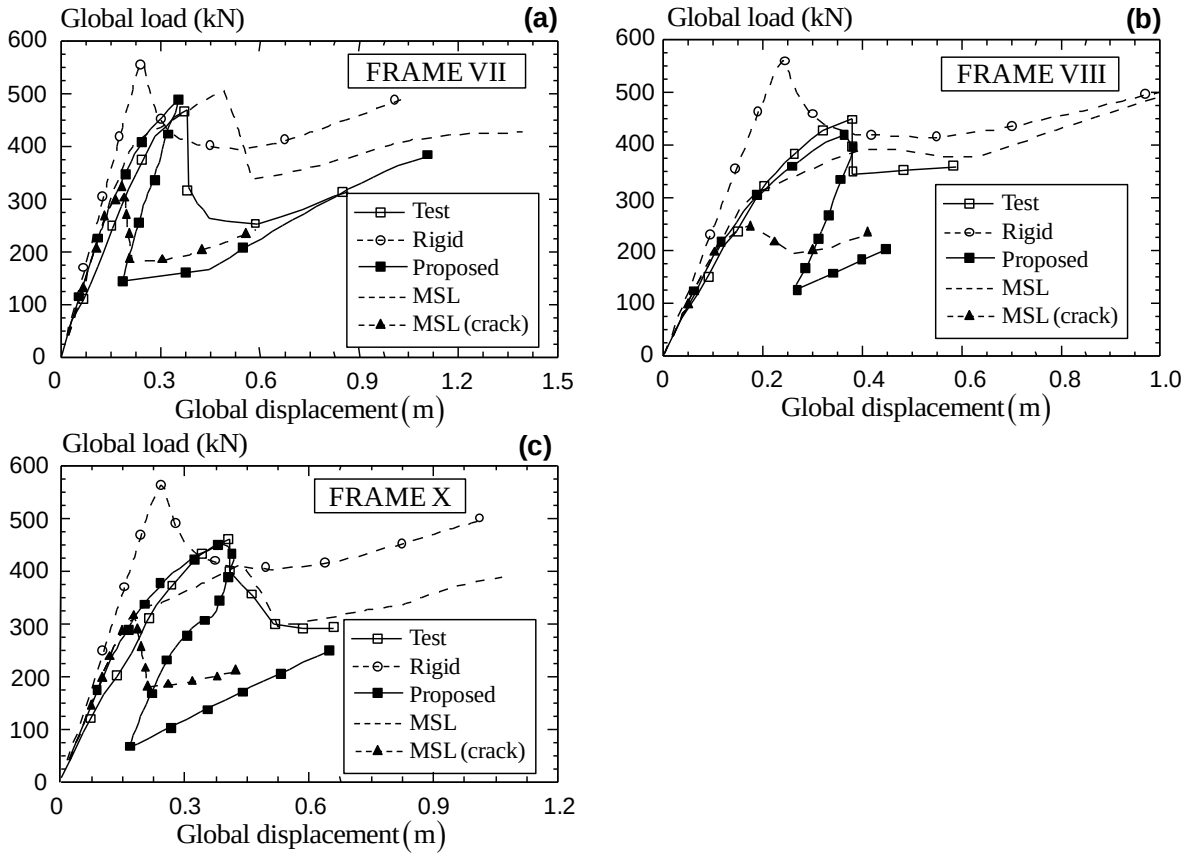

Fig. 7.9: Comparison of the experimentally measured load-displacement responses with numerical analyses based on different joint formulations for: (a) Frame VII; (b) Frame VIII; and (c) Frame X.

Figure 7.9a shows the predicted frame behavior using different joint formulations, compared with the test results for Frame VII. The experiment observes the yielding of the weak K-joint with plastic deformations in the chord material near the compression side, followed by further plastic deformations concentrated at the tension side. The subsequent loading initiates a crack near the weld toe of the tension brace, at the crown point in the chord gap region. The crack propagates rapidly around the weld toe generating an

abrupt and significant reduction in the joint capacity, which leads to a global unloading of the K-frame (Bolt, 1995). Without considering the local joint flexibility and the joint yielding, the rigid joint does not describe the joint fracture failure. Therefore, the rigid joint assumption predicts a high frame stiffness followed by the compression brace buckling. Both the default MSL joint formulation and the proposed joint formulation predict successfully the decrease in the global frame stiffness caused by the weakening of the K-joint. However, the MSL crack formulation derives from the empirical ductility limit and generates an early frame unloading behavior. The proposed joint formulation provides a good estimation of the frame collapse mechanism governed by the joint failure. The employment of J_{max} as the threshold, beyond which the joint unstable fracture occurs, provides a conservative estimation of the joint ductility.

Frame VIII employs an increased chord diameter which leads to a lower β ratio but a larger gap ratio compared to Frame VII, as shown in Fig. 7.8b. The finding in Chapter 5 demonstrate that, for CHS K-joints, the elastic-plastic crack driving force increases with the reduced β ratio, but decreases with the increasing gap ratio. The counterbalance of these two effects generates a similar frame ductility limit, corresponding to which the frame fracture failure occurs for Frame VII and VIII. Without considering the local weak joint effect, the rigid joint assumption generates a nearly identical curve (shown in Fig. 7.8b) as that of Frame VII (shown in Fig. 7.8a). The default MSL joint formulation assumes a joint ductility limit proportional to the chord diameter. Therefore, the default MSL joint formulation predicts the weakening of the joint, followed by a more ductile frame response than that observed in the test. Similarly, the early occurrence of the fracture failure in the MSL crack formulation leads to an unrealistically small frame resistance, as shown in Fig. 7.8b. The proposed joint formulation predicts closely the progressive deterioration in the frame response caused by the ductile crack extension. The proposed joint formulation also provides accurate estimations on the peak capacities

of Frame VIII, followed by a conservative evaluation on the residual strength of the frame.

Compared with Frame VII, Frame X utilizes the same β ratio but a larger gap ratio. The more ductile behavior of Frame X, as compared with Frame VII, proves the decrease in the crack driving force with an increasing joint gap ratio for gapped K-joints (as described in Chapter 5). Without considering the locked-in forces generated in the experimental test, all the weak joint formulations provide a slightly higher frame stiffness than that observed in the test. The early prediction of the joint yielding in the default MSL joint formulation generates a pronounced reduction in the global frame stiffness. The proposed joint formulation shows a relatively close estimation on the peak frame resistance, followed by a significant unloading caused by the unstable fracture failure. The proposed method assumes conservatively zero-residual strength of the tubular joint beyond the unstable fracture failure. Based on the strength estimation for the cracked joint, this corresponds physically to a complete separation between the tension brace and the chord member of the K-joint. This assumption thus leads to severe under-estimations of the post-peak resistance of the single-panel K-frames without locked-in redundancies, as reflected by the comparisons in Fig. 7.9. The proposed formulation therefore focuses mainly on the accurate prediction pre-peak responses (including the global stiffness and the peak resistance) of tubular steel frames with predominantly unstable fracture failure in the joint.

7.4 Behavior of Offshore Structures

Many old jacket structures employ K-brace as a major framing pattern sustaining the large deck gravity loading and wave forces (Zettlemoyer, 2010). The current section illustrates the effect of the local joint behavior to the global structure response through the pushover analysis of a realistic platform located in the Gulf of Mexico. The 4-legged

platform, denoted as Platform A, fails to sustain the significant wave force generated during the hurricane Rita (Energo, 2007). The post-hurricane investigation observes a completely toppled platform lying on the seafloor with no structure visible above the sea surface.

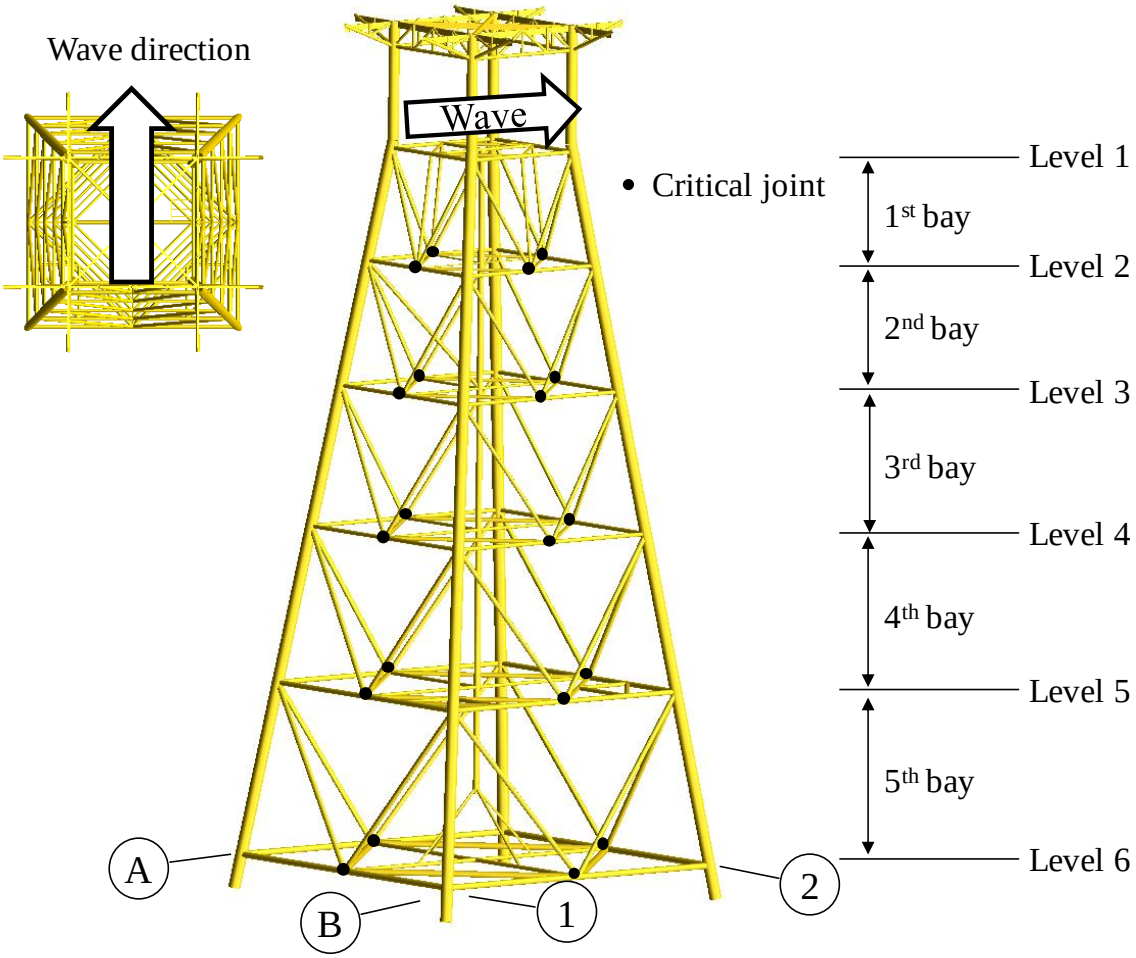

Fig. 7.10: Configuration of Platform A.

Figure 7.10 shows an overall view of Platform A modelled in USFOS. The pile supported platform employs five bays of K-braced configuration, with weak gapped K-joints $g' = 2.0$ at each bay, in the water depth of 66 m. The platform includes only one conductor supported at each horizontal framing level. The model consists of four levels of deck structure, with the lowest deck bottom located at 15.3 m above the mean sea level. The

member diameter ranges from 1.14 m for legs to 0.3 m for horizontal bracing members. The yield strength is kept 235MPa for all member materials.

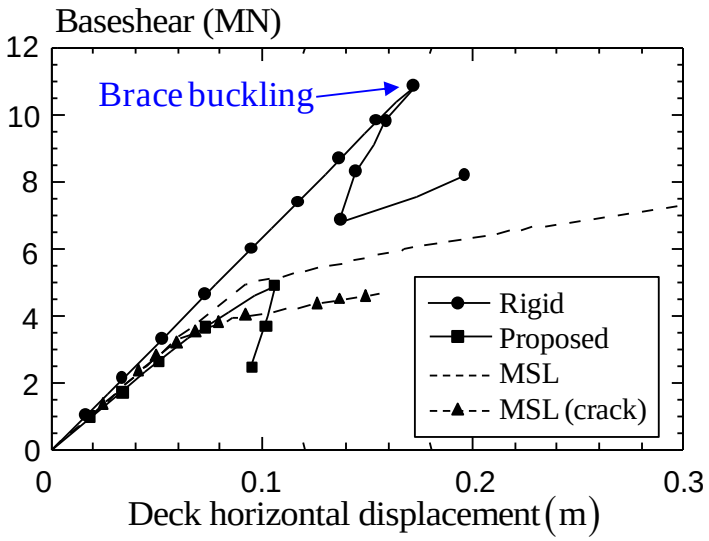

Fig. 7.11: Load-deformation responses of Platform A using different joint formulations.

The environmental information in the current study follows the wave data predicted during the hurricane Rita, where the wave height is 12.2 meters and the wave period is 14.25 seconds. The wave force derives from Morrison equation based on the kinematic information calculated using the first order 2D Newwave (Tromans *et al.*, 1991). The present model increases the leg thickness to reflect the composite effect between grouted legs and piles. The bottom nodes of four legs remain pin-supported as a further investigation finds very little effect from the foundation. The pushover analysis increases the horizontal wave force in every load step with a fixed gravity loading. The present model treats all the gapped K-joints as critical joints, as indicated in Fig. 7.10. Due to lack of detail material mechanical property data, the current study employs the fracture resistance J-R curve of the steel material S260 obtained in the previous section.

Figure 7.11 compares the base shear versus the load-line deck displacement curves for Platform A using different joint formulations. Table 7.5 lists the structure baseshear

Table 7.5: Jacket baseshear capacity corresponding to the first component (member or joint) failure.

Joint formulation	Jacket Baseshear capacity(MN)	Weak joint/Rigid joint
Rigid joint	10.9	1.00
Proposed	4.9	0.45
MSL	4.9	0.45
MSL(crack)	3.3	0.30

capacity corresponding to the first component (member or joint) failure. The rigid joint predicts a brittle frame response dominated by a sequence of compression brace bucklings. The perfect joint assumption fully develops the member capacity and predict a high jacket ultimate strength. By incorporating the local joint effect, weak joint formulations provide lower platform capacities with a sequence of K-joint failure. MSL joint formulation predicts more than 50% lower of the ultimate strength than that from the rigid joint assumption, followed by a ductile response. MSL joint crack formulation shows a even lower structure capacity by introducing the joint failure at an early stage. The proposed joint formulation captures the same global stiffness and failure mechanism as those from MSL formulations. The fracture failure in the proposed joint formulation leads to a total loss of the structure capacity. The comparison of the four joint formulations shows a considerable over-prediction of the structure capacity and a totally different global response caused by the rigid joint assumption.

7.5 Conclusion

This chapter proposes an integrated joint formulation based on the result obtained in the previous chapters to represent the load deformation behavior for CHS K-joints under the balanced axial loading in the global pushover analysis. The fracture toughness test pro-

vides mechanical properties for the equivalent BOMEL frame material. The calibration against the BOMEL frame tests demonstrates the validity of the proposed joint model. The extension to a realistic jacket structure proves the applicability of the proposed joint formulation. The study summarized above supports the following conclusions:

1. The fracture toughness test shows a dependence of critical fracture toughness J_{IC} on thickness existing for the current test steel material. The SE(B) specimen with the thickness $B = 50.8$ mm exhibits a combination of ductile tearing and brittle fracture process under the displacement controlled loading. Different crack formation processes leads to different crack surface characteristics.

2. The joint formulation provides a convenient approach to estimate the nonlinear joint behavior as well as the load-deformation relationship under the ductile tearing for CHS K-joints. The comparison between the frame analyses with various joint formulations and the experimental data demonstrates the significance of the nonlinear load-deformation joint behavior in the K-frame response. The comparison of the global responses from different frame patterns implies the dependency of the joint unstable fracture failure on the joint geometry. The pushover analysis of a realistic offshore platform shows the significant effect of the joint formulation on the global structure behavior.

Chapter 8

Conclusions

8.1 Brief Overview

This study proposed a new joint load-deformation formulation for CHS X- and K-joints, based on numerical investigations with judicious calibrations against test results, to be implemented in the pushover analysis for offshore frames. The joint representation describes the behavior of the as-welded X- and gapped K-joint with the joint brace-to-chord diameter ratio (β) ranging from 0.3 to 1.0, the chord radius-to-thickness ratio (γ) varying from 7 to 25, and the gap between the two brace weld toes over the chord wall thickness ratio (g') changing from 2 to 10. The study aims to incorporate the proposed joint formulation into the analysis of the frame response to account for the nonlinear joint behavior.

The numerical simulation benefits from a finite element procedure, which transfers the mesh generated by Patran Command Lauguage (Patran, 2012) into another finite element package ABAQUS (2012) for the computation and post-processing. The subsequent discussion establishes the proper mesh density, element type, boundary condition and material properties for the finite element models to generate effective and accurate results

as compared to those from the reported experimental tests. To incorporate the joint fracture failure as reliable phenomenological representations, the study thus investigates different numerical techniques to compute the domain integral, J-value, for cracks located at hot-spot positions in CHS joints. The discussion focuses on two intuitional modeling processes: continuous mesh and mesh-tie.

To represent an accurate nonlinear relationship for the load-deformation responses of CHS X- and K-joints, including both the elastic and elastic-plastic responses, the study proposes a new C^2 continuous function, where the change in the joint stiffness remains continuous before any unstable failure occurs. The proposed formulation describes the load-deformation relationship of the CHS X- and K-joint through a simple function with the coefficients dependent on the ultimate strength and the geometric parameters of the joint. The strength-dependent parameter follows the mean strength equations in the latest IIW recommendations (IIW, 2009), while the geometric-dependent parameters derive from the finite element results of the CHS X- and K-joints covering a practical geometric range. This study compares the predictions of the critical joint deformation at the peak load and the initial joint stiffness derived from the proposed joint formulation with the reported studies (Choo *et al.*, 2005; Lu *et al.*, 1994) to ensure that the proposed formulation provides reliable estimations on these important parameters. For X-joints under brace axial compression, the joint formulation includes the re-development of the joint strength occurs at a large deformation level due to the direct contact of the compression braces. The study also validates the accuracy of the proposed formulation, which is implemented in a nonlinear pushover analysis as joint-spring elements, against the experimental results reported by Bolt *et al.* (1994), Kurobane *et al.* (1986), and Bolt and Billington (2000).

To extend the joint formulation to represent the joint behavior under the fracture failure, the study utilizes the elastic-plastic crack driving force to characterize the status of cracks located at hot-spot regions. To avoid the complex pre-processing work and

substantial computational resources required in the existing J-integral evaluation methods, the current study proposes an energy-based η approach. This approach evaluates the elastic-plastic energy release rate using the area under the load versus the load-line displacement curve for large-scale tubular X- and K-joints, similar to the conventional η approach used to calculate the energy release rate for fracture specimens described in material testing standards (ASTM E1820, 2011). The parametric study compares the energy release rate level for CHS joints with different geometries. The effective width (B_{eff}), via which the remaining ligament area (A_{lig}) is calculated, depends on the joint geometry. The study also compares the prediction of the elastic-plastic crack driving force computed from the plastic η approach with the proposed effective width B_{eff} with those from the domain-integral approach.

Coulpled with the nonlinear joint formulation and the η approach, the subsequent study presents a new fracture formulation to describe the ductile tearing and unstable fracture failure for circular hollow section (CHS) joints under monotonically increasing brace tension. The initiation of ductile tearing occurs when the crack driving force in an assumed initial shallow crack reaches the material fracture toughness determined from a standard fracture toughness test. The joint behavior prior to the ductile crack initiation follows a previously proposed nonlinear formulation based on the latest strength equations recommended (IIW, 2009). The load-deformation characteristics beyond the crack initiation assume that the energy release rate and the amount of crack extension adhere to the experimentally measured J-R curve, prior to the unstable fracture failure. Coupling an area reduction factor for cracked joints with a previous proposed η approach, the current study derives the load-deformation relationship for a tubular joint with an extending crack. Unstable fracture, which leads to the total loss of the joint capacity, occurs when the crack driving force reaches the maximum fracture resistance determined from the 1.5 mm offset line in the J-R curve test.

To validate the proposed joint fracture formulation with large-scale frame experimental results reported by Bolt *et al.* (1995), the current study conducts the fracture toughness test for the steel material of BOMEL K-frames, due to lack of the fracture resistance curves in the literature review. The fracture toughness test, following the material test standard (ASTM E1820, 2011), utilizes four single-edge-notched, SE(B), specimens, cut from the same plate with S260 steels. The test reports the yield strength, Young's modulus and fracture resistance J-R curve for S260 steels which satisfy the material requirement prescribed for the BOMEL steel pipe. The subsequent study compares the proposed joint fracture formulation with existing joint models by the verification against reported BOMEL K-frames (Bolt, 1995). The study also discusses the applicability of the proposed joint formulation to a realistic jacket structure.

8.2 Major Findings and Significance

The research work carried out for CHS X- and K-joints in the current study supports the following conclusions and observations:

1. The mesh-tie method proposed by Qian *et al.* (2005) offers a convenient approach to compute the energy release rate for surface cracks in tubular joints with a complex topology. The comparison of this approach against the continuous mesh technique (Bowness and Lee, 1995) shows good agreement in the domain integral between two methods. The isolation of the local crack front model exempts the tedious mesh transition procedure and permits the model of a complex global model.

2. For CHS joints, the load versus load-line displacement characteristics depend significantly on joint geometries. Thin wall joints with a larger γ ratio create pronounced variations in the joint resistance with increasing joint deformation. As the β ratio approaches 1.0, the dominant membrane action leads to a much higher joint capac-

ity, thus a larger variation of the joint resistance than that of a small β joint under dominant bending actions in the chord wall.

3. The proposed nonlinear joint formulation provides a convenient method to estimate the load-deformation relationship for CHS X- and K-joints before the joint resistance is limited by the material ductility. The parametric formulation eliminates the need for the elastic-plastic, large-deformation finite element analyses on CHS X- and K-joints. The proposed formulation, implemented as joint-spring elements in the frame analysis, provides close predictions on both the failure modes and the ultimate strength for 2-D and 3-D tested frames. The verification against the frame test results, reported by Bolt *et al.* (1994), Kurobane *et al.* (1986), and Bolt and Billington (2000), and various joint formulations demonstrates the significance of the nonlinear load-deformation joint behavior in the frame response, especially for simple 2-D frames with low redundancy.

4. For CHS joints with weld-toe surface cracks, the joint geometry plays a significant role on the crack driving force level at the deepest crack front location. For K-joints under brace balanced axial forces, the elastic-plastic crack driving force increases with reduced β ratios due to the decreasing weld length and the higher bending effect in the chord wall material. The J-value shows a small variation with respect to γ ratios due to the balance between the chord wall compliance and the remote loading. For joints with small gap ratios, the limited chord material between crown points constrains the plastic deformation within a localized region near the crack surface and leads to a higher crack driving force. For CHS X-joints under brace axial tension loading conditions, the elastic-plastic crack driving force increases with respect to the increased β ratios due to the concentration of the load transition area at the saddle point of the chord material between two tensile braces. Smaller γ ratios with a larger wall thickness generate the larger J-value through an increased remote

brace loading under the same applied displacement.

5. The current study extends the conventional plastic η approach for simple 2-D fracture specimens with through thickness cracks to large-scale 3-D tubular joints with surface cracks. Following the linear dependence of the cracked joint strength on the remaining intact area, established by previous experimental and numerical investigations for surface cracked tubular joints, the η_{pl} value equals 1. The plastic η approach with the proposed effective width B_{eff}, shows a close prediction of the elastic-plastic crack driving force compared with the domain-integral J-values. The plastic η approach provides a convenient alternative to estimate the J-values for cracked tubular K and X-joints using solely the load versus the load-line displacement curve. The strong correlation between the elastic-plastic crack driving force and the joint plastic work provides a theoretical base for the plastic limit approach (Choo *et al.*, 2003) and proves the plastic work as a possible criterion for establishing a ductility limit for tubular joints.

6. For K-joints with cracks located at the crown joint at the tension brace weld toe, the presence of a shallow surface crack shows a marginal effect on the global joint stiffness due to the stress redistribution along the brace-to-chord intersection area. At large deformations, the presence of the surface crack at the crown point deviates the load-displacement curve of the cracked joint from that of an intact joint. The load-displacement of the cracked K-joints shows strong correlations with the crack area while exhibits insensitive dependence on the different crack aspect ratios, a/c.

7. The current study proposes a new joint fracture formulation to describe the weakening of the joint resistance caused by the ductile crack extension, as well as the significant resistance reduction induced by unstable fracture failure. The proposed joint fracture formulation utilizes the elastic-plastic crack driving force, J-integral,

to characterize the initiation of the ductile tearing and the subsequent fracture failure after a limited amount of crack extension. The proposed joint formulation assumes an initial crack size to determine the onset of ductile crack extension at $J = J_{IC}$ for intact joints. The joint resistance during the stable ductile tearing process follows the joint capacity coupled with the an area reduction factor A_{RF}. During the crack extension, the crack driving force versus the crack extension relationship at the deepest crack-front location adheres to the J-R curve measured from a high-constraint fracture specimen. This approach estimates closely the deterioration in the joint strength as the crack extends, as demonstrated by the comparison against the experimental results on tubular joints. The proposed joint formulation assumes the occurrence of the joint unstable brittle failure at $J = J_{max}$ with a total loss of the joint resistance. The close agreement in the load-deformation behavior with the reported joint (Qian *et al.*, 2012, 2013; Wang *et al.*, 2000) proves the validity of the proposed joint fracture formulation.

8. The joint formulation, coupled with the nonlinear joint formulation and the η approach, offers a convenient approach to provide accurate assessments on the nonlinear frame response caused by the unstable fracture in the K-joint. The comparison of the global responses from different frame patterns, reported by Bolt *et al.* (1995), implies the sensitive dependence of the joint unstable fracture failure on the joint geometry. The pushover analysis of a realistic offshore platform shows the significant effect of the local joint behavior on the global structure behavior.

8.3 Future Work

The current study investigates the behavior of uni-planar X- and gapped K-joints. Some old platforms employ overlapped K-joints, where one of two braces is welded circumfer-

entially to the outface of the chord and the other brace. This application derives from Bouwkamp's (1968) research that if the overlap eccentricity relative to the chord centerline remains one-quarter of the diameter, the joint strength would dramatically improve. The fabrication procedure fits up both braces, followed by welding the exposed seam between members. The process leaves the hidden unwelded curve at the toe of the through brace. The partial connection between the brace and chord will cause severe stress concentrations under the remote brace loading. So far, the load-deformation behavior of these overlapped joints remains unknown and requires further investigation.

The current study conducts the fracture toughness test for S260 steels. During the experimental test, thick specimens, $B = 50.8$ mm, show fracture failure after certain amount of ductile tearing under the room temperature. Under the displacement controlled manner, the total fracture of the specimen does not occur. Specimens continues to experience certain amount of ductile tearing. Due to the insufficient database, the current study can not conclude a definitive fracture toughness, J-value, corresponding to which the fracture failure occurs. The internal mechanism of the unstable crack extension also remains unknown and requires further study.

Offshore structures often sustain cyclic wind and waves loadings. Depending on the location, earthquake loading remains of special concern to some structures. Frame behavior under cyclic and dynamic loading needs further study. The joint characteristics under cyclic and dynamic loading should be investigated in order for a correct prediction of the structure responses.

References

ABAQUS, 2012. ABAQUS/Standard: user's manual. Hibbitt, Karlsson & Sorensen.

Alanjari, P., Asgarian, B., Kia, M., 2011. Nonlinear joint flexibility element for the modeling of jacket-type offshore platforms. Applied Ocean Research 33 (2), 147–157.

Anderson, T. L., 2004. Fracture mechanics: fundamentals and applications, 3rd Edition. CRC Press.

API, 2010. Recommended practice for planning, designing, and constructing fixed offshore platforms. API RP2A-LRFD. American Petroleum Institute.

ASTM E1820, 2011. ASTM E1820-11 Standard test method for J-integral characterisation of fracture toughness. American Society of Testing and Materials (ASTM) International.

ASTM E8/E8M, 2011. ASTM E8/E8M-11 Standard test method for tension testing of metallic materials. American Society of Testing and Materials (ASTM) International.

AWS, 2012. Structural Welding Code-Steel, ANSI/AWS D1.1-98 Edition. American Welding Society.

Billington, C., Lalani, M., Tebbetl, I., 1982. Background to new formulae for the ultimate limit state of tubular joints. In: Offshore Technology Conference, 3-6 May 1982, Houston, Texas.

Bolt, H., 1995. Results from large scale ultimate strength tests of K-braced jacket frame structures. In: Offshore Technology Conference, 1-4 May 1995, Houston, Texas.

Bolt, H., Billington, C., 2000. Results from ultimate load tests on 3D jacket-type structures. In: Offshore Technology Conference, 1-4 May 2000, Houston, Texas.

Bolt, H., Billington, C., Wardenier, J., 1994. Results from large-scale ultimate load tests on tubular jacket frame structures. In: Offshore Technology Conference, 1-4 May 1995, Houston, Texas.

BOMEL, 1992. Analytical and experimental investigation of the behavior of tubular frames. phase II. part 4: summary and conclusions from phase I and phase II. Joint industry funded research programme, Billington Osborne-Moss Engineering Limited (BOMEL).

Bouwkamp, J., 1968. Behavior of tubular truss joints under stacit loads. College of Civil Engineering, University of California.

Bouwkamp, J., Hollings, J., Maison, B., Row, D., 1980. Effects of joint flexibility on the response of offshore towers. In: Offshore Technology Conference, 5-8 May 1980, Houston, Texas.

Bowness, D., Lee, M., 1995. The development of an accurate model for the fatigue assessment of doubly curved cracks in tubular joints. International Journal of Fracture 73 (2), 129–147.

Bowness, D., Lee, M., 1998. Fatigue crack curvature under the weld toe in an offshore tubular joint. International Journal of Fatigue 20 (6), 481–490.

BS7910, 2005. Guidance on methods for assessing the acceptability of flaws in metallic structures. British Standards Institution.

Buitrago, J., Healy, B. E., Chang, T., 1993. Local joint flexibility of tubular joints. In: 12th International Conference on Offshore Mechanics and Arctic Engineering (OMAE). Vol. 1. pp. 405–411.

Burdekin, F., Yang, G., Cao, J., 1998. Assesssment of fracture strength of cracked tubular joints. Offshore Technology Report OTH 554, Health and Safety Executive.

Cao, J., Packer, J., Yang, G., 1998a. Yield line analysis of RHS connections with axial loads. Journal of Constructional Steel Research 48 (1), 1–25.

Cao, J., Yang, G., Packer, J., Burdekin, F., 1998b. Crack modeling in FE analysis of circular tubular joints. Engineering Fracture Mechanics 61 (5), 537–553.

Chakrabarti, P., Mukkamala, A., Abu-Odeh, I., 2005. Effect of joint behavior on the reassessment of fixed offshore platforms in the Bay of Campeche, Mexico. In: 24th International Conference on Offshore Mechanics and Arctic Engineering (OMAE).

Chang, E., Dover, W., 1999. Parametric equations to predict stress distributions along the intersection of tubular X and DT-joints. International Journal of Fatigue 21 (6), 619–635.

Chen, B., Hu, Y., Tan, M., 1990. Local joint flexibility of tubular joints of offshore structures. Marine Structures 3 (3), 177–197.

Chen, T., Wang, Y., 1985. The stress analysis of tubular joints of offshore drilling platform by variation method. In: 4th International Conference on Offshore Mechanics and Arctic Engineering (OMAE).

Chen, T., Zhang, H., 1993. Local joint flexibility for multibrace tubular joints. China Ocean Engineering 7 (2), 125–138.

Chen, Y., Wang, W., Zhao, X., Jiang, X., Bai, X., Zhao, Z., 2001. Experiments on bending rigidity and resistance of unstiffened tubular joints. Journal of Building Structures 22 (6), 25.

Chen, Z., 2010. Static strength of ttubular X-joint with chord fully infilled with high strength grout. Ph.D. thesis, National University of Singapore.

Choo, Y., Li, B., Liew, J., Van Der Vegte, G., Zettlemoyer, N., 1998. Static strength of T-joints reinforced with doubler or collar plates. A. A. Balkema Publishers, Tubular Structures VIII(USA), 139–145.

Choo, Y., Qian, X., Foo, K., 2005. Nonlinear analysis of tubular space frame incorporating joint stiffness and strength. In: 10th International Jack-up Platform Conference.

Choo, Y., Qian, X., Liew, J., Wardenier, J., 2003. Static strength of thick-walled CHS X-joints part I. New approach in strength definition. Journal of Constructional Steel Research 59 (10), 1201–1228.

Choo, Y., Qian, X., Wardenier, J., 2006. Effects of boundary conditions and chord stresses on static strength of thick-walled CHS K-joints. Journal of Constructional Steel Research 62 (4), 316–328.

Clarke, G., Landes, J., 1979. Evaluation of the J integral for the compact specimen. Journal of Testing and Evaluation 7, 264–269.

Dexter, E., Lee, M., 1999. Static strength of axially loaded tubular K-joints. I: behavior. Journal of Structural Engineering 125 (2), 194–201.

Dier, A., Hellan, O., 2002. A non-linear tubular joint response model for pushover analysis. In: 21st International Conference on Offshore Mechanics and Arctic Engineering (OMAE).

Dier, A., Lalani, M., 1995. Strength and stiffness of tubular joints for assessment/design purposes. In: Offshore Technology Conference, 1-4 May 1995, Houston, Texas.

DNV, 1977. Rules for the Design Construction and Inspection of Offshore Structures. Det Norske Veritas.

DNV, 2011. Design of offshore steel structures, general (LRFD Method). Det Norske Veritas.

Efthymiou, M., 1985. Local rotational stiffness of unstiffened tubular joints. KSEPL Report RKER 85.

Energo, 2007. Assessment of fixed offshore platform performance in hurricanes Katrina and Rita. Tech. Rep. E06117, Energo Engineering.

FEA CRACK, 2011. FEA CRACK version 3.2 users'manual. Structural Reliability Technology (SRT).

Fessler, H., Mockford, P., Webster, J., 1986a. Parametric equations for the flexibility matrices of multi-brace tubular joints in offshore structures. In: ICE Proceedings. Vol. 81. pp. 675–696.

Fessler, H., Mockford, P., Webster, J., 1986b. Parametric equations for the flexibility matrices of single brace tubular joints in offshore structures. In: ICE Proceedings. Vol. 81. Ice Virtual Library, pp. 659–673.

Fessler, H., Spooner, H., 1981. Experimental determination of stiffness of tubular joints. In: 2nd International Symposium on Integrity of Offshore Structures, Institute of Shipbuilders and Engineers Scotland. Vol. 198.

Gates, W., Marshall, P., Mahin, S., 1977. Analytical methods for determining the ultimate earthquake resistance of fixed offshore structures. In: Offshore Technology Conference, 2-5 May 1982, Houston, Texas.

Greenwood, P., Nikulin, M., 1996. A guide to chi-squared testing. Wiley New York.

Grenda, K., Clawson, W., Grenda, H., Grenda, N., Shinners, C., 1988. Large-scale ultimate strength testing of tubular K-braced frames. In: Offshore Technology Conference, 2-5 May 1988, Houston, Texas.

Gurson, A., 1985. Plastic flow and fracture behavior of ductile materials incorporating void nucleation, growth, and interaction. Ph.D. thesis, Brown University.

Haswell, J., 1991. Simple models for predicting stress intensity factors for tubular joints. Fatigue & Fracture of Engineering Materials & Structures 14 (5), 499–513.

Hellan, O., 1995. Nonlinear pushover and cyclic analysis in ultimate limite state design and reassessment of tubular steel offshore structures. Ph.D. thesis, The Norwegian Institute of Technology.

Holmas, T., 1985. Approximate flexibility modeling of tubular joints in marine structures. Tech. Rep. No. 4.12, The Norwegian Institute of Technology.

Holmas, T., 1987. Implementation of tubular joint flexibility in global frame analysis. Tech. Rep. No. 87.1, The Norwegian Institute of Technology.

Hyde, T., Leen, S., 1997. Prediction of elastic-plastic displacements of tubular joints under combined loading using an energy-based approach. The Journal of Strain Analysis for Engineering Design 32 (6), 435–454.

Ian Tebbett, I., 1982. The reappraisal of steel jacket structures allowing for the composite

action of grouted piles. In: Offshore Technology Conference, 3-6 May 1982, Houston, Texas.

IIW, 2009. Static design procedure for welded hollow section joints - recommendations. Tech. rep., International Institute of Welding (IIW), 3rd Ed. IIW Annual Assembly.

Inoue, K., Igarashi, S., Wakiyama, K., Matsumoto, T., Kindan, I., 1984. Buckling strength and post-buckling behavior of tubular truss towers. Welding of Tubular Structures.

Karamanos, S., Romeijn, A., Wardenier, J., 2000. Stress concentrations in tubular gap K-joints: mechanics and fatigue design. Engineering Structures 22 (1), 4–14.

Kohoutek, R., Hoshyari, I., 1992. Parametric formulae of rigidity for semi-grid tubular T-joints. Vol. 1. pp. 605–609.

Kurobane, Y., Ogawa, K., Ochi, K., Makino, Y., 1986. Local buckling of braces in tubular K-joints. Thin-walled Structures 4 (1), 23–40.

Lalani, M., 1993. Post-yield and post-peak behaviour of tubular joints in offshore structures. Tubular Structures V.

Lee, M., Bowness, D., 2002. Estimation of stress intensity factor solutions for weld toe cracks in offshore tubular joints. International Journal of Fatigue 24 (8), 861–875.

Lie, S., Lee, C., Chiew, S., Shao, Y., 2005. Mesh modelling and analysis of cracked uni-planar tubular K-joints. Journal of Constructional Steel Research 61 (2), 235–264.

Lu, L., De Winkel, G., Yu, Y., Wardenier, J., 1994. Deformation limit for the ultimate strength of hollow section joints. In: 6th International Symposium on Tubular Structures. pp. 341–347.

Makino, Y., Kurobane, Y., Takizawa, S., Yamamoto, N., 1986. Behavior of tubular T- and K-joints under combined loads. In: Offshore Technology Conference, 5-8 May 1986, Houston, Texas.

Makino, Y., Kurobane, Y., Tozaki, T., 1989. Ultimate strength analysis of simple CHS joints using the yield line theory. In: 3rd International Symposium on Tubular Structures.

Makino, Y., Kurobane, Y., Wilmshurst, S., Lee, M., 1995. Proposed ultimate capacity equations for CHS KK-joints under anti-symetric loads. In: International Offshore and Polar Engineering Conference. pp. 6–11.

Merkle, J., Corten, H., 1974. J integral analysis for the compact specimen, considering axial force as well as bending effects. American Society of Mechanical Engineers, Pressure Vessels and Piping Division (Publication) PVP 96, 286–92.

Mirtaheri, M., Zakeri, H., Alanjari, P., Assareh, M., 2009. Effect of joint flexibility on overall behavior of jacket type offshore platforms. American Journal of Engineering and Applied Sciences 2 (1), 25–30.

Morin, G., Bureau, J., Contat, N., Goyet, J., 1998. Influence of tubular joints failure modes on jacket structures global failure modes. In: 17th International Conference on Offshore Mechanics and Arctic Engineering (OMAE).

Moses, F., Liu, Y., 1992. Methods of redundancy analysis for offshore platforms. In: 11th International Conference on Offshore Mechanics and Arctic Engineering (OMAE).

MSL, 2000. Assessment criteria and researve strength of tubular joints, phase II. Tech. Rep. C20400R014, MSL Engineering limited.

Nichols, N., Birkinshaw, M., Bolt, H., 1997. Systems strength measures of offshore structures. In: International Conference on Behavior of Offshore Structures.

Ogawa, K., Yamanari, M., Makino, Y., Kurobane, Y., Yamashita, M., Sakamoto, S., 1987. Buckling and post-buckling behavior of complete tubular trusses under cyclic loading. In: Offshore Technology Conference, 27-30 April 1987, Houston, Texas.

Paik, J., Shin, B., 1990. Theoretical and experimental study for the progressive collapse strength analysis of tubular offshore structures.

Pan, W., Leen, S., Hyde, T., 2002. Static analysis of frame by localized representation of tubular joint. In: 12th International Offshore and Polar Engineering Conference.

Paris, P., Ernst, H., Turner, C., 1980. A J-integral approach to development of η-factors. ASTM Special Technical Publication (700), 338–351.

Patran, 2012. Patran's user's guide. Costa Mesa, CA/USA.

Paul, J., Makino, Y., Kurobane, Y., 1993. Ultimate resistance of tubular double T-joints under axial brace loading. Journal of Constructional Steel Research 24 (3), 205–228.

Qian, X., 2005. Static strength of thick-walled CHS joints and global frame behavior. Ph.D. thesis, National University of Singapore.

Qian, X., 2013. Failure assessment diagrams for circular hollow section X- and K-joints. International Journal of Pressure Vessels and Piping 104 (0), 43 – 56.

Qian, X., Dodds, R., Choo, Y., 2006. Mode mixity for tubular K-joints with weld toe cracks. Engineering Fracture Mechanics 73 (10), 1321–1342.

Qian, X., Dodds, R., Choo, Y., 2007. Elastic–plastic crack driving force for tubular K-joints with mismatched welds. Engineering Structures 29 (6), 865–879.

Qian, X., Dodds Jr, R., Choo, Y., 2005. Mode mixity for circular hollow section X joints with weld toe cracks. Journal of Offshore Mechanics and Arctic Engineering 127, 269.

Qian, X., Li, Y., Ou, Z., 2013. Ductile tearing assessment of high-strength steel X-joints under in-plane bending. Engineering Failure Analysis 28 (0), 176 – 191.

Qian, X., Romeijn, A., Wardenier, J., Choo, Y., 2002. An automatic FE mesh generator for CHS tubular joints. In: 12th International Conference on Offshore and Polar Engineering. Vol. 4. pp. 11–18.

Qian, X., Swaddiwudhipong, S., Nguyen, C., Petchdemaneengam, Y., Marshall, P., Ou, Z., 2012. Overload effect on the fatigue crack propagation in large-scale tubular joints. Fatigue & Fracture of Engineering Materials & Structures.

Rice, J., Paris, P., Merkle, J., 1973. Some further results of J-integral analysis and estimates. ASTM special technical publication (536), 231–245.

Rice, J., Rosengren, G., 1968. Plane strain deformation near a crack tip in a power-law hardening material. Journal of the Mechanics and Physics of Solids 16 (1), 1–12.

Romeijn, A., Puthli, R., Wardenier, J., 1991. Flexibility of uniplanar and multiplanar joints made of circular hollow sections. In: 1st International Offshore and Polar Engineering Conderence. pp. 67–76.

Shih, C., Moran, B., Nakamura, T., 1986. Energy release rate along a three-dimensional crack front in a thermally stressed body. International Journal of Fracture 30 (2), 79–102.

Skallerud, B., 1995. Inelastic line springs in non-linear analysis of cracked tubular joints. Fatigue & Fracture of Engineering Materials & Structures 18 (4), 463–475.

Skallerud, B., 1996. A mixed mode I/II inelastic line spring. International Journal of Solids and Structures 33 (28), 4143–4166.

Skallerud, B., Amdahl, J., 2002. Nonlinear analysis of offshore structures. Research Studies Press Baldock, Hertfordshire, England.

Soh, C., Chan, T., Yu, S., 2000. Limit analysis of ultimate strength of tubular X-joints. Journal of Structural Engineering 126 (7), 790–797.

Søreide, T., Amdahl, J., Granli, T., Astrud, O., 1986. Collapse analysis of framed offshore structures. In: Offshore Technology Conference, 5-8 May 1986, Houston, Texas.

Stacey, A., Sharp, J., Nichols, N., 1996. Static strength assessment of cracked tubular joints. In: International conference of Offshore Mechanics and Arctic Engineering (OMAE). pp. 211–226.

Sumpter, J., 1987. J_c determination for shallow notch welded bend specimens. Fatigue & Fracture of Engineering Materials & Structures 10 (6), 479–493.

Sumpter, J., Turner, C., 1976. Method for laboratory determination of J_c. Cracks and Fracture, 3–18.

Talei-Faz, B., Brennan, F., Dover, W., 2004. Residual static strength of high strength steel cracked tubular joints. Marine Structures 17 (3), 291–309.

Togo, T., 1967. Experimental study on mechanical behavior of tubular joints. Ph.D. thesis, Osaka University.

Tromans, P. S., Anatruk, A., Hagemeijer, P., 1991. New model for the kinematics of large ocean waves application as a design wave. In: 1st International Offshore and Polar Engineering Conference. pp. 64–71.

Turner, C., 1981. The ubiquitous η factor. Fracture Mechanics 743, 314.

Ueda, Y., Rashed, S., Ishihama, T., Nakacho, K., 1986. Flexibility and yield strength of joints in analysis of tubular offshore structures. In: 5th International Conference on Offshore Mechanics and Arctic Engineering (OMAE). Vol. 1. pp. 293–301.

Ueda, Y., Rashed, S., Nakacho, K., 1990. An improved joint model and equations for flexibility of tubular joints. Transactions of the ASME. Journal of Offshore Mechanics and Arctic 112 (2), 157–168.

UEG, 1985. Design of tubular joints for offshore structures. Underwater Engineering Group.

USFOS, 2009. USFOS mannual. Marintek SINTEF group.

Van der Vegte, G., 1995. The static strength of uniplanar and multiplanar tubular T- and X-joints. Ph.D. thesis, Delft University.

Van der Vegte, G., Makino, Y., Wardenier, J., 2002. The effect of chord preload on the static strength of uniplanar tubular K-joints. In: 12th International Offshore and Polar Engineering Conference.

Wang, B., Hu, N., Kurobane, Y., Makino, Y., Lie, S., 2000. Damage criterion and safety assessment approach to tubular joints. Engineering structures 22 (5), 424–434.

Wang, W., Chen, Y., Zhao, X., 2007. State of the art and key issues on performance-based design of steel tubular joints. China Civil Engineering Journal 40 (11), 1–8.

Wang, X., Wu, J.-F., Qian, X., 2011. Crack driving force and ultimate strength of thick-walled CHS X-joints with near-toe cracks. In: International Offshore and Polar Engineering Conference. pp. 39–44.

Wardenier, J., 2002. Hollow sections in structural applications. CIDECT.

Xu, H., Chen, B., Hu, Y., Pan, H., 1996. Parametric analysis and experimental study on local flexibility of TY-type tubular joints. China Ocean Engineering 10 (1), 71–84.

Yura, J., Zettlemoyer, N., Edwards, I., 1980. Ultimate capacity equations for tubular joints. In: Offshore Technology Conference, 5-8 May 1980, Houston, Texas.

Zakeri, H., Alanjari, P., Assareh, M., 2009. Effect of joint flexibility on overall behavior of jacket type offshore platforms. American Journal of Engineering and Applied Sciences.

Zayas, V., Mahin, S., Popov, E., 1980. Cyclic inelastic behavior of steel offshore structures. University of California, College of Engineering, Earthquake Engineering Research Center.

Zettlemoyer, N., 2010. Life extension of fixed platforms. In: 13th International Symposium on Tubular Structures.

Publication

Qian, X., **Zhang, Y.** and Choo, Y. S. (2012). Nonlinear formulation for tubular joints in frame analysis. 14th International Symposium on Tubular Structures, London, UK.

Zhang, Y., Qian, X. and Choo, Y. S. (2012). A phenomenological fracture representation for tubular K-joints. 10th International Conference on Advances in Steel Concrete Composite and Hybrid Structures, Singapore.

Qian, X., **Zhang, Y.** and Choo, Y. S. (2011). A load-deformation formulation for CHS X- and K-joints in push-over analyses. Accepted by Journal of Constructional Steel Research.

Zhang, Y. and Qian, X. (2013). An eta-approach to evaluate the elastic-plastic energy release rate for weld-toe cracks in tubular K-joints. Engineering Structures, 51, 88-98.

Qian, X., **Zhang, Y.** and Choo, Y. S. (2013). A load-deformation formulation with fracture representation based on the J-R Curve for tubular joints. Engineering Failure Analysis, 33, 347-366.